Dissertation
submitted to the
Combined Faculties for the Natural Sciences and for Mathematics
of the Ruperto-Carola University of Heidelberg, Germany
for the degree of
Doctor of Natural Sciences

presented by
Dipl.-Phys. Volker Gaibler
born in: Ehingen (Donau), Germany
Oral examination: 12 November 2008

Very Light Extragalactic Jets with Magnetic Fields

Referees: **Prof. Dr. Max Camenzind**
Prof. Dr. Klaus Meisenheimer

Abstract

We explore the global structure and evolution of powerful radio sources located in clusters of galaxies and their interaction with the ambient gas, in particular with respect to the effects of magnetic fields. Recent observations of inverse-Compton emission from their cocoons at X-ray energies indicate that magnetic fields are present on a considerable (near-equipartition) level. To investigate the impact of magnetic fields on dynamics and morphology, we performed a series of magnetohydrodynamical simulations of bipolar jets, considering a wide range of density contrasts between the jet and the ambient gas and employing a globally consistent setup of the magnetic field and the jet–environment interaction. We find that already sub-equipartition fields ($\beta \sim 10$) stabilize the contact surface between the jet plasma and the ambient gas, resulting in pronounced jet heads and considerably suppressed entrainment. We identify a new shearing mechanism in the jet head, which efficiently amplifies magnetic fields and transfers part of the huge kinetic jet power to magnetic energy. We compare the propagation and shapes of the bow shocks and cocoons with self-similar models, finding deviations for the cocoon width evolution for sources approaching pressure balance with the environment. The simulations exhibit round and weak bow shocks for low jet densities, consistent with X-ray observations in galaxy clusters. Turbulent motion in the cocoon produces waves and ripples in the shocked ambient gas, and hereby provides a physical explanation for those recently found in Perseus A. We compute emission maps for synchrotron, inverse-Compton and bremsstrahlung emission for our simulation data, yielding overall agreement with observed sources within the assumed simplifications. Furthermore, two models for the emission-line nebulae in high-redshift radio galaxies are applied to the simulations, finding that none of them in their considered versions can explain all observed properties yet.

Zusammenfassung

In der vorliegenden Arbeit wird die globale Struktur und Entwicklung von leistungsstarken Radioquellen in Galaxienhaufen sowie deren Wechselwirkung mit dem umgebenden Gas untersucht, insbesondere im Hinblick auf die Auswirkungen von Magnetfeldern. Neue Beobachtungen der Invers-Compton-Emission ihrer Cocoons im Röntgenbereich zeigen, daß dort Magnetfelder von erheblicher Stärke (nahe der Äquipartition) vorhanden sind. Um deren Auswirkungen auf die Dynamik und das Erscheinungsbild zu untersuchen, wurde eine Reihe von magnetohydrodynamischen Simulationen von bipolaren Jets über einen weiten Bereich von Dichtekontrasten durchgeführt, unter Verwendung eines insgesamt konsistenten Setups der Magnetfelder und der Wechselwirkung von Jet und Umgebungsgas. Es zeigt sich, daß bereits Magnetfelder unterhalb der Äquipartition ($\beta \sim 10$) die Kontaktfläche zwischen Jetplasma und Umgebungsgas stabilisieren und ausgeprägte Jetköpfe mit deutlich unterdrücktem Entrainment zeigen. Ein Scherungsmechanismus im Jetkopf verstärkt Magnetfelder und wandelt einen Teil der gewaltigen kinetischen Jetleistung in magnetische Energie um. Die Ausbreitung und Form der Bugschocks und Cocoons werden mit selbstähnlichen Modellen verglichen, wobei sich zeigt, daß die zeitliche Entwicklung der Cocoonbreite für Quellen abweicht, die sich einem Druckgleichgewicht mit der Umgebung annähern. Die Simulationen zeigen für niedrige Jetdichten runde und schwache Bugschocks, wie sie auch in Röntgenbeobachtungen in Galaxienhaufen gefunden werden. Turbulenz im Cocoon erzeugt Wellen im geschockten Umgebungsgas und liefert damit eine physikalische Erklärung für die Beobachtung selbiger in Perseus A. Für die Simulationsdaten werden Synchrotron-, Invers-Compton- und Bremsstrahlungsemissionskarten berechnet, die innerhalb der verwendeten Näherungen mit Beobachtungen übereinstimmen. Des weiteren werden die Simulationen auf die Emissionsliniengas-Nebel in hochrotverschobenen Radiogalaxien angewendet, wobei allerdings keines der betrachteten zwei Modelle alle beobachteten Eigenschaften erklären kann.

Contents

1 Introduction **9**
- 1.1 Active Galactic Nuclei . . . 9
- 1.2 Radio Galaxies and Jets . . . 13
- 1.3 Galaxy Clusters . . . 21
- 1.4 Simulation of Jets . . . 22
- 1.5 Aims and Outline of the Thesis . . . 24

2 Theory, Numerics and Setup **27**
- 2.1 Magnetohydrodynamics . . . 27
- 2.2 Numerical Scheme . . . 30
- 2.3 Vectorization and Parallelization . . . 30
- 2.4 Code Optimization and Extension . . . 33
- 2.5 Setup . . . 34
  - 2.5.1 Parameter Study Setup . . . 36
  - 2.5.2 Force-balance Setup . . . 38
- 2.6 Resolution Study . . . 43
- 2.7 Visualization of Turbulent Vector Fields . . . 49

3 Evolution and Magnetic Fields **53**
- 3.1 Morphology . . . 53
- 3.2 Defining the Cocoon . . . 55
  - 3.2.1 Cell Assignment . . . 55
  - 3.2.2 Width Measurement . . . 57
- 3.3 Evolution of Bow Shock and Cocoon . . . 58
  - 3.3.1 Cocoon Pressure Evolution . . . 58
  - 3.3.2 Bow Shock . . . 61
  - 3.3.3 Cocoon . . . 64
  - 3.3.4 Aspect Ratio . . . 64
- 3.4 Entrainment . . . 66
- 3.5 Energy Budget . . . 69
- 3.6 Magnetic fields . . . 71
- 3.7 The Lightest Jets . . . 76
- 3.8 Discussion . . . 79
  - 3.8.1 Magnetic Fields . . . 79
  - 3.8.2 Dynamical Evolution . . . 81
- 3.9 Summary . . . 84

4 Emission Maps **85**
4.1 Emission Processes and Projection . . . 85
4.1.1 Synchrotron Emission . . . 85
4.1.2 Inverse-Compton Emission . . . 87
4.1.3 Bremsstrahlung Emission . . . 88
4.1.4 Projection Method . . . 89
4.2 Synchrotron Emission Maps . . . 91
4.2.1 Different Methods . . . 92
4.2.2 Viewing Angle . . . 97
4.2.3 Evolution . . . 100
4.3 Inverse-Compton Emission Maps . . . 100
4.3.1 Methods . . . 100
4.3.2 Inclination and Evolution . . . 101
4.4 Bremsstrahlung Emission Maps . . . 106
4.4.1 Viewing Angle and Evolution . . . 106
4.4.2 Energy Bands . . . 109
4.4.3 Pressure Waves . . . 109
4.5 Discussion . . . 111

5 Emission-Line Gas in High-Redshift Radio Galaxies **117**
5.1 Ionized Gas Nebulae and Alignment Effect . . . 117
5.2 Models of the Emission-Line Gas Location and Origin . . . 119
5.3 Results for the Shocked Ambient Gas Model . . . 119
5.4 Results for Cocoon Model . . . 123
5.5 Discussion . . . 128

6 Summary and Concluding Remarks **131**

A Abbreviations and Variables **135**
A.1 Abbreviations . . . 135
A.2 Units . . . 135
A.3 Variables . . . 136

Bibliography **137**

1 Introduction

1.1 Active Galactic Nuclei

Black holes are extremely simple but exotic solutions to Einstein's field equations of General Relativity. They have long been regarded as exotic objects, whose actual existence is quite uncertain. However, today there is considerable evidence that these objects do indeed exist, ranging from stellar mass black holes ($\sim 10\,M_\odot$) to supermassive black holes with 10^6 to several $10^9\,M_\odot$, and that the latter reside in the centers of most, if not all, massive galaxies (Magorrian et al., 1998; Kormendy, 2004; Camenzind, 2007). In active galactic nuclei (AGN) this central black hole currently accretes matter, giving rise to various phenomena which historically resulted in a large number of AGN classes. The elliptical galaxy M87, shown in Fig. 1.1, is a nearby example of an active galaxy.

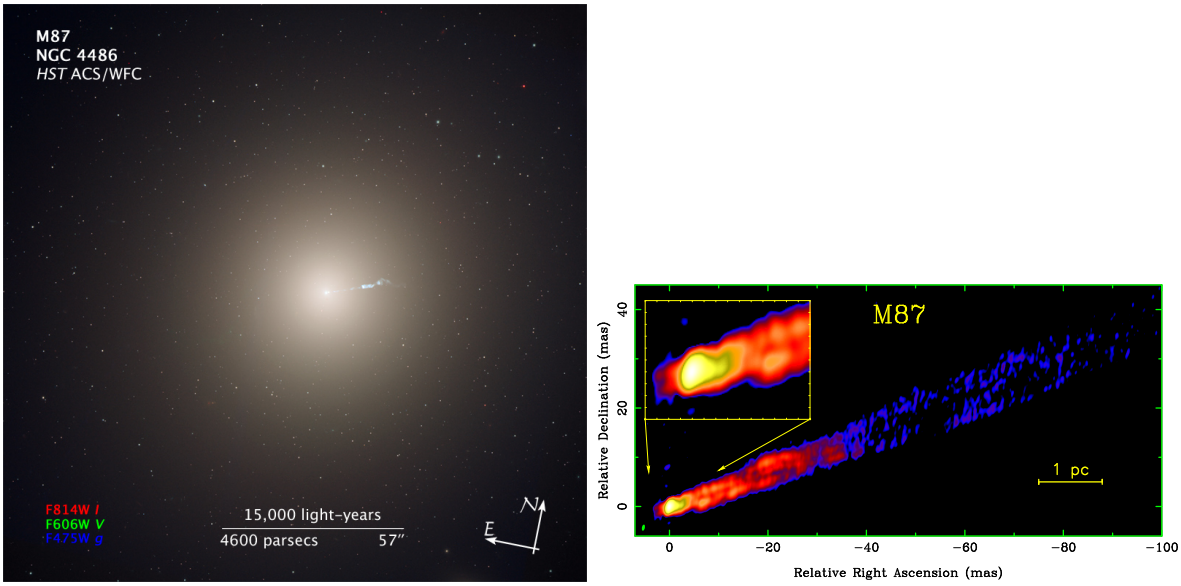

Figure 1.1: *Left:* The active galaxy M87, as seen in the optical by the Hubble Space Telescope, hosts one of the most massive ($3 \times 10^9\,M_\odot$, Macchetto et al., 1997) black holes known. An FR I jet (see Sect. 1.2) emerges from the core and reaches out to the kpc scale (Credit: NASA, ESA, and the Hubble Heritage Team, STScI/AURA). *Right:* VLBA radio image of the inner jet of M87. The jet is already well-collimated on the pc scale and a weak counterjet feature is visible on the opposite side of the core (Credit: Kovalev et al., 2007).

Examples for this are Seyfert galaxies, showing a bright point-like nucleus in the optical with a luminosity comparable with the host galaxy, and their even more luminous counterparts,

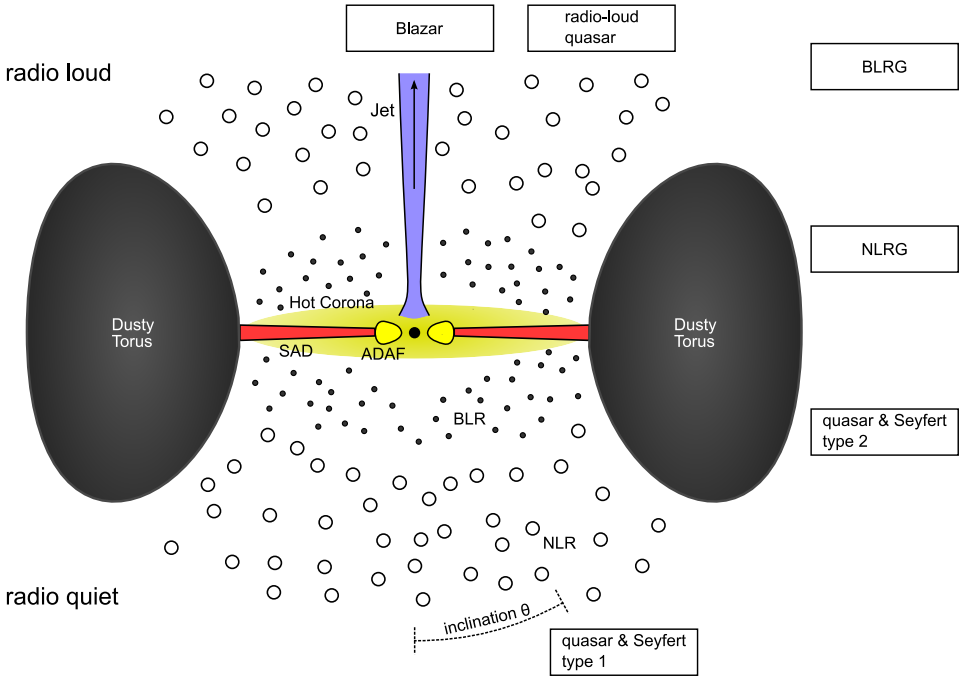

Figure 1.2: The AGN paradigm according to the unified model. The central black hole is surrounded by a thick accretion torus (ADAF) and a thin standard accretion disk (SAD). A dusty torus emitting at infrared wavelengths is located further out. The emitting clouds of the narrow-line region (NLR) are visible at all inclination angles θ, but the broad-line region (BLR) is obscured by the dusty torus for larger inclinations. The upper half corresponds to radio-loud objects, while the lower half describes radio-quiet AGN. Since the distances vary by several orders of magnitude, the figure is not drawn to scale. The boxed labels indicate typical viewing angles for different AGN classes. Note that if a jet is present, it extends in *both* directions.

quasars, where the active nucleus outshines the galaxy making them appear star-like at large distances. Both show an unusually blue continuum with strong broad and narrow emission lines ("type 1") or only narrow emission lines ("type 2"). When Baade & Minkowski (1954) identified the bright radio source Cygnus A with a distant galaxy in, another AGN class was added: radio galaxies. They show strong radio emission, which could be separated into two strong radio-emitting regions around the galaxy as well as a compact core in the center of the galaxy in high resolution data.

Detection of broad emission lines in the polarized light of type 2 Seyfert galaxies (Antonucci & Miller, 1985), however, indicated that the two types are not distinct classes but may rather result from different viewing angles on the same objects, if the polarized light was interpreted as scattered light. This idea ultimately lead to the development of the "unified model" (Barthel, 1989; Antonucci, 1993; Urry & Padovani, 1995), which explain most of the different classes by different viewing angles. Additionally, they include radio-loud and radio-quiet objects, depending on whether a prominent (radio-emitting) jet is present.

Fig. 1.2 shows a sketch of the basic constituents of an AGN according to the unified scheme. In the very center resides the black hole (BH) with a Schwarzschild radius

$$r_{\mathrm{S}} \approx 0.1\ \mathrm{mpc} \left(\frac{M_{\mathrm{BH}}}{10^9\, M_\odot} \right) . \tag{1.1}$$

For high accretion rates it is surrounded by an optically thick but geometrically thin standard accretion disk (SAD, Shakura & Sunyaev, 1973) which extends out to $\sim 1\,000\, r_{\mathrm{S}}$. For low accretion this evolves into an optically thin and geometrically thick ADAF (advection dominated accretion flow, originally by Narayan & Yi, 1995) and a truncated accretion disk. The accretion disk is responsible for the strong optical/UV continuum due to its high temperatures (multi-color black body), while the ADAF and a hot corona enclosing the accretion disk produce hard X-ray radiation by inverse-Compton scattering. The accretion disk is surrounded by a thick dusty torus, which is found on the scale of several pc and contains molecular gas and dust, which may form a matter reservoir for the accretion disk. It is heated by the intense radiation from the central components and reemits in the infrared. The inner part of the AGN also contains the broad-line region (BLR), which consists of dense and fast-moving clouds ionized by the intense disk radiation and shocks, and is responsible for broad (full width at half maximum corresponding to 1 000 to 10 000 km/s) permitted emission lines. Further outwards, extending beyond the dusty torus, lies the narrow-line region (NLR) with ionized clouds moving at lower velocity, showing both forbidden and permitted line emission of several 100 km/s line width.

While historically quasars have been discovered as radio sources with star-like counterparts at optical wavelengths, most of them ($\sim 90\,\%$) are radio-quiet. The lower half of Fig. 1.2 corresponds to the situation in radio-quiet sources like radio-quiet quasars and Seyfert galaxies. The upper half, in contrast, describes radio-loud sources like radio-loud quasars and radio galaxies, which form two highly directed plasma streams, jets, in opposite directions in the immediate environment of the black hole. The highly variable class of blazars is generally explained by having one of their jets pointing towards the observer, and relativistic effects as Doppler effect and beaming are responsible for the high variability on short time scales and flat spectra.

If viewed from a small inclination angle (between the observer and the disk/torus axis), both BLR and NLR are visible and the AGN is observed as "type 1" with broad emission lines. However, for larger inclination angles, only the NLR is visible since the BLR is obscured by the dusty torus, and the AGN appears as "type 2" with only narrow emission lines. This is not only valid for Seyfert galaxies and quasars, but also for radio galaxies (broad-line radio galaxies BLRG and narrow-line radio galaxies NLRG). Studies by Osterbrock & Shaw (1988), Barthel (1989) and Mullin et al. (2008) find that obscuration by the torus should correspond to inclinations θ of more than $\sim 45°$.

Radiation powers associated with AGN are enormous: for Seyfert-1 galaxies they are typically $\sim 10^{44}$ erg s^{-1}, and for quasars they even exceed 10^{46} erg s^{-1}. This power originates from accretion of matter onto the central black hole in its gravitational potential, which yields an energy of $\approx 0.1\, Mc^2$ for the accreted matter of mass M, independent of the black hole mass. The power is generally compared with the "Eddington luminosity"

$$L_{\mathrm{Edd}} = 1.26 \times 10^{47}\, \mathrm{erg\,s^{-1}} \left(\frac{M_{\mathrm{BH}}}{10^9\, M_\odot} \right) , \tag{1.2}$$

which gives the limiting luminosity of a spherically symmetric object, where radiation pressure on accreting matter equals the gravitational force. For higher luminosity, accretion onto the central object cannot be sustained anymore. Due to the great simplification it is only a soft limit (cf. slim disks, Abramowicz et al., 1988), but gives an idea of the maximum power radiated away by a quasar. If the luminosity is produced by mass accretion with

$$L = \eta \dot{M} c^2 \,, \tag{1.3}$$

where η is the efficiency of converting potential energy into radiation, the maximum accretion rate is

$$\dot{M}_{\mathrm{Edd}} = 22\, M_\odot\, \mathrm{yr}^{-1} \left(\frac{M_{\mathrm{BH}}}{10^9\, M_\odot}\right) \left(\frac{0.1}{\eta}\right) . \tag{1.4}$$

If the accreted matter emits all its potential energy at the innermost stable circular orbit of the black hole, then $\eta = 0.06$ for a non-rotating Schwarzschild black hole and $\eta \approx 0.42$ for a maximally rotating Kerr black hole. Generally, $\eta = 0.1$ is assumed.

Accretion converts gravitational energy of the accreted matter into thermal energy, which is then radiated away efficiently in an accretion disk. However, for accretion to be possible, the matter has to lose its angular momentum, which is believed to be caused by a "turbulent viscosity" in the accretion disk that transports angular momentum outwards and mass inwards. This behaviour is shown by the magneto-rotational instability (MRI, Balbus & Hawley, 1991), which is effective in weakly magnetized, differentially rotating disks. By magnetic stresses it provides the needed angular momentum transport on the dynamical time scale of the disk and causes turbulence, making it the favoured physical mechanism responsible for the turbulent viscosity. Launching of jets is found for AGN with accretion on the percent level of the Eddington accretion rate. The observed evolution of microquasars (accreting stellar mass black holes) indicates that launching of radio jets is linked with truncation of the accretion disk and the formation of an inner hot flow (ADAF in Fig. 1.2; Fender et al., 2004; Done et al., 2007). For actual jet formation, there are mainly two models considered: The acceleration and collimation of matter from the disk corona by the magnetic fields of the rotating disk (Blandford & Payne, 1982) and the formation of a jet by magnetic field lines that are dragged with the black hole rotation in the ergosphere (Blandford & Znajek, 1977). In the first case, energy originates from the accretion power, while in the second scenario, energy is extracted from the black hole spin. A particular feature of powering jets by the black hole spin is that a huge reservoir of energy can be tapped even in episodes of low accretion that are typical for strong jet formation and it could even be "refilled" by a subsequent stronger accretion phase.

The accretion dependence of AGN phenomena, however, beyond the purely geometric explanation within the unified model show that this models will have to be extended in the future by evolutionary effects within a source. Additionally, AGN vary considerably with cosmic evolution since observations indicate that quasars were brighter and much more common at redshifts of $z \approx 2$–3 (Willott et al., 2001; Croom et al., 2004; Richards et al., 2006), declining again for higher z, and the fraction of radio-loud AGN increases with galaxy mass, reaching $> 30\,\%$ for the most massive galaxies (Best et al., 2005). Hence, galactic evolution, the amount of matter available for accretion, black hole growth due to accretion as well as feedback of the AGN onto the environment influence the evolution and properties of these objects. Observations of radio galaxies at high redshifts, up to $z \approx 5.2$, will briefly be described in Chapter 5 (see also review by Miley & De Breuck, 2008).

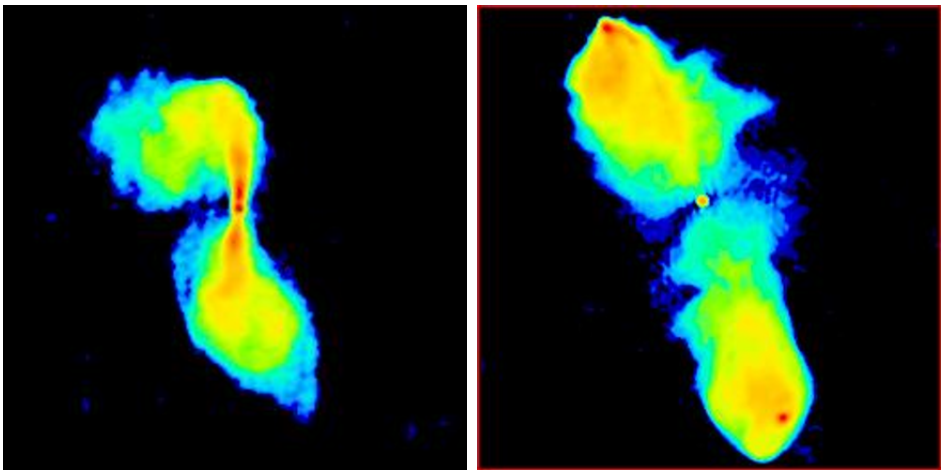

Figure 1.3: *Left:* Radio galaxy 3C 272.1 is a FR I class object, showing its highest brightness (red) in the center. The relativistic speeds are responsible for the beaming which lets the upper jet appear brighter. Further out, the jet decollimates and forms "plumes". *Right:* Radio galaxy 3C 98 belongs to the FR II class. It shows bright hotspots at the upper and lower edges (in red), where the beam impacts onto the ambient gas and forms two prominent lobes. Images from Leahy (2000).

1.2 Radio Galaxies and Jets

Jet activity is generally accompanied by synchrotron emission from relativistic electrons in the magnetized plasma, which is most prominently observable at radio frequencies and hence the reason why AGN with jet activity got names like "radio galaxies" or "radio-loud quasars". While resolution was quite limited at early times, these objects could be studied in much more detail with the advent of radio interferometers, exhibiting a plethora of details with a correspondingly rich nomenclature, and after a physical model for the double radio sources was established (Blandford & Rees, 1974; Scheuer, 1974), which interpreted double radio sources as being powered by an AGN via collimated powerful beams ("jets"), the situation became clearer.

Morphology Following Fanaroff & Riley (1974), double radio sources are divided into two classes: FR I sources are brightest in the center (separation between the brightest regions on opposite sides of the central galaxy is less then half the total extent of the source) and typically show a bright jet in the center which then decollimates and forms "plumes" at larger distances. In contrast, FR II sources are brightest at the outer edges (separation is larger than half the total extent) and show dim jets but extended lobes with bright hotspots at the outer edges. Two examples (3C 272.1 and 3C 98) are shown in Fig. 1.3. Fanaroff & Riley found that these morphological properties are correlated with the radio power of the sources, FR I sources being of low power ($\lesssim 10^{25}$ W Hz^{-1} at 1.4 GHz; Bridle & Perley, 1984) and FR II sources being of high radio power ($\gtrsim 10^{25}$ W Hz^{-1}). Hence FR IIs seem to be able to transfer their power with beams to large distances without dramatic losses, while this is not the case for FR Is. It is still unclear what the origin for this dichotomy is – whether it depends on the central source,

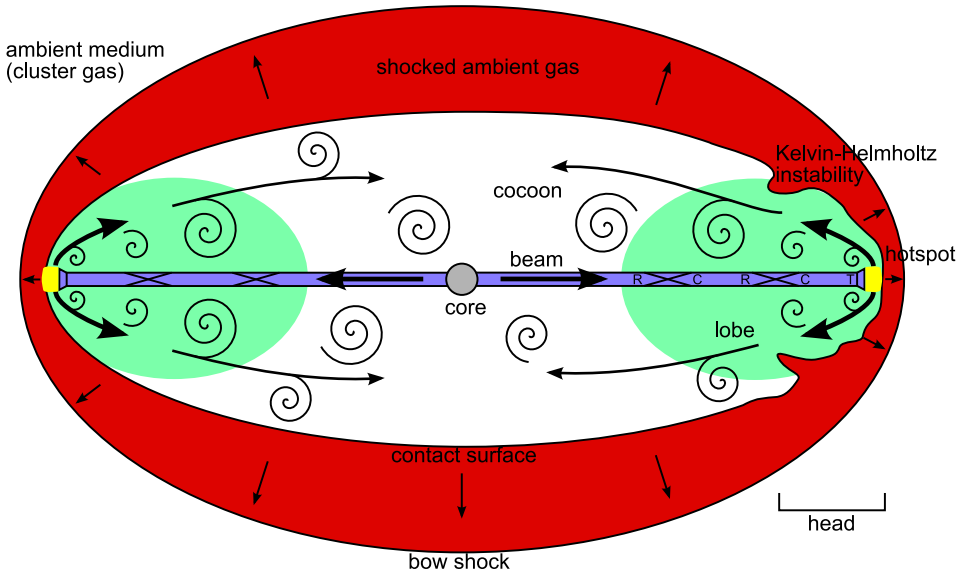

Figure 1.4: Schematic representation of an FR II radio source in jet simulations. The beam (blue) emerges from the core with the AGN and the plasma passes through regions of rarefaction (R) and compression (C) at internal shocks until it is strongly decellerated at a terminal shock (T). The shocked plasma streams out of the hotspot high-pressure region (yellow) and forms the backflow. Generated vortices are advected with the flow, inflating the cocoon (inner white region and green). The outer parts of the cocoon, where radio-emitting electrons did not yet cool down, are visible as "lobes". The overpressured cocoon drives a bow shock outwards into the ambient medium, forming a thick shell of shocked ambient gas. The strong shearing between the backflow and the shocked ambient gas excites Kelvin-Helmholtz instabilities, forming "fingers" of ambient gas that reach into the cocoon. The figure is rotated by 90° with respect to Fig. 1.2.

how the jet is formed, or whether it is caused by the environment the jet propagates through. Both classes are believed to have relativistic jets in the inner regions, making Doppler beaming effects important. However, while FR I sources show strong beaming near the center, they seem to entrain a significant amount of ambient matter, which slows down the jet on the scale of several kpc, letting both jets appear equally bright, and causes decollimation. FR IIs, in contrast, are thought to remain relativistic even on large scales.

Fig. 1.4 shows the schematic representation of an FR II source, as will be considered in the present work. The bipolar jet is formed in the active nucleus, visible in radio images as "core". Internal shocks are excited in the beam and the jet plasma passes through neighbouring regions of rarefaction and compression. Finally, the plasma impacts onto the ambient gas, forming a terminal shock (a Mach disk or an annular shock) and a post-shock "hotspot". The shocked plasma leaves this region of very high pressure sideways and forms the backflow, which inflates the cocoon. Vortices generated at the terminal shock are advected into the cocoon. Since the ambient gas is much denser than the jet plasma, the jet head propagates much slower than the beam speed and the backflow is correspondingly fast. The cocoon is overpressured with respect to the environment and drives a bow shock into the ambient medium, forming a thick shell of shocked ambient gas. Since the cocoon pressure is higher in the jet head

region with the hotspot, the axial propagation is faster than the lateral and the bow shock is elongated. The strong shearing at the contact discontinuity between the jet plasma and the ambient gas excites Kelvin-Helmholtz and Rayleigh-Taylor instabilities due to possible short-term acceleration. These instabilities grow and form fingers that are entrained with the backflow and are finally mixed into the cocoon. The outer regions of the cocoon, where the synchrotron-emitting electrons are still energetic, are visible at radio frequencies as "lobes".

Jets Although double radio sources are powered by the jets, those are not always visible. When jets are detected in high-power sources, they mostly appear one-sided, which is explained by relativistic beaming. It brightens the approaching jet and dims the receding one. Mullin et al. (2008) find jet detection rates of 60 % to 80 % for 98 FR II sources from the sample by Laing et al. (1983). They find that the detection rates are higher for broad-line radio galaxies and quasars ($\approx$ 73 %) than for narrow-line radio galaxies ($\approx$ 60 %), also consistent with beaming, which is expected to be stronger in broad-line sources due to smaller inclination angles. Observed jets remain well-collimated over long distances and show zero or small opening angles ("strong-flavour jets" with $< 5°$, Leahy, 2000; Bridle & Perley, 1984), which indicates that the jets are supersonic. Composition of the jet plasma is still under debate. In the standard model of Blandford & Rees (1974), a proton-electron plasma is assumed, while Kundt & Gopal-Krishna (1980) argue for an electron-positron plasma with only minor contributions from baryons, which may also be motivated by certain jet formation scenarios (Celotti & Blandford, 2001). Ghisellini (2008) finds indication that protons carry most of the power, and simulations by Scheck et al. (2002) show that at least the source morphology is not dependent on the composition.

Emission Radio emission from jets is polarized (typically in the range of 10 to 40 %, locally $>$ 50 % are not unusual, Bridle & Perley, 1984) and interpreted as synchrotron radiation by relativistic electrons spiralling in a magnetic field. According to synchrotron theory (e.g. Rybicki & Lightman, 1979; Pacholczyk, 1970, but see also Chapter 4), the observed brightness depends on the magnetic field as well as the distribution of the emitting electrons; the latter includes both the density as well as the energy distribution. Power law behaviour of the synchrotron spectra ($F_\nu \propto \nu^{-\alpha}$) indicate that the emitting electrons also show a power law distribution of energies. These non-thermal electrons are believed to be accelerated to high energies either in shocks by first order Fermi acceleration (diffusive shock acceleration) or stochastically, not restricted to shocks though less efficient, by second order Fermi acceleration (see Longair, 1994). Electron acceleration may also occur by reconnection of magnetic fields (Romanova & Lovelace, 1992). However, there is also a thermal population of electrons, which is relativistic, correspondingly has energies according to the Maxwell-Jüttner distribution and is the reservoir of electrons available for acceleration to high energies. It is so far not clear, what fraction of electrons is part of the nonthermal distribution and what fraction is part of the thermal "bulk". Particle acceleration will not only increase the number of nonthermal particles but also the spectrum. First order Fermi acceleration in strong nonrelativistic shocks results in a power law exponent $p = 2$ for the energy distribution, corresponding to a spectral index $\alpha = (p - 1)/2 = 0.5$, which is indeed often found in hotspots (e.g. Carilli et al., 1991; Meisenheimer et al., 1997).

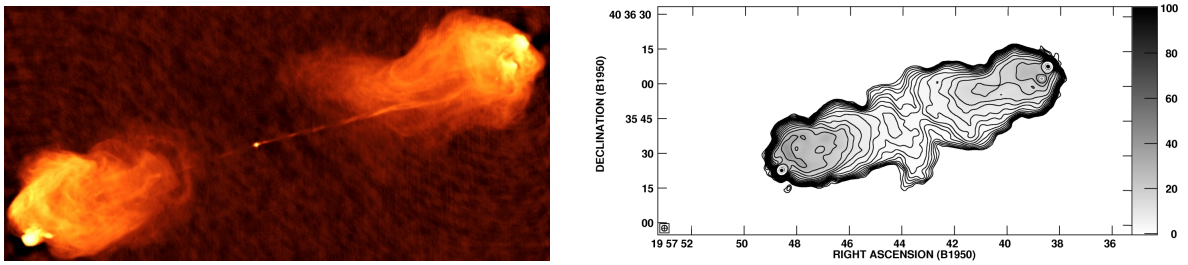

Figure 1.5: *Left:* 5 GHz map of Cygnus A (Perley et al., 1984), showing two prominent lobes. *Right:* The 327 MHz map (Lazio et al., 2006) shows that the cocoon fills up the whole region between the lobes.

Synchrotron emitting electrons observable at radio frequencies typically have Lorentz factors $\gamma \sim 10^4$. Since losses by synchrotron emission are larger for higher particle energies, electrons with high Lorentz factors, emitting at higher frequencies, cool more rapidly and the spectrum steepens (Heavens & Meisenheimer, 1987). Corresponding breaks in the radio spectra hence allow the determination of the time since the last acceleration. Spectral ages give a minimum age of the source and are generally of the order of 10^7 years (Alexander & Leahy, 1987; Carilli et al., 1991; Liu et al., 1992). Since the jet plasma streams from the hotspot into the cocoon, radio spectra steepen towards the midplane (Leahy et al., 1989). Due to this ageing, only low-frequency emitting electrons are observable further away from the hotspots, making the whole cocoon visible only at low radio frequencies, while at higher frequencies only the outer parts of it are visible as lobes. Low frequency maps, however, generally suffer from low resolution, which becomes critical for small or distant radio sources. Fig. 1.5 shows this frequency dependence exemplarily with radio maps of Cygnus A at low (327 MHz) and high (5 GHz) radio frequencies.

Magnetic Fields Though the synchrotron emissivity depends on the magnetic field magnitude, it is impossible to determine the field magnitudes from observations without further assumptions, since the emissivity also depends on the unknown electron density. However, it is common to assume equipartition between magnetic energy and the energy density of the nonthermal particles, which minimizes the total energy (Longair, 1994) and yields a minimum energy density. By using this approximation, magnetic field magnitudes may be determined from radio observations, yielding field strengths of $\sim 300\,\mu$G or more in hotspots and typically tens of μG in lobes (Alexander et al., 1984; Alexander & Leahy, 1987; Carilli et al., 1991; Meisenheimer et al., 1989). The magnetic field topology can be derived from polarization measurements, though projection and resolution effects complicate interpretation of the observations. Close to the core, projected magnetic fields are usually parallel to the jet axis. In weak, two-sided jets, magnetic fields usually change within the first 10 % of the jet length to perpendicular at the center and parallel near the edges or they become perpendicular to the jet axis throughout the jet. Powerful one-sided jets, in contrast, show projected magnetic fields parallel to the axis for almost their entire length. However, in some knots and at bright hotspots, magnetic fields become dominated by the perpendicular component, possibly by shocks (Bridle, 1982; Bridle & Perley, 1984). The threedimensional magnetic configuration

in the beams of powerful jets hence may be helical with some random component or randomly tangled fields, which get stretched at the beam boundaries (Matthews & Scheuer, 1990b).

Cocoons Observed cocoon aspect ratios (full length to full width) vary much between different sources. Leahy & Williams (1984), Leahy et al. (1989) and Mullin et al. (2008) find values mostly between 2 and 12. Mullin et al. give a median value of 5 for narrow-line radio galaxies and 3.5 for quasars and broad-line radio galaxies, consistent with the unified model (but note that their aspect ratio definition differs by a factor of 2). However, while for full source sizes below 100 kpc the cocoon aspect ratios appear constant (self-similar growth, aspect ratios between 2 and 5), the distribution is wider with generally larger values for sizes above 100 kpc.

While radio observations are the traditional way to explore jets, the advent of modern X-ray space telescopes like Chandra or XMM-Newton opened up a complementary view on extragalactic radio sources. Jet beams, knots and hotspots are visible over a huge spectral range from radio to optical and X-ray energies. Additionally, extended X-ray emission from the cocoon and the ambient gas are observable. Inverse-Compton scattering of cosmic microwave background (CMB) photons by relativistic electrons in the jet and cocoon plasma is now thought to mainly produce the observable X-ray emission from the cocoon and it gives information about electrons with energies of $\gamma \sim 10^3$, lower than accessible with today's radio telescopes. These electrons are far less affected by the cooling complications described above and hence illuminate the entire jet cocoon. Additional contributions may come from inverse-Compton scattering of AGN infrared photons in the cocoon (Brunetti et al., 1997) or from up-scattered jet-originated synchrotron photons (synchrotron self-Compton, Harris et al., 1994) in hotspots. For FR I sources, there is strong support that X-ray emission from the jet beams comes from synchrotron emission of ultrarelativistic ($\gamma \sim 10^7$) electrons, but for FR II sources both synchrotron and inverse-Compton scattered CMB photons are discussed for beam X-ray emission (for a recent review, see Harris & Krawczynski, 2006). For beam emission, relativistic beaming will have large impact. Jets with a "spine–sheath" structure (Celotti et al., 2001), consisting of a mildly relativistic sheath around a highly relativistic inner spine, are discussed to explain differences between observations at different inclination angles.

For X-ray emission from the cocoon, inverse-Compton scattered CMB photons seem to be the dominant contribution for most sources. Fig. 1.6 shows an X-ray image of Pictor A with inverse-Compton emission from both the lobes as well as from the jet (Feigelson et al., 1995; Croston et al., 2005; Kataoka & Stawarz, 2005; Hardcastle & Croston, 2005). Since inverse-Compton emission does not depend on the magnetic field strength, it can be used, in combination with radio observations, to measure field strengths without equipartition assumptions. Croston et al. (2005) find cocoon magnetic fields with typically 0.7 the equipartition value and field strengths of $\sim 10\,\mu$G, however with several sources lying in the range of 2 to $\sim 100\,\mu$G. Goodger et al. (2008) find evidence for spatially varying field strength within the lobes.

X-ray Cavities Jets propagate into the interstellar, intra-cluster or extragalactic medium – depending on the source size and the environment. Especially in clusters of galaxies, emission from the ambient cluster gas dominates the X-ray emission with its thermal bremsstrahlung, possibly making the emission from inverse-Compton scattered CMB photons unobservable. The compressed ambient gas, enclosed by the leading bow shock, causes enhanced emission,

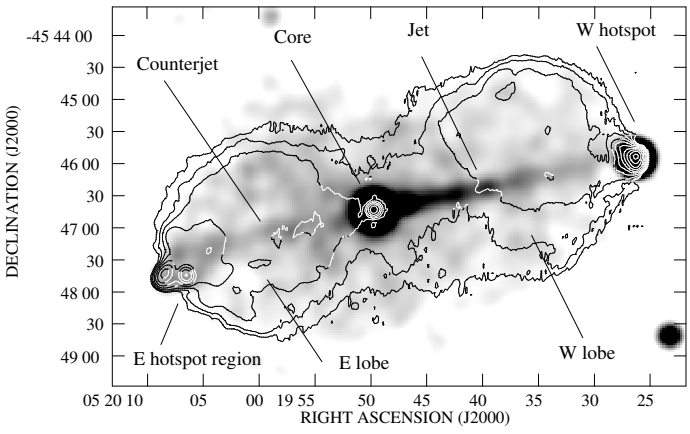

Figure 1.6: X-ray image of Pictor A (taken from Hardcastle & Croston, 2005). The X-ray emission is believed to originate from inverse-Compton scattered CMB photons and is displayed as greyscale (0.5–5 keV). Radio contours from 1.5 GHz are overlaid. The raw data (their Fig. 1, however without radio overlay) shows even better that whole cocoon is filled with X-ray emission.

while the cocoon, filled with low density plasma, then appears as cavity – in some cases only after the ambient gas profile has been subtracted. This has been observed for more than three dozen sources and a similar number of giant ellipticals and groups (McNamara & Nulsen, 2007). While it does not show the jet-originated matter, it provides much information about the history and the power of the outburst. Four cavities associated with radio sources are depicted in Fig. 1.7. Since emission from the thermal ambient gas does not suffer from uncertain assumptions about the jet plasma, it provides a much more robust diagnostic tool for the radio source (Bîrzan et al., 2004). The bow shocks visible in Cygnus A, Hercules A and MS0735.6+7421 can be used to estimate the mechanical power of the jets and can easily be compared with results from numerical simulations (see Sect. 3.3). The bow shock aspect ratios (length to width) are generally not much above unity and Mach numbers are found to be in the range between 1 and 2 (McNamara & Nulsen, 2007). Outburst powers can be estimated from the bow shock position and strength. Another way is to determine the work needed to inflate the observed cavities ($p\mathrm{d}V$) and the corresponding cavity enthalpy, since ambient pressure and cavity volume can be measured from the X-ray data.

An extreme example is MS0735.6+7421 (McNamara et al., 2005), where radio emission shows a weak source of 550 kpc size, while X-ray cavities with an enthalpy of 8×10^{61} erg reveal the true average power of the AGN (1.7×10^{46} erg s^{-1}), which is a factor of $\sim 10^5$ higher. For the other three sources in Fig. 1.7, inferred kinetic powers are 1.6×10^{46} erg s^{-1} for Hercules A (Nulsen et al., 2005), 1.2×10^{45} erg s^{-1} for Cygnus A (Wilson et al., 2006) and 1.5×10^{44} erg s^{-1} for Perseus A (Rafferty et al., 2006) as a relatively low-power system. Wise et al. (2007) find an extensive cavity system for Hydra A with three cavity pairs, indicating that there have been three activity cycles within the last 500 million years.

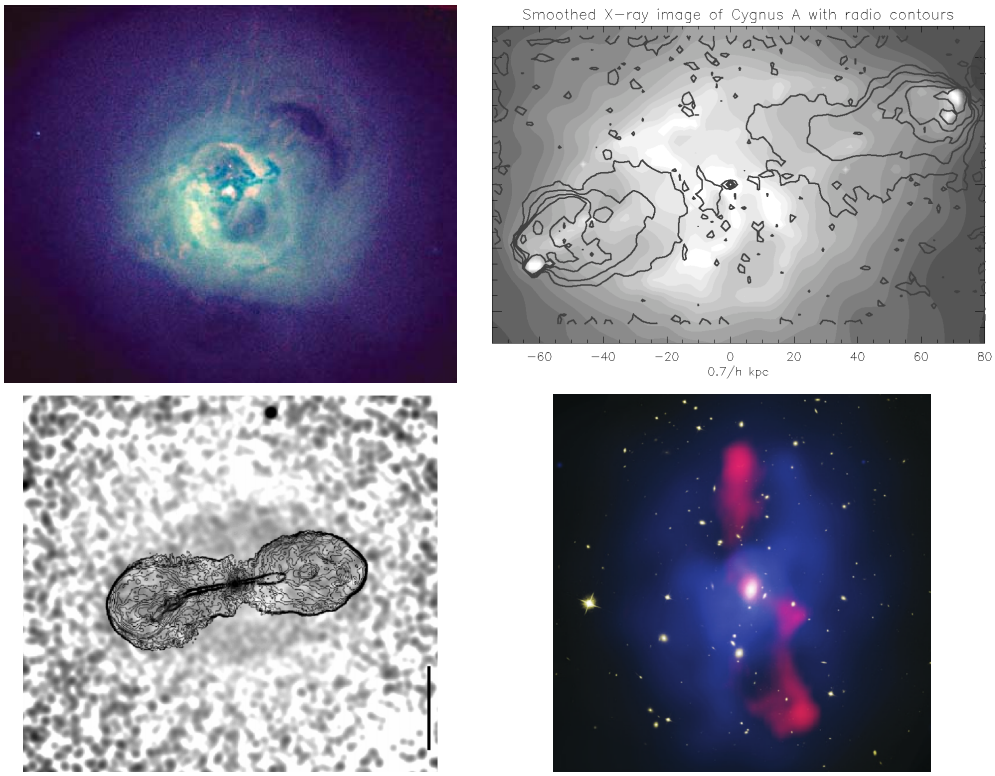

Figure 1.7: Four radio sources showing prominent X-ray cavities and shocked ambient gas shells. *Top left:* Perseus A. X-ray color composite image from the 0.3–1.2 (red), 1.2–2 (green) and 2–7 keV (blue) energy bands, from Fabian et al. (2006). *Top right:* Cygnus A with a Mach 1.3 bow shock. X-ray greyscale image with 5 GHz radio contours, from Krause (2005). *Bottom left:* Hercules A with a Mach 1.65 bow shock. X-ray greyscale image with 1.4 GHz radio contours, from Nulsen et al. (2005). *Bottom right:* Cavities in the MS0735.6+7421 cluster with a Mach 1.4 bow shock. Optical image overlaid with an X-ray image (blue) and 330 MHz radio image (red), from McNamara & Nulsen (image from 2007).

Jet parameters Finally, we address the question of physical jet parameters, which are important especially with regard to the subsequent simulations. The important parameters are mainly the jet speed, the jet density and (as just discussed) the jet power. It is generally assumed that extragalactic jets show relativistic speeds on the parsec scale. Most direct evidence for this are VLBI (very-long baseline interferometry) observations of jet knots moving at apparently superluminal speeds (Zensus, 1997). On the kiloparsec scale, however, bulk speeds are harder to infer since Doppler shifting cannot be measured for the continuum spectra. Evidence usually refers to Doppler beaming effects, which are only significant if bulk speeds are relativistic. High-power jets are generally found to be one-sided or show strong jet–counterjet brightness ratios. If jets are always formed as bipolar flows, suggested by the double extended radio structure, then the receding jet will be dimmer than the approaching jet. Strong support for this scenario comes from the Laing–Garrington effect: Radio lobes are found to be depolarized by a foreground Faraday screen, and the approaching lobe consequently is less depolarized. One-sided jets are found to be usually associated with the less depolarized (approaching) lobe

(Laing, 1988; Garrington et al., 1988) – an effect that is hard to explain except by beaming, which provides a natural explanation. This argument has been explored in more detail by Wardle & Aaron (1997) and Hardcastle et al. (1999): they conclude that relativistic speeds between $0.5\,c$ and $0.7\,c$ are necessary to explain the observations ($v = 0.6\,c$ corresponds to $\gamma = 1.25$) and find that the jetted side on the kiloparsec scale generally matches the side of the parsec-scale VLBI jet, for which evidence for relativistic speeds is much stronger. Mullin et al. (2008) find that the Laing–Garrington effect is significant in their sample of 98 FR II sources at the 99.8 % confidence level and that the jet detection rate and core prominence is higher for quasars and broad-line radio galaxies compared to narrow-line radio galaxies. This is expected from the unified model, since beaming effects are stronger for smaller inclination angles. The high variability seen in blazars also is strong evidence for relativistic motion, though it is not clear for the correspondingly low inclinations, out to which distances the relativistic speeds persist. Direct evidence for mildly relativistic speeds at distances larger than the parsec scale is found for the case of M87, where Hardcastle et al. (2003) find speeds of $0.5\,c$ at hundreds of parsecs and Cheung et al. (2007) detect superluminal motion at the knot HST-1 at a projected distance of 60 pc from the core. However, we note that Steenbrugge & Blundell (2008) derive jet speeds in the range of $0.3\,c$ to $0.5\,c$ for Cygnus A by fitting a precession model to the deviations from a straight line.

The density of the jet is very hard to constrain, since the nonthermal synchrotron emission carries no information about this – in particular since the observed radio-emitting particles are an unknown fraction of the total jet matter. However, we mention four ways to indirectly estimate the jet density, one being via the observed jet powers. The kinetic power L_j of bipolar jets is related with the jet speed v, the density ρ and the jet beam radius r_j by $L_\mathrm{j} = \pi r_\mathrm{j}^2 \rho v^3$. For a typical beam radius $r_\mathrm{j} = 1$ kpc, the density is less than 10^{-4} particles per cm^3 for a powerful jet with 10^{46} erg s^{-1} and less for weaker ones. Compared to ambient densities on the order of 10^{-2} to 10^{-1} cm^{-3}, these jets obviously have much lower densities than the ambient gas. Another way is to estimate what jet density we would expect if, as an upper limit, a black hole would accrete at 10 % of its Eddington limit (1.4) and transfer all matter to the jet ($0.1\,\dot{M}_\mathrm{Edd} = 2\pi r_\mathrm{j}^2 \rho v$). For a powerful source with a $10^9\,M_\odot$ black hole, this would correspond to a density of 10^{-4} cm^{-3}. For all realistic scenarios, the mass flux in the jet will be much smaller than this.

The two remaining ways use a simple one-dimensional model for the jet head propagation. The jet head ploughs through the ambient gas (density ρ_a and at rest) with a speed v_h. This can be estimated by momentum balance in the jet head frame, assuming the jet cross section as working surface,

$$\rho_\mathrm{a} v_\mathrm{h}^2 = \rho_\mathrm{j} (v_\mathrm{j} - v_\mathrm{a})^2 \tag{1.5}$$

yielding the head propagation speed

$$\frac{v_\mathrm{h}}{v_\mathrm{j}} = \frac{\sqrt{\eta}}{1 + \sqrt{\eta}}\,, \qquad \eta = \rho_\mathrm{j}/\rho_\mathrm{a}\,. \tag{1.6}$$

Note that in view of the subsequent simulations, this is only a simple estimate and any change in the working surface will yield somewhat different results. Scheuer (1995) finds that the head advance speeds are generally $\leq 0.1\,c$, Alexander et al. (1984) finds $\leq 0.05\,c$ for Cygnus A. These support the above estimates that jet densities are $< 10^{-3}$ cm^{-3}. The fourth exploits

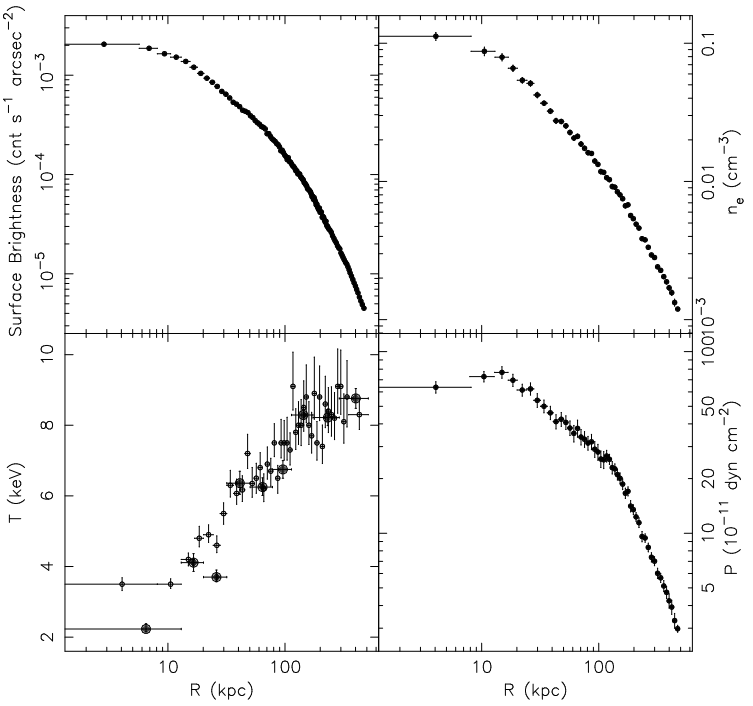

Figure 1.8: Intra-cluster gas in A478. The four panels show the observed surface brightness and temperature as well as the derived density and pressure profiles. Figure from Sun et al. (2003).

that the hotspot pressure will approximately equal $\rho_{\rm j}(v_{\rm j} - v_{\rm h})^2$. If the gas pressure is similar to the magnetic pressure in the hotspot (equipartition) with typical hotspot field strengths, this yields a jet density of $< 10^{-4}$ cm^{-3}. We conclude that extragalactic jets possess densities that are smaller than a factor of 10^{-2} with respect to the ambient density, but largely unconstrained otherwise.

1.3 Galaxy Clusters

Powerful AGN with correspondingly very massive central black holes are generally found in massive galaxies, which are almost exclusively giant ellipticals. While quasars are often located in galaxy groups, powerful radio galaxies as Cygnus A mostly live in clusters of galaxies, often in the central dominant cD galaxy. Since the jets propagate out to large distances, they interact with the hot, dilute plasma in the cluster.

Galaxy clusters are concentrations of galaxies over a region of several megaparsecs in diameter. They consist of typically 50 to 1000 galaxies and have masses of 10^{14} to $10^{15}\,M_\odot$. The cluster masses are dominated by dark matter and only $\sim 10\,\%$ (Lin et al., 2003; Vikhlinin et al., 2006), varying with radius, is baryonic. The latter is mostly in the hot intra-cluster medium, approximately $10\,\%$ of it is in stars. The cluster gas shows temperatures in the range 10^7 to 10^8 K, corresponding to the virial temperature within the dark matter halo, and radiates mostly in thermal bremsstrahlung with X-ray luminosities of 10^{43} to $\gtrsim 10^{45}$ erg s^{-1} (McNa-

mara & Nulsen, 2007). Both temperatures and density profiles can be reconstructed from the X-ray data, and often a β-model is used to fit the electron density,

$$n_{\mathrm{e}}(r) = n_0 \left(1 + (r/r_{\mathrm{c}})^2\right)^{-3\beta/2} , \tag{1.7}$$

with $\beta \approx 2/3$. At larger radii, the density declines with r^{-2}, but flattens towards the core. Central electron densities typically are $n_0 \sim 0.01$ cm^{-3} or higher (Rafferty et al., 2006) and temperature profiles drop towards the center by a factor of 2–3. Figure 1.8 exemplarily shows a cluster gas profile with surface brightness, electron density, temperature and pressure. The gas temperature is correlated with the cluster mass (Vikhlinin et al., 2006)

$$M \propto T^{\alpha} , \qquad \alpha \simeq 1.5 - 1.6 , \tag{1.8}$$

as expected from theoretical studies (Evrard et al., 1996).

Some clusters exhibit a strongly enhanced central X-ray surface brightness of up to a factor of 100. This is due to increased density ascribed to "cooling flows" (Fabian, 1994). Radiative cooling times in these regions become $\lesssim 10^9$ years and cooling gas is expected to flow towards the center. However, observations of cooling flow clusters did not find the expected amounts of cooled gas despite the strong X-ray emission(Peterson et al., 2001; Tamura et al., 2001; Bregman et al., 2006), indicating that cooling flows are much weaker. While thermal conduction seems to be suppressed by magnetic fields in clusters, feedback by AGN is discussed as mechanism that could quench cooling flows and increase the cluster gas entropy (Zanni et al., 2005). The intra-cluster gas also is pervaded by magnetic fields of typically microgauss field strength, although fields can be stronger in cooling cores of clusters. These fields may have been produced by injection of magnetic fields from radio sources, but several other models also have been considered in the literature as well (Carilli & Taylor, 2002).

1.4 Simulation of Jets

There has been a considerable amount of theoretical research about jets within the last decades. The "twin-exhaust" model by Blandford & Rees (1974) described double radio sources as being powered by collimated plasma flows, though details of the evolution were beyond the possibilities of such an analytical description. With the early numerical simulations of supersonic jets (Norman et al., 1982, 1983) in axisymmetry, the basic structures of double radio sources (beam, internal shocks, working surface/hotspot/Mach disk, cocoon, bow shock) could be reproduced, as well as new effects that could not be modelled analytically, such as nonlinear growth of Kelvin-Helmholtz instabilities, vortex shedding at the jet head, stability of the beam and cocoon as well as the backflow dynamics. Furthermore, these models showed that pronounced cocoons are characteristic for jets with much lower density than the ambient medium (light jets), although the slow propagation of the jet makes simulations of these computationally very demanding.

With the availability of more computing power and new codes, there has been progress in various directions (for reviews, see Norman, 1993; Ferrari, 1998). Massaglia et al. (1996) studied the propagation properties of jets, Cioffi & Blondin (1992) studied the cocoon hydrodynamics and evolution of the jet head with respect to self-similar models, and long-term evolution of

radio sources, after the jet is switched off, was addressed by Reynolds et al. (2002). Simulations were extended to three dimensions (Cox et al., 1991; Balsara & Norman, 1992; Clarke et al., 1997; Heinz et al., 2006), which removed symmetry restrictions and allowed to model moving hotspots and narrow-angle-tail sources, to study the effects of the third dimension on stability and propagation as well as impact of a more realistic environment from cosmological simulations. The question of stability of the jet was addressed by several authors (e.g. Hardee, 1984; Hardee & Clarke, 1992; Bodo et al., 1994; Hardee et al., 1995; Hardee & Clarke, 1995a; Bodo et al., 1996, 1998; Hardee, 2007; Perucho et al., 2007), by analytical and numerical means to examine both the linear growth of instabilities as well as the nonlinear growth or saturation.

Models have also been extended to include effects of magnetic fields, both passive and dominant, and for poloidal, toroidal and helical field configurations (Clarke et al., 1986, 1989; Lind et al., 1989; Kössl et al., 1990a,b,c; Matthews & Scheuer, 1990a,b; Hardee & Clarke, 1995b; Rosen et al., 1999a; O'Neill et al., 2005; Li et al., 2006). For strong toroidal fields, "nose cones" were found in the simulations, which do not possess wide cocoons anymore, but weaker or poloidal fields reduced mass entrainment into the beam.

Acceleration of electrons was additionally modelled by Tregillis et al. (2001, 2004) by evolving the momentum distribution explicitly. Development of relativistic codes allowed to explore effects of relativistic jet speeds on propagation, morphology and stability (Marti et al., 1997; Komissarov & Falle, 1998; Aloy et al., 1999; Rosen et al., 1999b; Hardee, 2000; Scheck et al., 2002; Perucho & Martí, 2007), and to combine relativistic simulations with magnetic fields (Nishikawa et al., 1997; Komissarov, 1999; Leismann et al., 2005; Mizuno et al., 2007; Keppens et al., 2008; Roca-Sogorb et al., 2008). However, all magnetohydrodynamic simulations to date only considered density contrasts $\eta \geq 10^{-2}$ and unipolar (one-sided) jets, which do not allow a description of the global bow shock and jet properties.

As argued earlier, extragalactic jets are very light (underdense with respect to the ambient gas) at kiloparsec scales. Increased computing power made simulations of more realistic density contrasts available. However, up to now only purely hydrodynamic simulations of very light jets have been performed. Saxton et al. (2002a,b) compared their simulations specifically with the sources Hercules A and Pictor A, and Carvalho & O'Dea (2002a,b) studied the global properties of the sources in a uniform and β-model atmosphere and compared it with self-similar solutions. The X-ray emission from the shocked ambient gas and cocoon cavities was addressed in detail by Zanni et al. (2003), while Saxton et al. (2005) and Sutherland & Bicknell (2007) explored the interaction of jets with an inhomogenous medium on small scales in two and three dimensions.

Krause (2003) conducted a hydrodynamic parameter study for a wide range of density contrasts and Mach numbers. He examined the bow shock and cocoon evolution and identified the bow shock aspect ratio to be a good diagnostic tool for the density contrast. Krause also found an initial blast wave phase, which can be used to infer a lower limit to the density contrast. Strong backflows occur in these simulations and more realistic global behaviour was reached when simulations included both jets (back-to-back). This was done by Krause (2005), who used a cluster density profile and found that the cocoon shape changed from elliptical to elongated cylindrical shape due to the declining ambient density and the weaker density contrast. Furthermore, simulations were extended to three dimensions and effects on the beam stability specific for very light jets were described. Simulations also were used to compute X-

ray emission maps, which were then compared to observations of Cygnus A. The simulations in this thesis are based on the preliminary work by Krause.

Parallel to numerical studies of radio sources, several groups worked on self-similar models of jet evolution (Begelman & Cioffi, 1989; Falle, 1991; Begelman, 1996; Bicknell et al., 1997; Kaiser & Alexander, 1997; Alexander, 2000), improving the models along with the numerical simulations. A list of these models was compiled by Carvalho & O'Dea (2002a) and compared to their simulations.

1.5 Aims and Outline of the Thesis

Jets are essentially magnetized plasma streams. For all currently discussed formation models, strong magnetic fields are mandatory, since they accelerate and collimate the plasma. On larger scales, however, the situation is much less clear. Combined radio and X-ray observations indicate that magnetic fields are present on a near-equipartition level in the lobes of radio sources. Depending on their topology and magnitude, they may affect the dynamics, morphology and interaction with the ambient gas significantly. The jet heads and cocoon–ambient gas interfaces of double radio sources appear smooth and stable in radio maps (e.g. Pictor A, Hercules A, Cygnus A: Perley et al., 1997; Gizani & Leahy, 2003; Lazio et al., 2006). Since hydrodynamic simulations, in contrast, show prominent Kelvin-Helmholtz instabilities at these locations, we conjecture that magnetic fields have a stabilizing role there. Magnetohydrodynamic (MHD) simulations so far have concentrated on the effect of dominant magnetic fields on the propagation, the stabilization of the jet beam and the observed emission properties. Furthermore, due to computational limitations, simulations with realistically low jet densities have long not been possible and correspondingly MHD simulations were only performed with weak density contrasts. With more computational power becoming available, it is now possible to examine the effects of magnetic fields for more realistic parameters, with better resolution and on observationally relevant length scales. Since hydrodynamical simulations showed that the global appearance depends on the density contrast, it is important to examine the the combined effects of magnetic fields and low jet densities. Furthermore, it is presently unclear, how equipartition fields in the beam create equipartition fields in an extended cocoon (De Young, 2002). One would expect from flux conservation arguments that the plasma expansion from the narrow beam to the extended lobes would be accompanied by a weakening magnetic field.

We examine these questions by magnetohydrodynamic simulations of very light jets on scales up to 200 kpc (200 jet radii) with a wide range of density contrasts (down to 10^{-4}) and explore the behaviour of very light jets with non-dominant magnetic fields in a cluster environment, taking much care to use a globally consistent setup for both the jet–ambient interaction and the magnetic field. The magnetohydrodynamic code NIRVANA (Ziegler & Yorke, 1997) is used for this. Its suitability and convergence for magnetohydrodynamic simulations have been checked before by Krause & Camenzind (2001) and it was used previously for the hydrodynamical simulations by Krause (2003, 2005). To see the effects of magnetic fields clearly and isolate them from possibly stabilizing effects of a declining ambient density, we choose a uniform ambient medium and restrict ourselves to axisymmetry. Simulations are analyzed with respect to the impact of magnetic fields and the evolution of the cocoon and the bow shock, which

are accessible observationally. Although we do not aim for modelling specific sources with this setup, simulation results are put in context to typical observational findings.

After this introductory chapter, the theoretical and numerical basis of this work is described, along with computational details and a detailed setup description (Chapter 2). The actual results are then presented in the following chapters: we analyze the data with respect to the evolution and morphology as well as the energy budget of the source, compare the data with self-similar models and investigate the impact of magnetic fields on the jet head and the cocoon as well as the underlying physical processes (Chapter 3). By means of emission maps, the observable morphology of the simulated sources is explored and limitations of the emission methods are addressed (Chapter 4). Finally, the simulations are applied to the observed "alignment effect" for high-redshift radio galaxies, which is briefly introduced and possible scenarios for the observed emission-line gas are examined (Chapter 5).

Part of this work has been published already (Krause, Gaibler, & Camenzind, 2005; Gaibler, Vigelius, Krause, & Camenzind, 2006; Gaibler, Camenzind, & Krause, 2007, 2008), is accepted for publication (Gaibler & Camenzind, 2008) or is submitted (Gaibler, Krause & Camenzind, 2008, submitted to A&A).

2 Theory, Numerics and Setup

In this chapter, basic concepts of our numerical simulations, implementation on supercomputers and the chosen setup for the simulations are described. Furthermore numerical reliability and convergence are addressed and a method later used for visualization of vector fields is introduced.

2.1 Magnetohydrodynamics

Both jet matter as well as ambient gas are modelled by means of continuum mechanics. Since a particle description of the plasma is impossible due to the huge number of particles, they are assumed to be in local equilibrium and collisionally dominated by their stochastic thermal motion or interaction with waves. In this case, the fluid can be described by its macroscopic properties such as density ρ, pressure p, thermal energy density e and velocity $\mathbf{v}$. These macroscopic variables can be derived from the (microscopic) phase-space distribution of the particles by forming statistical momenta of the particle properties (e.g. Shu, 1992). Instead of Boltzmann's equation, the evolution of the system is then described by the Euler equations, which are the special case of the Navier-Stokes equations, if diffusive terms are neglected (nonviscous fluids). This is reasonable as typical molecular viscosities are way to small to contribute to the dynamics. Furthermore, an equation of state (EOS) is needed to close the set of equations.

However, since the plasmas considered here are hot ($T > 10^7$ K) and hence almost completely ionized, moving electrical charges (current density $\mathbf{j}$) are affected by the presence of magnetic fields $\mathbf{B}$ due to the Lorentz force. Accordingly, the Euler equations can be coupled to Maxwell's equations and we find the set of hyperbolic differential equations of ideal magnetohydrodynamics (MHD) for a one-component plasma:

$$\frac{\partial \rho}{\partial t} + \nabla \cdot (\rho \mathbf{v}) = 0 \tag{2.1}$$

$$\frac{\partial (\rho \mathbf{v})}{\partial t} + \nabla \cdot (\rho \mathbf{v} \otimes \mathbf{v}) = -\nabla p - \nabla \left(\frac{\mathbf{B}^2}{8\pi} \right) + \frac{1}{4\pi} (\mathbf{B} \cdot \nabla) \mathbf{B} \tag{2.2}$$

$$\frac{\partial e}{\partial t} + \nabla \cdot (e \mathbf{v}) = -p \nabla \cdot \mathbf{v} \tag{2.3}$$

$$\frac{\partial \mathbf{B}}{\partial t} = \nabla \times (\mathbf{v} \times \mathbf{B}) \tag{2.4}$$

In this approach, electrons and ions move differently but charge neutrality is fulfilled for slow changes, as the resulting electric fields will act as a restoring force. Thus, charge separation will not occur for macroscopic disturbances with frequencies below the plasma frequency

$$\omega_\mathrm{p} \approx 5.6 \times 10^4 \left(n_\mathrm{e} / \mathrm{cm}^{-3} \right)^{1/2} \mathrm{s}^{-1}, \tag{2.5}$$

where n_e is the electron number density – being fulfilled at all times for our simulations. Despite their different motion, electrons and ions then behave as a single fluid and displacement currents can be neglected in Ampère's law for non-relativistic speeds. Electric fields $\mathbf{E}$ are not part of the MHD equations, as they only appear as (weak) induced fields and are always tied to the magnetic field via

$$\mathbf{E} = -\frac{1}{c}\mathbf{v} \times \mathbf{B}. \tag{2.6}$$

Maxwell's equations with these approximations then become

$$\begin{aligned} \nabla \times \mathbf{E} &= -\frac{1}{c}\frac{\partial \mathbf{B}}{\partial t} && (2.7)\\ \nabla \times \mathbf{B} &\approx \frac{4\pi}{c}\mathbf{j} && (2.8)\\ \nabla \cdot \mathbf{E} &\approx 0 && (2.9)\\ \nabla \cdot \mathbf{B} &= 0. && (2.10) \end{aligned}$$

The Lorentz force density can be expressed as

$$\begin{aligned} \mathbf{f}_\mathrm{L} &= \frac{1}{c}\mathbf{j} \times \mathbf{B} && (2.11)\\ &= \frac{1}{4\pi}(\nabla \times \mathbf{B}) \times \mathbf{B} && (2.12)\\ &= -\nabla\left(\frac{\mathbf{B}^2}{8\pi}\right) + \frac{1}{4\pi}(\mathbf{B} \cdot \nabla)\,\mathbf{B}, && (2.13) \end{aligned}$$

where the latter form shows that it manifests as magnetic pressure (first term in Eqn. 2.13) and magnetic tension (second term). Magnetic pressure gives additional pressure support to thermal gas pressure, while magnetic tension provides a restoring force against bending of field lines.

Ideal MHD assumes that electrical conductivity of the plasma is infinite and hence resistive terms are neglected in the equations. Particularly reconnection phenomena hence can not be modelled within ideal MHD, but need additional resistive terms in the energy (2.3) and induction equation (2.4).

Furthermore, we assume the plasma to behave as an ideal gas, with the equation of state

$$p = (\gamma - 1)e = nk_\mathrm{B}T, \tag{2.14}$$

where n is the particle number density, k_B the Boltzmann constant, T the temperature and γ the adiabatic index of the gas.

The continuum approximation is only valid, if particles are thermalized and reach local thermodynamical equilibrium. The collisional mean free path for the particles is (Jones, 2008)

$$l_\mathrm{c} = 22\,\frac{(T/\mathrm{keV})^{5/2}}{(n/0.01\,\mathrm{cm}^{-3})}\,\mathrm{pc}. \tag{2.15}$$

While for the ambient cluster gas, this microscopic equilibrium may just be established, this will clearly not be true for the jet plasma with its high temperature and low density. However,

in the presence of magnetic fields, particle interaction can still be effective due to the spiral motion of the particles around the field lines with a gyration radius

$$r_\mathrm{g} = 10^{-9}\,\frac{(m/m_\mathrm{p})^{1/2}\,(T/\mathrm{keV})^{1/2}}{(B/\mu\mathrm{G})}\,\mathrm{pc}\,, \tag{2.16}$$

which is much smaller than collisional mean free path and makes MHD models reasonable, since "collisions" then occur due to magnetic fields instead of Coulomb forces. Observations of shocks and sharp discontinuities in the intra-cluster medium confirm this behaviour, which is known from the interaction between the Earth's magnetosphere and the solar wind (Shu, 1992).

Within MHD, there exist two additional waves compared to pure hydrodynamics: the Alfvén waves and the slow magnetosonic waves. When ψ is the angle between wave vector and magnetic field, the Alfvén waves propagate with

$$v_\mathrm{A} = c_\mathrm{A}\cos\psi\,, \qquad c_\mathrm{A} = \frac{B}{(4\pi\rho)^{1/2}}\,, \tag{2.17}$$

where c_A is the Alfvén speed. They are transverse waves, very similar to vibrating strings (magnetic field lines are bent and oscillate due to their magnetic tension). Furthermore, there are slow and fast magnetosonic waves with phase velocities of

$$v_\mathrm{fast,slow} = \frac{1}{2^{1/2}}\left((c_\mathrm{A}^2 + c_\mathrm{s}^2) \pm \left[(c_\mathrm{A}^2 + c_\mathrm{s}^2)^2 - 4\,c_\mathrm{A}^2 c_\mathrm{s}^2\cos^2\psi\right]^{1/2}\right)^{1/2}\,, \tag{2.18}$$

where the "+" sign gives the fast and the "−" sign gives the slow wave, c_s being the sound speed. The magnetosonic waves are acoustic-like compression–rarefaction waves including the effects of magnetic pressure.

All three waves have non-isotropic propagation speeds, but the fast magnetosonic wave turns into an ordinary (isotropic) sound wave for vanishing magnetic field strengths. Additionally, it always is the fastest of the three, with a maximum speed of

$$c_\mathrm{ms} = \left(c_\mathrm{A}^2 + c_\mathrm{s}^2\right)^{1/2}\,. \tag{2.19}$$

We thus have 7 characteristics: two fast and slow magnetosonic and Alfvén waves, respectively, and the contact (entropy) wave of the flowing plasma.

Ideal MHD, neglecting resistive effects, shows the phenomenon of flux freezing: the magnetic field is tied to the plasma and $\mathbf{B}/\rho$ is transported by the flow (Pelletier, 2007). For weak magnetic fields, they are passively advected with the plasma, for very strong fields, the plasma flows along the field lines. The importance of magnetic fields generally is expressed by the plasma β parameter

$$\beta = \frac{8\pi p}{B^2}\,, \tag{2.20}$$

which is the ratio of thermal gas pressure to magnetic pressure. Weak magnetic fields have high β values (hydrodynamics: $\beta \to \infty$), dominating fields have values between 0 and 1. Equipartition between thermal pressure and magnetic pressure has $\beta = 1$. It should be noted, however, that plasma β only accounts for magnetic pressure as one manifestation of magnetic forces. Effects of magnetic tension are not considered, but may still be strong even for $\beta \gg 1$.

2.2 Numerical Scheme

The simulations were performed using the NIRVANA code (Ziegler & Yorke, 1997), which numerically solves the nonrelativistic magnetohydrodynamic equations in three dimensions in cartesian, cylindrical or spherical coordinates on a staggered grid, where scalar variables are defined at the cell centers, but vectors are defined at the face centers. To solve the system of partial differential equations, physical variables are discretized on a grid and derivatives are approximated by finite-differences discretization in an explicit formulation. Operator splitting is used for the different computational substeps and hydrodynamic fluxes are interpolated according to van Leer's scheme, which is second-order accurate. The advection part is solved in a conservative form. As for every explicit code, time steps are restricted by the Courant-Friedrichs-Lewy (CFL) condition

$$\Delta t = \frac{C\Delta x}{\max(c_{\mathrm{ms}}, |v| + c_{\mathrm{ms}})} \quad \text{with } C < 1, \tag{2.21}$$

where a CFL number $C = 0.5$ is used (Δx: grid resolution, Δt: time step, v: fluid speed, c_{ms}: fastest characteristic). This means that no signal may be transported further than the neighbouring cell, otherwise the scheme becomes unstable.

Magnetic fields are evolved using the constrained transport (CT) method (Evans & Hawley, 1988), which conserves $\nabla \cdot \mathbf{B}$ to machine round-off errors, and the method of characteristics (MOC), which accurately propagates all MHD waves (Stone & Norman, 1992). Artificial viscosity is added to damp high-frequency oscillations and overshooting at shocks. The latter are thereby smeared out over some grid cells.

The code was vectorized and shared-memory parallelized (Krause et al., 2005; Gaibler et al., 2006) for the NEC SX-6 and SX-8. It furthermore evolves a population of passively advected tracer particles, injected from the jet nozzle.

2.3 Vectorization and Parallelization

The simulations are performed in cylindrical coordinates (Z, R, ϕ) on a uniform grid of 4000×1600 cells for the lightest jets, giving a spatial resolution of 0.05 kpc. Typical time steps due to the CFL condition (2.21) are in the range of 30 to 40 years physical time. For the jet to propagate out to a scale of 200 kpc, roughly 50 Myr are to be simulated, giving more than 10^6 time steps.

We found NIRVANA to run with a speed of $\approx 4\,\mu$s per computed time step and cell on a 3 GHz Pentium IV machine, scaling nicely with (reciprocal) CPU frequency. Hence, one simulation run would take more than one year on a workstation, and supercomputers with faster and multiple processors are necessary. The NEC SX-6 and SX-8 at the HLRS in Stuttgart were chosen for this task, as it is well-suited for fluid dynamical computations and the hydrodynamics part of the code was already running well, using both vectorization and shared-memory parallelization. Still, the magnetic field routines had to be optimized, as they were running very inefficiently.

Contrary to widespread cluster architecture, where a large number of processors are connected over a fast network and computational work is distributed to them (massive parallel

computing), the NEC SX-6/8 are vector supercomputers with a hybrid architecture. They consists of several nodes (SX-6: 6 nodes, SX-6: 72 nodes), which are connected with an internode crossbar switch, allowing immediate data transfer between all nodes (SX8: 16 GB/s bidirectional per node). Each node consists of 8 shared-memory vector processors (operated at 2 GHz, 16 Gflops), which can access system memory at 64 GB/s per CPU, with 128 GB shared memory available for each node. The vector processors have multiple vector parallel pipelines, allowing them to work on "vectors" of input data instead of single elements. This pipelining concept is known from PC processors for instructions, but is extended here to data pipelining, which needs fast access to the whole memory. This memory bandwidth is provided by use of 4096 independent modules, which significantly lower memory latency (bank conflicts).

Vectorization performs the same instruction on a vector of data (multiple elements), which is the key to much better performance than usual scalar CPUs. However, this only works if the amount of data to be processed is large and can keep the vector units busy; for high-performance computing, this usually is the case. Additionally, the actual instructions have to be the same for a large amount of data, meaning that conditionals and dependencies between the different elements are not allowed. This constraint usually can be relaxed, if conditionals are moved to outer loops, and inner loops then can be vectorized completely. Also, conditionals are possible to a certain degree, as compilers can "mask" them by computing both cases and selecting the correct one later. Although this means some unnecessary computations, overall performance still is much higher compared to scalar evaluation.

Shared-memory parallelization was implemented in an OpenMP-like way, called "microtasking" on the SX. By means of compiler pragmas, the program can automatically or manually guided distribute work to the eight processors. Thus, it provides an additional and easy way to increase speed of computation. Since this relies on shared-memory, it is only possible within one node, and access to other nodes has to be done with MPI (message passing interface), which is a library that handles network communication between nodes or processors.

For the case of NIRVANA, the following approach for vectorization/parallelization was chosen (Fig. 2.1): The dimension with most elements (Z) was vectorized, allowing maximum vector performance. The other dimensions were parallelized, using shared-memory parallelization for the R dimension and MPI parallelization for the ϕ dimension. For cluster architecture, MPI parallelization usually is done by splitting the computational domain into cubes of roughly equal edge length to minimize communication overhead, which depends on the cube surface. For the hybrid architecture of the SX-6/8, domain decomposition by dimensions is best suited, as communication overhead only contributes in one direction, while vectorization and shared-memory parallelization do not use network communication. Additional MPI parallelization was implemented by Martin Krause (Gaibler et al., 2006), and allows domain decomposition in ϕ direction or in the ϕ–R plane.

A significant performance increase comes from "smart domain handling", which exploits the fact that in a jet setup, where the ambient gas is in hydrostatic equilibrium, nothing can change outside the bow shock. Hence, it is only necessary to compute a region which is just somewhat larger than the extent of the bow shock – the computational domain grows with the bow shock. Especially in the early phase, when the jet is still small, a significant gain in performance can be achieved. In every time step, the axial (Z) and lateral (R) position of the bow shock is determined and the area for actual computation in the next time step is then set to 10 cells outside the bow shock. Although this implies that vectorization is rather inefficient

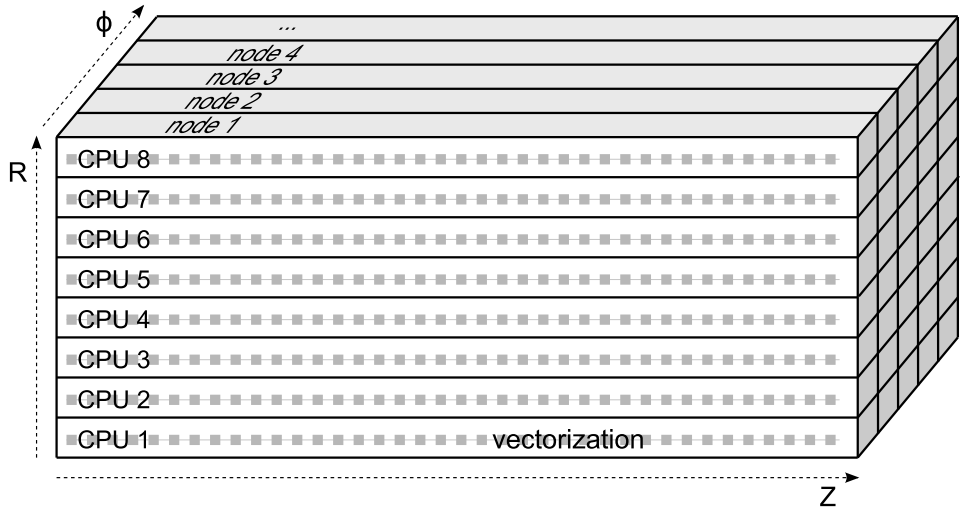

Figure 2.1: Vectorization/parallelization scheme chosen for NIRVANA. The dimension with most elements (Z) was vectorized and the others were parallelized with OpenMP-like "microtasking" (R) and MPI parallelization (ϕ).

at early times due to the small number of elements in Z direction, for a simulation with a 4000×800 cells grid, the necessary CPU time per cell and time step decreased from $1.1\,\mu$s to $0.5\,\mu$s, corresponding to a speedup of 2.

Despite the various techniques to gain computational speed mentioned above, the large number of time steps still poses a serious problem, which can not be overcome by parallelization techniques and is important to point out. Causality enforces a serial execution in time direction unless larger domain decomposition blocks overlap significantly, resulting in increased communication costs. Lowering computation time for one time step offers to be an obvious solution. While in general this is the idea of parallelization, it only works for "large" problems, meaning that communication time can be kept small compared to the computation time. If the number of processors or nodes becomes too large, computation time decreases due to the smaller problem size for each processor, but communication between the processors after every time step is dominated by network latency instead of network bandwidth. In this sense, the axisymmetric setup we deal with is too small despite having millions of cells. Both enlarging the domain or enlarging the resolution offer no solution.

Another idea is to decrease the number of time steps by using an implicit numerical scheme. Here, the CFL stability condition does not apply and the time step can be chosen arbitrarily with respect to numerical stability. However, the time scales of the occuring physical processes still have to be resolved by the time step. While this method is ideal for setups approaching a steady state, where the time steps can be increased continuously, cocoon turbulence and rapid changes in the beam do not allow larger time steps even at late times and hence make the larger computational effort per time step for implicit methods impractical.

For the performed axisymmetric simulation, we decided not to use the MPI parallelization and rely on both vectorization and shared-memory parallelization instead. Here, no network latency and bandwidth restrictions apply, high efficiency is reached and total runtime on one

Table 2.1: Performance results from a short test run of the non-optimized code and the version with optimized vectorization on a single SX-6 processor. The output from `sxftrace` profiler is shown for the five most time-consuming routines. It gives the cumulative and single CPU time, the speed in MOPS (million integer operations per second) and MFLOPS (million floating point operations per second), the vectorization ratio, the average vector length and the bank conflict time (memory dead time).

non-optimized:

PROG.UNIT	FREQUENCY	EXCLUSIVE TIME[sec](%)	AVER.TIME [msec]	MOPS	MFLOPS	V.OP RATIO	AVER. V.LEN	BANK CONF
ct	30	16.868(55.1)	562.253	2252.0	629.4	99.73	256.0	1.1183
lorentz	30	6.816(22.3)	227.200	3465.8	1026.6	99.67	255.8	0.1290
advect	30	2.934(9.6)	97.791	7344.1	2634.6	99.46	254.9	0.1362
data	4	1.821(6.0)	455.215	276.4	152.8	2.95	205.0	0.0046
scr	30	0.680(2.2)	22.665	5878.3	3093.3	99.40	255.6	0.0123

optimized:

PROG.UNIT	FREQUENCY	EXCLUSIVE TIME[sec](%)	AVER.TIME [msec]	MOPS	MFLOPS	V.OP RATIO	AVER. V.LEN	BANK CONF
ct	30	4.679(33.8)	155.954	6487.5	2560.4	99.64	256.0	0.0276
advect	30	2.893(20.9)	96.422	7452.4	2676.6	99.60	254.9	0.1357
lorentz	30	2.552(18.4)	85.070	7612.3	2718.4	99.61	255.8	0.0218
data	4	1.826(13.2)	456.512	275.6	152.3	2.95	205.0	0.0063
scr	30	0.545(3.9)	18.172	6746.7	3902.8	99.38	255.6	0.0071

SX-6 node is still practical with $\sim$ 10 days real time for a simulation with density contrast $\eta = 10^{-3}$. For future 3D simulations, however, MPI parallelization is critical, as cell numbers are about two orders of magnitude higher and a higher number of nodes can be used efficiently (despite at necessarily somewhat lower resolution).

2.4 Code Optimization and Extension

Because of large loops with many temporary variables and conditional expressions for the array indices, the vector performance for MHD runs initially was very disappointing. The upper part of Table 2.1 shows the results of a performance measurement with the NEC profiler `sxftrace` for a short test run. The first goal was to improve the performance on a single CPU.

The most important change was splitting the loops into three different cases which made it possible to move conditionals outside of the loop. It was now possible to completely eliminate minimum/maximum expressions for the array indices or at least improve performance by calculating two possible results for conditional expressions and selecting the needed one afterwards – similar to the approach called "masking" which the compiler would choose in more simple cases. This yields an improved performance by a factor of 3, and with 2.6 Gflops it is of the same order as the advection routine, which is the most time-consuming part for pure hydrodynamics. The lower part of Table 2.1 shows the results of a test run. The production performance is higher without profiling overhead and about 3 Gflops are achievable.

Table 2.2: Performance of an axisymmetric MHD run of a typical jet simulation as shown in this theses with the optimized code on 8 CPUs (one restart cycle of simulation run M3P), when coarse snapshots were saved every 2000 years (≈ 60 time steps).

Real Time (sec)	70040.819267	Max Concurrent Proc.	8
User Time (sec)	537729.639354	Conc. Time(>= 1)(sec)	69766.840905
Sys Time (sec)	767.447488	Conc. Time(>= 2)(sec)	67074.527617
Vector Time (sec)	473340.184437	Conc. Time(>= 3)(sec)	67059.252945
MOPS	7057.142145	Conc. Time(>= 7)(sec)	66921.879860
MFLOPS	2725.560661	Conc. Time(>= 8)(sec)	65929.140583
MOPS (concurrent)	54393.096367	Lock Busy Count	56035374
MFLOPS (concurrent)	21007.325718	Lock Wait (sec)	5243.409426
A.V. Length	248.053921	I-Cache (sec)	288.736881
V. Op. Ratio (%)	99.423935	O-Cache (sec)	3902.467089
Memory Size (MB)	1312.000000	Bank (sec)	3904.562187

The next step was to extend this optimization to multiple CPUs. Originally, shared-memory parallelization (microtasking) already worked very well for the hydrodynamic parts. Now this could be achieved for the magnetic subroutines, too. A speedup of 6.9 was reached for runs with 8 CPUs (1 node). When smart domain handling is switched on, the average vector length (usually above 254) is worse because of shorter loops, but the overall CPU time decreased up to a factor of 2. Typical performance values with smart domain handling are shown in Table 2.2.

The large amount of data for one simulation snapshot (≈ 440 MB for simulation run M3P, containing all physical variables of the whole grid) naturally limits the number of possible snapshot frames. But even when several hundred frames are saved, quick changes in the domain are unavailable for analysis and evolution of shocks within the beam can not be seen. Additionally, simulations are pretty much slowed down due to the strong I/O activity. Data compression is no solution, as the compression rates for light jets with highly turbulent cocoons are too small (typically 50%) and would require much additional computation.

The solution to this is to save only a reduced dataset additionally in shorter time intervals. One third of the spatial resolution is used for this and only scalar variables (density, pressure and magnetic pressure) are saved. Since the range of values is high (for densities more than four orders of magnitude, for pressure even more), the values are scaled logarithmically into byte range. This still gives accuracy better than 5%. The full dataset is still available at coarser time intervals for more detailed analysis.

The method naturally gives a strong (but lossy) compression by a factor of ≈ 200 and allows saving 10 000 snapshots per run without storage difficulties. It proves very practical and allows high-resolution animations to be made and get a more detailed view of the time evolution.

2.5 Setup

The simulations were performed on a uniform grid in cylindrical coordinates (Z, R, ϕ), assuming axisymmetry ($\partial/\partial\phi = 0$), but using 3D vectors ($\mathbf{B} = B_Z\mathbf{e}_Z + B_R\mathbf{e}_R + B_\phi\mathbf{e}_\phi$). This is commonly referred to as 2.5-dimensional simulation. The inclusion of 3D vectors allows rotation of the

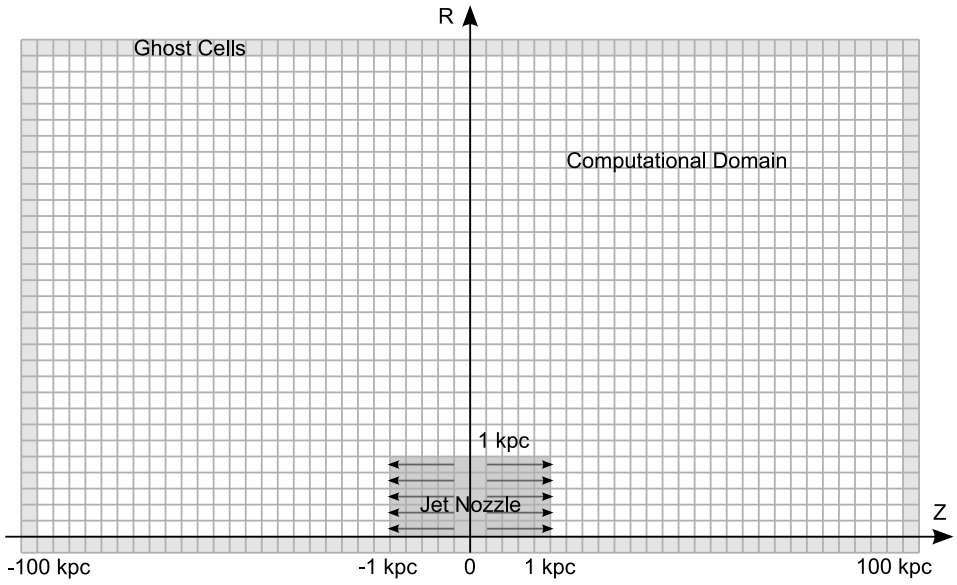

Figure 2.2: Sketch of the initial jet setup. The computational domain is bounded by "ghost cells" (light grey), which enforce the chosen boundary conditions. The jet plasma is injected in a cylinder at the origin $(Z, R) = (0, 0)$ aligned with the Z axis, which is shown as a grey rectangle with radius r_j and full axial length $2\,r_\mathrm{j}$.

jet plasma around the symmetry axis as well as a toroidal magnetic field component, which will later turn out to be important.

The grid extends over 200 kpc in axial (Z) and 40 or 80 kpc in radial (R) direction and is resolved by 4000×800 or 4000×1600 cells, corresponding to a spatial resolution $\Delta Z = \Delta R = 0.05$ kpc. The simulations were run until the bow shock leaves the computational domain. The plasma is assumed to be an ideal gas of fully ionized hydrogen (electrons and protons), corresponding to a mean particle mass $\bar{\mu} m_\mathrm{p}$ with $\bar{\mu} = 0.5$ and an adiabatic index $\gamma = c_\mathrm{p}/c_\mathrm{v} = 5/3$, which is also the ratio between enthalpy and internal energy.

The jet originates from a cylindrical nozzle (a rectangular area in the Z–R plane, Fig. 2.2), with a radius of $r_\mathrm{j} = 1$ kpc, centered on the origin of the coordinate system $Z = R = 0$. The jet radius is thus resolved by 20 cells. The jet nozzle actually is a boundary condition within the computational domain, describing a jet which is formed on much smaller scales, but which propagates outwards, widens and remains well-collimated. It also can be regarded as a model of an observed jet beam at kpc scales, too. Since high-power jets remain collimated even on large scales, the velocity in the nozzle is purely axial.

The low jet density with respect to the ambient gas causes strong deflection of the beam plasma and forms a strong backflow. To avoid artifacts near the midplane ($Z = 0$), where the two jets interact, both jets have to be simulated, since no realistic boundary condition can be prescribed: for open (outflow) boundary conditions, matter and energy are driven out of the domain by the cocoon pressure, thereby falsifying the cocoon pressure, which again drives the lateral expansion and the bow shock; reflective boundary conditions widen the cocoon artificially when cocoon vortices move towards the midplane and get reflected (Saxton et al.,

2002b). Simulating bipolar (back-to-back) jets, turbulent interaction is allowed and the lateral expansion becomes more realistic.

Optically thin cooling is included in the code but was switched off since its effects would be negligible. For a temperature range applicable to the cluster gas, the cooling function Λ for solar metallicity (Sutherland & Dopita, 1993) with integrated volumetric emission $\epsilon = n^2\Lambda/4$ is

$$\Lambda < 10^{-22.5}\,\mathrm{erg\,cm^3\,s^{-1}}\,, \tag{2.22}$$

giving a cooling time scale

$$t_\mathrm{c} = \frac{e}{\epsilon} = 2\times10^9\,\frac{\left(T\,/\,5\times10^7\,\mathrm{K}\right)}{\left(n\,/\,0.02\,\mathrm{cm^{-3}}\right)\left(\Lambda\,/\,10^{-22.5}\,\mathrm{erg\,cm^3\,s^{-1}}\right)}\,\mathrm{yr} \tag{2.23}$$

which is just too long to effect the simulation during the activity timescale of typically 10^7 to 10^8 years. However, for the long term evolution, cooling would become important, particularly as central gas densities are one order of magnitude higher. Effects of a cooling flow are ignored, since on our simulation time scale they simply would correspond to somewhat different initial conditions.

Two setups are used in this work: a simpler one for the parameter study (varying the density contrast η) and an improved "force-balance" version for a fixed density contrast, which is later used for the emission maps and avoids some deficiencies of the former setup. However, the overall behaviour is not affected by the setup differences.

2.5.1 Parameter Study Setup

The jets are injected into an ambient medium of constant density $\rho_\mathrm{a} = 0.01\,m_\mathrm{p}\,\mathrm{cm^{-3}}$ and temperature $T_\mathrm{a} = 5\times10^7$ K, which is at rest ($v_\mathrm{a} = 0$). The jet density ρ_j is varied with density contrasts $\eta = \rho_\mathrm{j}/\rho_\mathrm{a}$ ranging from 10^{-1} to 10^{-4}. Jet speed and sound speed are kept fixed to $0.6\,c$ and $0.1\,c$ within the nozzle, respectively, keeping the sonic Mach number fixed at a value of 6. To break symmetry between the left and the right jet, density perturbation were added randomly to the ambient gas: the density value of a cell was increased by a (uniformly distributed) random factor between 1 and 1.4 with a probability of 10 %.

A summary of the fixed parameters is given in Table 2.3, the varied parameters in Table 2.4. The simulations are labelled by a letter and a numeral, which will be used throughout the thesis, indicating the inclusion of magnetic fields (M) or pure hydrodynamics (H), as well as their density contrast. Jet density, pressure and velocity magnitude are set constant within the nozzle, but velocity changes sign at the midplane ($v_Z > 0$ for $Z > 0$, $v_Z < 0$ for $Z < 0$). The sound speed

$$c_\mathrm{s} = \sqrt{\frac{\gamma p}{\rho}} \tag{2.24}$$

in the jet is kept constant to fix the Mach number while varying the density contrast. This necessarily changes the thermal jet pressure, yielding over- or underpressured jets. This is, however, not critical, as supersonic jets are dominated by kinetic energy rather than thermal energy, making ram pressure the dominant pressure component.

For global simulations, the $\nabla\cdot\mathbf{B}$ constraint enforces closed field lines, which is satisfied, for example, by a dipolar field configuration, but not by the common setup of an infinite axial

Table 2.3: Common setup parameters for the parameter study. Nozzle averages are restricted to $R \leq 0.9\, r_\mathrm{j}$ ($\leq 0.8\, r_\mathrm{j}$ for M4 and M4L).

jet speed	v_j	$0.6\, c$
jet internal sonic Mach number	M_int	6
jet external Mach number	M_ext	153
jet radius	r_j	$1\,\mathrm{kpc}$
ambient gas density	ρ_a	$10^{-2}\, m_\mathrm{p}\,\mathrm{cm}^{-3}$
ambient gas temperature	T_a	$5 \times 10^7\,\mathrm{K}$
jet nozzle magnetic field	$\langle B_\mathrm{p} \rangle$	$18.1\,\mu\mathrm{G}$ (M4L: $1.81\,\mu\mathrm{G}$)
	$\langle B_\phi \rangle$	$7.5\,\mu\mathrm{G}$ (M4L: $0.75\,\mu\mathrm{G}$)

Table 2.4: Parameters for the different runs of the parameter study and the force-free setup. Kinetic jet powers $L_\mathrm{kin} = \pi r_\mathrm{j}^2 \rho_\mathrm{j} v_\mathrm{j}^3$ include both jets. Nozzle averages are restricted to $R \leq 0.9\, r_\mathrm{j}$ ($\leq 0.8\, r_\mathrm{j}$ for M4 and M4L). β values are typical for the respective simulation run. More details about the M3P setup is given in Sect. 2.5.2.

Run	$\eta = \rho_\mathrm{j}/\rho_\mathrm{a}$	L_kin [erg/s]	$\langle \beta^{-1} \rangle^{-1}$	t_max [Myr]
M1	10^{-1}	2.9×10^{47}	810	6.7
M2	10^{-2}	2.9×10^{46}	81	10.9
M3	10^{-3}	2.9×10^{45}	8.1	16.5
M4	10^{-4}	2.9×10^{44}	0.89	47.5
M4L	10^{-4}	2.9×10^{44}	36	50.0
M3P	10^{-3}	2.9×10^{45}	7.6	42.6

field (Tregillis et al., 2001, 2004; O'Neill et al., 2005), which locally, but not globally fulfills the constraint. If dynamic effects of magnetic fields are to be examined, this is crucial as two effects are ignored otherwise: (1) Jet magnetic fields are carried outwards by the beam, and since the jet head is the outermost part of the jet, magnetic fields have to turn backwards there. Since plasma and field are tied together by flux freezing, this ultimately will drive additional plasma off the axis. For a homogeneous axial field, however, all field lines are effectively anchored in the ambient gas, thereby artificially changing the plasma flow in the jet head. (2) Magnetic field topology is changed by these anchored fields. The backflow carries the initially straight field lines into the cocoon, thus bending them and performing work against magnetic tension, which would be different for globally closed field lines.

Thus, we use a setup where magnetic fields are essentially confined to the jet with a globally closed field structure, letting them propagate into nonmagnetic ambient gas. For the magnetized jets, magnetic fields were set as follows: Toroidal fields were kept constant in the jet nozzle at all times, employing only a radial dependence.

$$B_\phi = 30\,\mu\mathrm{G}\ \mathrm{sgn}(Z)\,(R/r_\mathrm{j})\,\sin^4(\pi R/r_\mathrm{j}) \tag{2.25}$$

The ambient matter carries no toroidal field. For M4L, field magnitude was lowered by a factor of 10 to avoid dominating magnetic fields. Poloidal fields $B_\mathrm{p} = B_Z\mathbf{e}_Z + B_R\mathbf{e}_R$ were set for the whole computational domain using a magnetic dipole field

$$\mathbf{B}(\mathbf{x}) = \frac{3\mathbf{n}\,(\mathbf{n}\cdot\mathbf{e}_Z) - \mathbf{e}_Z}{|\mathbf{x}|^3}\cdot m\,, \qquad \mathbf{n} = \mathbf{x}/|\mathbf{x}|\,, \tag{2.26}$$

with $m = 100\,\mu\mathrm{G}\,r_\mathrm{j}^3$. To avoid the singularity at the origin for numerical reasons, a constant (r_j) was added to the distance from the origin in the denominator. Unfortunately, the solenoidal constraint is violated by this. The errors, however, are small ($(\Delta Z/B)\ \nabla\cdot\mathbf{B} < 0.14$), concentrated towards the nozzle edges and swept away at later times. This problem is solved in the improved setup, but no changes attributable to this were found.

The initial magnetic fields in Tab. 2.3 are "nozzle-averaged" initial values. For this, the area-averaged value of quantity Q is defined as

$$\langle Q\rangle = \frac{2}{r_\mathrm{j}^2}\int_{R=0}^{R=r_\mathrm{j}} Q\ R\,\mathrm{d}R \qquad \text{at } Z = \pm r_\mathrm{j}\,. \tag{2.27}$$

As the poloidal field can not be kept constant without violating $\nabla\cdot\mathbf{B} = 0$ at every time step, this field can evolve with time due to the interaction with the enclosing cocoon, quickly adjusting to $13\,\mu$G ($1.5\,\mu$G for M4L) and then stays constant. For these nozzle averages, only 90 % of the jet radius were considered for M1, M2, M3 and 80 % for M4 and M4L to exclude cells at the shearing boundary of the nozzle, where high magnetic fields and opposite field directions can occur, while the core of the jet is unchanged.

Historically, plasma β is defined as p/p_m. Unfortunately this becomes singular for non-magnetized plasma ($p_\mathrm{m} = 0$, $\beta\to\infty$) and gives a wrong impression when averaged arithmetically (one cell of nearly non-magnetic plasma outbalances many strongly magnetized cells). The more descriptive variable for MHD simulations is $p_\mathrm{m}/p = 1/\beta$. Thus for plasma β, the harmonic mean is used, giving an average value of $\langle\beta^{-1}\rangle^{-1}$.

Additional boundary conditions for the nozzle–ambient interface were set; at the radial boundary, reflective conditions were used, at the axial (outlet) boundaries, magnetic fields were set to have only axial direction. Boundary conditions for the outer border of the computational domain were set according to axial symmetry on the axis and to zero gradient at the other boundaries. However these did not have any effect, as they were only reached by the bow shock at the end of the simulation.

2.5.2 Force-balance Setup

The second setup used for our MHD simulations is generally the same as the parameter study setup, but differs in some details which have been found to be problematic previously: it uses a smoothed dipolar field, which guarantees the solenoidal constraint by using the vector potential, radial force-balance is established within the beam, the jet speed is ramped up to suppress immoderate dissipation during the startup phase, and the compressible tracer variable is proportional to the injected relativistic particles in the jet plasma, allowing detailed computation of emission maps. Since the global behaviour is largely identical, only a magnetized jet with density contrast $\eta = 10^{-3}$ was simulated with this setup. This setup is referred to as M3P ("M3 Plus").

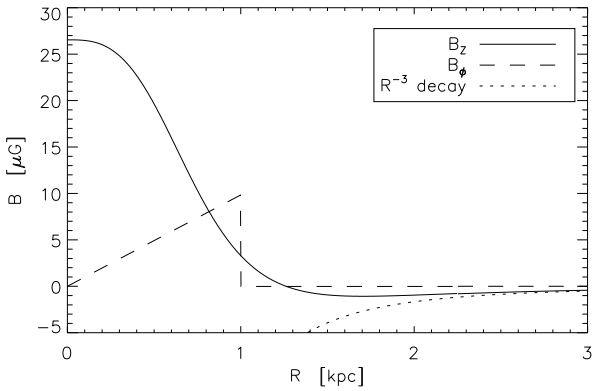

Figure 2.3: Radial profiles of the poloidal and toroidal magnetic field used for M3P in the midplane $Z = 0$, as well as the dipole decay of the poloidal field $\propto R^{-3}$. While the poloidal field lines are closed outside of $R \approx 1.26$ kpc, the toroidal field is confined to the nozzle.

The poloidal field $\mathbf{B}_\mathrm{p} = B_Z \mathbf{e}_Z + B_R \mathbf{e}_R$ was inspired by (although not identical to) the Taylor expansion of the magnetic field of a current loop (Jackson, 2002, page 213), and described by its vector potential $\mathbf{A}$ by the definition $\mathbf{B} = \nabla \times \mathbf{A}$, which ensures the solenoidal constraint $\nabla \cdot \mathbf{B} = 0$.

$$\mathbf{A} = \frac{1}{2}\,\hat{B}_\mathrm{p}\, a\, \frac{\varrho}{1+\sigma^3}\,\mathbf{e}_\phi \tag{2.28}$$

$$B_Z = \hat{B}_\mathrm{p}\, \frac{1+\sigma^3-\frac{3}{2}\,\varrho^2\sigma}{(1+\sigma^3)^2} \tag{2.29}$$

$$B_R = \hat{B}_\mathrm{p}\, \frac{\varrho\zeta\sigma}{(1+\sigma)^2} \tag{2.30}$$

$$j_\phi = \frac{9c\hat{B}_\mathrm{p}}{4\pi a}\,\frac{\varrho\sigma}{(1+\sigma^3)^3} \tag{2.31}$$

where a is a length scale parameter, $\hat{B}_\mathrm{p}$ is the peak value of the poloidal field and the normalized coordinates are $\varrho = R/a$, $\zeta = Z/a$ and $\sigma = \sqrt{\varrho^2+\zeta^2}$. It has no singularities, shows a flat behaviour in the midplane

$$B_Z = \hat{B}_\mathrm{p}\, \frac{1-\varrho^3/2}{(1+\varrho^3)^2} \qquad \text{for } Z = 0\,, \tag{2.32}$$

thus avoids strong gradients at the nozzle boundary and declines as magnetic dipole $\propto r^{-3}$. To have the field roughly scaled to the size of the nozzle we set $a = 3r_\mathrm{j}/2$. Fig. 2.3 shows the radial dependence of both the poloidal and the toroidal field component (described later) as well as the decay of the poloidal field with R^{-3}. For $R > 1.26$ kpc, the field shows the opposite sign; here the field lines are closed.

The toroidal field cannot violate $\nabla \cdot \mathbf{B} = 0$ in axisymmetry as field lines are always closed. Hence, we prescribe a toroidal field corresponding to a uniformly distributed axial current

density within the cylindrical jet nozzle. From Ampère's equation (2.8), considering the circular cross section of a cylinder with radius R, we find for an axial current density $\mathbf{j} = j\mathbf{e}_Z$ by using Stokes' theorem

$$\int_S (\nabla \times \mathbf{B}) \cdot \mathrm{d}\mathbf{S} = \int_{\partial S} \mathbf{B} \cdot \mathrm{d}\mathbf{l} = 2\pi R\, B_\phi(R) \tag{2.33}$$

$$= \int_S \frac{4\pi}{c}\, \mathbf{j} \cdot \mathrm{d}\mathbf{S} = \frac{4\pi}{c}\, j\pi R^2 \tag{2.34}$$

and hence a radially linear magnetic field behaviour and an axial current density

$$B_\phi = \hat{B}_\phi\ (R/r_\mathrm{j}) \tag{2.35}$$

$$\mathbf{A}_\mathrm{p} = \hat{B}_\phi\, (R/r_\mathrm{j})\, Z\mathbf{e}_R \tag{2.36}$$

$$j_Z = \frac{c\hat{B}_\phi}{2\pi r_\mathrm{j}} \tag{2.37}$$

with toroidal field peak value $\hat{B}_\phi$ at the outer radial boundary of the nozzle. We note that contrary to the parameter study setup, direction of the toroidal field does not change at the midplane. Effects on the dynamics, however, were found to be smaller than the effects of turbulence.

For significantly magnetized flows, the toroidal field component leads to radial forces (hoop stress) on the plasma and results in a collimation of the flow and possibly the appearance of "nose cones" (Clarke et al., 1986). To get a stable magnetic field configuration at the nozzle, the radial forces should be balanced and this constrains the combination of pressure and magnetic field profiles. We do not aim at exactly solving this for the whole jet nozzle, since the strong interaction with the ambient matter at the bow shock will lead to much stronger forces. Yet, we want our radial profile for the magnetic field in the equatorial ($Z = 0$) plane not to lead to collimation or expansion of the jet, as this could render the parameter "jet radius" meaningless.

We make the simplified assumption that the magnetic field has no radial components, and may vary as a function of R but not Z. This is motivated by magnetic field lines with purely axial orientation of the poloidal components, which seems reasonable in the jet nozzle and is fulfilled for our poloidal profile at $Z = 0$. Hence, in the MHD momentum equation (2.2), we only take the pressure gradient and the magnetic forces into account, where then the magnetic tension $(\mathbf{B} \cdot \nabla)\, \mathbf{B}$ only depends on the toroidal magnetic field, but the poloidal components come into play via the magnetic pressure.

The forces onto the plasma are then constrained to:

$$\frac{\partial p}{\partial R} = -\frac{1}{8\pi}\left(\frac{\partial B_Z^2}{\partial R} + \frac{\partial B_\phi^2}{\partial R}\right) - \frac{B_\phi^2}{R} \tag{2.38}$$

Using the poloidal magnetic field configuration described above, we then find the pressure profile depending on the toroidal field profile. We considered different pressure profiles and demanded that the pressure must be positive and finite inside the nozzle for the chosen toroidal field and that it should not vary extremely, since internal perturbations and shocks would quickly destroy this balance. The toroidal field described above was chosen, since it meets these constraints well.

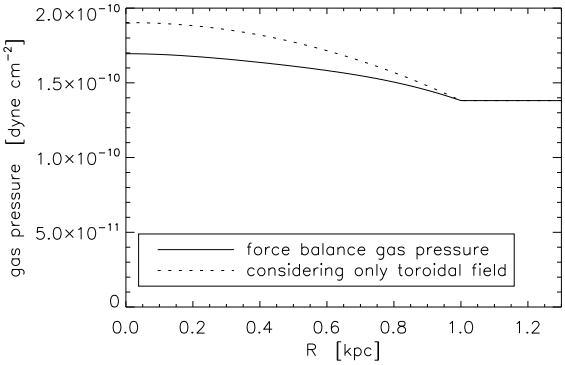

Figure 2.4: Radial pressure profile $p(R)$ used for the jet nozzle in the M3P setup. The solid line gives the (used) profile which exactly fulfils force balance in the midplane $Z = 0$, while the dotted line is the approximate solution if only the toroidal field component is used for force balance.

Equation (2.38) allows us, at least numerically, to integrate the gas pressure from the jet radius inwards – with $p(R = r_\mathrm{j}) = p_\mathrm{a}$ setting the nozzle in pressure balance with an ambient gas pressure p_a. Not considering the poloidal field for a moment, a radial dependence for gas pressure is found as

$$p(R) = p_\mathrm{a} + \frac{1 + 4\pi}{8\pi} \hat{B_\phi}^2 \left(1 - \frac{R^2}{r_\mathrm{j}^2}\right) . \tag{2.39}$$

The poloidal field component makes the radial pressure profile more complicated due to its magnetic pressure but still can be solved exactly. We use this function to setup the gas pressure inside the whole jet nozzle at all times. Slight deviations from exact force balance are expected for cells outside the equatorial plane. Fig. 2.4 shows the radial pressure profile for the M3P simulation setup for the case of using all magnetic field contributions and for the "toroidal field only" approximation as in (2.39).

With these magnetic fields, nozzle-averaged values (2.27) for the magnetic field components and their magnetic pressure contribution can be computed

$$\langle B_\mathrm{p} \rangle = \frac{27}{35} \hat{B}_\mathrm{p} \approx 0.7714 \, \hat{B}_\mathrm{p} \tag{2.40}$$

$$\langle B_\phi \rangle = \frac{2}{3} \hat{B}_\phi \approx 0.6667 \, \hat{B}_\phi \tag{2.41}$$

$$\langle B_\mathrm{p}^2 \rangle \approx 0.6184 \, \hat{B_\mathrm{p}}^2 \tag{2.42}$$

$$\langle B_\phi^2 \rangle = \frac{1}{2} \hat{B_\phi}^2 = 0.5 \, \hat{B_\phi}^2 \tag{2.43}$$

as well as the nozzle-averaged gas pressure

$$\langle p \rangle \approx p_\mathrm{a} - 0.3614 \, \frac{\hat{B_\mathrm{p}}^2}{8\pi} + 3.392 \, \frac{\hat{B_\phi}^2}{4\pi} \tag{2.44}$$

$$\approx p_\mathrm{a} - 0.01438 \, \hat{B_\mathrm{p}}^2 + 0.2699 \, \hat{B_\phi}^2 . \tag{2.45}$$

Table 2.5: Simulation parameters for the force-balance setup M3P.

ambient gas density	ρ_a	$10^{-2}\, m_\mathrm{p}\,\mathrm{cm}^{-3}$
ambient gas temperature	T_a	$5 \times 10^7\,\mathrm{K}$
ambient pressure	p_a	$1.38 \times 10^{-10}\,\mathrm{dyne\,cm}^{-2}$
density contrast	η	10^{-3}
jet speed	v_j	$0.6\,c$
jet internal sonic Mach number	$M_\mathrm{int,s}$	4.5
jet internal magnetosonic Mach number	$M_\mathrm{int,ms}$	4.3
jet external Mach number	M_ext	153
jet thermal pressure	$\langle p \rangle$	$1.61 \times 10^{-10}\,\mathrm{dyne\,cm}^{-2}$
jet temperature	T	$5.8 \times 10^{10}\,\mathrm{K}$
jet radius	r_j	$1\,\mathrm{kpc}$
jet kinetic power	L_kin	$2.9 \times 10^{45}\,\mathrm{erg\,s}^{-1}$
jet nozzle magnetic field	$\langle B_\mathrm{p} \rangle$	$20.5\,\mu\mathrm{G}$
	$\langle B_\phi \rangle$	$7.87\,\mu\mathrm{G}$
	$\hat{B}_\mathrm{p}$	$26.5\,\mu\mathrm{G}$
	$\hat{B}_\phi$	$9.84\,\mu\mathrm{G}$
	β	8
	λ	0.9
jet speed ramp-up time	t_ramp	$8.59 \times 10^3\,\mathrm{yr}$
simulation end	t_max	$42.6\,\mathrm{Myr}$

Here, the poloidal magnetic field provides an additional (but small) pressure contribution, whereas the toroidal field by its magnetic tension pinches the plasma, which has to be balanced by additional gas pressure. As the poloidal field is stronger than toroidal field in the M3P setup, it provides appreciable pressure support in Fig. 2.4. However, for poloidal fields with only 30 % of this value, the "toroidal field only" formula provides a reasonable approximation to the full force balance solution.

Using all these expressions for the nozzle-averaged values, magnetic fields can be set up by defining an average plasma β

$$\langle \beta \rangle = \frac{8\pi \langle p \rangle}{\langle B^2 \rangle} \tag{2.46}$$

and the fractional contribution of the poloidal field to the magnetic pressure

$$\lambda = \frac{\langle B_\mathrm{p}^2 \rangle}{\langle B^2 \rangle}\,. \tag{2.47}$$

For simulation M3P, we set $\beta = 8$, $\lambda = 0.9$ for the magnetic fields and find the values listed in Table 2.5.

While the vector potential $\mathbf{A}$ and the magnetic field $\mathbf{B}_\mathrm{p}$ are analytically equivalent and satisfy $\nabla \cdot \mathbf{B} = 0$, it cannot be guaranteed in general that the discretization of $\mathbf{B}$ on a grid still satisfies this constraint exactly. However, since NIRVANA uses a staggered grid where magnetic fields are defined in the centers of the cell faces by the flux through the respective face, magnetic fields can be derived from the vector potential in a way consistent with the CT

scheme used to conserve $\nabla \cdot \mathbf{B}$ to machine round-off errors, where the induction equation is solved in the integral formulation for the magnetic flux $\Phi = \int_S \mathbf{B} \cdot \mathrm{d}\mathbf{S}$

$$\frac{\partial \Phi}{\partial t} = -c \int_S (\nabla \times \mathbf{E}) \cdot \mathrm{d}\mathbf{S} \tag{2.48}$$

$$= -c \int_{\partial S} \mathbf{E} \cdot \mathrm{d}\mathbf{l}\,. \tag{2.49}$$

For computing the flux Φ through a cell face i with area $\mathbf{S} = |S|\,\mathbf{n}$ and thus the respective magnetic field component $B_i = \mathbf{B} \cdot \mathbf{n}$, instead of using the differential definition of $\nabla \times \mathbf{A}$, we use Stokes' theorem for the vector potential components A_j, which are defined in the centers of the cell edges Δl_j.

$$\int_S \mathbf{B} \cdot \mathrm{d}\mathbf{S} = \int_S \mathbf{B} \cdot \mathbf{n}\, \mathrm{d}S = B_i\, S \tag{2.50}$$

$$= \int_S (\nabla \times \mathbf{A}) \cdot \mathrm{d}\mathbf{S} = \int_{\partial S} \mathbf{A} \cdot \mathrm{d}\mathbf{l} = \sum_j A_j \Delta l_j\,. \tag{2.51}$$

This easily can be applied to our curvilinear grid. The corresponding expressions for B_i are then used for the poloidal field setup and guarantee a divergence-free magnetic field at machine accuracy.

Jet density and velocity magnitude are set constant in space and time as before, with the velocity pointing in opposite directions for the two nozzle halves. However, during a short startup phase, jet speed is linearly ramped up, reaching its final magnitude after 8.59×10^3 years. This was included to reduce dissipation in the violent early phase and limit influence of the initial conditions to a shorter time scale. Since NIRVANA does not solve the energy equation in a conservative manner, artificial viscosity applied to strong shock in the early phase could lead to unphysical dissipation. This can be reduced by weakening the (artifically strong) shocks arising from the initial condition. Also for the M3P setup, the ambient density was randomly perturbed with a probability of 10 %, in this case by a random factor between 0.7 and 1.3.

The compressible tracer field was set to 1 in the jet nozzle and to 10^{-25} in the ambient medium. Thus, it can be assumed to be proportional to the density of injected relativistic electrons. This can be used for computation of emission maps later. However, this only describes adiabatic compression, not reacceleration in shocks. The non-zero tracer in the ambient matter allows to trace the bow shock by a changed tracer value, but still is small enough to not interfere with tracing the nonthermal particles.

2.6 Resolution Study

NIRVANA uses a finite-differences discretization to solve the MHD equations. Derivations are approximated by the difference quotient, e.g. forward differences

$$\frac{\mathrm{d}f}{\mathrm{d}x} = \lim_{h \to 0} \frac{f(x+h) - f(x)}{h} \approx \frac{f(x + \Delta x) - f(x)}{\Delta x}\,. \tag{2.52}$$

This discretization converges towards the accurate result for small time steps Δx. However, while small time steps give higher accuracy, achievable numerical resolution is limited and thus results have to be checked, whether they strongly depend on the chosen resolution, which is an indication that the simulation is not (yet) converged. This also applies to other numerical methods, as finite-volume methods, which are based on the integral formulation (fluxes through cell surfaces and volume-averages of variables) rather than differential equations.

While a rigorous convergence check is beyond our possibilities and subject to current numerical research, we note that a detailed convergence study and comparison with other codes for NIRVANA with a similar setup has been performed by Krause & Camenzind (2001), showing that reasonable accuracy is achieved with our resolution of 20 cells per beam radius ("R20"). However, even with the highest resolution no full convergence could be reached, as vortical structures arising from Kelvin-Helmholtz instabilities show more and more substructure for higher resolutions. Since numerical viscosity decreases with higher resolution, all viscosity-related quantities cannot be expected to converge fully, except when a fixed physical viscosity were included in the simulation.

Here, we restrict ourselves to a resolution study of the simulations. For this, the simulation M3P was additionally performed with lower resolution (10 cells per beam radius, "R10") for the full simulation time and with higher resolution (80 cells per beam radius, "R80") until $t = 4.8$ Myr. With these, we almost span one order of magnitude in resolution. Note that the resolutions do not differ by a constant factor, but there is a larger jump between 20 and 80 cells per beam radius, which might influence ones impression of convergence or non-convergence (often fixed factors are used).

Fig. 2.5 shows density maps for two different times with the three different resolutions. At the earlier time ($t = 0.2$ Myr, where the first full dataset was saved), the jet has not yet propagated far. For the lowest resolution, the map still looks quite symmetric with respect to the midplane ($Z = 0$). Prominent features are the two vortices in the backflow at $(Z, R) \approx (\pm 2, 3)$ kpc and ambient matter flowing towards the nozzle, then being carried along with the beam. For the medium resolution (R20), more perturbations at the contact surface (red–blue interface) are present and asymmetries between the two sides are visible. For the highest resolution (R80), the backflow already shows filamentary structures and symmetry between both jets is broken. The fine structures are due to Kelvin-Helmholtz instabilities, which grow at the contact discontinuity due to the strong shearing (fast moving jet plasma, ambient gas at rest), and are very sensitive to small perturbations. The higher the resolution is, the more Kelvin-Helmholtz modes can be resolved, yielding more and finer structures in the cocoon, which then exhibits turbulent flow. Strictly speaking, the simulation is not converged, as more and more structures appear for higher resolutions. However, turbulence intrinsically is characterized by chaotic behaviour on small scales, evolving differently for only slightly different initial conditions. Due to the exponential growth of the perturbations, symmetry is broken already at this early time. At later times, visible in the density plots at $t = 3.8$ Myr, differences are even larger. Hence, turbulent systems are described by their statistical or global properties, and convergence of those is then examined.

In our simulations, the cocoon is highly turbulent, while the bow shock is only marginally perturbed by the neighbouring cocoon. The axial bow shock positions are practically identical for the early time step. However, at $t = 3.8$ Myr the positions differ slightly: $Z = 22$ kpc for R10, 21.2 kpc for R20 and 20.3 kpc for R80. This can as well be seen from Fig. 2.6, which

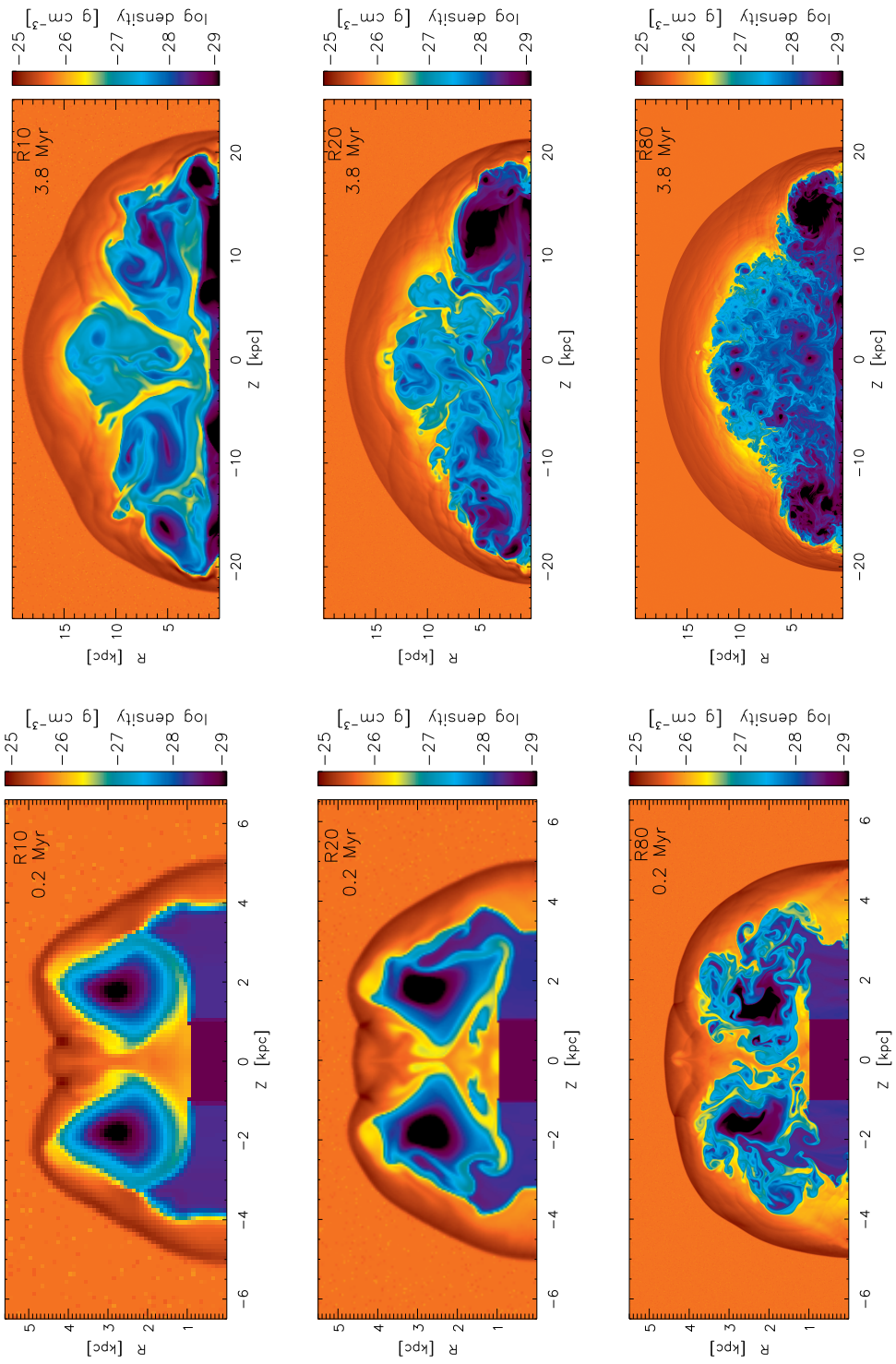

Figure 2.5: Density plots of M3P for the three different resolutions, labelled by R10, R20 and R80, for two different times: $t = 0.2$ Myr and $t = 3.8$ Myr.

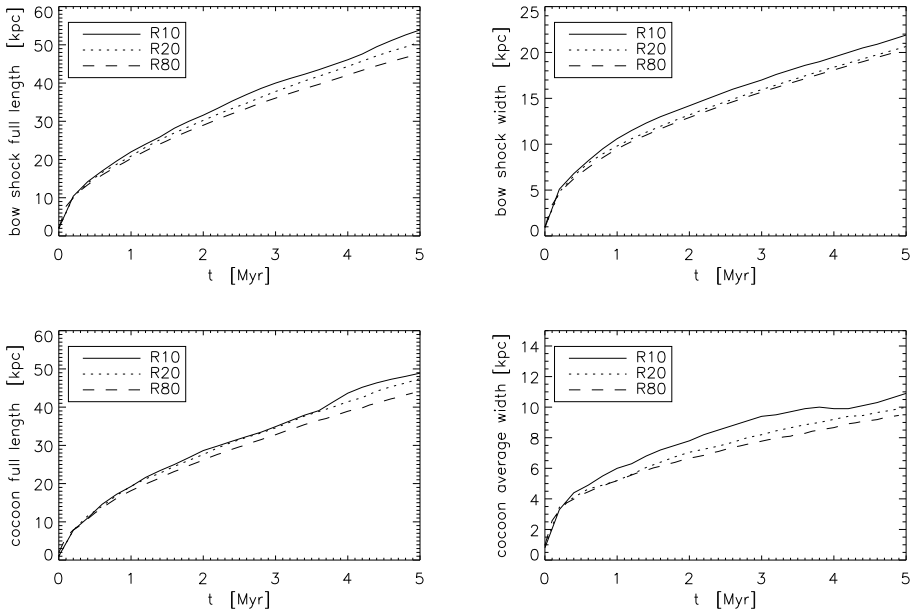

Figure 2.6: Evolution of bow shock and cocoon sizes for the M3P setup using different resolutions: 10, 20 and 80 cells per beam radius.

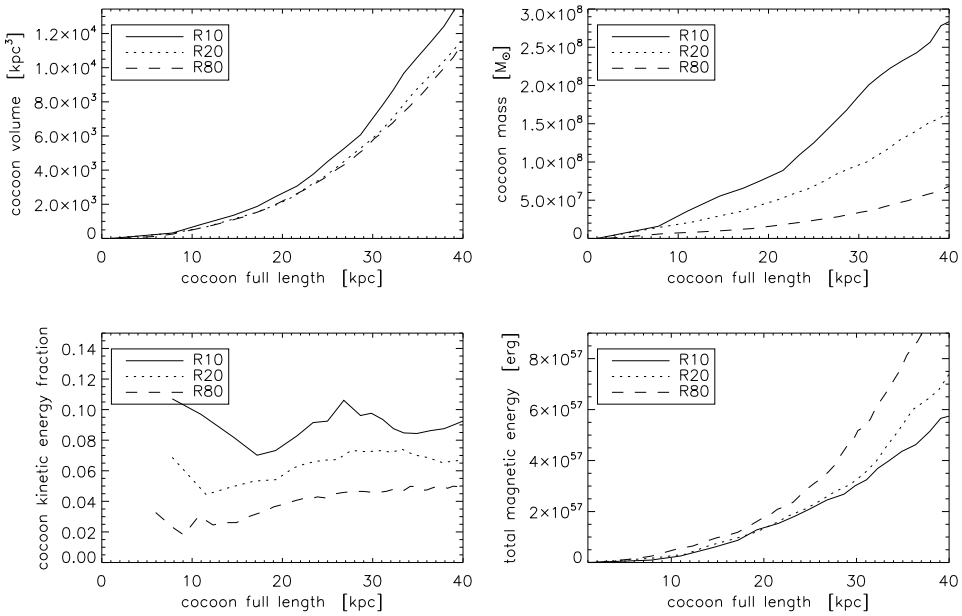

Figure 2.7: Evolution of some selected quantities for the M3P setup using different resolutions. Cocoon volume, mass and kinetic energy fraction (relative to the total injected energy), using a tracer limit of 10^{-3}, and the measured total magnetic energy. Values are plotted as function of cocoon length to avoid effects from systematically slower propagation with higher resolution.

shows the evolution of the bow shock and cocoon axial diameter and lateral width as function of time for the three resolutions. The bow shock speed converges to somewhat slower values for the higher resolutions in both directions. This was also found by Krause & Camenzind (2001), who explored convergence for resolutions up to 400 cells per beam radius. We find similar behaviour for the cocoon length and the averaged cocoon width and conclude that the global properties of simulations are reasonably converged, showing differences on the percent level only.

However, some quantities show larger differences for varying resolution and hence their values have to be taken with care. They are shown in Fig. 2.7. While the cocoon volume shows very nice convergence, differences in cocoon mass are more than a factor of 3. This is not too surprising, as cocoon masses are mostly made up of entrained ambient gas, where entrainment strongly depends on the resolved instabilities at the contact surface. However, for higher resolution dependence of cocoon masses on the chosen tracer limit tends to be weaker.

Similarly, the fraction of the cocoon kinetic energy relative to the total injected energy varies with resolution. For higher resolutions the fractions become smaller by a factor of ≈ 2. The measured total magnetic energy, in contrast, is higher for the higher resolutions. This may indicate that the transfer of kinetic to magnetic energy, as will be shown in Chapter 3, is even more efficient at higher resolutions and thus underestimated by our simulations.

As mentioned before, onset of turbulence in the jet head and the cocoon makes simulations susceptible to smallest perturbations. While our prescribed random density fluctuations in the ambient gas are initially the main reason for symmetry breaking and different behaviour at different resolutions, even inaccuracies at the level of machine round-off errors will impact the local structures in a turbulent flow after sufficient time. Despite not anticipated, it is clear that compiler choice and optimization hence will have an impact on this, since the exact choice of compiler optimizations may change the last bits in floating point computations (for example, associativity is not ensured in floating-point arithmetics).

Accordingly, we noticed that the turbulence in the jet backflow is quite sensitive to compiler optimization. The results of three simulations with identical code, two on an Intel-CPU based workstation with gcc 3.2 and gcc 3.3.5, and one on the SX-6 (sxcc rev. 063), are shown in Fig. 2.8. The two gcc runs have identical initial conditions, while the sxcc run has slightly different initial conditions due to a different implementation of the random number generator. Already after 210 000 time steps, differences are quite obvious. Not only are spatial structures different, but also the points in time of certain events can be shifted. Differences in the length of the jet are mainly caused by "pumping" of the jet (due to pressure variations in the beam), which occurs at only slightly different times for the simulations but hence give relatively large differences in space for equal times. The differences in the extent of the bow shock are 1.5 % in axial and 0.7 % in radial direction on average. Fig. 2.9 shows the time evolution. However, there doesn't seem to be a systematical trend or increase with time.

We conclude that turbulence in the jet head and the cocoon makes simulations susceptible to uncontrollable perturbations due to its chaotic character. This does not only apply to our simulations, but to all systems with turbulence or chaotic behaviour. However, statistical or global properties of turbulence as well as quantities not directly related to turbulence (as the bow shock or the beam) are reasonably converged on the level of several percent. Simulations thus are expected to correctly model the considered system.

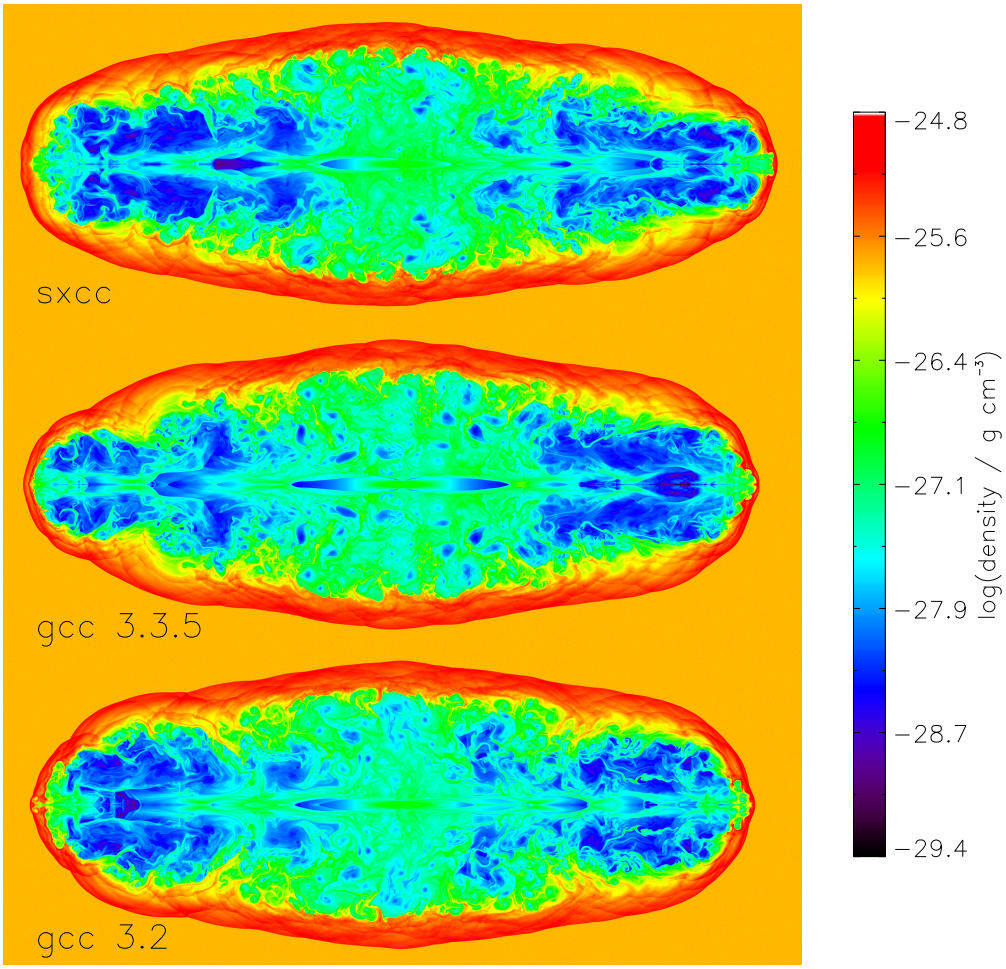

Figure 2.8: Comparison between three runs with identical initial conditions for M1, compiled on different systems. This snapshot shows the logarithmically scaled density after 6.0 Myr with a resolution of $4\,000 \times 800$ cells (200×40 kpc^2). After some Myrs, the differences become visible, as the turbulence is very sensitive to numerical inaccuracies, but the global behaviour is not affected.

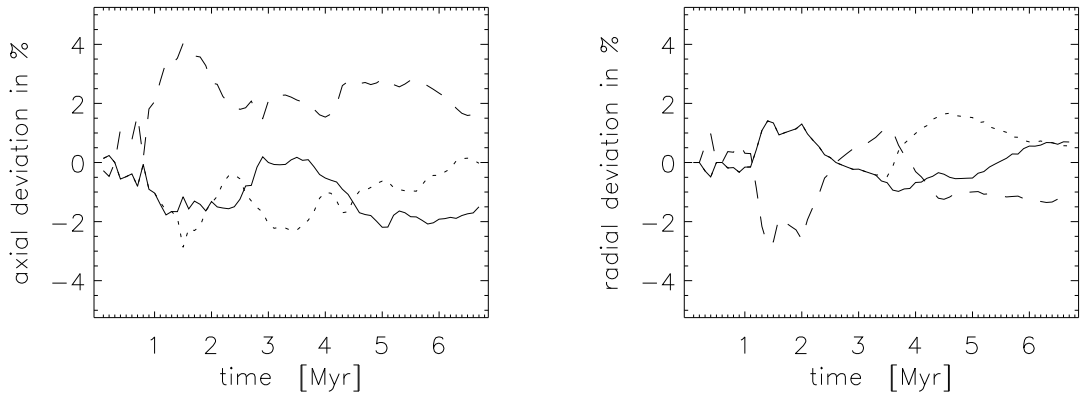

Figure 2.9: Time evolution of the differences in the axial and radial extent of the bow shock for runs with different compilers (solid: gcc 3.2, dotted: gcc 3.3.5, dashed: sxcc). The deviation in percents is expressed relative to the common average of the three runs. Aside from sxcc producing slightly longer bow shocks, there isn't a systematical increase of the deviations with time.

2.7 Visualization of Turbulent Vector Fields

Finally, we will briefly discuss a method which is well suited for the visualization of turbulent vector fields and which was implemented and used for this thesis. While visualization of 2D scalar fields can easily be done by using color maps, the traditional approach for vector fields is to use arrows pointing in direction of the vector fields. This gives a reasonable representation for ordered fields, but is mostly useless for turbulent vector fields or fields with small-scale structures.

Line Integral Convolution (LIC) was described by Cabral & Leedom (1993) and is based on computation of stream lines. It gives a representation similar to iron filing on a paper tracing the field lines of a magnet. Each pixel in the LIC image is obtained by integrating over a white noise image along a streamline of certain length through the respective pixel position, and writing the result to that pixel. The stream line is computed from the vector field array aligned with the noise image. Vector field, noise field and output field need to have the same size for this. Often a constant integration kernel (averaging) is used, but other kernels can be chosen at will (e.g. increasing weight in direction of the vector field). Furthermore, the noise image can be replaced by any other image or pattern, which is then blurred in direction of the vector field.

Due to a large number of stream lines to be computed, LIC is rather computationally demanding. However, current computers are fast enough for this and the method is easily parallelizable. Though this technique is already 15 years old, it has not been included in any all-purpose visualization software yet. Thus it has been implemented in IDL for the present work, with a run time of less than an hour for a simulation snapshot at full resolution.

LIC images, however, do not contain information about the vector field magnitude. To add this, we extended the method to represent the field magnitude by colors: working in HLS (hue–lightness–saturation) color space instead of RGB (red–green–blue) the LIC image was

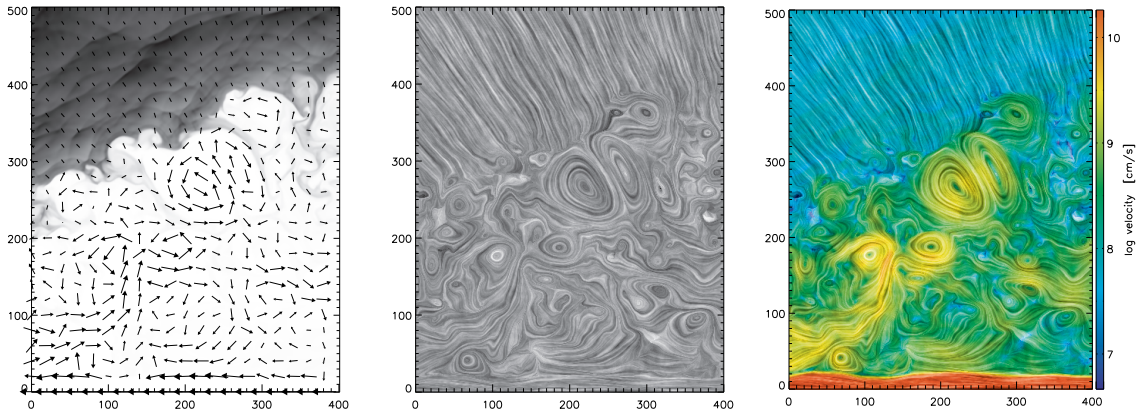

Figure 2.10: Visualization of a velocity vector field using different techniques: asinh(x)-scaled arrows aligned with the field direction as overlay of a density map, LIC representation in greyscale, and LIC representation in color, where color shows the field magnitude and brightness modulation shows the field orientation.

encoded as lightness and the field magnitude as hue value (color). Saturation could be used, theoretically, to encode another field, but in practice this is not perceived well enough by the human eye to add any real value. Similar results could be achieved by adding or multiplying the LIC field and the magnitude scalar field and displaying it with a usual color scale, but here it might occur that stream line and magnitude contribution can not be disentangled anymore, while for the HLS approach the information is clearly separate. To account for difficulties in distinguishing colors for high or low brightness, the lightness parameter should be limited in range (e.g. $[0.05, 0.95]$) and the saturation value should be somewhat lower than unity (e.g. 0.8).

Fig 2.10 shows the comparison of an arrow plot and the LIC representations. For arrow plots, usually arrow lengths are chosen to be proportional to the field magnitude. Since the field magnitude varies by more than two orders of magnitude, only arrows within the beam (shown red in the color LIC image) were visible then. For the present case of jet simulations, the arrow plot uses an asinh function applied to the arrow lengths, resulting in a logarithmic-like display of the field strength, where even slow moving regions are easily recognizable. Yet it is evident that the LIC images show much more flow details than possible with arrows. This is even more drastic for images showing only part of the flow with relatively large vortices but the whole computational domain, where vortex sizes generally will be much smaller than spatial resolution of the arrows. For largely varying field magnitudes, it is however very important to include the magnitudes to be able to judge the "importance" of motion, as possible with our color LIC images.

It is important to mention that there is still a limitation with this representation: direction of the flow (forward vs. backward) cannot be displayed with LIC images. While use of asymmetric kernels (e.g. linearly increasing in direction of the flow) may include this information, this was found to be only of limited use for turbulent fields with their fine-grained structures; direction of the flow, though, is not very important in this case due to the stochastic nature of turbulent patterns, and regions of well-ordered flow (beam and shocked ambient gas) have directions which are already clear from the physical setup. If directional information were important, the

LIC images would have to be supplemented by arrow plots. Image-guided stream lines (OSTR, Turk & Banks, 1996; Laidlaw et al., 2001) might then provide a compromise between arrow plots and stream line techniques as LIC.

3 Evolution and Magnetic Fields

Magnetic fields, which are present in extragalactic jets and are responsible for the observed synchrotron radiation, can affect the morphology and dynamics of the jets and their interaction with the ambient cluster medium. The idea behind the present study is to explore the behaviour of very light jets with non-dominant magnetic fields in a cluster environment using a plausible global setup for the plasma and the magnetic fields. We performed 2.5D simulations (Sect. 2.5.1) of both purely hydrodynamic and MHD jets on the scale of up to 200 kpc with a uniform ambient gas density, for a wide range of density contrasts and examined the jet propagation, morphology, magnetic field structure and evolution. Though the uniform ambient density differs from measured cluster profiles, it allows us to exclude any effects possibly resulting from a declining density profile. Also, effects from a cluster profile are known and are discussed later. After a description of the morphology and dynamics, we describe the evolution of the bow shock and the cocoon; then entrainment of ambient gas and the energy budget; and finally the magnetic fields and their evolution as well as their impact on morphology and propagation. Results are then discussed and put in context with observational findings.

In the following, we will focus on the MHD jets and use their hydro counterparts only for comparison, as they are set up exactly as the MHD jets, but have zero magnetic field. To compensate for different propagation speeds of jets with differing density contrasts, plots will use the axial bow shock diameter or jet length, where appropriate. "Full length" refers to the whole simulated length (considering both jets), while "full width" refers to twice the measured (radial) distance from the axis.

3.1 Morphology

The density and temperature maps of Fig. 3.1 show snapshots of all MHD runs at a full jet length of 100 kpc, respectively. In the following, simulation run M3 (see Table 2.3 and 2.4) mostly will be used for figures as it has the strongest non-dominant magnetic fields, therefore showing effects of the magnetic fields best and allowing for comparison of features between different figures.

The jet backflow blows up a pronounced cocoon, surrounded by a thick shell of shocked ambient matter. Dense ambient gas is mixed into the cocoon in finger-like structures due to Kelvin-Helmholtz instabilities at the contact surface. Near the jet heads, this instability is suppressed by the magnetic field, which leads to a smoother appearance there. In purely hydrodynamic simulations, this stabilization is absent. The cocoon is highly turbulent and vortices hitting the jet beam can easily destabilize, deflect or disrupt it if jet densities are low. The Mach number varies considerably along the beam (Krause, 2003; Saxton et al., 2002b) and there is no stable "Mach disk" as seen for heavier jets – the terminal shock moves back and forth and often is not clearly defined.

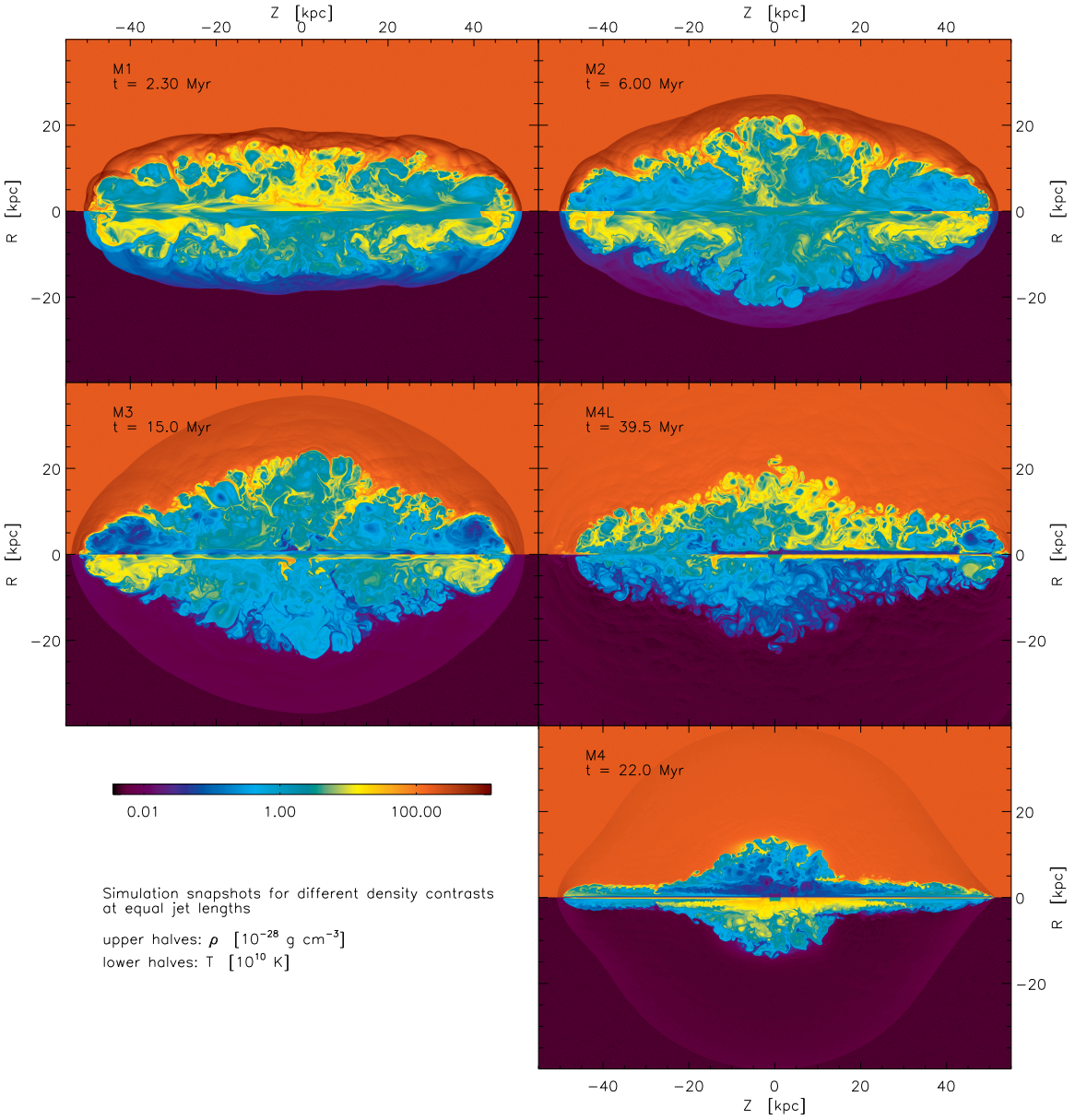

Figure 3.1: Density and temperature for all MHD runs, each at a jet length of ≈100 kpc. The upper halves of each panel show the logarithmic density in units of 10^{-28} g/cm^3, the lower halves show the logarithm of temperature in units of 10^{10} K. Panels additonally are labelled by their respective time.

Because very light jets only propagate slowly, basically hitting the ambient gas as a "solid wall", the backflow is strong and the turbulence makes the interaction between both jets in the midplane important. Such jets have to be simulated bipolarly to describe the lateral expansion and hence the global appearance correctly. If only one jet were simulated, for very light jets the result would strongly depend on the boundary condition in the equatorial plane (Saxton et al., 2002b).

The surrounding ambient gas is pushed outwards by the cocoon pressure, driving a bow shock outwards. The bow shock for very light jets is different in its shape and strength from that of heavier jets (see Sect. 3.3). It is additionally affected by a density profile in the external medium (Krause, 2005), which increases the aspect ratio with time because η increases at the jet head and thus shows cylindrical cocoons.

Differences between the runs of different density contrast are discussed in the following sections. Simulations M1, M2, M3 and M4L form a series of runs with non-dominant magnetic fields and continuously decreasing jet density. The bow shocks become weaker and rounder, and the shells of shocked ambient gas become wider. The cocoons mostly are wider near the midplane, but at larger distances (corresponding to later times) they become somewhat narrower. The beam is M4L is particularly unstable due to its low density and is disrupted on the left side. In contrast to the other runs, M4 is magnetically dominated and forms "nose cones". The two lightest jets (M4L and M4) are discussed in more detail in Sect. 3.7.

3.2 Defining the Cocoon

In the following, we not only measure properties of the bow shock, which is easy to pin down, but also of the cocoon. While generally we define the cocoon as the region, which is filled by jet-originated matter (not including the beam itself) this definition has to be made in more detail for the simulation analysis. The strong backflow and the fragile beams of very light jets make the distinction between cocoon and beam difficult, while mixing at the contact discontinuity complicates the assignment of cell to cocoon or ambient matter. While we do not attempt to distinguish between beam and cocoon if not stated explicitly (it only seems necessary for energetic investigations), the distinction between cocoon and ambient matter is necessary especially for the entrainment measurements later and thus is described in more detail, along with the measurement of the cocoon properties.

3.2.1 Cell Assignment

Two properties can be used for the distinction between cocoon and ambient matter: the (compressible) tracer field and the toroidal magnetic field. Tracer field values of 1 and above indicate undisturbed and shocked ambient matter. This is available in all simulations, but mixing with jet matter at the contact discontinuity (due to finite resolution) lowers the tracer and thus requires a threshold value. The cocoon mass is especially sensitive to this threshold value, as the density of the ambient gas is much higher and thus causes large changes of the cocoon mass if the border is shifted. Figure 3.2 shows the cocoon mass for a range of tracer thresholds. The injected mass at this time is only $4 \times 10^6\,M_\odot$; measured mass above this value is the entrained ambient gas mass.

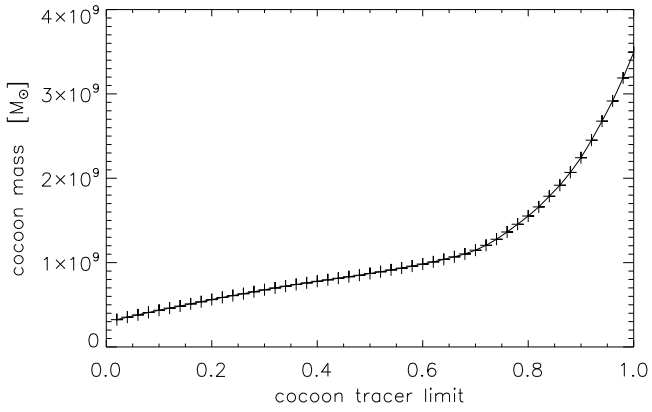

Figure 3.2: Cocoon mass depending on tracer field threshold (mass of all cells with tracer below the threshold), for simulation M3 at $t = 15$ Myr.

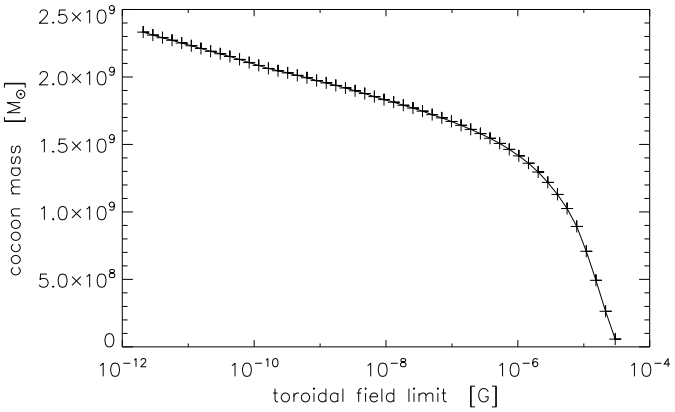

Figure 3.3: Cocoon mass depending on toroidal field threshold (mass of all cells with toroidal field magnitude above the threshold). Simulation M3 at $t = 15$ Myr.

In contrast, the toroidal field strength can be used for separation, as the toroidal field is zero initially in the ambient medium and is conserved independent from the other field components. Figure 3.3 shows the cocoon mass depending on the toroidal magnetic field threshold. Using this method, even cells with only a small mass fraction of jet matter can be assigned to the cocoon. There is a clear break visible, but the cocoon mass continuously increases for lower threshold values until machine accuracy is reached. This has two major problems: First, it naturally is not available for the pure hydro simulations and thus cannot be used to compare HD with MHD simulations. Second, the high sensitivity to jet matter is not a real advantage, as the mass values do not nicely converge and we have to choose a threshold.

In the following we will use a tracer threshold of 0.5 which is available for HD and MHD models and gives cocoon masses that do not strongly depend on the tracer threshold. Furthermore, it selects the regions one would consider belonging to the cocoon also by looking at the other physical variables.

3.2.2 Width Measurement

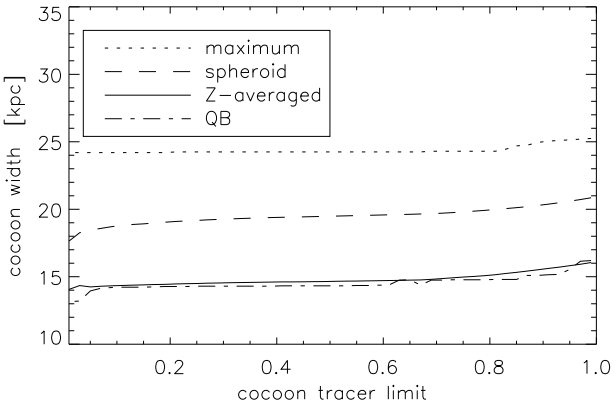

Figure 3.4: Cocoon width for different width definitions as function of the used tracer limit. For simulation M3 at 15 Myr.

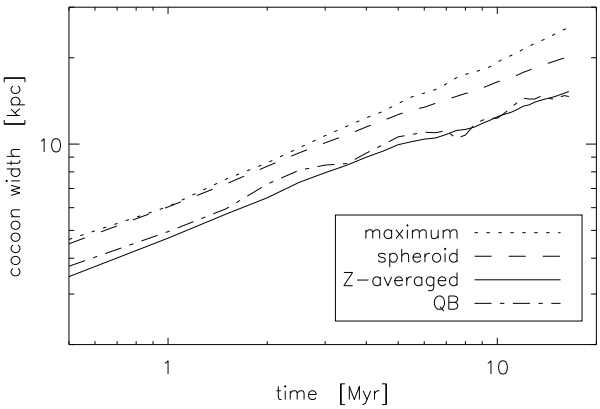

Figure 3.5: Evolution of the cocoon width for different width definitions for simulation M3. A tracer limit of 0.5 was used for cell assignment.

To characterize the width of the cocoon, we checked four different measures, which will generally give different results due to the ragged shape of the contact surface. Widths are

measured from the symmetry axis ($R = 0$, jet channel) and thus are only "half widths". Figure 3.5 shows the temporal evolution of the cocoon width, defined in four different ways:

- maximum width: measured at the maximum R position of a cocoon cell
- average width: Z-averaged over the full jet length
- QB width: measured at one quarter of the full jet length backwards of the jet head
- spheroid width: semi-minor axis of a spheroid with a volume equal to the cocoon volume and the semi-major axis equal to half the full jet length

The QB width is very much dependent on vortices near the contact surface and hence not as as smooth as the other lines. Despite that, it grows similar to the Z-averaged width, which mostly has the lowest width value. The spheroid width lies between the maximum width and the Z-averaged width. All of theses measures can be approximated by powerlaws, but with somewhat different parameters. For the following analysis, the average width will be used if not stated explicitly.

In contrast to the cocoon mass, the cocoon shape does not depend strongly on the tracer limit that is used for its determination (Fig. 3.4). For limits around 0.5, the differences between width definitions is larger than the dependence on the tracer limit.

3.3 Evolution of Bow Shock and Cocoon

3.3.1 Cocoon Pressure Evolution

The low jet density has two main consequences for the evolution of the cocoon pressure: one is the lower jet power (for a fixed jet bulk velocity), which results in a lower cocoon pressure and a generally weaker bow shock. The other is the slow jet head propagation, which increases the propagation time scale compared to the dynamical time scale of travelling pressure waves within the cocoon. Pressure waves from the jet head together with waves induced by turbulent motion and mixing in the cocoon, try to establish pressure balance within the cocoon and between cocoon and ambient gas, driving the lateral expansion of the cocoon.

Figure 3.6 shows pressure maps of jets with $\eta = 10^{-1}$ and $\eta = 10^{-3}$ at the same lengths. The cocoon of the heavier jet is overpressured by a factor of 20 with respect to the ambient gas, while it is only a factor of 1.5 for the lighter jet (and 4.9 for this jet at the time of the M1 image).

The strong evolution towards pressure balance is responsible for the much less pronounced high-pressure regions between Mach disk and the advancing bow shock. The bow shock has an elliptical shape with less directional dependence of its strength, more similar to an overpressured bubble, although it is still stronger in axial direction (see Sect. 3.3.2).

The quick pressure adjustment can also be seen in the pressure–density diagrams of Fig. 3.7. The ambient gas is described by the patch near $(-26, -10)$, the jet nozzle by the cells around $(-29, -10)$. Adiabatic compression and expansion lead to the oblique and longish features present at different positions. Top right of the jet nozzle position are the cocoon grid points, which spread over a large range of density to the right because of mixing with shocked ambient gas, which is the elongated feature top right of the ambient gas position. Comparing the

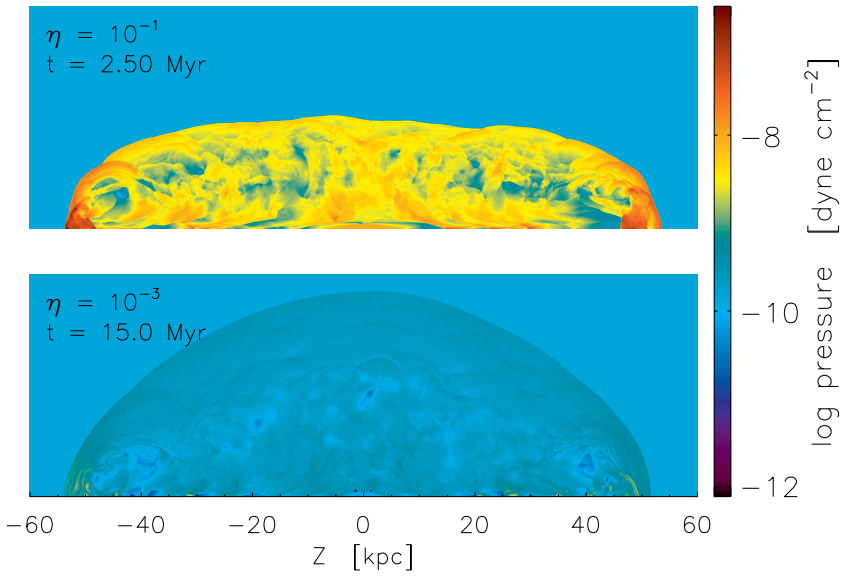

Figure 3.6: Pressure maps in logarithmic scaling for simulation M1 (top) and M3 (bottom) at equal lengths. The corresponding times are annotated.

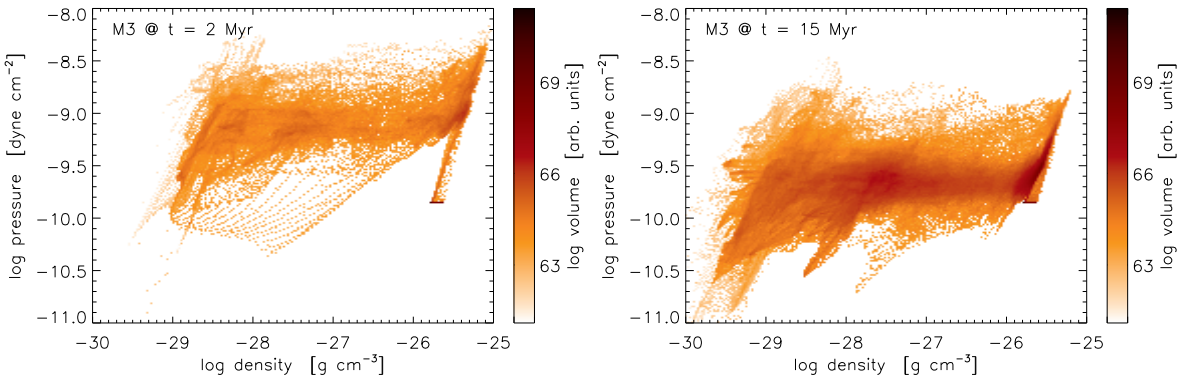

Figure 3.7: Pressure vs. density histogram for the M3 jet after 2 and 15 Myr. Volume-weighted counts, pressure and density are shown logarithmically.

two different simulation snapshots, we find that the pressure distribution is quickly adjusting towards the external pressure, in agreement to the findings of Krause (2003), and the cocoon is not strongly overpressured anymore.

Another view on this is the average cocoon pressure, shown in Fig. 3.8, which has a powerlaw-like behaviour. For the three models M1, M2 and M3, it strikingly decreases with the reciprocal jet length (Tab. 3.1). While M1 at the end of the simulation is still very overpressured, the cocoon pressure of M3 is already near the ambient gas pressure.

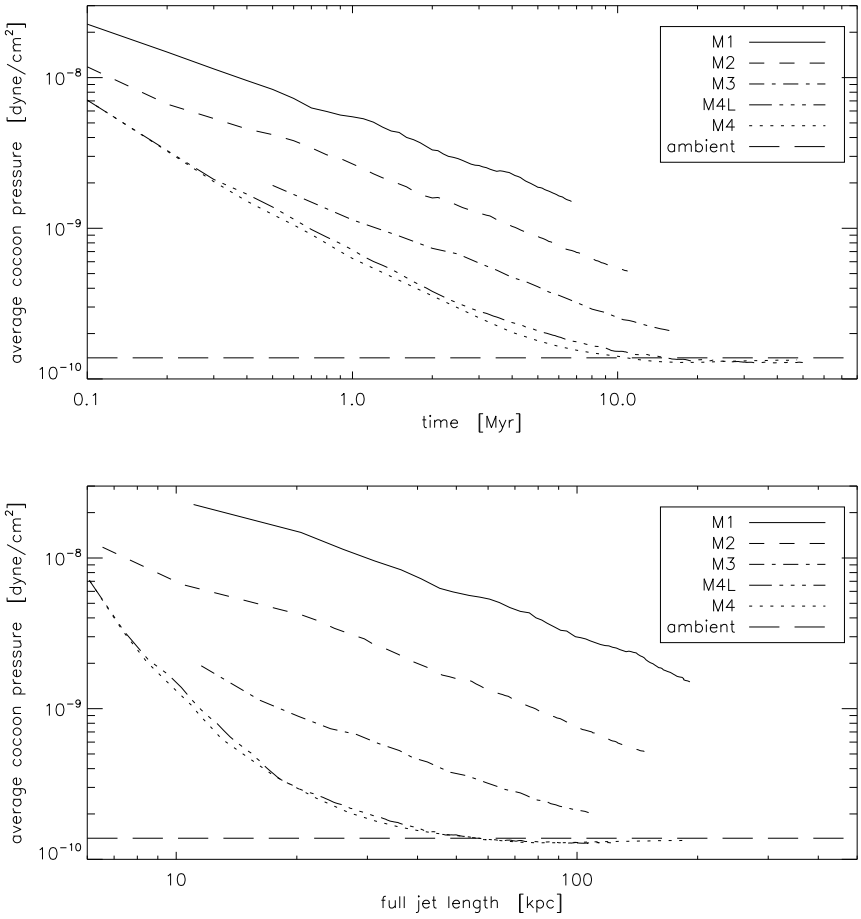

Figure 3.8: Evolution of the volume-averaged cocoon pressure as function of time or the jet length for the different models. The cocoon is defined by a tracer limit of 0.5.

M4 and M4L seem to deviate from this behaviour. At the beginning this is mainly a consequence of the longer-lasting relaxation from initial conditions, where strong shocks are thermalized efficiently, increasing the pressure in the early "cocoon bubble", and because the early phase is shown with higher time resolution. After a jet length of 20 kpc has been reached, they fit into the behaviour of the other simulations, but, as they soon reach the ambient pressure, settle to its value.

It is clear that the cocoon pressure cannot drop much below the ambient pressure and thus approach its value. At this point we expect the bow shock to softly turn into an ordinary sound wave. This is just about to happen in the last snapshots of M4 and M4L, where there is only a very weak density jump, corresponding to Mach 1.05. The exact value of the average cocoon pressure is insensitive to the exact definition of the cocoon (see Sect. 3.2), but can drop slightly below the ambient pressure due to pressure variation within the cocoon (which can still be as strong as a factor of 2).

The past bow shock is not the only sound wave testifying to the expanding cocoon. Already long before the shock decays, waves and ripples can be seen in the shocked ambient gas (Fig. 3.9).

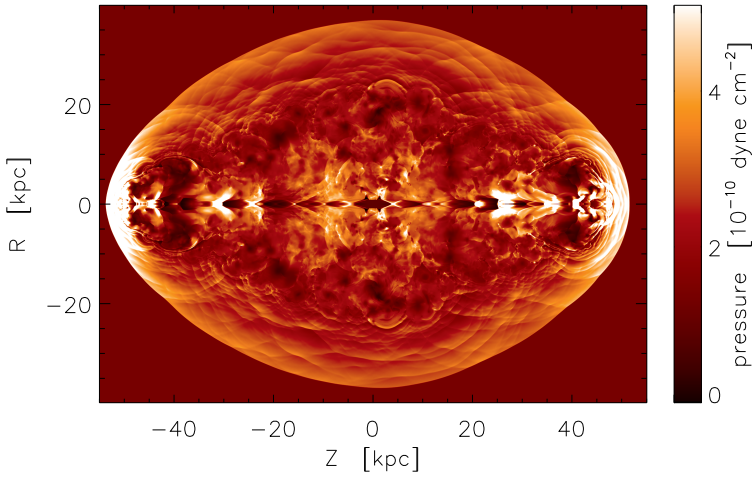

Figure 3.9: Linearly scaled pressure map of M3 at 15 Myr. Values above 5×10^{-10} dyne cm^{-2} are clipped.

3.3.2 Bow Shock

The quick decrease in cocoon pressure naturally affects the strength of the bow shock as it is this pressure that drives the shock laterally. Figure 3.10 shows the temporal evolution of the bow shock strength, in terms of external Mach numbers, for the forward direction (at $R = 0$) as well as the lateral direction (at $Z = 0$) for jets with different density contrasts.

Table 3.1: Power law exponents for the bow shock and cocoon evolution. The exponents p in the table are fits to power laws as function of time t (for the lengths and widths) or as function of full jet length l (for the average cocoon pressure), considering only the data points which match the criterion in the third line. A minus (-) denotes that no reasonable power law fit could be done.

model	bow shock		cocoon		
	full length	width	full length	average width	average pressure
	$\propto t^p$	$\propto t^p$	$\propto t^p$	$\propto t^p$	$\propto l^p$
	$\geq$ 30 kpc	$\geq$ 15 kpc	$\geq$ 30 kpc	$\geq$ 5 kpc	
M1	0.63	0.64	0.64	0.59	-0.99
M2	0.63	0.61	0.64	0.52	-1.04
M3	0.68	0.65	0.71	0.39	-0.95
M4L	0.69	0.71	0.64	0.24	-
M4	0.80	0.71	0.82	-	-

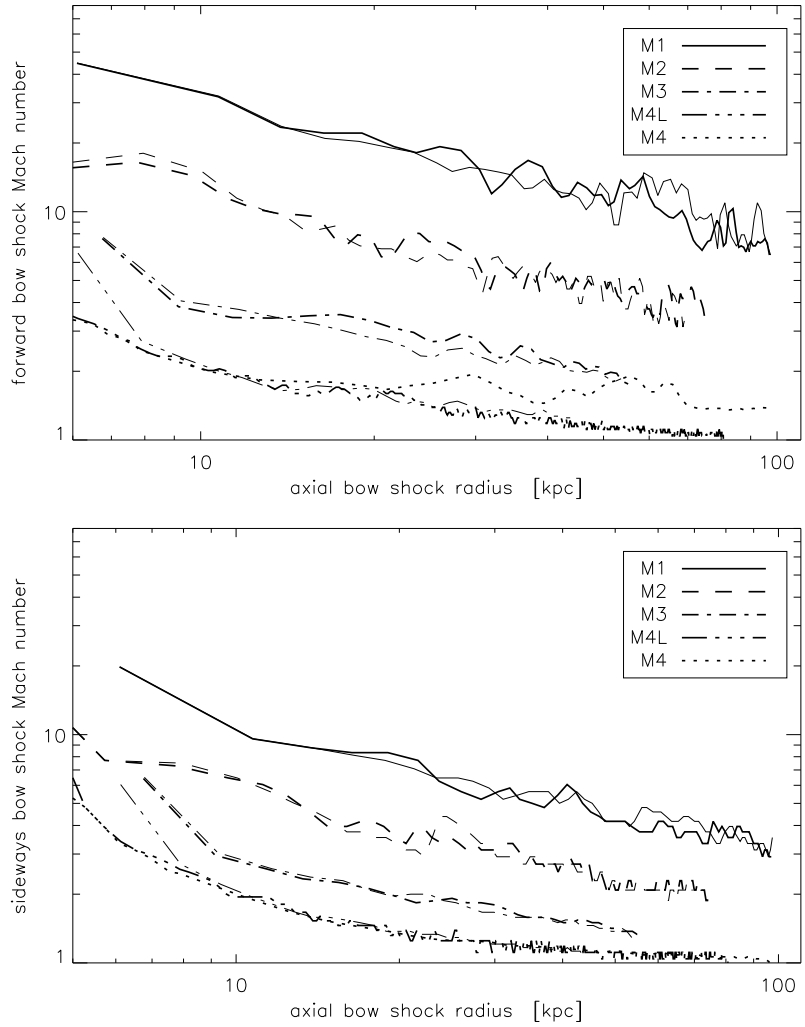

Figure 3.10: Evolution of the forward (top panel) and sideways (bottom panel) bow shock strength as a function of the monotonically increasing axial bow shock radius. Thick lines are MHD models, thin lines the corresponding hydro models for comparison.

The bow shocks in forward direction are always stronger than the sideways shocks due to the direct impact of the jet onto the ambient gas. The lighter jets have a much weaker bow shock in all directions and the differences between the axial and lateral direction are much less pronounced.

The axial diameter of the bow shock grows as a power law with exponents ≈ 0.65 (Fig. 3.11 and Table 3.1). For the lateral propagation we find similar exponents. This behaviour agrees with self-similar jet models (Falle, 1991; Begelman, 1996; Kaiser & Alexander, 1997) and the spherical blastwave approximation (Krause, 2003), which predict an exponent of 0.6. At early times and lasting longer for the lighter jets, we find lower exponents, as for a Sedov blast wave ($l \propto t^{0.4}$) from the initial conditions.

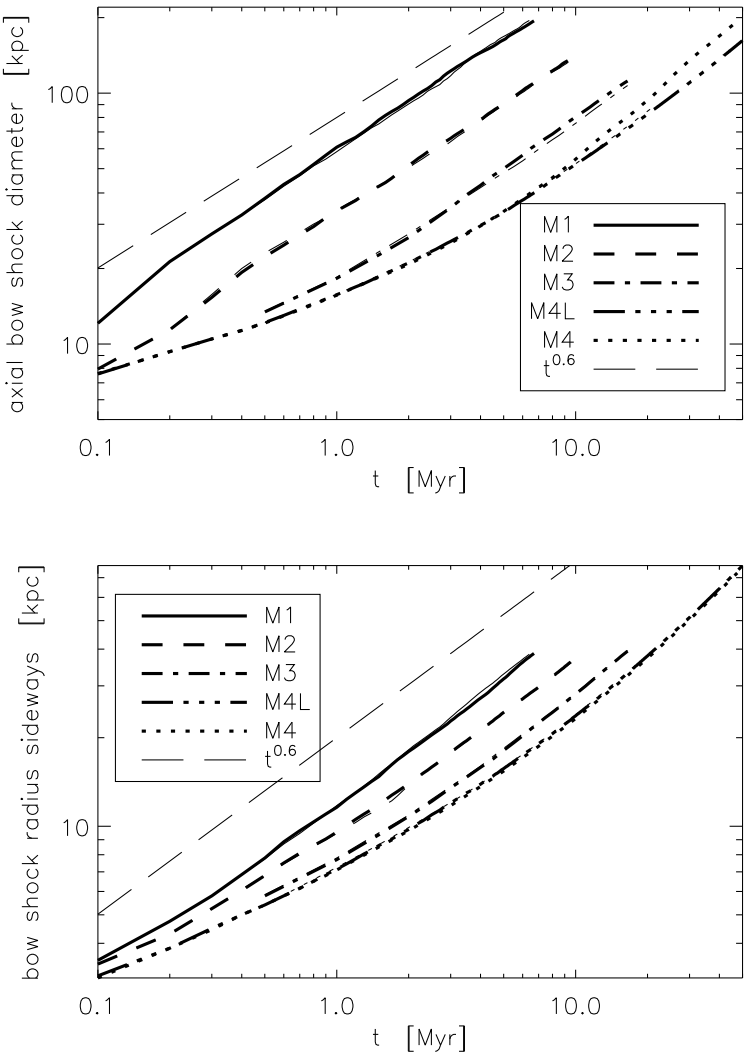

Figure 3.11: Propagation of the bow shock in axial (top panel) and lateral direction (bottom panel) for the simulated models as function of time. Thick lines are MHD models, thin lines the corresponding hydrodynamic models.

The lighter jets have generally lower Mach numbers, as their kinetic power is lower, thus showing smaller bow shock velocities. The aforementioned analytical models yield an expansion speed

$$v(r) = k \left(\frac{L_\mathrm{j}}{\pi \rho_\mathrm{a}} \right)^{1/3} r^{-2/3} = k\, v_\mathrm{j}\, \eta^{1/3} \left(\frac{r}{r_\mathrm{j}} \right)^{-2/3}, \tag{3.1}$$

that directly translates into the bow shock Mach number and describes the scaling behaviour of the simulations reasonably well (L_j: jet power). We find values for k between 1.5 and 2 in axial direction and between 0.5 and 2 (M4L) in lateral direction, the latter being increasingly

higher for lighter jets. A clear deviation from this behaviour is M4 at $t > 10$ Myr in axial direction. The bow shock propagates much faster due to the formation of a nose cone. The strong toroidal magnetic field collimates the jet, suppresses the pronounced backflow of M4L, and the Lorentz force of the radial current gives the jet additional thrust for the propagation (see 3.7). The other light jets (M3 and M4L) also may propagate somewhat faster due to their appreciable magnetic fields.

3.3.3 Cocoon

As the jet pushes the bow shock forward in axial direction, the cocoon length (Fig. 3.12) grows similar to the bow shock length, showing a power law behaviour with similar exponents. Again, M4 shows a higher exponent (0.82) due to its additional thrust support in the nose cone. There might also be a slightly faster propagation for the M3 and M4L jets, where the magnetic field is not too much below equipartition at the jet inlet (see Fig. 2.4), although this might also be just a temporal effect due to the jet–cocoon vortex interaction.

The cocoon width, in contrast, shows different powerlaw exponents depending on the density contrast, after the start-up phase is over. We find exponents of 0.59 (M1), 0.52 (M2), 0.39 (M3) and 0.24 (M4L) for the different models (Table 3.1). Thus there seems to be a clear trend of decreasing exponents for lower jet densities, which holds true for all our cocoon width measures (Fig. 3.13). Widths approaching an asymptotic value might mimic a similar behaviour, but so far, this is beyond our simulation data (except for M4). It seems reasonable to assume that this is due to less overpressured cocoons for lighter jets, as it is the cocoon pressure that drives the lateral cocoon expansion (Kaiser & Alexander, 1997). If the cocoon pressure equals the ambient pressure, the sideways expansion of the cocoon may come to an end. Another consequence of this is that the lateral bow shocks are, compared to the corresponding cocoon width, much further away for light jets (Fig. 3.14), as found by Zanni et al. (2003), too. Hence, except for the H1/M1 models, the thick layer of shocked ambient gas grows continuously.

The expansion of the cocoon for M4 is much different. After the initial phase, the cocoon width settles down to a constant value and does not grow anymore. This is a consequence of the suppressed backflow in the nose cone, which then cannot inflate the cocoon anymore.

All simulations with non-dominant magnetic fields show pronounced turbulence in their cocoons. This is evident from Fig. 3.15, which shows the vector fields of velocity and poloidal magnetic fields in LIC (line integral convolution) representation, as described in Sect. 2.7. The colours show the field magnitude, the brightness modulation shows the flow direction). Cocoon turbulence is driven by quasi-periodic "vortex shedding" (Norman et al., 1982) in the jet head, which injects vortices into the cocoon. As these vortices move around and interact, vortex shedding affects the whole cocoon and drives its turbulence. While it occurs in our heavier jets, too, narrow cocoons suppress vortex interaction and the establishment of turbulence. We note that there may be feedback on the driving mechanism, as cocoon vortices perturb the jet beam and thus influence the vortex sheeding process itself.

3.3.4 Aspect Ratio

A characteristic property of the bow shock or cocoon is their aspect ratio $\mathcal{R}$ = length/width (Fig. 3.16). Dependent on the density contrast, after a short initial phase of spherical expansion

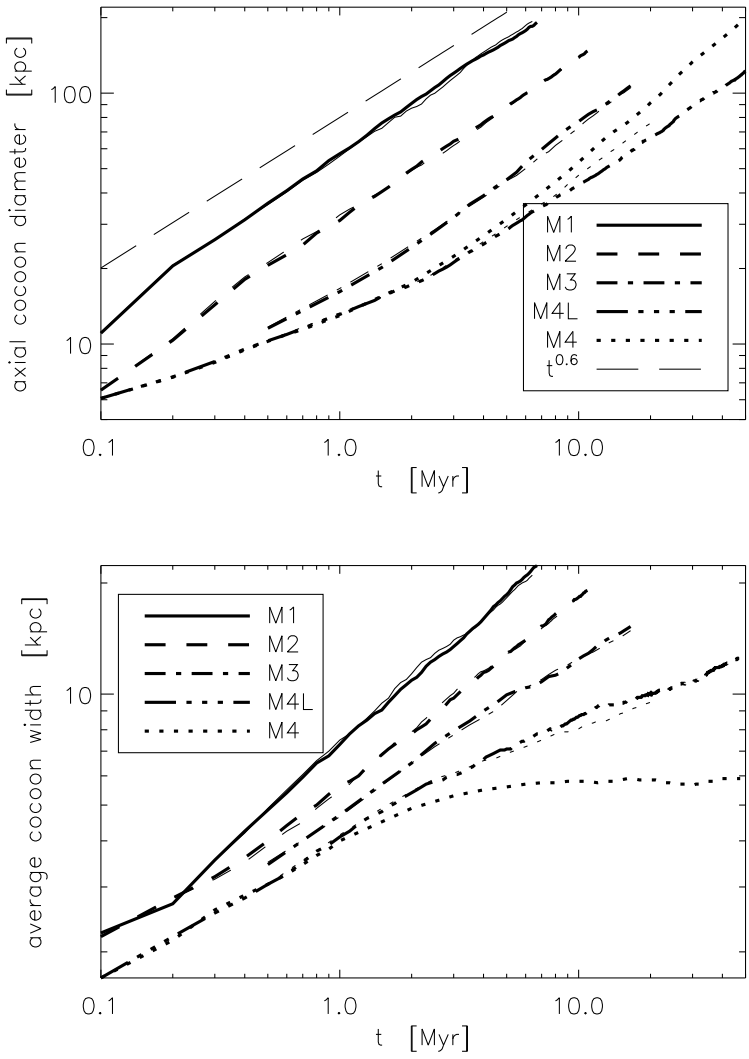

Figure 3.12: Time evolution of the cocoon: full length and average width as function of time. MHD models in thick lines, corresponding hydro models in thin lines.

(aspect ratio ≈ 1), the bow shock aspect ratios grow but converge for large bow shock diameters, approaching 1 for lighter jets ($\mathcal{R} = 1.4$ for M3 and 1.1 for M4L). This means, the bow shock approaches a spherical shape for very light jets. Once again, M4 is different, as the propagation in axial direction is faster, yielding significantly higher aspect ratios then M4L.

The aspect ratios for the cocoons generally increase with jet length and are at early times systematically lower for the lighter jets. However, the light jets soon increase their aspect ratio (earlier for lighter jets) and then at later times, show aspect ratios even higher than their heavy counterparts. As for the cocoon width evolution, we argue that this may be due to cocoons,

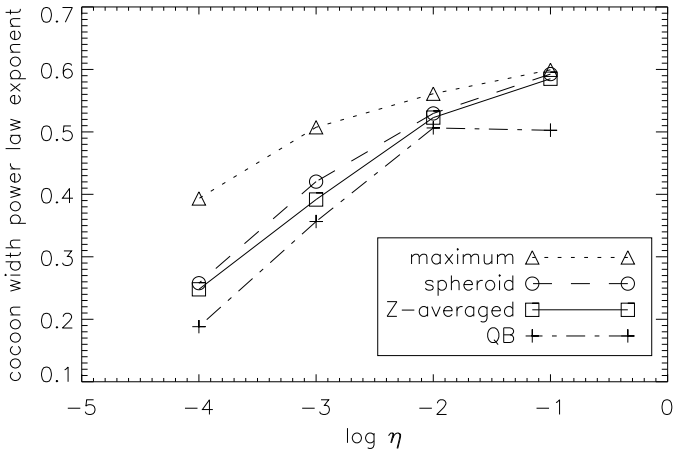

Figure 3.13: Power law exponents for cocoon widths as function of density contrast. Fits considered only data points where width ≥ 5 kpc.

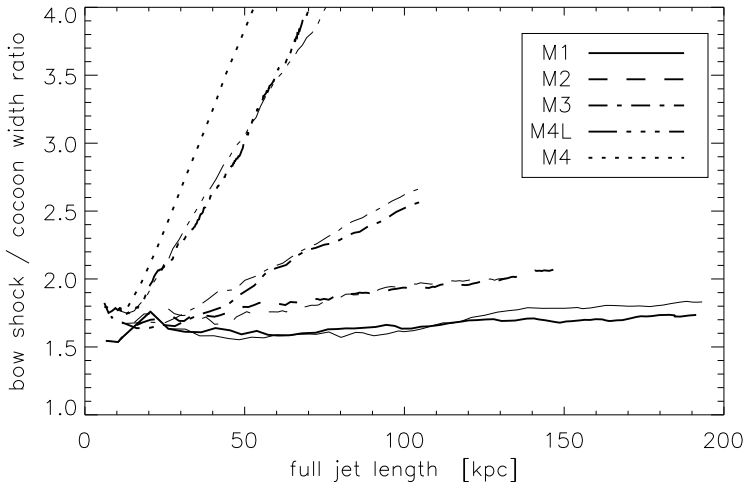

Figure 3.14: Bow shock / cocoon width ratio over time for the different simulations as function of the full jet length. MHD models in thick lines, corresponding hydro models in thin lines.

which come to pressure balance with the ambient gas earlier, so that lateral cocoon expansion stalls, but the axial propagation is still growing self-similarly.

3.4 Entrainment

The jet backflow at the contact surface between the cocoon and the ambient gas makes it Kelvin-Helmholtz unstable, and thus creates fingers of dense ambient matter that reach into

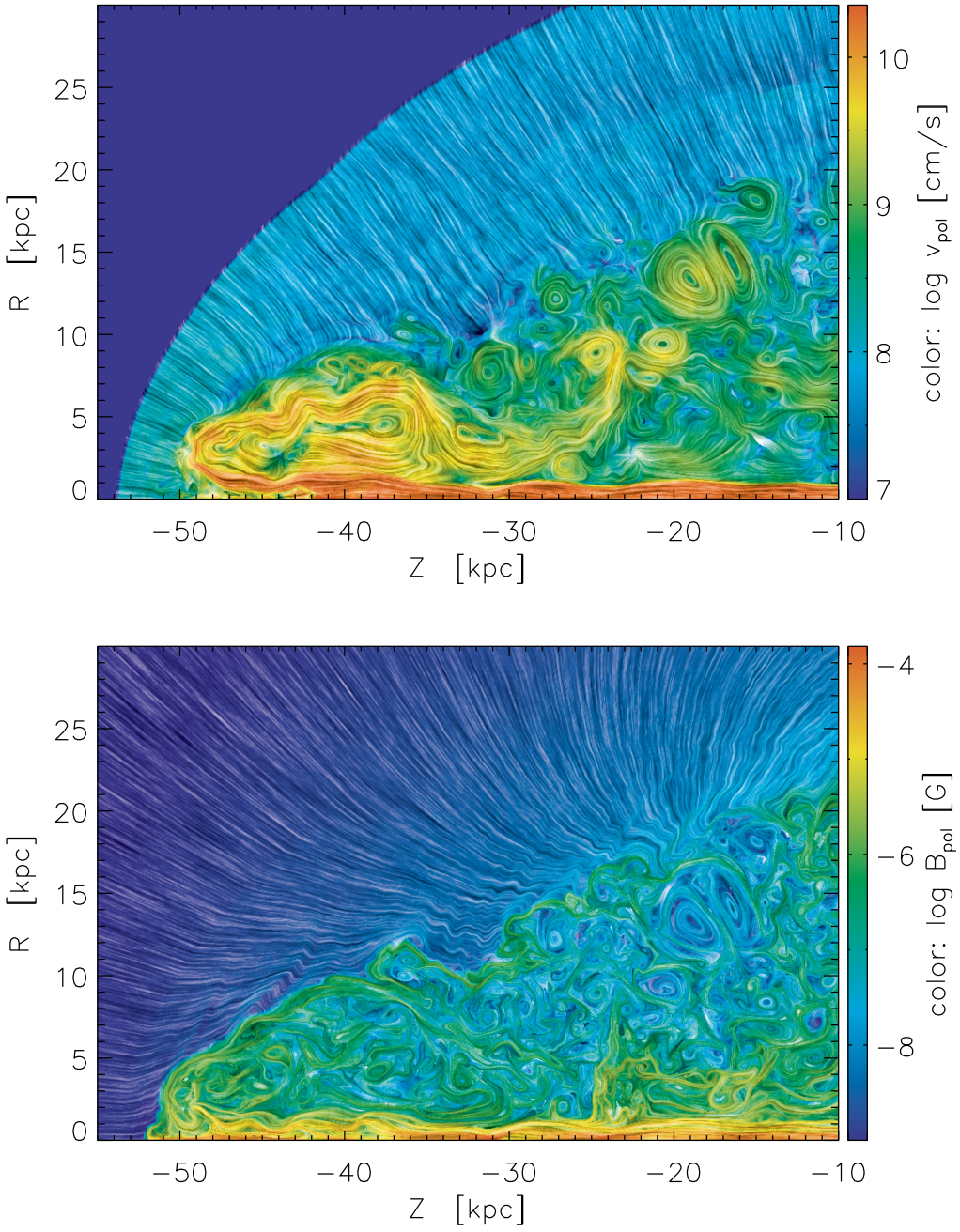

Figure 3.15: Velocity field (upper panel) and poloidal magnetic field (lower panel) around the jet head of M3 at $t = 15$ Myr, displayed in LIC (line integral convolution) representation to show the small-scale vector field structure. The colors show the vector field magnitude, while the brightness modulation shows the field lines.

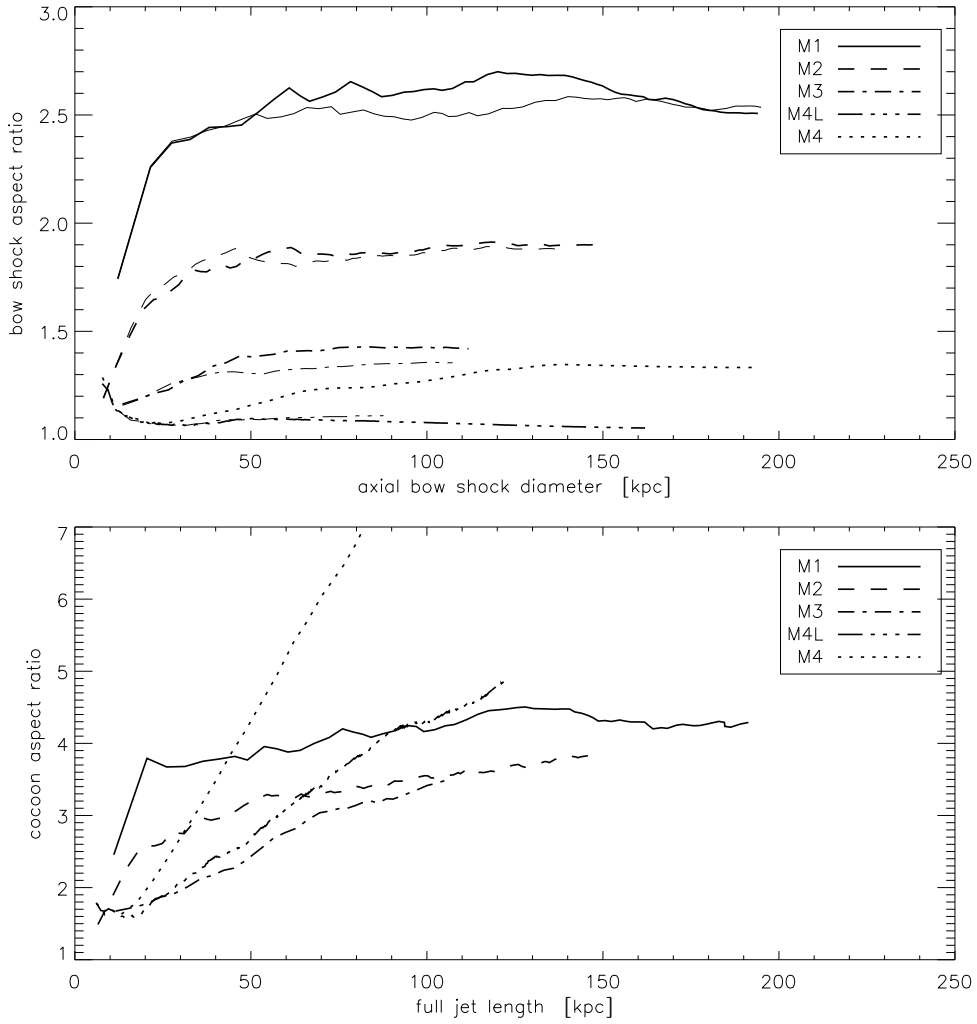

Figure 3.16: Aspect ratios $\mathcal{R}$ of bow shock (upper panel) and cocoon (lower panel) over full length. For the cocoon aspect ratios, the hydro models are omitted for clarity.

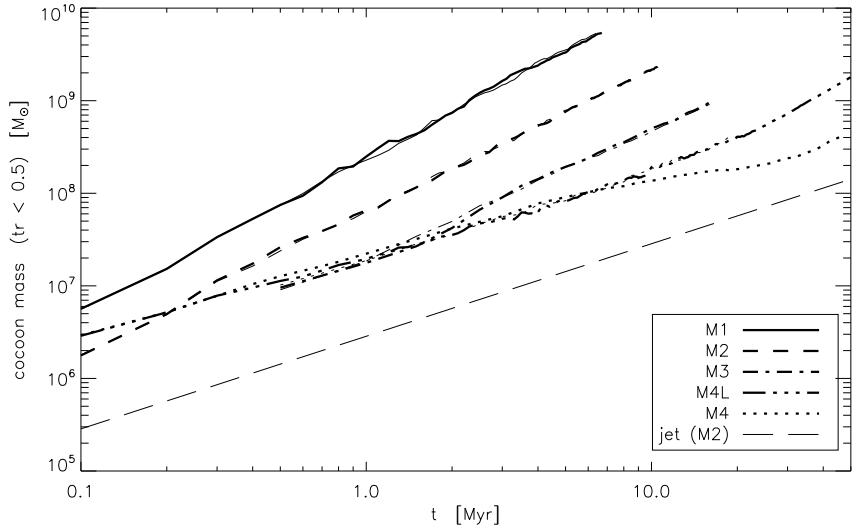

Figure 3.17: Evolution of the cocoon mass as measure for the entrainment of dense ambient gas. The long-dashed line gives the injected jet mass M_j for the M2 run for comparison ($M_\mathrm{j} \propto \eta\, t$). MHD models as thick lines, corresponding hydro models as thin lines.

the cocoon and are entrained. In numerical simulations this entrained gas is additionally mixed with the jet plasma due to finite numerical resolution. The amount of entrainment can be measured in terms of the cocoon mass since the mass of jet plasma usually is small compared to the measured cocoon mass. Although the exact numbers depend on the exact cocoon measurement definition (Sect. 3.2), this seems to be a reasonably robust method.

Figure 3.17 shows the time evolution of the cocoon mass. The entrained mass grows with a power law exponent only slightly below the exponent of the cocoon volume, showing a slowly decreasing but roughly constant fraction (5–10 %) of the initial mass in the occupied volume. There is no difference visible between purely hydrodynamic and MHD simulations in the entrained mass, as would have been expected. The reason for this is the missing stabilization of the contact surface, which is discussed later. However, it is evident from M3 in Fig. 3.18 that the entrainment in the jet head is significantly smaller: the mass in a cylindrical volume ($Z \in [-45, -35]$ kpc, radius 4 kpc) in the head region of M3 is $3 \times 10^5\, M_\odot$ without magnetic fields (H3), compared to $9 \times 10^4\, M_\odot$ in the magnetized case, which is more than a factor of 3 lower. Hence, entrainment is significantly suppressed in the jet head, but no change could be measured regarding the whole cocoon volume.

3.5 Energy Budget

From the quick balancing of pressure within the cocoon, one might expect a strong conversion of (kinetic) jet power to thermal energy. This, in fact, is measured for our simulations.

Figure 3.19 shows the increase in thermal energy as fraction of the total injected power. Already for the heaviest jet (M1), most of the injected (kinetic) power appears as thermal

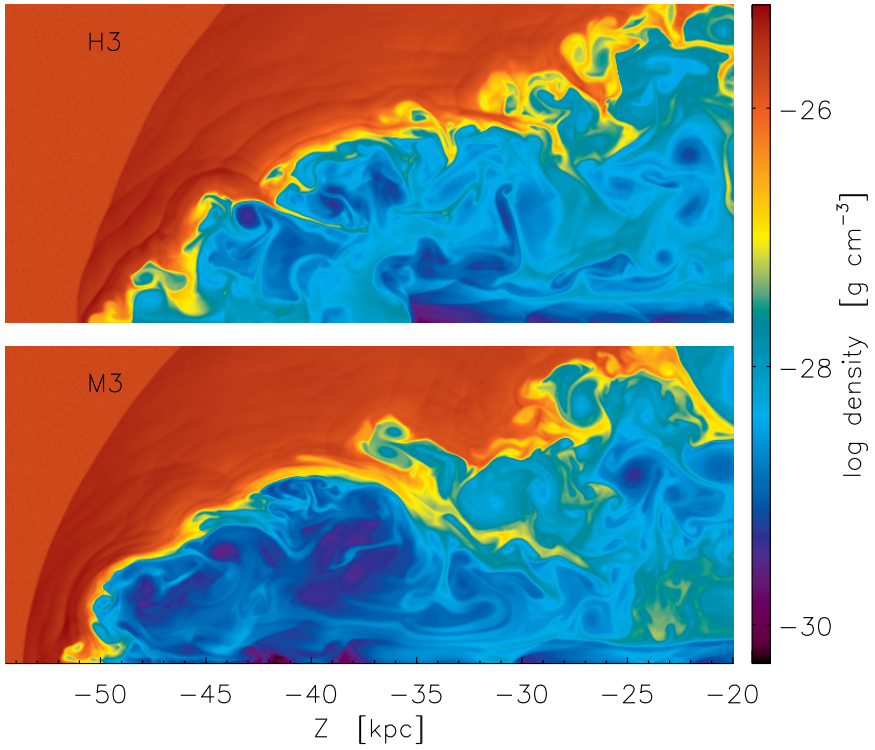

Figure 3.18: Comparison of hydro (H3) and MHD (M3) simulations at 15 Myr. The jet head region is much more pronounced and Kelvin-Helmholtz instabilities are damped.

energy due to compression and irreversible entropy generation at shocks. The thermal fraction increases not only with time, but is also much stronger for the lighter jets, where a thermalization of $\gtrsim 80\,\%$ is reached. Half of the thermal energy gain is found in the cocoon and half in the (shocked) ambient gas. O'Neill et al. (2005) find $\approx 40\,\%$ of the jet power in the thermal ambient gas for their 3D jets with density contrast 0.01 in a uniform atmosphere, while in our simulations we find $\approx 35\,\%$, which is quite good agreement.

Magnetic energy only has a very small contribution (below 1 %), except for M4, which is magnetically dominated and which has a magnetic energy contribution rising up to 5 %. More than 90 % of the magnetic energy is located in the cocoon. For all runs except M4, the actually measured magnetic energy is significantly larger than the injected magnetic energy, this effect becoming stronger for the lighter jets (Fig. 3.20). It even grows faster than just linearly in time – approximately with a power law exponent of 1.2. Hence, other forms of energy seem to be converted into magnetic energy. For M4, the measured magnetic energy is lower than expected from the nozzle values, which may indicate that the additional thrust in the nose cone actually consumes magnetic energy. The remaining fraction is kinetic energy, which is decreasing more and more for lower jet densities. 50 to 70 % of the measured kinetic energy is in the outward moving shocked ambient gas, while 30 to 50 % is in the cocoon plasma. The jet beam holds $\leq 10\,\%$ of the total measured kinetic energy.

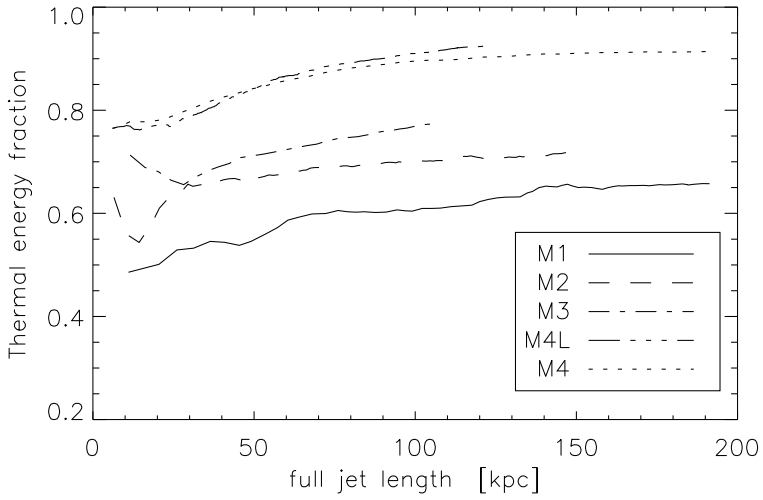

Figure 3.19: Gains in thermal energy as fraction of the measured total injected energy, as function of the full jet length.

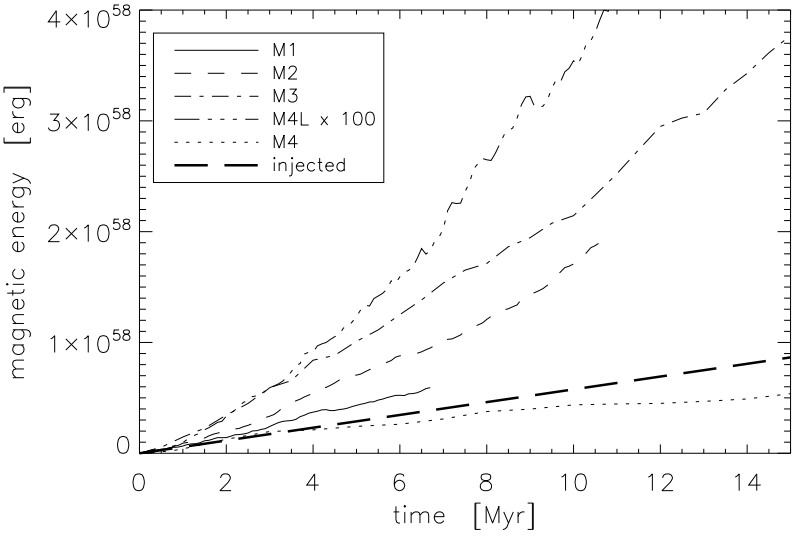

Figure 3.20: Evolution of the magnetic energy with time. The long-dashed line shows the injected amount of magnetic energy. For the case of M4L, magnetic energy was multiplied by 100 to account for the 10 times smaller field strengths.

3.6 Magnetic fields

Magnetic fields are not only passive properties of the jet plasma, but an active ingredient for the dynamics. Especially for jet formation, magnetic fields have a very active role, being

responsible for acceleration and collimation. A parameter describing the contribution of the magnetic field on the dynamics is the ratio between thermal and magnetic pressure of the plasma ($\beta = 8\pi p/B^2$). For the simulations described here, we used a fixed value for jet speed, Mach number and magnetic field. Thus, the plasma β cannot be constant throughout the different runs (see Tab. 2.4). While M1 and M2 have passive magnetic fields, M3 and M4L have fields with significant impact, and for M4 they are even dominant.

The helical field configuration in the jet initiates an interesting interplay between kinetic and magnetic energy. Although the jet matter is injected without any rotation, the Lorentz force from the helical field generates a toroidal velocity component, as also found by Kössl et al. (1990a). This effect is stronger for the runs with stronger magnetic fields (lower plasma β). The rotation does not originate from persisting angular momentum from the jet formation, which should be very small due to the expansion of the jet. Also, it is not continuous throughout the beam and is even changing sign at some internal shocks and interaction with cocoon vortices.

When the plasma reaches the terminal shock, it flows away from the axis radially and turns back, forming the backflow that inflates the cocoon. Rough conservation of angular momentum l then produces a radially declining angular velocity $\Omega = l/R^2$ (differential rotation, Fig. 3.21). Writing the induction equation in cylindrical coordinates,

$$\frac{\partial B_\phi}{\partial t} = -R\,(\mathbf{u}_\mathrm{p}\cdot\nabla)\,\frac{B_\phi}{R} - B_\phi\nabla\cdot\mathbf{u}_\mathrm{p} + R\,(\mathbf{B}_\mathrm{p}\cdot\nabla)\,\Omega, \tag{3.2}$$

it becomes evident that the shearing $(\mathbf{B}_\mathrm{p}\cdot\nabla)\,\Omega$ transforms poloidal field B_p into toroidal field B_ϕ, also transferring kinetic energy into magnetic energy. This explains why in the previous subsection the measured contribution of the magnetic field to the total energy was higher than its injected contribution.

We note that this creation of toroidal field in the jet head is not an artifact of axisymmetry, but merely a consequence of allowing three-dimensional vectors in the simulation ($\mathbf{u}$ and $\mathbf{B}$). We do not expect this to be much different in full 3D, apart from a naturally more complex structure in the details. What, in contrast, most probably is an artifact of axisymmetry is the persistance of the toroidal field component in the cocoon. The cocoon plasma is highly turbulent (Sect. 3.3.3) with relatively little systematic motion, which is an intrinsically three-dimensional phenomenon. This can easily convert toroidal and poloidal fields into one another, establishing some dynamical equilibrium between those components, but maintaining the overall field strength.

Comparing purely hydrodynamical models with the MHD models (Fig. 3.18), we find that the global properties, such as bow shock and cocoon sizes, are generally robust if the magnetic fields are not dominant (as with M4). The details, though, are different. While the hydro models show a ragged contact surface between jet plasma and ambient gas due to Kelvin-Helmholtz (KH) instabilities excited by the backflow, the MHD runs show a pronounced jet head, which is clearly more stable, since the KH instability is damped by the magnetic fields (e.g. Miura & Pritchett, 1982). Magnetic tension acts as a restoring force on the growing instabilities, suppressing entrainment of ambient matter and "fingers" of dense gas reaching into the backflow, which is evident from the clearly lower average density in the jet head region. The stabilizing effect appears at $\beta \sim 10$ in the jet head (Fig. 3.24). For the simulations with weaker fields there is no noticable difference between the magnetized and the pure hydrodynamics case. Damping of the KH instability by magnetic fields, however, only works with the field

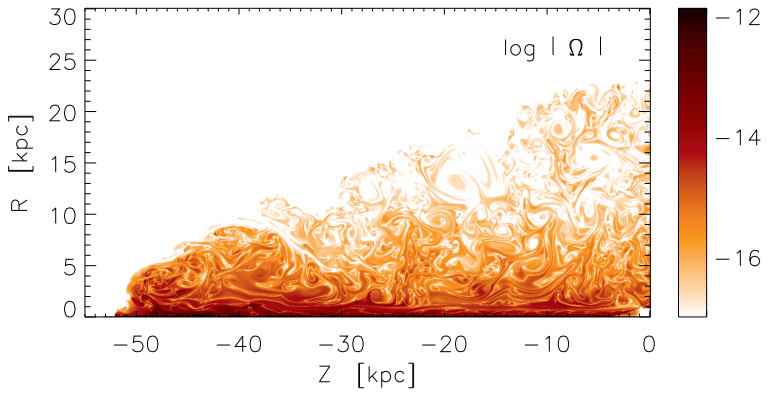

Figure 3.21: Angular velocity $|\Omega| = |v_\phi|/R$ in units of s^{-1}, scaled logarithmically. Note that there is a strong decline from the beam to the backflow.

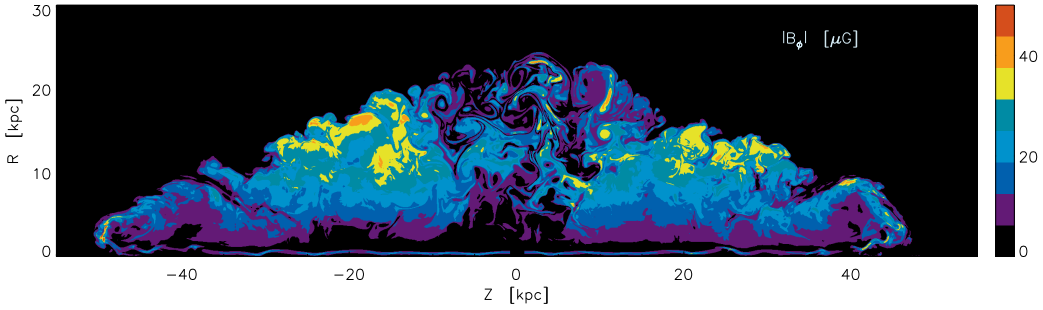

Figure 3.22: Toroidal magnetic field magnitude for M3 at 15 Myr. The right jet has positive toroidal field, the left jet has negative sign.

component parallel to the instability wave vector, which in turn means that in axisymmetry only the poloidal magnetic field can damp the instabilities at the contact surface.

Although the earlier-mentioned shearing mechanism amplifies magnetic fields and should therefore provide even more damping of KH instabilities, we cannot see this effect further away from the jet head, because in axisymmetry the backward reaction (toroidal to poloidal) cannot work, resulting in a weak poloidal (Fig. 3.15) and a dominant toroidal field (Fig. 3.25). As the magnitude of the magnetic field in the cocoon is as strong as in the jet head, it seems reasonable that with balanced magnetic field components in reality, the contact surface could be stabilized.

The toroidal field B_ϕ is directly related to the generating current $\mathbf{j}_\mathrm{p}$, which is shown in Fig. 3.26 as field lines. Our toroidal field setup describes a situation where the poloidal currents leave the nozzle axially in the jet core, turning back in the sheath. As the backflow develops, the poloidal current flows along the contact surface with typical integrated currents of several 10^{18} amperes. These currents are also expected theoretically (Camenzind, 1990; Blandford, 2008). The toroidal field in the cocoon, built-up by the shearing in the jet head, seems to

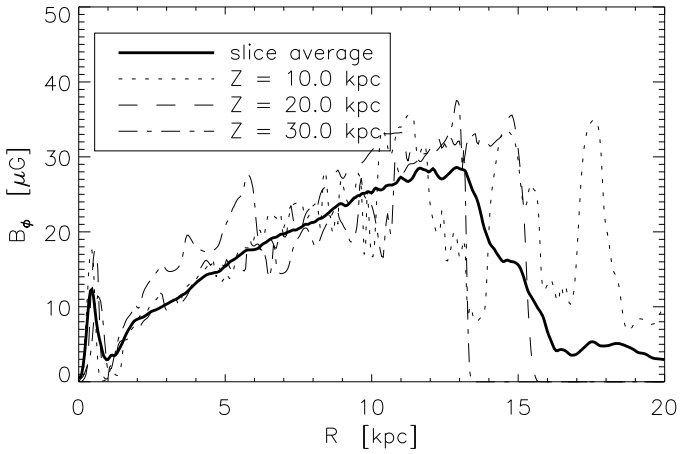

Figure 3.23: Toroidal field B_ϕ in three slices parallel to the midplane, and the average of the whole region $Z = 10 \ldots 30$ kpc. Outside the jet radius $r_\mathrm{j} = 1$ kpc, the toroidal field shows a roughly linear increase with R. Although in every slice B_ϕ drops to 0 at $R \approx 1$ kpc, the average does not drop to 0 (and thus is a bit misleading), as the positions are slightly offset for different slices.

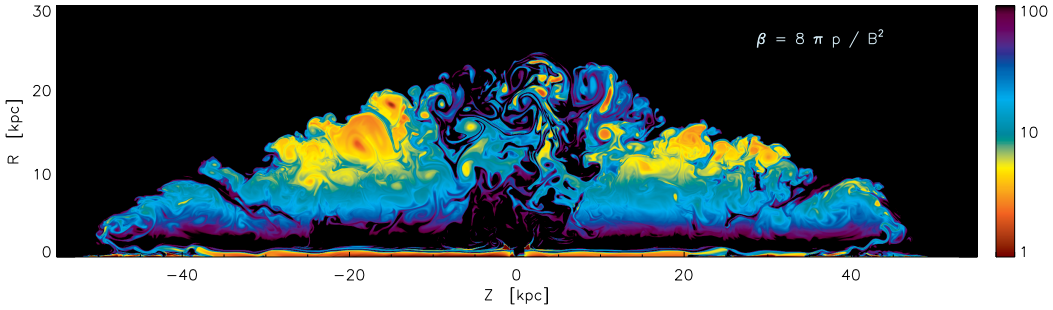

Figure 3.24: Plasma β distribution for M3 at 15 Myr, in logarithmic scaling.

form its own current circuits. The gross radial behaviour $B_\phi \propto R$ (Figs. 3.22 and 3.23) can be attributed to the relatively uniform distribution of the axial current through the planes perpendicular to the jet beam.

If the toroidal field is strong in the jet head region, the Lorentz force $f_\mathrm{L} = \mathbf{j} \times \mathbf{B}/c$ produces additional thrust for the jet propagation due to the strong radial current component, which is evident for M4, showing a pronounced nose cone, and may also explain the slightly faster propagation of M3 with respect to H3 (Fig. 3.12). Inside the beam, the magnetic field stays mostly poloidal, as injected, but near the terminal shock it is compressed axially, directed off the axis and sheared, producing strong toroidal field loops (Fig. 3.27).

Finally, we turn to 2D volume-weighted histograms of magnetic pressure $p_\mathrm{m} = B^2/8\pi$ and thermal gas pressure p in Fig. 3.28, where the contributions from only the jet beam and all the jet plasma is shown separately.

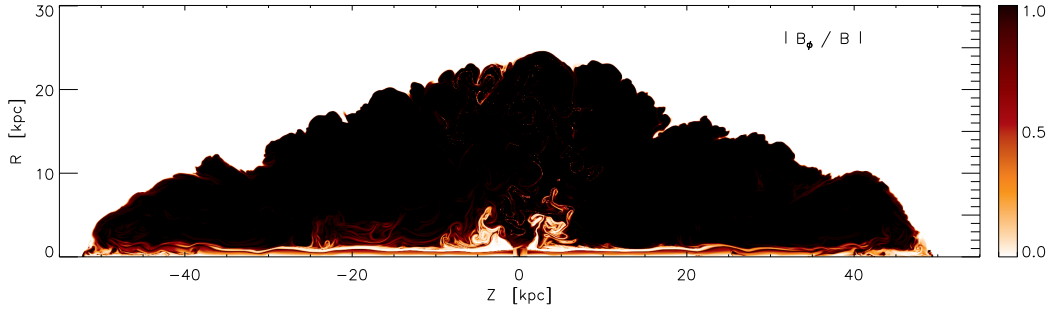

Figure 3.25: Fractional contribution of toroidal field to the total magnetic field. Simulation M3 at 15 Myr.

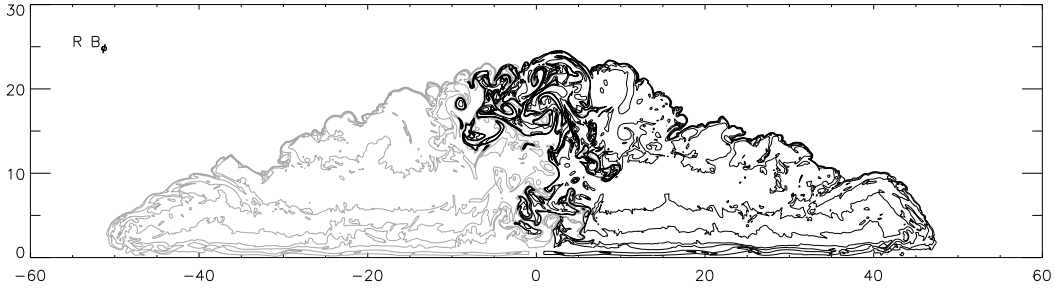

Figure 3.26: Poloidal current field lines (contours of RB_ϕ). Grey: negative values, black: positive values. Model M3 at $t = 15$ Myr.

The jet nozzle is located at $(\log p, \log p_\mathrm{m}) \approx (-10, -10.5)$ as a vertical line (constant pressure, but radially varying magnetic field). As the matter flows through the beam, internal shocks (cf. Figs. 3.6 and 3.18) cause strong changes in pressure whereas the plasma β remains unchanged (magnetic field is compressed with the plasma), leading to lines originating from the nozzle location parallel to the overplotted $\beta = \mathrm{const}$ lines. The plasma β somewhat increases along the beam when it interacts with the cocoon vortices, and thus creates some down-shifted parallels. There is no clear separation between the beam and the enclosing cocoon in the beam-only diagram, hence both shear layers of the beam and cocoon gas are contained in the wide area below $\beta = 10$. Still, there are strong pressure changes indicated by the wide horizontal distribution.

The distribution of cocoon cells widely spreads both to higher and lower magnetic fields from this area. The pronounced trail downwards is the transition to the ambient gas through entrainment; since the ambient gas is essentially unmagnetized, it is located even below the lower border of the figure (Fig. 3.28). The radial increase of magnetic field in the cocoon yields the extension towards lower plasma β (see also Fig. 3.24). The spiky features around $\beta \sim 2$ are single vortices in the outer parts of the cocoon, where the pressure drops towards the center

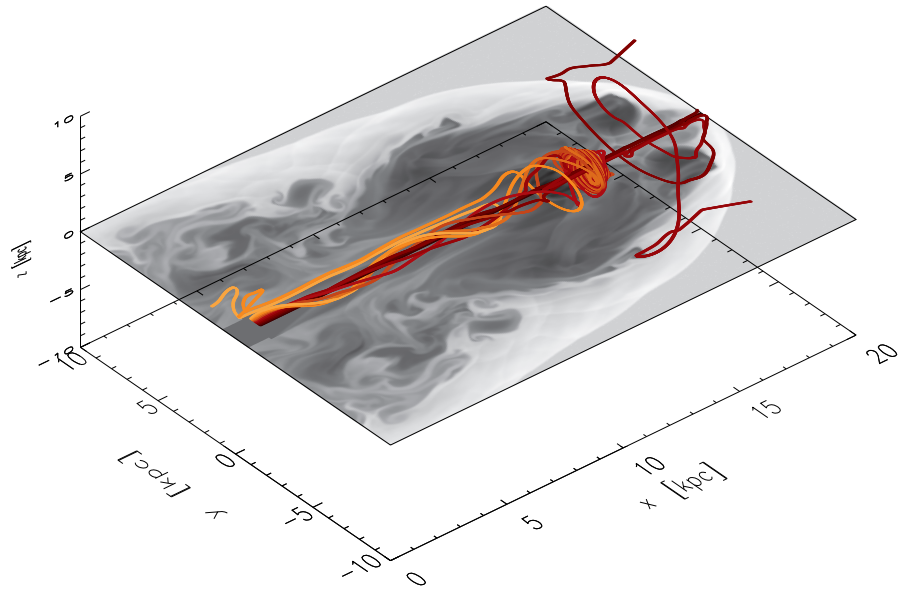

Figure 3.27: 3D magnetic field lines from within the beam with a transparent grey-scale logarithmic density slice in a plane through the jet axis. Model M2 at $t = 1.3$ Myr.

due to centrifugal forces together with a slight increase of toroidal field. Altogether, the spread of the cocoon cells is considerably larger in magnetic pressure than in thermal pressure.

The situation shown in Figs. 3.28 and 3.29 is typical for the time evolution of these diagrams. Clearly, some features are appearing, changing and disappearing continuously, such as individual internal shock lines or the cocoon vortex spikes. The general structures in the diagrams persist at all times. There are, however, two systematic changes with time: Firstly, the "cocoon bump" in Fig. 3.29 ($\log \beta \sim 1$) grows due to cocoon expansion, eroding the "ambient bump" ($\log \beta \sim 9$), and moves to the left, faster at early times and then becoming continuously slower. Secondly, as the cocoon pressure drops, the cocoon distribution of Fig. 3.28 moves towards the left (and somewhat down due to the mostly constant distribution in β at late times), and grows with cocoon volume, too.

3.7 The Lightest Jets

The lightest jet in the series, M4, shows a very different behaviour from the other runs due to its strong magnetic fields, thus a run with lower magnetic fields (M4L) was performed in addition. In this section, we focus on the specific properties of and differences between these two runs.

Both simulations show unstable beams, which are temporally stopped, deflected or disrupted. This is quite natural for the very light jets; the impact of cocoon vortices hitting the beam is stronger when the beam shows lower inertia but the cocoon gas is dense due to entrainment and mixing with the dense ambient gas. This destabilization is particularly strong in axisymmetry, as the vortices cannot "miss" the beam as they could in 3D. For M4L, after a strong deflection

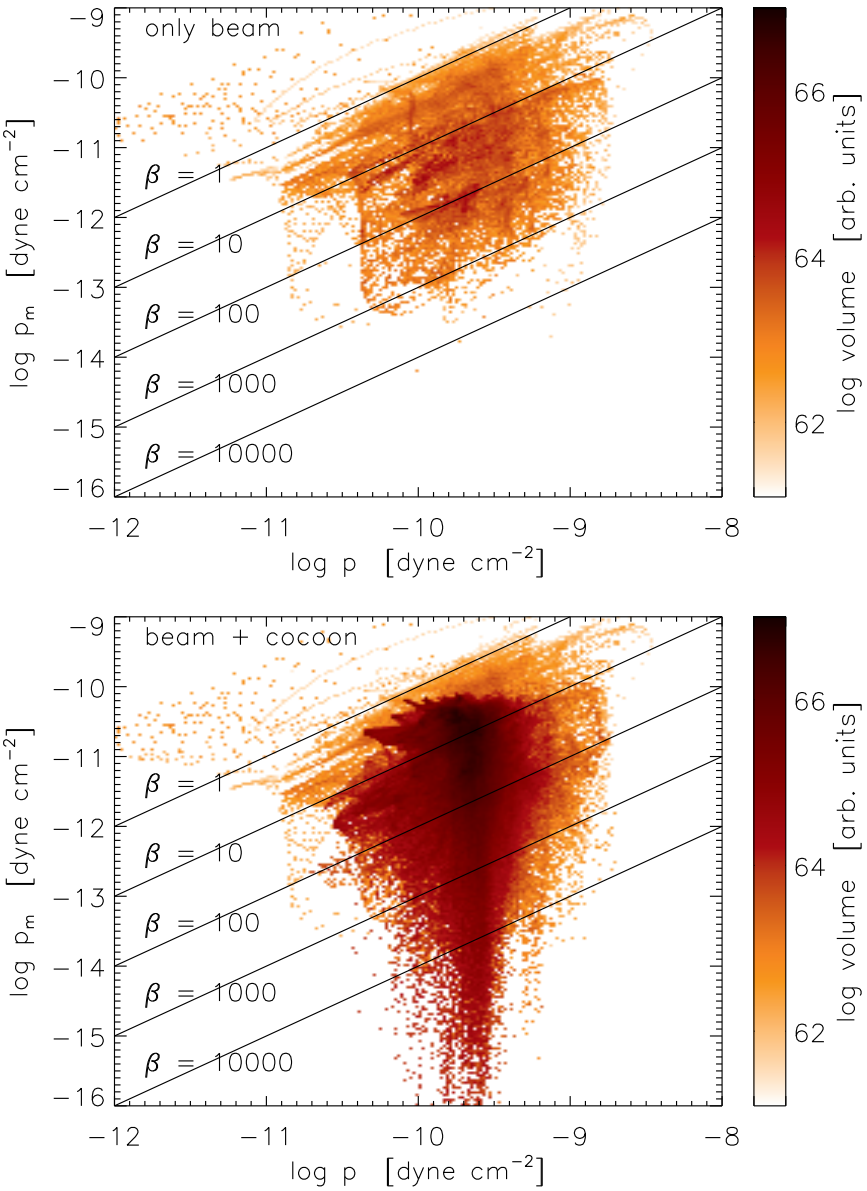

Figure 3.28: p_{m}–p histogram for the beam (defined by kinetic energy flux ≥ 1 % of the maximum value) and all the jet matter from simulation M3 after 15 Myr. Lines of constant plasma β with values of 1, 10, 100, 1000 and 10 000 are overlaid.

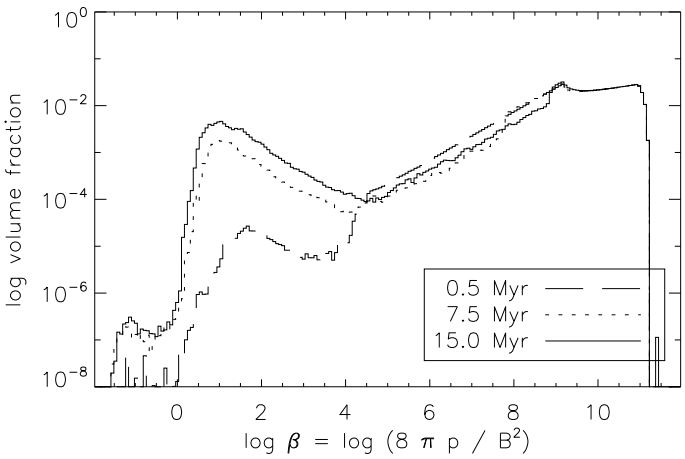

Figure 3.29: Volume-weighted histogram of plasma β for M3 at 0.5, 7.5 and 15 Myr.

of the right beam near the nozzle ($t \approx 20$ Myr), a small region with strong poloidal field piles up just next to the nozzle and creates a magnetic layer ($\beta \gtrsim 1$) at the beam boundary. This protects the beam from cocoon vortices and entrainment, and from there on inhibits disruptions of the right jet, which then propagates more quickly than the left jet. At the end of the simulation, the right jet is $\approx 20\,\%$ longer than the left jet and shows an almost undisturbed beam up to the jet head. More detailed examination of this phenomenon may be interesting, but as it was only introduced by chance, the details are difficult to reproduce and beyond the scope of this thesis. Nonetheless, the overall propagation of the jet within the simulated time (Sect. 3.3.3) is not much affected by this.

Keeping the jet speed and the Mach number fixed, the ratio of the thermal pressures of ambient gas and jet nozzle changes with density contrast, yielding an underpressured jet for M4 and M4L. For M4, the magnetic field in the nozzle is already stronger than equipartition and the Alfvén speed is higher than the sound speed. This run is dynamically dominated by the magnetic field and shows a pronounced nose cone, which is known for jets with strong toroidal fields (Clarke et al., 1986). Magnetic tension pinches the jet matter into an narrow tube of 2.5 to 3.5 kpc radius, completely suppressing a backflow and thus preventing the formation of a wide cocoon. The simple case of a plasma column in radial magnetostatic equilibrium keeps $p + B_\phi^2/4\pi$ constant. If $B_\phi^2/4\pi$ approaches the thermal pressure, the magnetic pinch becomes important. In our case, the toroidal field in the plasma column is relatively homogenous, showing a (volume-weighted) distribution mostly between 30 and 50 μG, while the thermal pressure lies (radially decreasing) in the range $1 \ldots 3 \times 10^{-10}$ dyne/cm^2, thus matching $p \sim B_\phi^2/4\pi$ and being just around equipartition. These values are not the ones set by the jet nozzle, although those obey $p \sim B_\phi^2/4\pi$, too. The twisting and shearing processes described in the previous section are very strong due to the equipartition-level magnetic fields, the rotation around the jet axis can make up a large fraction of the total velocity, and the toroidal field component grows to the measured values.

Krause & Camenzind (2001) examined the convergence of a nose cone simulation and found that the Mach disk retreated towards the nozzle and thus did not converge. Also in M4, the Mach disk is very near to the jet nozzle, and the velocities after that shock are subsonic (although the nose cone itself propagates faster than the jet head in M4L). Thus, it is unclear, how reliable the run is. We also note that the magnetic pinch is subject to MHD instabilities (Clarke, 1993), which might produce blobs and disrupt the plasma column in 3D. However, as this nose cone is produced by the magnetic tension of the strong toroidal field, this is not applicable to strong poloidal fields, which cannot provide the necessary hoop stress, although it seems difficult to maintain a strong poloidal field along an interacting beam without converting part of it into toroidal field, which then might again pinch the plasma.

3.8 Discussion

3.8.1 Magnetic Fields

Effects of magnetic fields naturally depend on their strength. Trying to understand the smoothness of jet cocoons in galaxy clusters, we concentrated on magnetic fields which are not dominant, but still have significant effects on the jet dynamics, the best example for this being the M3 run with average plasma $\beta = 8$. It is well known that magnetic tension can damp or suppress Kelvin-Helmholtz (KH) instabilities (e.g. Miura & Pritchett, 1982) and hence it may be the key to stabilizing the contact discontinuity between jet and ambient gas. However, how this applies to the complex case of jet–ambient interaction is not yet known.

We emphasize that much care was taken to use a globally consistent setup for our very light jets, in particular: keeping the bow shock inside the computational domain at all times; simulating bipolar (back-to-back) jets to remove an artificial boundary condition in the midplane and allow interaction of the backflows for a realistic lateral expansion; and using a configuration which confines the magnetic field to the jet and has closed field lines instead of a homogenous magnetic field reaching to infinity, which is then effectively anchored in the ambient gas. The assumed simplifications, axisymmetry and a constant ambient density, make extraction of the underlying physics easier, and effects of relaxing the corresponding limitations for hydrodynamic jets were previously investigated by Krause (2005). Thus we expect to at least qualitatively model the situation realistically.

Two main effects arise from the inclusion of magnetic fields: Firstly, in the jet head, we see that the provided magnetic fields in the jet do indeed stabilize the contact surface, which produces a pronounced jet head and lobes, similar to the ones seen in Cygnus A (Carilli et al., 1991) and other classical double radio sources. Effects from an ambient density profile can be excluded due to the prescribed constant density atmosphere. Furthermore, the entrainment of ambient gas is significantly smaller there than without magnetic fields.

Secondly, jets prove to be efficient generators of magnetic energy, transferring part of their huge kinetic power to magnetic fields through shearing in the jet head. This relies on some rotation of the beam plasma, which will (as seen in the simulations) generally be present for a non-zero toroidal field component. Some toroidal field is expected if the mostly axial field in the beam (Bridle & Perley, 1984) is perturbed three-dimensionally, and also from jet formation models, where the toroidal field is necessary for jet collimation at least at small scales. The shearing mechanism provides a source of magnetic energy for the cocoon and furthermore

affects the magnetic field structure at the hotspots and possibly some internal shocks. A radial and toroidal field component in the beam is known to be compressed by the terminal shock and is then visible as a strong magnetic field perpendicular to the jet axis. The jet head shearing provides another mechanism, independent from compression, to greatly enhance the toroidal field and thus produce a perpendicular field component stronger than that expected from compression. For jets pointing more towards the observer, the toroidal field around the hotspot region may become visible.

This may be relevant for several observational findings, one being the smoothness of radio cocoons. We have shown that even if the plasma β is of order ten only, the fields in the backflow and the cocoon respectively will be strong enough to damp KH instabilities at the cocoon–ambient gas interface and yield a morphology much smoother than seen in hydrodynamic simulations, reconciling simulations with observations of sources as Cygnus A (Lazio et al., 2006), Pictor A (Perley et al., 1997) or Hercules A (Gizani & Leahy, 2003), where the latter seems to be a past high-power source. Due to the 2.5D nature of the simulations, the effect is restricted to the jet head region. In a full 3D simulation, we expect therefore the cocoon–ambient gas interface to be more stable even further back from the hotspots. The amplification of beam magnetic fields in the "jet head machine" furthermore is consistent with the observation of magnetic fields in the cocoon just somewhat below equipartition (Hardcastle & Croston, 2005; Migliori et al., 2007). Additionally, the magnetic field predominantly perpendicular to the jet axis in weak FR I sources might be related to the expansion of the jet, which by the shearing would create strong toroidal fields in the absence of strong turbulence. Even though the beam rotation can change much due to interaction with the cocoon and shocks and even change sign, the helicity of the toroidal field is not changed and can thus link the field at large scales with the field topology near the black hole (Gabuzda et al., 2008).

For the magnetic field topology in the cocoon, axisymmetry is a major limitation, contrary to the effects discussed before. Magnetic field in a toroidal configuration cannot damp KH instabilities in axisymmetry since no magnetic tension is available as restoring force, while poloidal field could do so. Fortunately, the jet head-generated toroidal field in the turbulent cocoon partly would be converted into poloidal field in three dimensions, establishing some dynamical equilibrium between the components but keeping the overall field magnitude or amplify it even further, and this makes the cocoon magnetic field a reasonable explanation for the smooth contact surfaces. We plan to examine this effect in three dimensions in the future to be able to quantify the amount of damping and suppressed entrainment of ambient gas in the cocoon.

However, despite the inability to actually produce the expected smooth contact surfaces in axisymmetry away from the jet head region, there is no reason to assume that the amplification of magnetic fields should be in three dimensions any different than shown in our simulations, since the plasma dynamics is not very different and the shearing mechanism in the jet head simply relies on the off-axis flow of plasma, which also happens in 3D. Furthermore, we are not aware of any reason that the field magnitude in the cocoon should be considerably different in three dimensions. It is unclear, though, how the spatial distribution of the magnetic field would look like: 3D turbulence might want to distribute field strength rather uniformly in the cocoon, but formation of a large-scale poloidal current may try to establish a radially increasing toroidal field. Observations indicate that magnetic field strengths within the cocoon may vary significantly (Goodger et al., 2008).

It may be interesting to note that the amplification of magnetic field is quite related to dynamo action as in the sun. The shearing (Ω-effect) is just the same and solar convection is replaced by jet-driven cocoon turbulence, but the locations of these actions are different and they are externally powered (by the beam thrust) instead of self-sustained. The spatial separation of the two effects and the (at least roughly) isotropic turbulence, however, prevent the formation of an outstanding large-scale poloidal field.

The uncertainty in the magnetic field topology in the cocoon also applies to the distribution of plasma β in the system. We (expectedly) found that plasma β is unchanged throughout shocks despite a gradual increase along the beam (which might also be due to limited resolution of the beam and entrainment). Thus, the assumption of a fixed fraction of equipartition to generate synchrotron emission maps from hydro simulations seems to be quite justified. However, this was not found to be true for the cocoon, where a wide distribution of β was found and derivation of synchrotron emission from hydro models thus may considerably deviate from MHD results (as will be seen in Chapter 4). But as mentioned, this result is expected to change in 3D, apart from having relatively low β in the cocoon. Emission maps of our simulations and comparision to hydro emission models are are presented in the following chapter.

The amplification of magnetic fields is also particularly interesting for the question of the origin of lobe magnetic fields. De Young (2002) pointed out that equipartion fields in the lobes cannot be passively advected with the plasma from the jet beam due to flux conservation arguments. The beam magnetic fields would have to be of order 0.01 G or higher, certainly above equipartion, which would result in enormous synchrotron losses, luminosities incompatible with observational limits and probable disruption of the jet due to the magnetic pressure. Hence, the magnetic field must be amplified by some mechanism, and De Young argues for turbulent amplification in the hotspot flow, though it is not easy to meet the necessary requirements for this. The shearing in the jet head, which is seen in our simulations, in contrast, naturally provides this amplification and can therefore explain the strong lobe magnetic fields or at least contribute to their field strength. In fact, the simulations exhibit fields magnitudes in the cocoon that are comparable to field magnitudes in the beam and consequently have similar plasma β since the beam and cocoon pressures came to balance. We conclude that shearing due to off-axis flow of the plasma provides a natural explanation for the lobe magnetic fields and allows equipartition jets to inflate an equipartition cocoon.

3.8.2 Dynamical Evolution

X-ray observations of the ambient cluster gas contain valuable information about several jet and AGN properties and self-similar models can give easy access to underlying physical parameters. We are able to confirm agreement of our numerical simulations with self-similar models (Falle, 1991; Begelman, 1996; Kaiser & Alexander, 1997) for the bow shock propagation. Excentricity of the bow shock and its Mach number provide an easy way to compare theoretical models with observations and determine the density contrast, without the need for uncertain assumptions on the emission of the radio plasma.

The weak and roundish bow shocks in observations indicate that models of very light jets (with density ratios $< 10^{-2}$) are indeed necessary for most cluster sources. Although we chose a simplified setup with a constant ambient gas and axisymmetry, the simulations are in the regime of observed values for various sources (see Sect. 1.2) and self-similar models generalize

this behaviour for declining cluster profiles, which was already examined for very light hydrodynamic jets by Krause (2005). As our runs, with the clear exception of the magnetically dominated M4, propagate as their hydro counterparts, only minor deviations from those results are expected, except where specific source properties are to be included.

Contrary to the bow shocks and the jet length, we find that the cocoon width does not evolve self-similarly but for lighter jets rather grows with lower power law exponents and the mean cocoon pressure drops more slowly than expected. Although this may seem unexpected, it was already stated by Kaiser & Alexander (1997), that contrary to the bow shock, the self-similar evolution of the cocoon depends on the physical model for the post-hotspot flow and thus, deviations are to be expected if these assumptions do not hold in the simulations. Since very light jet cocoons are less overpressured and approach the ambient pressure sooner, the sideways expansion becomes slower and may even stall, letting their aspect ratio (length to width ratio) grow. Similar behaviour would be expected for the heavy jets, although at much later times. Thus, cocoon evolution depends sensitively on the question of overpressure, which can be addressed by the strength of the lateral bow shock. Furthermore, cluster density profiles make cylindrical cocoons rather than elliptical ones due to the weaker density contrast at larger distances (Krause, 2005). Altogether, this makes us confident that our simulations reasonably well describe observed cluster sources.

In contrast to bow shocks, measurements of the cocoon shape are complicated by cooling of the relativistic electrons, which limits observations to the outermost parts (lobes). While radio observations show the high-energy electrons in the cocoon as lobes, single-fluid MHD simulations only trace the low-frequency emitting matter and can only show the low-frequency radio morphologies (cf. high and low frequency images in Carilli et al., 1991), which generally suffer from low spatial resolution. This situation fortunately will much improve in the future with new instruments as LOFAR or the SKA, which will allow more detailed studies of cocoon dynamics and turbulence. Until then, X-ray images of cavities and (in some cases) the inverse-Compton emission of cosmic microwave background photons may supplement available low-frequency radio maps.

Scheuer (1982) introduced the “dentist’s drill” to refer to a moving working surface, which therefore widens the jet head and the lobes. Very light jets naturally show extensive cocoons and varying deflection of the beam widens the jet head and hence, even in axisymmetry, show something very similar to a “dentist’s drill”. While this does not exclude beam precession (Steenbrugge & Blundell, 2008), it does not require it and no large precession amplitudes are needed.

We expect for multiple outbursts of different power in the same cluster, indicated by “ghost cavities” (e.g. Fabian et al., 2006; Wise et al., 2007), that their evolution crucially depends on the history of the past outbursts, as these push the dense cluster gas aside, letting the new outburst propagate with a different density contrast. In this case, the new jet might quickly push forward to the old jet size, then resuming its work on the dense ambient gas. The morphology of the cavities may allow the determination of the respective density contrasts and thus could shed light on the outburst history.

The thermal interaction of jets with the intra-cluster medium is less accessible to direct comparison with observations. Slower jet propagation is responsible for the strong impact of the beam at the working surface and a high thermalization; some conversion of kinetic to thermal energy will additionally occur near or in the beam due to beam destabilization, but

may be less efficient in 3D. Although the dominant power source is the kinetic jet power, this strong thermalization converts most of the input power to thermal energy – about half of this in the shocked ambient gas and half in a cocoon filled with high-entropy plasma, which eventually may transfer at least part of its energy to the entrained cluster gas. This is in line with findings of other authors (e.g. Reynolds et al., 2002; O'Neill et al., 2005; Zanni et al., 2005), where the latter authors conclude that up to 75 % of the energy can be dissipated irreversibly and thus is available for heating in the intra-cluster medium, as required by the X-ray luminosity–temperature relation (Magliocchetti & Brüggen, 2007) and to provide "radio-mode" feedback for models of galaxy evolution (Croton et al., 2006).

Another interesting result of the present simulations is the excitation of sound waves in the ambient gas by vortices in the turbulent cocoon, which is more effective for the very light jets with their extended cocoons. Vortex shedding (Norman et al., 1982) quasi-periodically occurs in the jet head, and the vortices then are advected with the backflow into the cocoon and provide an intermittent source for the turbulent cascade, producing pressure waves. Waves like these are visible in the Perseus cluster (Fabian et al., 2006; Shabala & Alexander, 2007) and, although being hard to observe, may be an ubiquitous feature in galaxy clusters with current or past jet activity. Their typical wave length might yield a link to jet dynamics and cocoon turbulence. In the lightest of our jets (M4L), the bow shock is just about to turn into a sound wave and then simply would join the enclosed sound waves. Viscous damping may be a mechanism to reduce the amplitudes additionally to the growing wave area and is another candidate for preventing cooling flows (Fabian et al., 2005), but in our scenario would be more related to the jets than the AGN itself.

Axisymmetry naturally imposes some constraints on the dynamics, which have to be considered carefully. Jet beams in high-power sources are essentially axisymmetric objects and effects of the full third dimension are merely perturbations from axisymmetry. However, this obviously is not true when beam stability or non-axisymmetric effects are explored specifically. While generally 3D jets are subject to a greater number of instabilities, for very light jets there is an opposing effect of an increased number of dimensions. In 3D, cocoon vortices often will miss the beam or are slightly deflected, this is not possible in axisymmetry and the beam thus is destabilized, deflected or disrupted more easily which is most evident from our lightest run (M4L). As seen in the very light jets of Krause (2005), the beam stability improves when going to full three dimensions. For most results, however, energetics and scaling behaviour are not expected to change significantly in 3D, notable exceptions to this being cocoon turbulence, magnetic field topology and stability of the contact discontinuity.

Cocoon turbulence further away from the jet head certainly will differ with increased dimensionality as the increased number of degrees of freedom for vortices allow them to turn in all directions and interactions between colliding vortices will be different. Though, we expect the effects on cocoon morphology to be within reasonable limits, as the kinetic energy in the cocoon is lower than the thermal energy by factors of $\gtrsim 3$ for $\eta \leq 10^{-2}$ and hence, effects of thermal pressure will dominate.

3.9 Summary

Performing axisymmetric MHD simulations of bipolar very underdense jets in a constant density atmosphere, we find that magnetic fields damp Kelvin-Helmholtz instabilities in the jet head and stabilize it, producing smoother and more pronounced outer lobes, seen from plasma $\beta \sim 10$ on. This becomes even more effective since the backflow from the jet head efficiently amplifies magnetic fields from the beam by shearing, thus significantly enhancing toroidal fields for matter moving off the beam axis. We confirm self-similar behaviour of the bow shock as well as the jet length, but find slower growth of the cocoon width if sources approach pressure balance with the ambient gas. Weak and round bow shocks as well as generally wide radio cocoons (cavities) are properties of light jets and indicate that strong density contrasts are necessary to explain properties of many high-power jets in galaxy clusters, although cocoon widths sensitively depend on the cocoon overpressure and density profiles in the ambient medium. Vortices in the turbulent cocoon furthermore excite sound waves in the shocked ambient gas and high thermalization allows efficient heating of the intra-cluster medium.

4 Emission Maps

In the following chapter, the simulated jets are analyzed with respect to their observable properties to supplement the previous analysis, which considered only the fluid variables. Since many terms (as "lobes" or "cavities") refer to observed structures, it is not unquestionable whether conclusions drawn from the fluid variables are actually correct. Hence we examine synthetic observations of the simulated jets and include a critical analysis of the employed emission methods. To avoid confusion between the emission maps of different methods, synchrotron maps are shown in with a blue, inverse-Compton with a green and thermal bremsstrahlung with a red colortable.

4.1 Emission Processes and Projection

Observed jet properties are almost entirely ascribed to three emission processes for the case of extragalactic jets: non-thermal emission by the relativistic particle population in the jet plasma via synchrotron radiation as well as inverse-Compton radiation and thermal bremsstrahlung (free-free) emission observed from the ambient gas.

4.1.1 Synchrotron Emission

The classical way to observe jets is at radio frequencies. Additionally to the "bulk fluid", which is simulated, the energy spectrum of electrons contains a nonthermal component, which extends to high Lorentz factors. These relativistic electrons move in the magnetic field of the jet plasma and gyrate around the magnetic field lines with angular frequency

$$\omega_{\mathrm{B}} = \frac{eB}{\gamma mc}. \tag{4.1}$$

This accelerated motion is responsible for emission of electromagnetic waves and the relativistic motion mostly confines this emission to a narrow cone (half opening angle $\sim 1/\gamma$) around the forward direction for each electron, yielding very short electromagnetic pulses for an observer, if a light cone encloses his line of sight. For a whole population of mono-energetic and isotropic electrons, the summed-up effect of these short pulses is radiation, which extends to frequencies

$$\omega_{\mathrm{c}} = \frac{3}{2}\gamma^3 \omega_{\mathrm{B}} \sin\theta = \frac{3\gamma^2 eB \sin\theta}{2mc} \tag{4.2}$$

much higher than ω_{B}, since the Fourier spectrum of short pulses is broad and extends to high frequencies. θ is the angle between the observer's line of sight and the magnetic field. Detailed calculation of this process (Rybicki & Lightman, 1979) shows that the emitted spectrum at low frequencies rises as $P(\omega) \propto \omega^{1/3}$ and drops off exponentially at high frequencies $P(\omega) \propto$

$\omega^{1/2}\, e^{-\omega/\omega_c}$. The emitted power has its maximum value at $\omega = 0.29\,\omega_c$. Hence, the maximum emission is at frequencies of

$$\nu_{\max} \approx 1.22\,\mathrm{MHz}\,\gamma^2 B\,[\mathrm{G}]\sin\theta \tag{4.3}$$

and synchrotron radiation observed at frequencies between 0.1 and 10 GHz correspondingly originates from electrons with Lorentz factors γ in the range of 3 000 to 30 000, assuming a typical magnetic field magnitude of 10 μG in the lobes (Croston et al., 2005). Only the magnetic field projected on the plane of sky, $B_\perp = B\sin\theta$, enters these emission properties. The total emitted power per electron is

$$P = \frac{4}{9} r_0^2 c\,\beta^2\,\gamma^2 B^2 \tag{4.4}$$

$$\approx 1.06\times 10^{-15}\beta^2\,\gamma^2\,(B\,[\mathrm{G}])^2\ \mathrm{erg\,s^{-1}} \tag{4.5}$$

with the classical electron radius $r_0 = e^2/mc^2$ and the Lorentz factor $\gamma = (1-\beta^2)^{-1/2}$.

For a power law distribution of electron energies,

$$n_{\mathrm{rel}}(\gamma)\mathrm{d}\gamma = C\gamma^{-p}\mathrm{d}\gamma, \quad \gamma_1 < \gamma < \gamma_2 \tag{4.6}$$

the resulting synchrotron spectrum becomes a power law, too, and the volumetric emissivity is

$$\epsilon_\nu^{\mathrm{syn}} = \frac{\mathrm{d}W}{\mathrm{d}V\,\mathrm{d}t\,\mathrm{d}\nu} \propto n_{\mathrm{rel}}\,(B\sin\theta)^{\frac{p+1}{2}}\,\nu^{-\frac{p-1}{2}} \tag{4.7}$$

$$\propto n_{\mathrm{rel}}\,(B\sin\theta)^{\alpha+1}\,\nu^{-\alpha}, \tag{4.8}$$

where n_{rel} is the particle number density of the contributing relativistic electrons and the parameter $\alpha = (p-1)/2$ is the spectral index, sometimes defined with opposite sign. Typical radio spectra show $F_\nu \propto \nu^{-0.7}$, thus $p = 2.4$. The degree of polarization (for a homogeneous magnetic field) is $\Pi = \frac{p+1}{p+7/3}$ and therefore can reach up to $\approx 70\,\%$.

With these results, emission maps can be computed if the density of the relativistic particles and the projected magnetic field were known, assuming a constant spectral index, i.e. no reacceleration or cooling taking place. Since the relative fraction of contributing relativistic particles in the bulk fluid is not known (they are not simulated), the emission maps can only show relative contributions and the proportionality is sufficient in the following. Furthermore, for a fixed observation frequency, also $\nu^{-\alpha}$ is only a proportionality constant.

Clearly, this emission leads to cooling of the relativistic electrons. Since the total emission power per electron is $P \propto \gamma^2 B^2$, the cooling time scale

$$t_c = \gamma mc^2/P \approx 8\times 10^8\,\mathrm{s}\ (B\,[\mathrm{G}])^{-2}\,\gamma^{-1} \tag{4.9}$$

is shorter for strong magnetic fields and electrons with high Lorentz factors. As a consequence, the computed synchrotron emission maps correspond to observations at low frequencies where cooling did not yet change the spectrum.

Hydrodynamic simulations do not evolve the magnetic fields in the plasma and hence simulations cannot be compared with observations without additional assumptions. Since we compare

different methods in Sect. 4.2, we briefly mention the techniques commonly used for computing the emission from hydro simulations, as described by Mioduszewski et al. (1997). For this, it is assumed that both density of the relativistic electrons as well as magnetic pressure are traced by thermal pressure, as suggested by minimum energy arguments (Mioduszewski et al., 1997).

$$n_{\mathrm{rel}} \propto p \tag{4.10}$$

$$\frac{B^2}{8\pi} \propto p \tag{4.11}$$

Then the emissivity simply scales as

$$\epsilon_\nu^{\mathrm{syn}} \propto p^{(\alpha+3)/2} \tag{4.12}$$

and a passively advected tracer variable can be used to consider only jet-originated plasma.

Reacceleration of relativistic particles and cooling is not modelled in any of the methods. This might be mimicked by using $n_{\mathrm{rel}} \propto p$, since emission would then be higher in shocked regions. However, is a very crude assumption, as high-pressure regions do not necessarily track shocks. We do not pursue this any further except for including it in the methods comparison (Fig. 4.3) and note that effects from this may be estimated "by eye" from comparison of maps that include magnetic fields with hydrodynamic emission maps, the latter highlighting high-pressure regions.

4.1.2 Inverse-Compton Emission

For this emission process, low-energy photons are scattered to high energies by the relativistic electrons. This works for any photon field; for jets, inverse-Compton scattering (IC) of the cosmic microwave background (CMB) photons (e.g. Croston et al., 2005; Kataoka & Stawarz, 2005; Hardcastle & Croston, 2005; Goodger et al., 2008) and of infrared radiation from the quasar nucleus has been reported (e.g. Brunetti et al., 2002), as well as synchrotron self-Compton emission (e.g. Harris & Krawczynski, 2006), where the inverse-Compton process works on Doppler-beamed synchrotron photons emitted by the electrons themselves. However, this is not relevant for the cocoon appearance, as fluid speeds there are not relativistic anymore.

Interaction of relativistic electrons in the jet plasma with the pervasive radiation field of the cosmic microwave background with temperature $T = 2.73$ K (Fixsen et al., 1996) will be used here. It provides a high density of low-energy photons with typical energies of 6.6×10^{-4} eV and an energy density of $U_{\mathrm{ph}} = 4.2 \times 10^{-13}$ erg cm^{-3}. For inverse-Compton scattering, the photon energy increases by a factor of $\approx \gamma^2$. Detailed calculation (Rybicki & Lightman, 1979) yields a volumetric emissivity

$$\epsilon_\nu^{\mathrm{IC}} = \frac{\mathrm{d}W}{\mathrm{d}V\,\mathrm{d}t\,\mathrm{d}\nu} \propto C T^{(p+5)/2} \nu^{-(p-1)/2} F(p) \tag{4.13}$$

$$\propto n_{\mathrm{rel}} T^{\alpha+3} \nu^{-\alpha}, \tag{4.14}$$

where T is the temperature of the CMB photon field. As for synchrotron radiation, only relative intensities are computed here due to our ignorance of the density ratio between relativistic particles and bulk fluid. While the inverse-Compton process works similarly for AGN infrared photons, their radial radiation intensity decline would then have to be considered.

Inverse-Compton radiation shows results similar to synchrotron, but does not depend on the magnetic field, giving a more direct link to the relativistic particles. Furthermore, in the X-rays ($h\nu \sim 1$ keV) it tracks electrons of significantly lower energy ($\gamma \sim 10^3$) than GHz synchrotron emission, making the whole cocoon visible, since cooling for these electrons was not yet effective. The totally emitted power per electron is found to be

$$P = \frac{4}{3}\sigma_\mathrm{T} c \beta^2 U_\mathrm{ph} \gamma^2 \tag{4.15}$$

$$\approx 2.66 \times 10^{-14}\,\mathrm{cm^3\,s^{-1}}\, U_\mathrm{ph}\, \gamma^2, \tag{4.16}$$

with the Thomson cross section σ_T, very similar to the synchrotron result:

$$\frac{P_\mathrm{syn}}{P_\mathrm{IC}} = \frac{U_\mathrm{B}}{U_\mathrm{ph}} \tag{4.17}$$

IC/CMB emission power is equal to synchrotron emission power assuming a magnetic field magnitude of $3\,\mu$G. Since the energy density of the cosmic microwave background increases with redshift as $U_\mathrm{ph} \propto (1+z)^4$, it is conjectured that this process may be more important at high redshift.

4.1.3 Bremsstrahlung Emission

Contrary to synchrotron and inverse-Compton radiation, bremsstrahlung emission is independent of the relativistic electrons. It is simply caused by deflection of moving charges (electrons), which emit electro-magnetic waves as they are accelerated, and is also referred to as free-free emission. For Maxwell-Boltzmann distributed electron velocities, thermal bremsstrahlung is produced, as will also be used in the following. For the intra-cluster gas with temperatures of $\sim 10^7$ K, bremsstrahlung is the dominant energy loss process and thus galaxy clusters shine brightly in X-rays (energies of $kT \sim 1$ keV).

Detailed calculation of the Coulomb scattering for a thermal electron distribution yields the spectral volumetric emissivity for fully ionized hydrogen (Rybicki & Lightman, 1979)

$$\epsilon_\nu^\mathrm{ff} = \frac{\mathrm{d}W}{\mathrm{d}V\,\mathrm{d}t\,\mathrm{d}\nu} = \frac{2^3\pi e^6}{3mc^3}\left(\frac{2\pi}{3km}\right)^{1/2} T^{-1/2} n^2 e^{-h\nu/kT} \bar{g}_\mathrm{ff} \tag{4.18}$$

$$\approx 1.71 \times 10^{-38}\, n^2 T^{-1/2} e^{-h\nu/kT} \bar{g}_\mathrm{ff} \quad \text{in cgs units.} \tag{4.19}$$

The emissivity is constant for low frequencies and drops exponentially for $h\nu > kT$. Setting the Gaunt factor $\bar{g}_\mathrm{ff} = 1$ gives good order of magnitude estimates. However, we note that for high temperature regions ($h\nu \ll k_\mathrm{B}T$) the Gaunt factor increases logarithmically (Fig. 4.1) and emission from these at low frequencies will be higher than computed with $\bar{g}_\mathrm{ff} = 1$; for $h\nu/k_\mathrm{B}T = 10^{-2}$ this can make up a factor of 3. Since for very light jets the shocked ambient gas generally is not very hot, this will not make much difference and we stick with the above simplification. For the heavier jets at early times, though, the bow shock near the jet head will appear somewhat brighter than shown in the emission maps, where it can be quite dim due to the $T^{-1/2}$ factor in the emissivity.

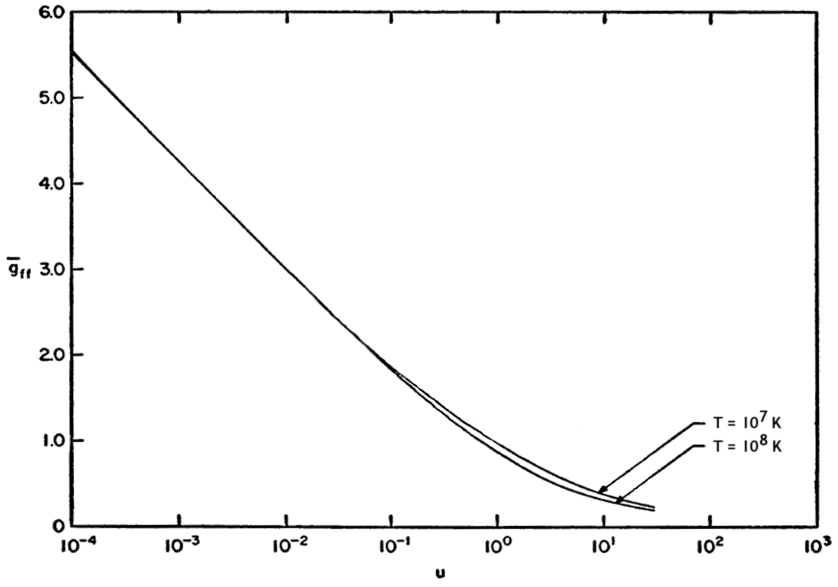

Figure 4.1: Temperature-averaged Gaunt factor $\bar{g_{\mathrm{ff}}}$ as function of $u = h\nu/k_{\mathrm{B}}T$ for two selected temperatures. Adapted from Fig. 5 of Karzas & Latter (1961) for our setup.

Integrating over all frequencies, we find the total volumetric emissivity

$$\epsilon^{\mathrm{ff}} = \frac{\mathrm{d}W}{\mathrm{d}V\,\mathrm{d}t} = \left(\frac{2\pi kT}{3m}\right)^{1/2} \frac{2^3\pi e^6}{3hmc^3} n^2 \bar{g}_{\mathrm{B}} \tag{4.20}$$

$$\approx 3.56 \times 10^{-28}\, n^2 T^{1/2} \bar{g}_{\mathrm{B}} \quad \text{in cgs units.} \tag{4.21}$$

Setting the velocity-averaged Gaunt factor $\bar{g}_{\mathrm{B}} = 1.2$ gives about 20 % accuracy. The cooling time for thermal bremsstrahlung can then be defined as

$$t_{\mathrm{c}} = \frac{p}{(\gamma - 1)\,\epsilon^{\mathrm{ff}}} \tag{4.22}$$

$$\approx 490\, \frac{\left(T \,/\, 10^7\,\mathrm{K}\right)^{1/2}}{n \,/\, 0.1\,\mathrm{cm}^{-3}}\,\mathrm{Myr}\,. \tag{4.23}$$

4.1.4 Projection Method

The MHD simulations were performed in axisymmetry on a cylindrical grid. For the emission maps from different viewing angles (inclination θ), the volume emissivity data points were mapped onto a 3D cartesian grid (x, y, z), aligned with the observer's line of sight (Fig. 4.2). To do this, cylindrical source coordinates (Z, R, ϕ) were computed for every cartesian grid cell

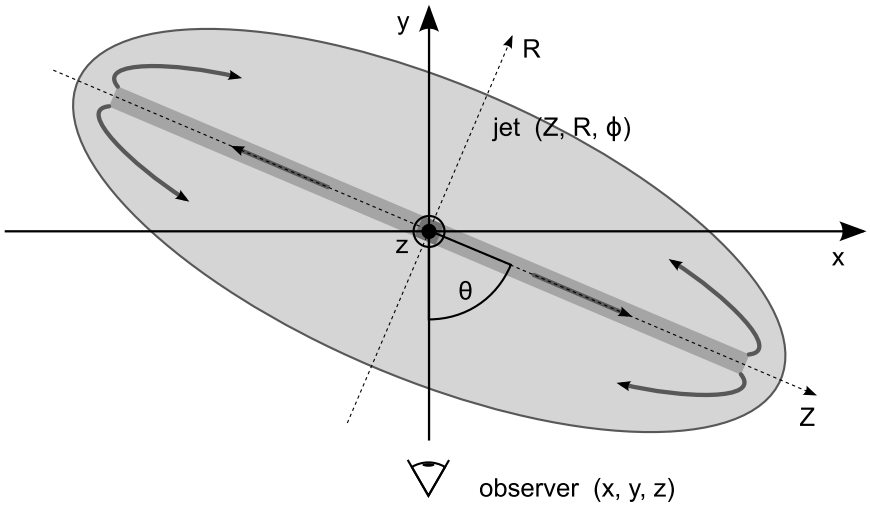

Figure 4.2: Projection of the cylindrical grid (Z, R, ϕ) onto the plane of the sky (x, z) for an observer with inclination angle θ between the line of sight and the jet axis. For the emission maps, emission is integrated along the y direction.

and respective data were copied after applying a smoothing mask for antialiasing, corresponding to the chosen resolution.

$$\alpha = \theta - 90^\circ \tag{4.24}$$
$$x_\mathrm{j} = x\cos\alpha + y\sin\alpha \tag{4.25}$$
$$y_\mathrm{j} = -x\sin\alpha + y\cos\alpha \tag{4.26}$$
$$z_\mathrm{j} = z \tag{4.27}$$
$$Z = x_\mathrm{j} \tag{4.28}$$
$$R = \sqrt{y_\mathrm{j}^2 + z_\mathrm{j}^2} \tag{4.29}$$
$$\phi = \arctan(z_\mathrm{j}/y_\mathrm{j}) \tag{4.30}$$

For vector-aware synchrotron emission maps, magnetic field vectors in cylindrical geometry were projected onto the 3D cartesian grid (giving B_x, B_y, B_z) and then their components in the plane of the sky were considered for the volumetric emissivities.

$$B_{x\mathrm{j}} = B_Z \tag{4.31}$$
$$B_{y\mathrm{j}} = B_R\cos\phi - B_\phi\sin\phi \tag{4.32}$$
$$B_{z\mathrm{j}} = B_R\sin\phi + B_\phi\cos\phi \tag{4.33}$$
$$B_x = B_{x\mathrm{j}}\cos\alpha - B_{y\mathrm{j}}\sin\alpha \tag{4.34}$$
$$B_y = B_{y\mathrm{j}}\sin\alpha + B_{y\mathrm{j}}\cos\alpha \tag{4.35}$$
$$B_z = B_{z\mathrm{j}} \tag{4.36}$$

Finally, the total emission was computed by summing up along the line of sight, assuming optically thin emission. The projection routine was implemented in IDL and returns floating

point images and the corresponding coordinate axes X and Z. Viewing angles are measured by the inclination angle θ between the jet axis and the line of sight.

4.2 Synchrotron Emission Maps

The synchrotron appearance of the jets depends on the details of the relativistic electrons emitting this radiation. We state in advance, that from single-fluid MHD simulations, realistic synchrotron emission cannot be derived, as this necessarily implies knowledge about the complex processes of acceleration and cooling of the relativistic electrons, and even simulations modelling this (e.g. Tregillis et al., 2001, 2004) are still not able to produce globally satisfactory emission maps, in the sense that lobe brightness and shape would look as they do in observations. It is, however, instructive to compute such emission maps to get a rough impression of the source properties, to find out which features can be reproduced and which are missing, and to see the effects of magnetic field distribution and topology. In order to clarify the large uncertainties in the emission maps, which are generally omitted in the literature, we will first present emission maps computed with different methods and only then turn to the inclination dependence and source evolution. We do not present polarization maps, since the general behaviour was already examined by Clarke et al. (1989) and the large uncertainties in emissivity and cocoon magnetic field orientation would strongly affect the polarization results, yet we address the projected magnetic field direction where this is appropriate and the field direction in the simulation is sufficiently reliable. The computed synchrotron maps correspond to radio emission at low frequencies, where cooling of the nonthermal electrons did not yet have an effect.

The importance of projection on the observed synchrotron radiation and consequences for the appearance and polarization have already been pointed out by Laing (1981). Since the projected magnetic field magnitude in the plane of the sky determines the contribution to the observed surface brightness, both inclination angle of the source as well as pitch angle of the magnetic field (between field and plasma flow direction) affect the appearance. However, these models were simply geometrical models of the jet and not dynamical. Since most jet simulations were and still are purely hydrodynamical, synthetic observations of simulated MHD jets are rare. Clarke et al. (1989) describe the brightness and polarization properties of simulated jets with helical magnetic fields (density contrast $\eta = 10^{-1}$) and their dependence on the inclination and pitch angle. They find that for an initially axial field in the jet beam, the beam can clearly be distinguished from the cocoon background emission, since flux freezing lowers the magnetic field in the cocoon and hence its contribution to the total brightness. Expansion losses and the resulting decreased magnetic field magnitude in the beam result in considerable dimming of the jet way before the jet terminus. For toroidal fields, in contrast, the cocoon emission almost completely masks the jet due to smaller decrease in magnetic field magnitude of the toroidal field in the cocoon. Furthermore, Clarke et al. (1989) note that generally an axisymmetric jet can exhibit patterns which are not perfectly axisymmetric since the apparent orientation of the helical field projected on the plane of the sky is not axisymmetric. Clearly this also applies to our emission maps, despite deviations are subtle and are only visible when poloidal and toroidal field have similar strength. Additionally, we note that relativistic Doppler beaming is

not included, which may increase or decrease the beam brightness relative to the cocoon for low or high inclination angles, respectively.

4.2.1 Different Methods

To compute synchrotron emission maps in the following, we employ three different methods.

EMV: emission is computed from MHD simulations, taking into account the magnetic field vectors with their magnitude and their direction:

$$\epsilon_\nu^{\mathrm{syn}} \propto n_{\mathrm{rel}}\, B_\perp^{\alpha+1} \nu^{-\alpha} \tag{4.37}$$

EMS: emission is computed from MHD simulations, taking into account only the magnetic field magnitude (scalar), ignoring their directions by assuming isotropically tangled fields with $\langle B_\perp^2 \rangle = (2/3)\,\langle B^2 \rangle$.

$$\epsilon_\nu^{\mathrm{syn}} \propto n_{\mathrm{rel}}\, (2/3)^{(\alpha+1)/2}\, B^{\alpha+1} \nu^{-\alpha} \tag{4.38}$$

EH: pseudo-emission is computed from simulations employing the same emissivities as hydrodynamic simulations (Smith et al., 1985; Mioduszewski et al., 1997; Saxton et al., 2002a,b; Carvalho & O'Dea, 2002a; Heinz et al., 2006; Choi et al., 2007; Sutherland & Bicknell, 2007) assuming equipartition.

$$\epsilon_\nu^{\mathrm{syn}} \propto p^{(\alpha+3)/2} \tag{4.39}$$

This can be applied to either hydrodynamic or MHD simulations. Only jet nozzle-originated matter (as indicated by a tracer limit) is considered for emission.

Identical proportionality constants were used for EMV and EMS to allow direct comparison of relative emission strength. However, for EH the constant is unconstrained. Hence, all emission maps are shown in arbitrary surface brightness units. We assume a spectral index $\alpha = 0.7$ (defined by $S_\nu \propto \nu^{-\alpha}$) for the emission maps, which is a typical value found in observations (Bridle & Perley, 1984). Different spectral indices would change contrast between strong and weak magnetic field regions, but not the overall appearance.

In Fig. 4.3, emission maps for these methods are compiled. For simulation M3P, emission with all three methods is computed, and additionally, the hydrodynamic EH method is applied to simulations M3 and H3 at the same physical time. Additionally, an emission map labelled "EMSp" is computed with the EMS method for a relativistic particle density proportional to the gas pressure instead of the tracer value. EMV and EMS are not computed for M3, since the density of the relativistic particles cannot be determined clearly with the tracer due to the simulation tracer setup, despite full magnetic field information is present. For M3P, the tracer is set to unity in the jet plasma leaving the nozzle and thus is proportional to the density of relativistic particles (ignoring all reacceleration). It is directly used for n_{rel} in equations (4.37) and (4.38).

The three emission methods, applied to the simulation M3P, evidently have quite different results. Most prominent is the central cocoon region, which shows strong diffuse emission in all three cases. In EH, it is concentrated towards the beam axis, due to quite uniform pressure within the cocoon and since the line of sight through the cocoon is longest there.

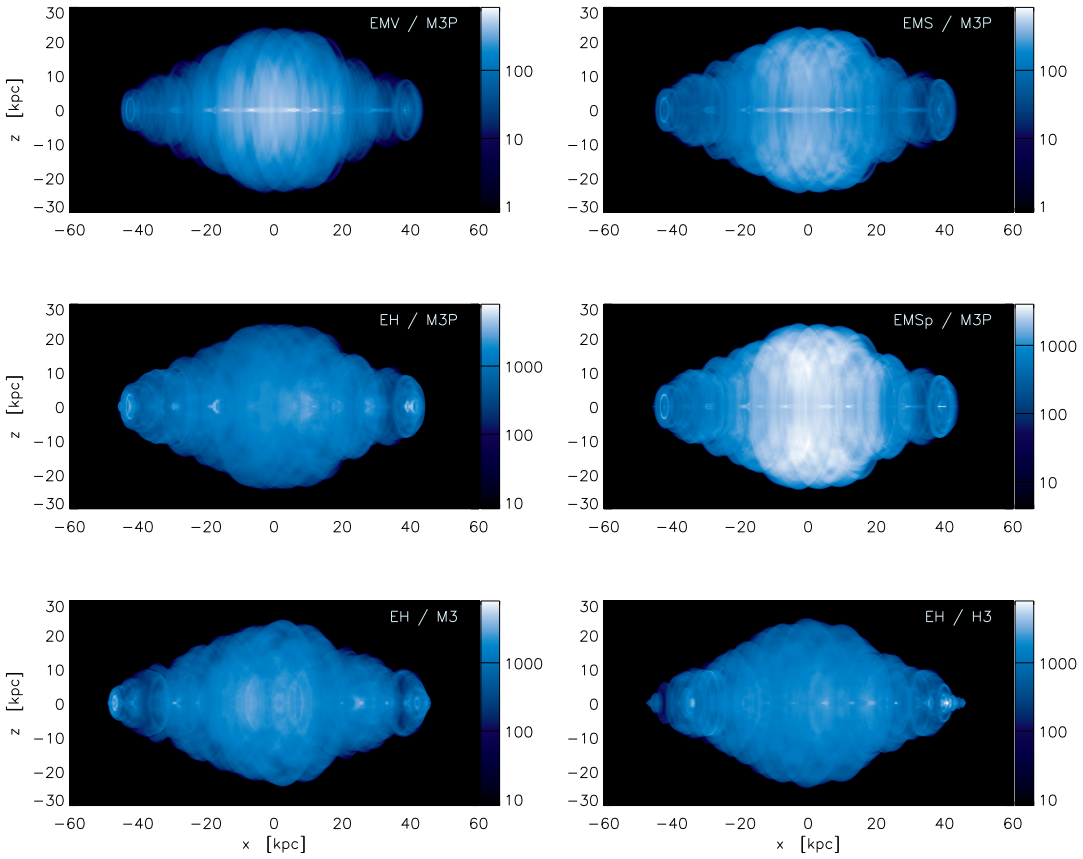

Figure 4.3: Synchrotron emission: comparison of three different methods (EMV, EMS, EH), for simulations M3P, M3 and H3 at $t = 15$ Myr and inclination angle $\theta = 70°$. EMSp shows the result of EMS when setting $n_{\mathrm{rel}} \propto p$. All images correspond to low-frequency radio emission, where cooling of the nonthermal electrons was not yet effective.

For the methods including the magnetic field, the emission is more spread out: in case of EMV, it continuously declines outwards, as the magnetic field in the cocoon is predominantly toroidal and its projection onto the plane of the sky there becomes smaller. For EMS, however, only magnetic field magnitude is considered and as the cocoon is filled with magnetic field of significant strength, the emission is distributed out to the projected cocoon border. Although EMV better describes the simulation data, it suffers from the artificially predominating toroidal field in the cocoon due to axisymmetry (as discussed in Sect. 3.6), while EMS describes the emission as if magnetic fields were tangled isotropically, which might be expected for a highly turbulent cocoon. Thus EMS seems closer to expectations, if axisymmetry were relaxed.

For all methods, the cocoon region around the jet head shows lower diffuse emission than the central cocoon, which disagrees with observations (e.g. Fig. 1.5). However, in reality relativistic electrons are reaccelerated in the beam (e.g. at knots or even continuously) and the hotspot, contributing much more to the emission in that region compared to the present simulation. In the simulation, no particle acceleration is included and density of the emitting

particles (as described by the tracer field) can only decrease apart from adiabatic compression. As mentioned before, this is also seen in the emission maps of Clarke et al. (1989). The emission map labelled "EMSp" might mimick reacceleration by assuming a relativistic particle density proportional to the gas pressure. Contrary to the EMV and EMS panels, it shows more pronounced hotspot regions. However, since this method is purely phenomenological, we do not pursue this approach any further. Yet, it shows that some kind of reacceleration may indeed provide a solution to this deviation from observational findings. Additionally, our cocoons are wider near the midplane, while in more realistic cluster profiles, they become more cylindrical (Krause, 2005) due to the weaker density contrast at larger radii, adding up to less emission along the line of sight. This would result in decreased emission easily by a factor of ~ 2 and show a more balanced emission distribution. These maps are relevant for low-frequency observations, as will be possible with LOFAR, since cooling is unimportant there.

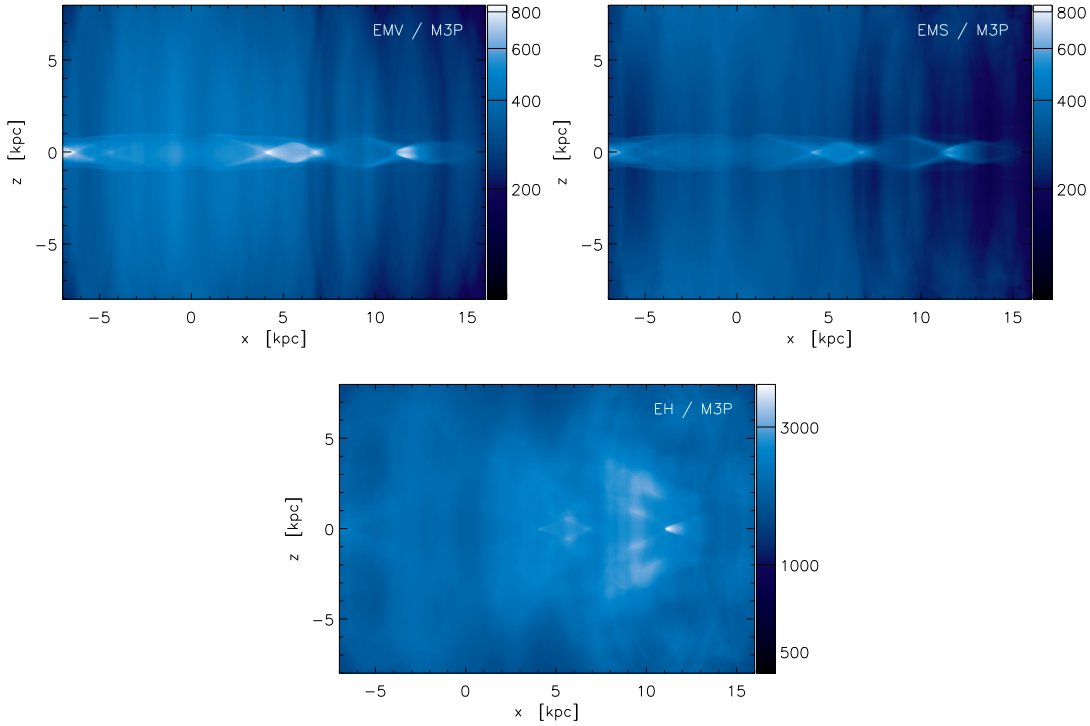

Figure 4.4: Synchrotron emission close to the jet nozzle region as probed by different methods. Simulation M3P at $t = 15$ Myr, $\theta = 70°$.

Further differences are seen for the hotspot regions and the jet beams. The latter can be seen in more detail in Fig. 4.4, which shows the central part around the jet nozzle at $x = z = 0$. In case of the EH emission method, the beam is almost invisible inside the cocoon. It quickly comes to pressure balance with the surrounding cocoon plasma and hence has the same emissivity when only gas pressure considered. Internal shocks in the beam, however, are visible as small spots (cones) on the axis where the gas pressure reaches high values; the size of these spots is considerably smaller than the jet radius. The other two methods, including the magnetic field strength, highlight the beam much better. Due to its magnetic fields, which are stronger than

in the surrounding cocoon gas, the beams are clearly visible in the diffuse cocoon emission. They also show enhanced emission at internal shocks – stronger for EMV than for EMS, since the magnetic field lies almost in the plane of the sky. Note that relativistic beaming is not accounted for in the emission maps, which could significantly reduce the beam brightness for jets roughly in the plane of the sky.

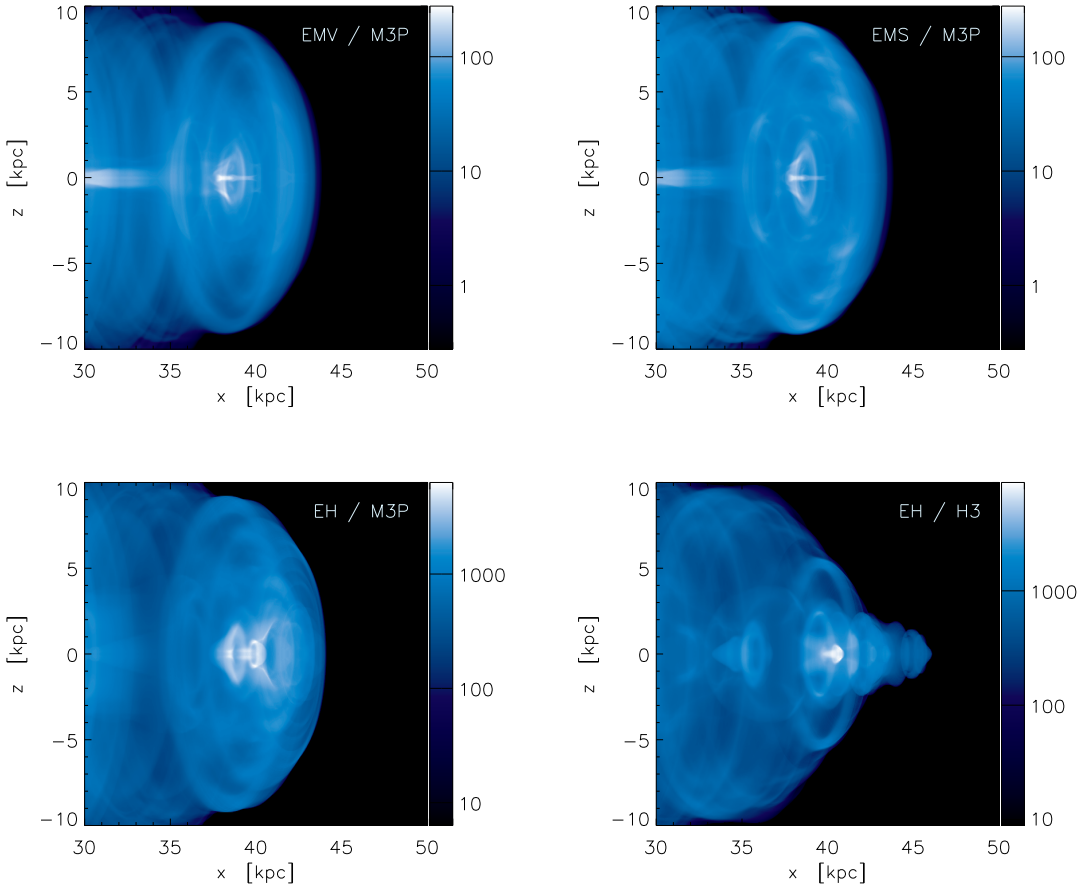

Figure 4.5: Synchrotron emission from the jet head region. Different methods for M3P and the hydrodynamic simulation H3 are shown in comparison. $t = 15$ Myr, $\theta = 70°$.

Turning towards the jet head region, more differences are evident. Fig. 4.5 shows maps for different methods applied to M3P as well as a map computed for the hydrodynamic simulation H3. Both EMV and EMS result in very similar images. The ring-like structures from EMS, however, appear somewhat different in EMV. They have mostly toroidal magnetic field and at the upper and lower edges the projected field component is smaller, yielding weaker synchrotron emission. Depending on how strong the toroidal field is as well as depending on the inclination angle, these rings break up into two curved halves (Clarke et al., 1989). Especially for the outer edges of the cocoon, this results in a gradual decline in cocoon brightness for EMV, but edge-brightened emission for EMS. For hydrodynamic simulations as H3, a small spike of roughly the beam diameter is present which outreaches the rest of the cocoon. While effects like this

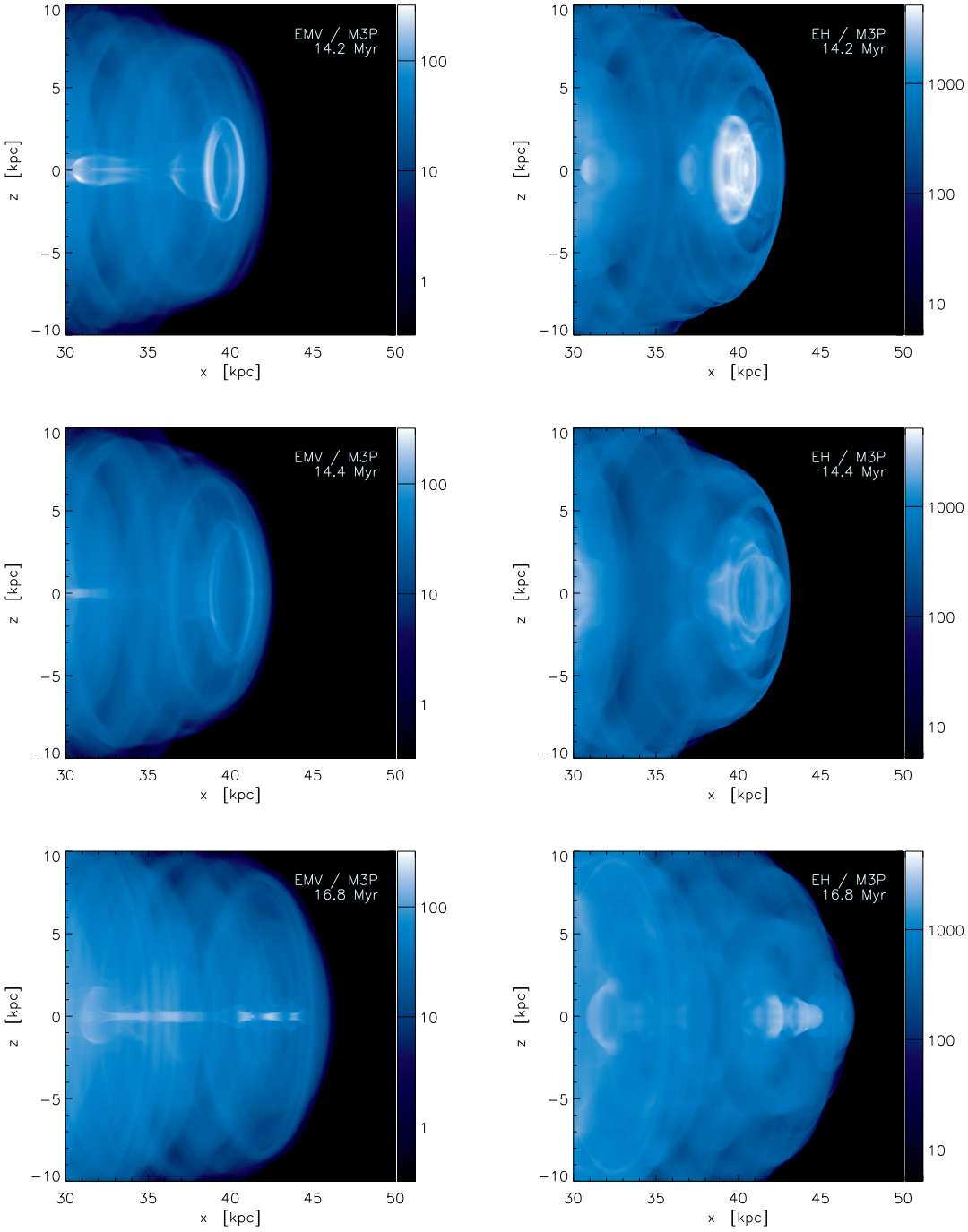

Figure 4.6: Synchrotron emission: jet head region of M3P at different times (as labelled in the panels). Emission mechanisms EMV and EH are used, with an inclination of $\theta = 70°$. The morphology of the jet head structures changes quickly – evolution of the features between 14.2 and 14.4 Myr is an example of *slow* changes.

may also occur (on a smaller level) with MHD simulations at the symmetry axis, it is clear from the density plots (Fig. 3.18) that this is caused by Kelvin-Helmholtz instabilities quickly growing in the jet head. Since the thereby entrained ambient gas is not shining in synchrotron emission, the "dark region" from outside reaches into the cocoon and forms this spike. Yet, we note that in the synchrotron emission the contact surface does not look as ragged as might be anticipated from the fluid variable plots. Projection effects and the annular (thus smoother) morphology of the instable regions in axisymmetry are probably the main causes for this.

Regarding the presence of hotspot features, we find that they cannot be reproduced as expected from observations. While there are regions of higher emission around the jet terminus, they do not outshine the other parts of the source, as found for FR II sources. This is not really astonishing since reacceleration, which is discussed as an important process in jet beams, knots and hotspots, is not modelled by the simulations. Yet these hotspots, if we dare to call them so, are generally more prominent in maps based on the gas pressure (EH). Despite all beam destabilization, high pressure regions are usually present, often with annular shape resulting from off-axis deflection (cf. Lind et al., 1989, who describe annular terminal shocks). Annular or conical structures are also seen in the EMV and EMS images. All these hotspot features are found to be highly transient. They are often hard to track between two high-resolution data frames due to their temporal spacing of 0.2 Myr. Fig. 4.6 shows the jet head regions at three different times: at $t = 14.2$ Myr, a prominent ring (EMV) is found, which is significantly larger and has almost decayed in the next frame at 14.4 Myr. Contrary to the annular shape, emission is considerably more concentrated (disk-like) for the EH method – due to high pressure at this location which is responsible for widening the structure and advecting it into the backflow. Evidently at 16.8 Myr no hotspot can be seen for the EMV image, though the pressure-based EH indicates a high-pressure region there.

In many of the images, a bright on-axis linear feature can be seen, which is narrower than the jet radius and extends over a considerable length. It is present in particular for jets extending over more than ~ 50 kpc per side. The feature is easily destroyed by shocks (e.g. in Fig. 4.5 at $x \approx 37$ kpc), but then appears again later. We find that these structures are due to axisymmetry rather than erroneous implemention of the boundary conditions. The reason is that within axisymmetry poloidal field lines very near the axis are difficult to push off the axis. Their creation may be continuously stimulated by internal shocks, which compress the beam, form spots of high magnetic field strength with similar widths but do not relax completely to their previous state. Since these features are only resolved by a few cells and artificially stabilized by the symmetry axis, we consider them artifacts which, however, are harmless as they do not have any dynamical impact.

4.2.2 Viewing Angle

Observed properties of jets clearly are dependent on the inclination angle θ. Synchrotron emission maps are thus computed for a wide range of inclinations and shown in Fig. 4.7 for all three emission methods considered before. Low inclination angles are generally assumed for broad-line radio galaxies, quasars and blazars. In case of the latter two, relativistic bulk speeds will cause Doppler boosting and relativistic effects will greatly change the observed properties. As this cannot be modelled correctly with our code, we consider the low inclination maps ($\theta = 10^\circ$ and 25°) of limited value. Clearly, structures are mostly circular due to the assumed

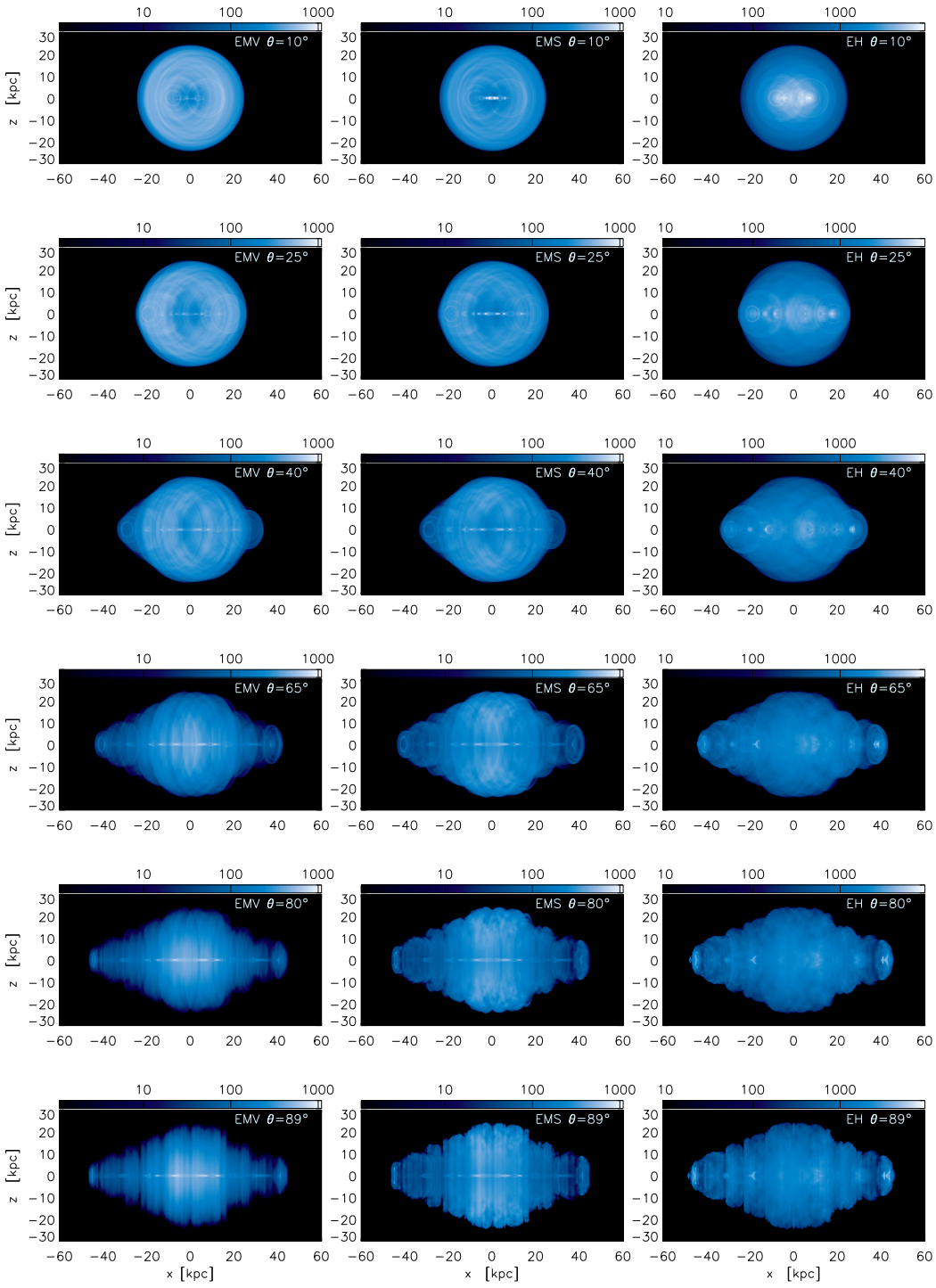

Figure 4.7: Synchrotron emission: varying inclination angle for simulation M3P with methods EMV, EMS and EH.

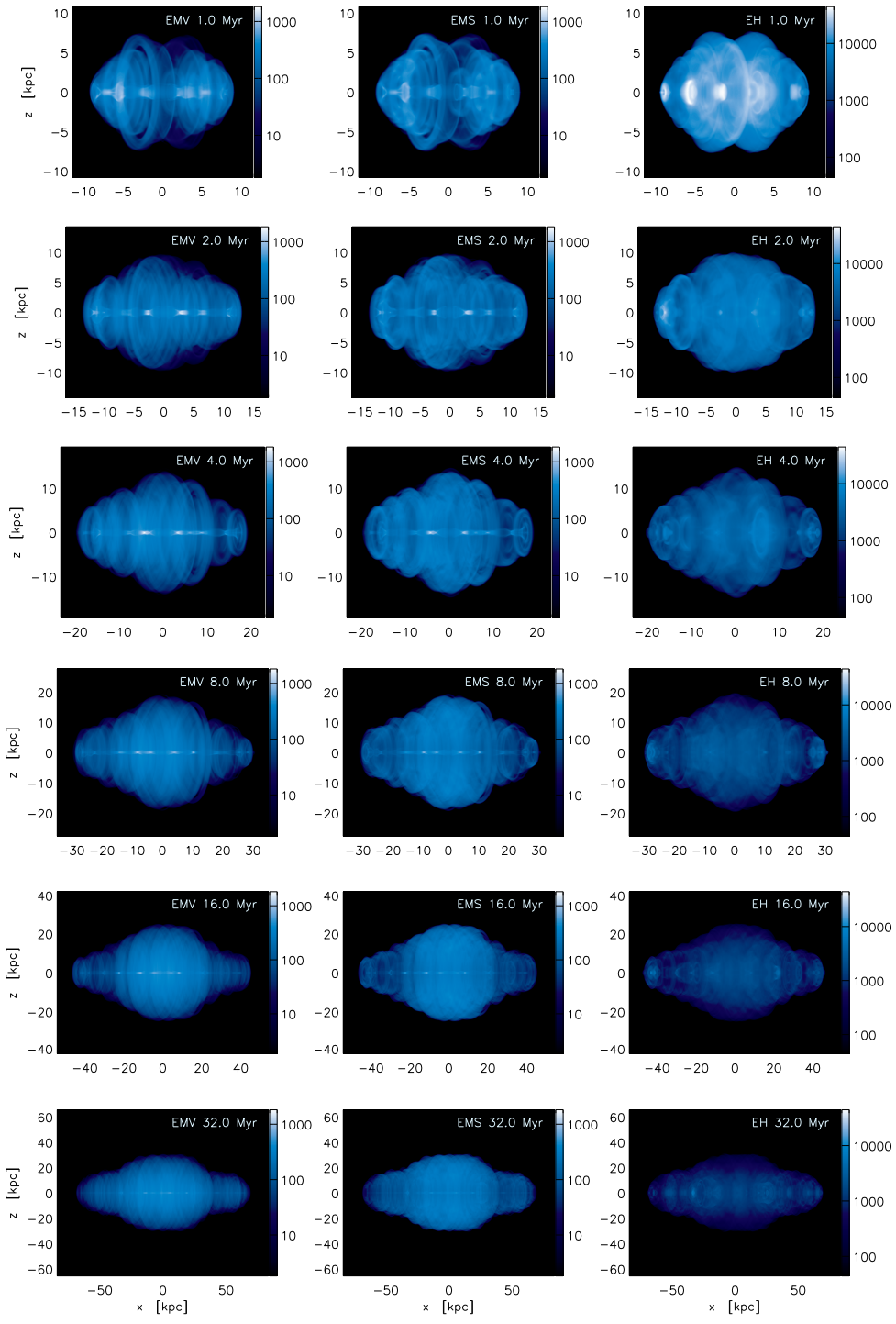

Figure 4.8: Synchrotron emission: evolution of simulation M3P with methods EMV, EMS and EH, displayed for times of 1, 2, 4, 8, 16 and 32 Myr and an inclination angle $\theta = 70°$.

axisymmetry and beams appear only as short features. Yet, they are prominent on the EMS maps due to more contribution along the line of sight for these inclination angles and they are almost absent for EMV, since the component in the plane of the sky is small for the mostly axial field in the beam. At a critical angle of $\sim 25°$, the outer lobes are just inside the circular region of the central cocoon. For higher inclinations, they are visible as extensions to the central region. In contrast, dependence on the exact inclination angle is rather weak for the three largest inclinations. The hotspot regions are only slightly recessed relative to the cocoon boundary, despite their morphology changes from linear to annular for inclinations decreasing from $\theta \approx 90°$ on. Hence the used "standard inclination" of $\theta = 70°$ in most of the emission maps is quite representative for high-inclination sources.

For low inclinations, the hotspots will be considerably recessed (set back with respect to the outer lobe edge), although an annular terminal shock may extend further outwards (see EMV/EMS at $\theta = 40°$). Yet, for this case there should be another more recessed hotspot visible. The recession simply is the consequence of a finite lobe width.

4.2.3 Evolution

Fig. 4.8 shows the changes of the synchrotron appearance due to an evolving source. For the first snapshot, the source still shows hotspots for all emission methods. Since the beam is still short, destabilization and expansion cannot weaken it much and the impact onto the ambient gas is strong. At later times, the hotspots suffer from a more instable beam, fade gradually and only the inner parts of the beam remain bright. At early times, the effects of the initial conditions are still considerable, as interaction of the two backflows in the midplane. Later, these effects become smaller and since the scale changes, the cocoon also becomes smoother. The cocoon aspect ratio clearly increases – starting from an almost spherical but distorted shape to an elongated cocoon for the latest times depicted. As discussed in Sect. 3.3.3, this is a result of a less overpressured source, where pressure support for the lateral expansion fades. Only little structure is seen within the cocoon for the EMV and EMS methods. However, the observed radio lobes as the outer parts of the cocoon, are not reproduced since this would require modelling the cooling of cocoon electrons. While missing reacceleration most likely is responsible for problems of reproducing a continuous beam and hotspots, this may be considerably less critical for the cocoon. A similar result is found for inverse-Compton emission in the next section, but since cooling of the synchrotron emitting electrons happens on the source evolution time scale, more deviations will occur for the synchrotron case, making only the outer cocoon parts visible.

4.3 Inverse-Compton Emission Maps

4.3.1 Methods

Since the inverse-Compton emissivity for a given frequency and photon field only depends on the density of relativistic particles, it is easier to compute and no distinction has to be made how to treat the magnetic fields, as for the synchrotron case before. However, there is still the difficulty that the density of relativistic electrons is not handled by the simulation but only modelled by the compressible tracer. If electrons are reaccelerated from low energies to higher

energies, then contributing to the observed IC/CMB radiation, or if cooled-down electrons from high energies contribute to the observed radiation, this is absent in the emission maps. However, cooling times of these electrons are longer than for those emitting at radio frequencies, which generally should allow observation of most parts of the cocoon instead of only the radio lobes. Due to the power-law behaviour, the emission maps are not for a specific energy. However, for soft X-rays the power law behaviour for the scattering electrons should still hold (not yet at the low-energy cutoff) and cooling is not expected to be relevant. Correspondingly, the images should be comparable to the typical observations of Chandra or XMM-Newton.

The inverse-Compton emission maps presented hence suffer less from model restrictions than the synchrotron maps. Two methods are used for computation:

IC: emission is computed from the compressible tracer field. For the emissivity (4.14) we use the tracer value for the density of relativistic electrons n_{rel}.

ICp: emission is computed from the plasma pressure, assuming it traces the density of the relativistic electrons. $n_{\mathrm{rel}} = p$ is set for the emissivity (4.14). However, only jet nozzle-originated matter is considered by using a tracer limit for the cocoon.

While the IC method gives more strict results, any reacceleration effects are missing. These might be, to some degree, mimicked by the ICp method since reacceleration might preferentially occur near high-pressure regions.

4.3.2 Inclination and Evolution

Fig. 4.9 shows the appearance for different inclination angles. Again, the larger inclinations are more suitable for radio galaxies, while the lower more correspond to quasars and for those, relativistic beaming effects may contribute. Emission from the cocoon is quite uniform for the IC method. It shows considerably less structure than the synchrotron images and, apart from the central region, varies mostly within a factor of 2 (Fig. 4.10). Its global morphology is expected from maps of simulated physical quantities (as density, temperature or the tracer variable), which clearly identify the cocoon of relativistic particles. At low inclinations, the cocoon appears nearly circular due to projection, but higher inclination angles reveal its true aspect ratio. The beam is the dominant feature in the maps, but for relativistic motion and large inclinations, Doppler beaming is expected to make it dimmer. As for the synchrotron case, no bright hotspots are visible due to beam expansion, entrainment in the beam, and missing reacceleration.

For the ICp method, mimicking reacceleration effects with pressure changes, these hotspots appear, though not very strong. Also, there is more structure visible within the cocoon, which can be attributed to pressure differences within the cocoon and beam–cocoon interaction regions, especially near the central region with the jet nozzle. However, here the beam is invisible due to its general pressure equilibrium with the surrounding cocoon.

The same is true for other times, as can be seen in Fig. 4.11, which shows the evolution of M3P over 40 Myr. Strong interaction of the beam plasma with the ambient and resulting local compression is responsible for the structures visible at early times. Additionally, the strong compression within the beam at internal shocks makes them shine brightly. Later, the cocoon is mostly in pressure balance and these structures vanish. The beam, for the IC method, is

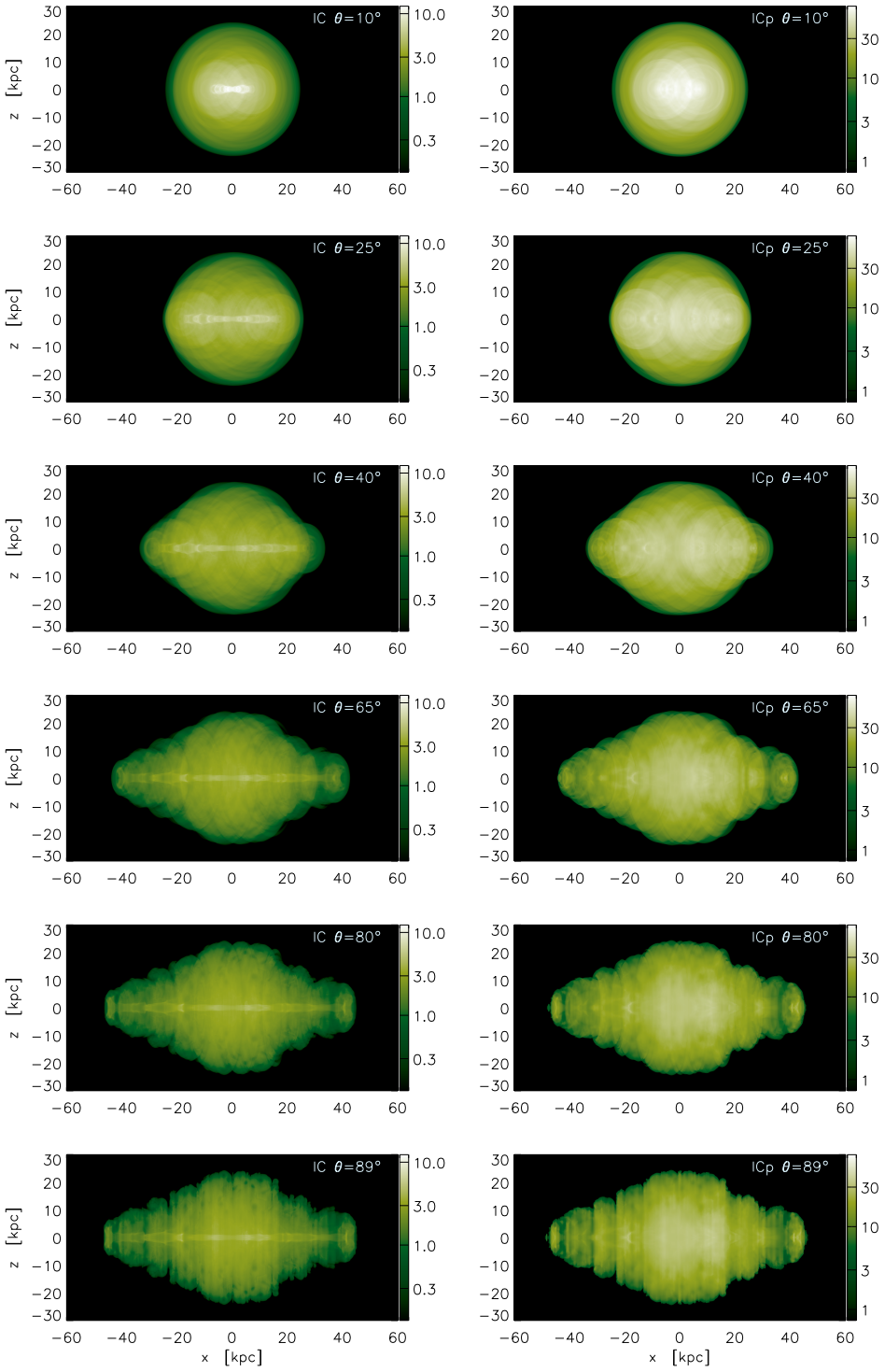

Figure 4.9: Inverse-Compton emission: different inclination angle for simulation M3P at $t = 15$ Myr, for the two different methods IC and ICp.

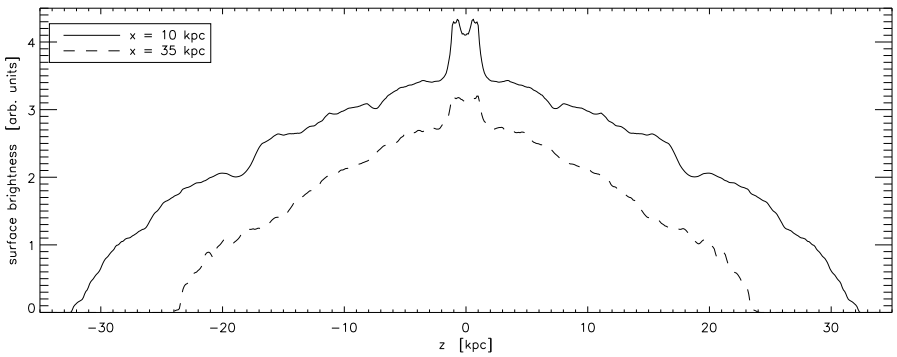

Figure 4.10: Inverse-Compton emission: slice through the cocoon of M3P perpendicular to the beam at $t = 40$ Myr with $\theta = 70°$ at two different positions (see bottom right panel of Fig. 4.11).

again clearly visible and the considerable decrease in brightness with larger distance from the core is evident. At earlier times, the beam brightness is rather uniform and more affected by the internal beam structure, such as shocks.

The dependence on the density contrast and the temporal evolution is depicted in Fig. 4.12 for the simulation data of the parameter study. The heavier jets, M1 and M2, have clearly visible hotspots at all times. For the lightest jet M4L, they are completely absent due to the unstable beam, which cannot impact strongly onto the ambient gas. This is at least partly due to axisymmetric restrictions, as argued in Sect. 3.8.2, causing the beams to be considerably less stable. These restrictions are less severe for heavier jets. However, the aspect ratios do not vary strongly. Except for the heavy jet M1 and the early phases of the light jets M3 and M4L, they are quite similar. This shows that the results of Sect. 3.3 are also true for their observable properties: in their strongly overpressured phase, light jets have wider cocoons, but cocoon aspect ratios grow when they approach pressure balance and jets cannot – by their aspect ratio – be distinguished easily from their overpressured heavy counterparts. The computed emission maps show considerable structure within the cocoon. However, this is typical for the ICp (see Fig. 4.11) maps, which rely on the cocoon pressure and hence reflect pressure perturbation, while the IC method better describes smoother jet-originated matter distribution.

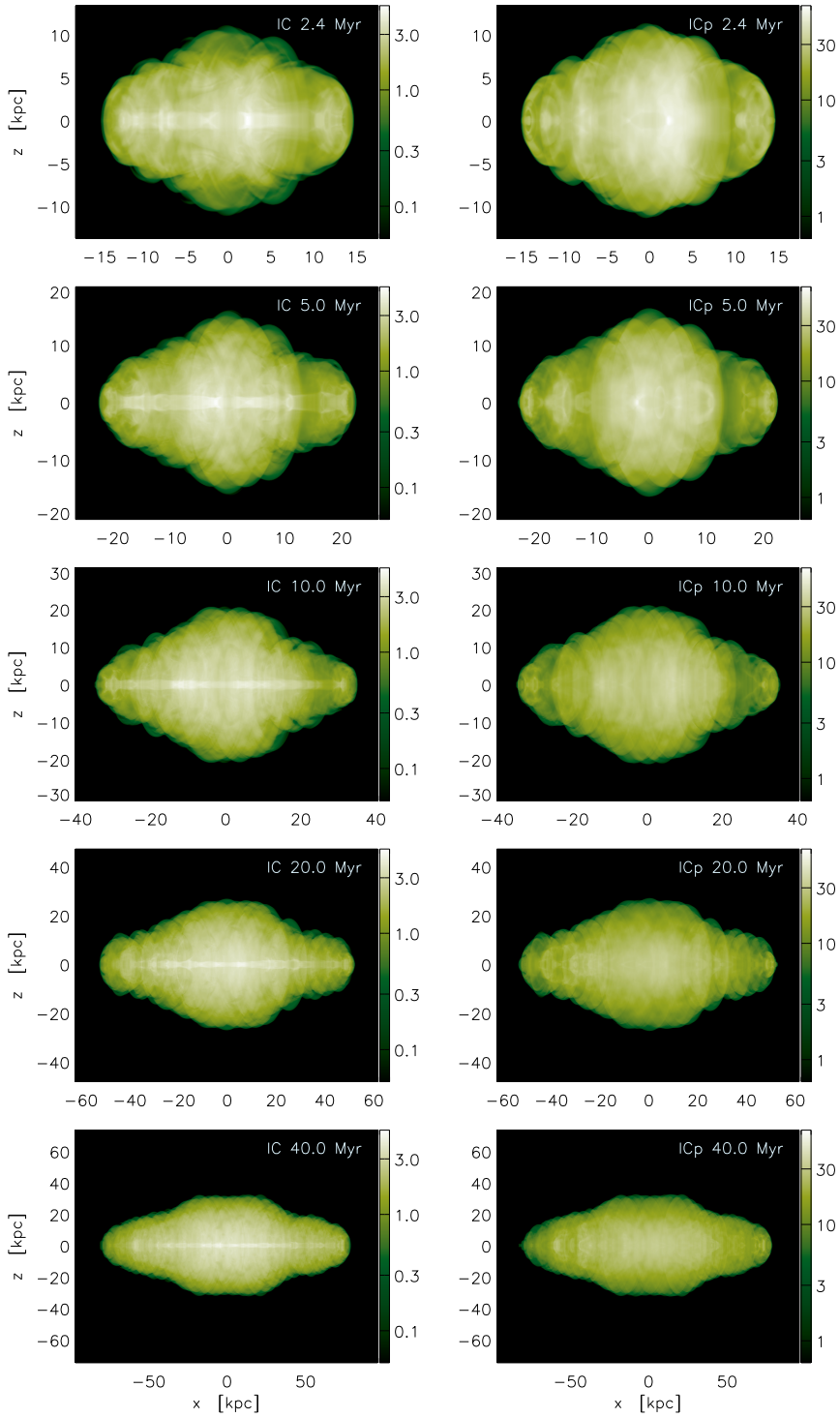

Figure 4.11: Inverse-Compton emission: evolution of simulation M3P, for the two methods IC (using the tracer value) and ICp (using the gas pressure for the density of relativistic particle).

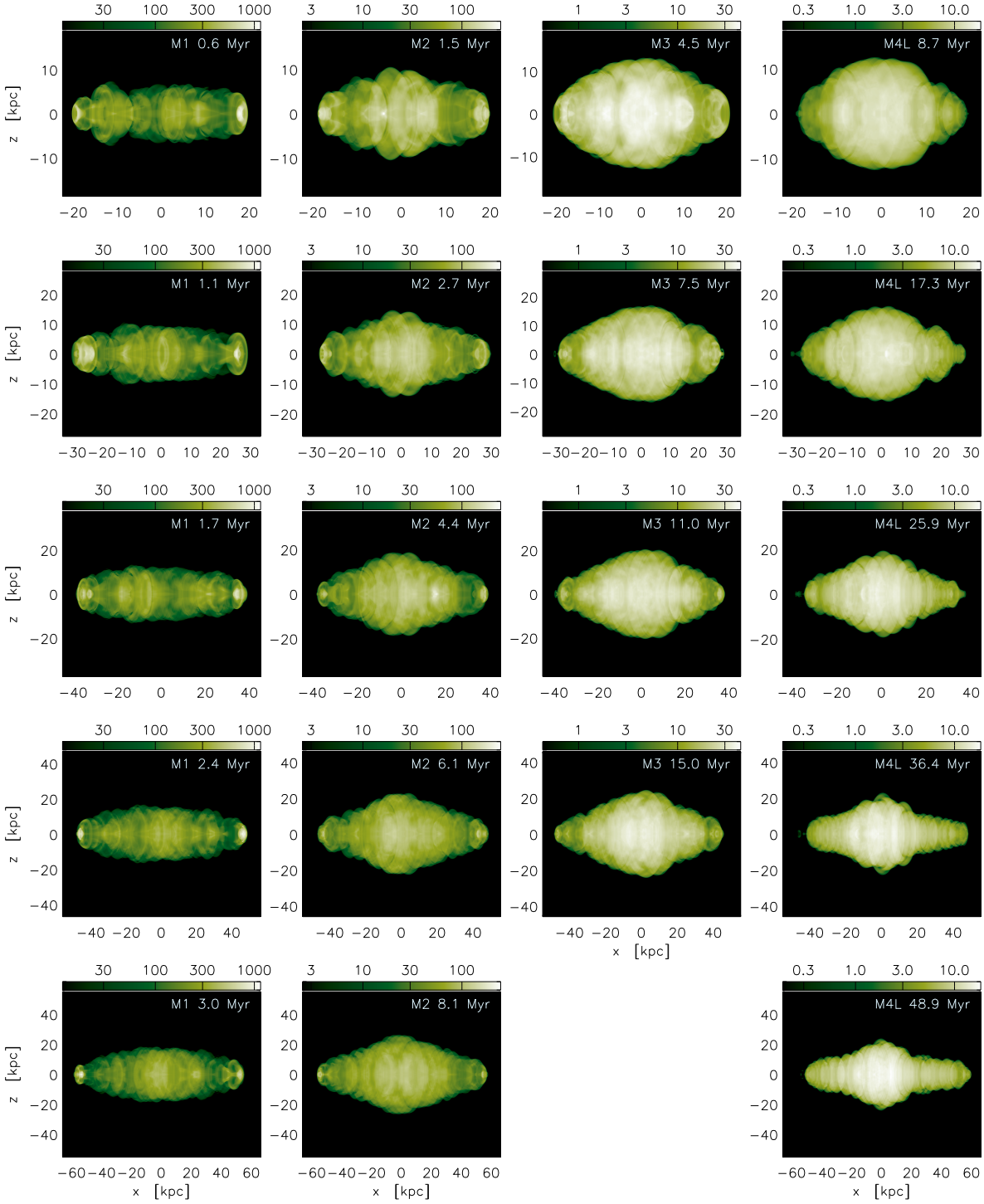

Figure 4.12: Inverse-Compton emission: evolution of the parameter study simulations M1 to M4L with the ICp method. The images are annotated with the simulation labels and the corresponding times.

4.4 Bremsstrahlung Emission Maps

In contrast to synchrotron and inverse-Compton emission, all the information needed to compute bremsstrahlung radiation (density and temperature) is directly contained in the simulations, allowing computation of realistic emission maps. This reduces limitations of the images to the limitations inherent to the simulation setup, namely axisymmetry and the constant ambient density.

4.4.1 Viewing Angle and Evolution

While synchrotron and inverse-Compton emission originate from the nonthermal particles of the jet plasma, bremsstrahlung is emitted by the ambient thermal gas. Jet activity is visible both due to "missing" ambient gas (so-called X-ray cavities) and the shocked ambient gas between the leading bow shock and the contact discontinuity. Fig. 4.13 shows this emission for the M3 and the M3P simulations at $t = 15$ Myr. Differences between the respective images are due to the slightly different setup and different evolution of the turbulent cocoon.

Already for an inclination $\theta = 25°$, two distinct cavities are visible. They are caused by the pronounced jet heads with only little entrained gas. However, they are still contained in the circular cocoon cavity and the bright shocked ambient gas forms a surrounding spherical shell. For higher inclinations, the jet head regions extend further out and form an elongated cavity. In the central region, this cavity shows less emission than seen from the background, as it is filled by very hot and rare jet plasma with much less emission at observable energies, although there is some contribution by entrained ambient gas. Differences for inclinations of $\theta = 60°$ and higher are small, as projection effects decrease. Vertical linear features within the cocoon, particularly visible for M3 at $\theta = 89°$, are caused by entrainment of ambient gas and appear artificially pronounced for inclinations near 90° in axisymmetry. At lower inclinations they have ring-like shapes.

Turning towards the shocked ambient gas with its strong X-ray emission, we see that the bow shock is elliptically shaped and only for low inclinations becomes circular. Transition between these two cases happens roughly when the cavity turns from elongated to circular, between $\theta = 40°$ and 65°. For high inclinations with extended cavities, the observed bow shock aspect ratio only slightly underestimates the true aspect ratio. Since the bow shock is strongest in axial direction due to impact of the jet beam onto the ambient gas, compression there is significantly enhanced compared to the other regions of the shocked ambient gas. This appears as a thin "cap" on the jet head and is further enhanced due to the stable head region of the MHD jets.

Evolution with time is shown for the parameter study simulations in Fig. 4.14 for the jets at comparable jet lengths, respectively. It is evident that the bow shocks become more spherical for lower jet densities. Additionally, the width of the shocked ambient gas becomes larger for the maps with density contrast $\eta \leq 10^{-3}$. Here, the bow shock expands sideways according to the blast wave approximation, while the lateral cocoon expansion slows down as it approaches pressure balance. It is clear from this that the thickness of the shocked ambient gas layer increases. For M4L, the bow shock is found at a considerable distance from the cavities since the lateral cocoon expansion stalled. At late times, the axial propagation towards the left is reduced and the "compression cap", which is visible clearly for the right jet, disappears on the

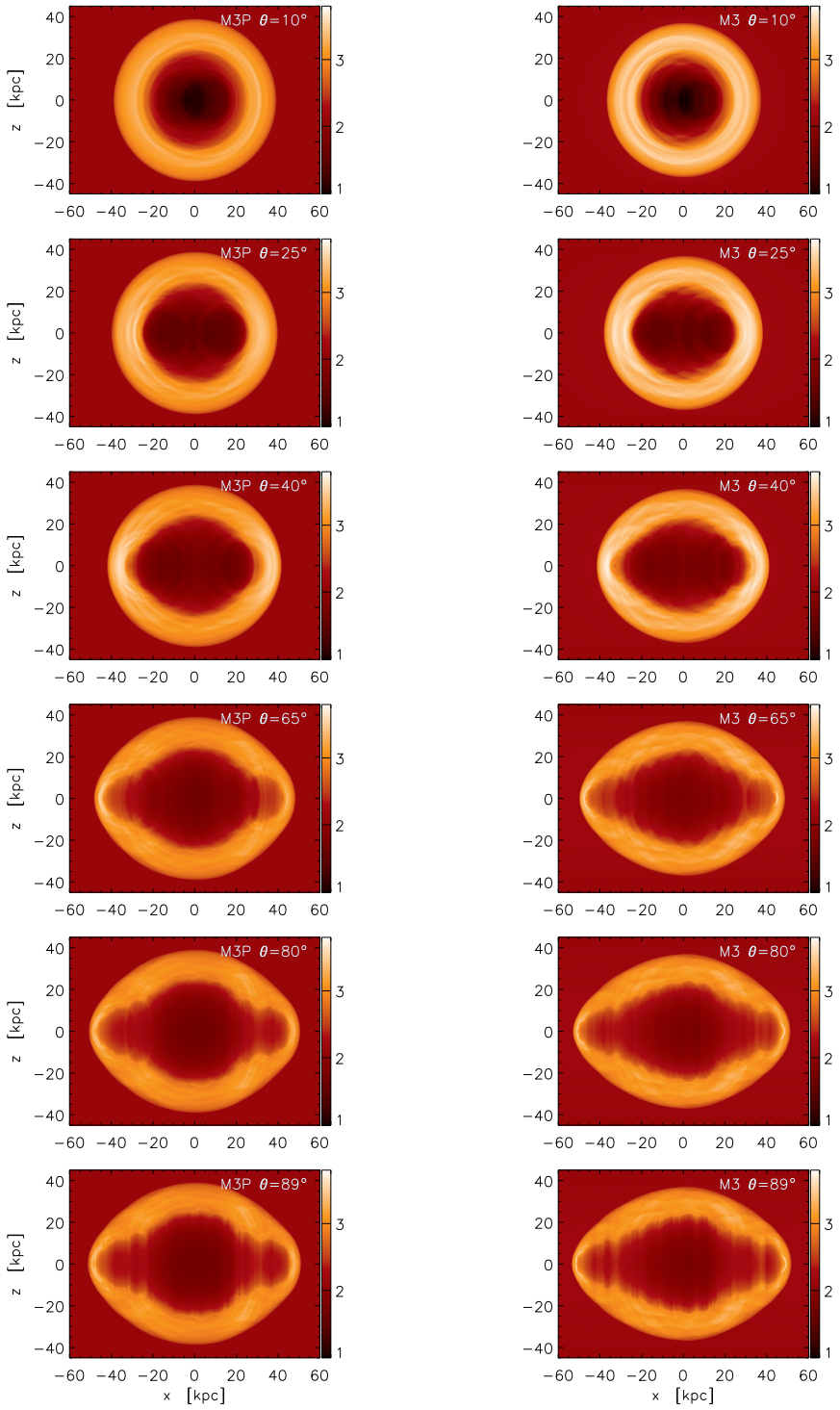

Figure 4.13: Bremsstrahlung emission: varying inclination angle for simulations M3P and M3 in energy band 1–7 keV at $t = 15$ Myr.

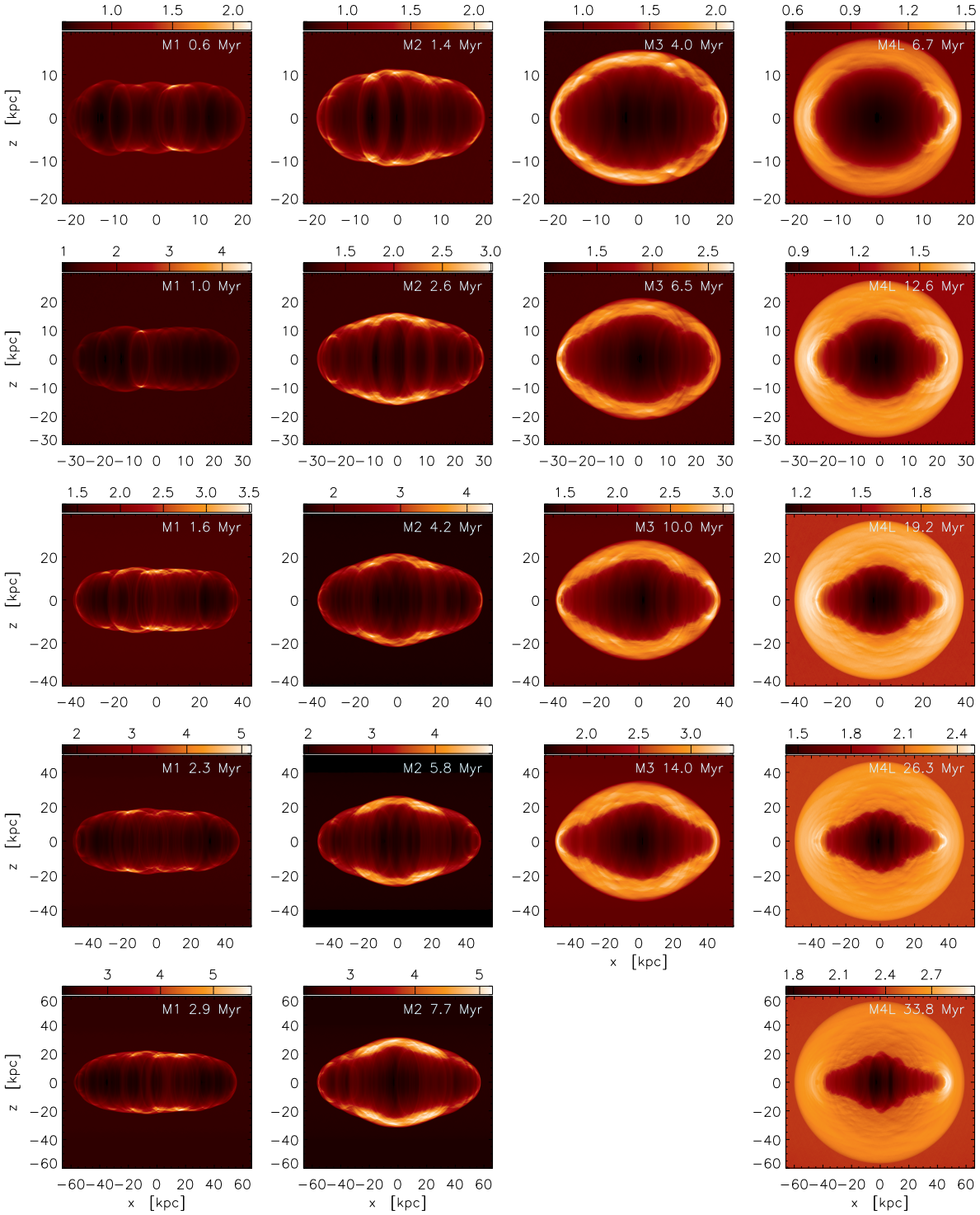

Figure 4.14: Bremsstrahlung emission: evolution of the parameter study simulations M1 to M4L in energy band 1–7 keV for an inclination angle of $\theta = 70°$. Note that the colorbar range varies.

left side. We conjecture that this is caused by the instable left jet beam and the stabilized right jet beam, which were discussed in Sect. 3.7. Apart from the jet head, the cocoon mostly is in pressure balance with the ambient gas, and the shocked ambient gas shows only slightly increased emission, bounded by a weak bow shock.

The heavier jets, M1 and M2, exhibit roughly self-similar expansion as they are still much overpressured with respect to the ambient medium. They show only a thin layer of ambient gas, which is weaker towards the jet heads. The main effect responsible for that is ambient gas near the jet head being heated to high temperatures by the bow shock (see Fig. 3.1), which then shows less emission at the chosen X-ray energy due to the $T^{-1/2}$ factor in the emissivity (4.19), which cannot be balanced by the maximum density increase by a factor of 4 (which is found from the Rankine-Hugoniot shock jump conditions). Furthermore, the contributions along the line of sight become smaller. However, part of this might be balanced by the increasing Gaunt factor (Sect. 4.1.3), which is not included in the emission maps.

4.4.2 Energy Bands

This immediately provokes the question, whether there is a strong dependence of the observed morphology on the chosen X-ray energy band. As can be seen from Fig. 4.15, the changes are rather small. Most notably, the brightness of the cavity and its rim changes. While for M1 at low energies ($0.1 - 2.0$ keV), the cocoon appears as a cavity with weaker emission than the ambient gas, this changes for higher energies ($5 - 20$ keV), where the "cavity" is brighter than the surrounding gas, letting the shocked ambient gas appear like a cocoon. This is not due to the jet plasma (which is still way too hot and too diffuse), but caused by entrained ambient gas. It has higher temperatures than the ambient gas but is still rather dense, and hence is visible at energies where the contribution of the ambient gas already disappeared due to the exponential decay for $E > k_{\mathrm{B}}T$, leading to images with stronger contrast. The same, although less clear, is found for the lighter jet M3P. We conclude that differences with energy are small, apart from the relative brightness of ambient gas and shocked ambient layer due to their respective temperatures, as well as contributions from cocoon-entrained matter.

4.4.3 Pressure Waves

Images of stronger contrast, however, make waves and ripples in the shocked ambient gas visible, as in the high-energy map of Fig. 4.15. These waves have been addressed already in Sect. 3.3.1 by considering the physical variables, whereas now we check the observable (projected) properties. Similar features are seen in deep ($\sim 10^6$ s) Chandra observations of Perseus A (Fabian et al., 2006; Sanders & Fabian, 2007), and were interpreted as isothermal sound waves generated by cyclical bubbling of the central AGN. They were made visible by unsharp-masking of the image. Fabian et al. find that the pressure residuals, after subtracting a smooth profile, are on the level of several percent of the pressure, and the ripples are seen out to 50 kpc or more. While the morphology of the Perseus A radio source cannot be described by our simulations, as in contrast to our setup this source has no currently strong jet activity (FR I source, no hotspots), there is yet an intriguing similarity between the observed waves and ripples in the observations and those in the shocked ambient gas in the simulations.

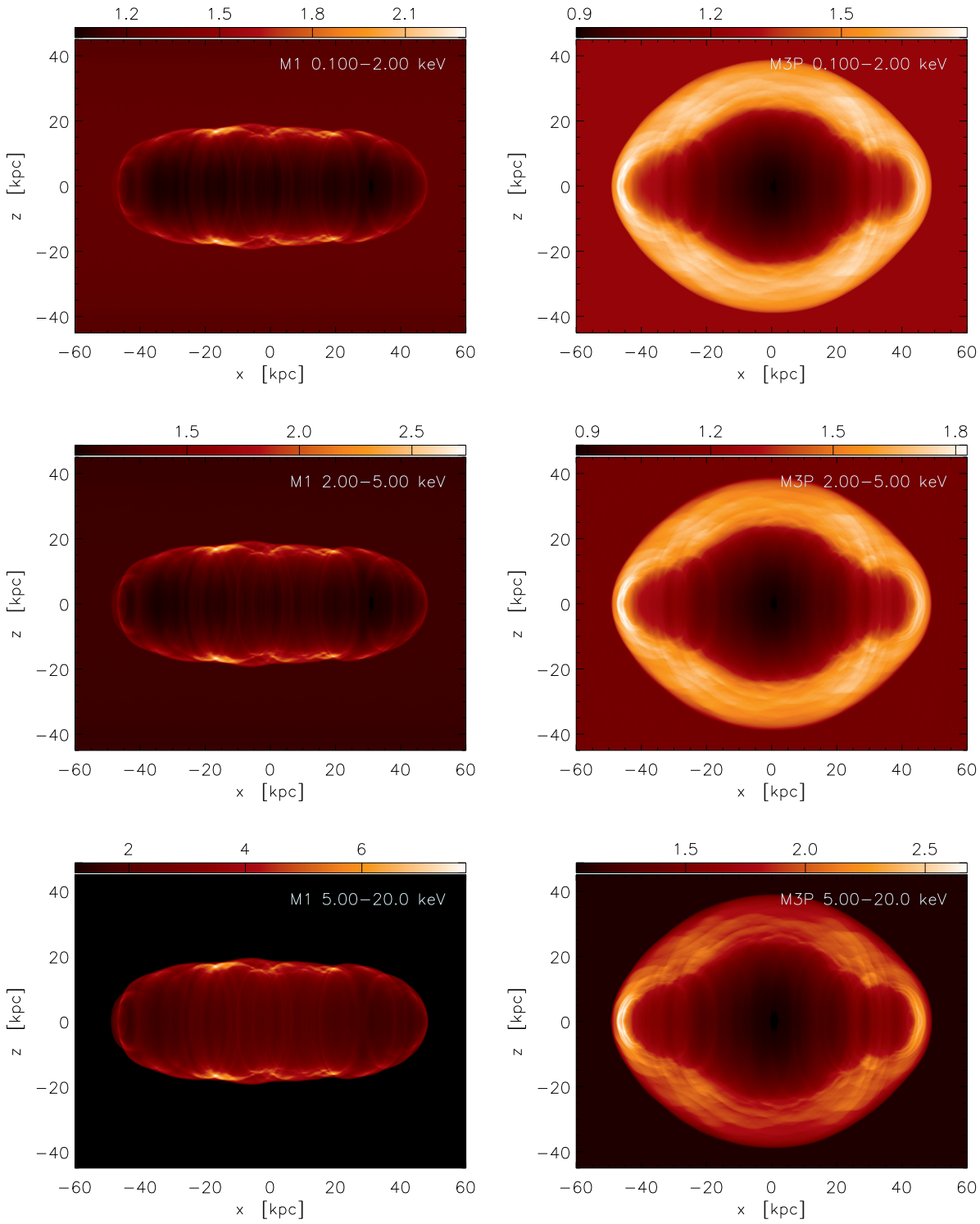

Figure 4.15: Bremsstrahlung emission: simulations M1 and M3P in different X-ray energy bands.

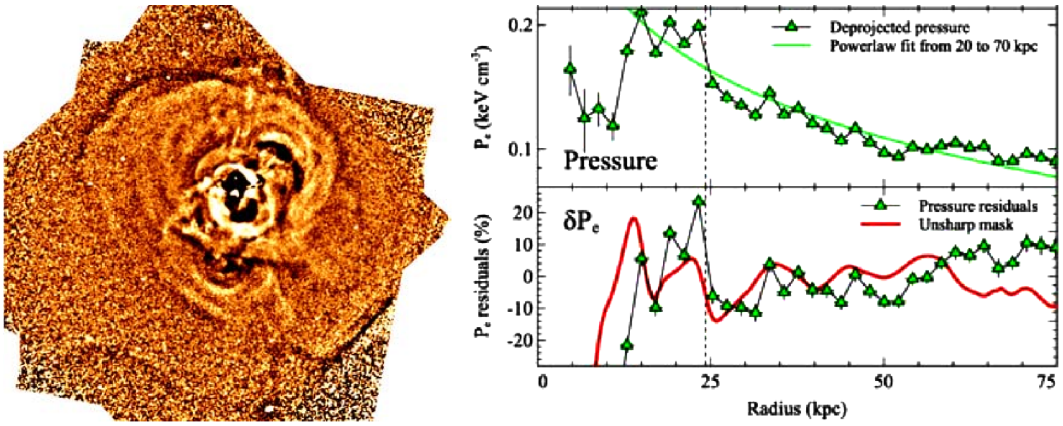

Figure 4.16: *Left:* Unsharp masked X-ray image of Perseus A, showing the waves, ripples and shocks moving outwards from the cavities (visible in black). Taken from (Fabian et al., 2006, Fig. 2). *Right:* from Fig. 2, and pressure and pressure residuals δP in NE direction (of Fig. 8) of (Fabian et al., 2006).

X-ray cavities of Perseus A clearly indicate that there has been considerable jet activity in the past. But after a break in activity, propagation of the bow shock and the shocked ambient gas will not stop suddenly but continue and fade away with time, the bow shock turning into an ordinary sound wave or "sonic boom" (Reynolds et al., 2001). Hence it seems compellent that these waves are present in the ambient gas of a dead radio galaxy for quite some time (see also Graham et al., 2008). Since they do not dissipate energy, contrary to shocks, they will not weaken besides the effects of growing wave surface during propagation. Viscous damping (Fabian et al., 2005) is expected to be only relevant on longer timescales.

Figure 4.16 shows the unsharp masked image of Fabian et al. (2006), where ripples, waves and shocks are visible all around the central source. The pressure residuals show the sound wave amplitude to be on the level of 5 to 10 %. In comparison, projected pressures for the simulations M3 and M3P as well as slices in two different directions, are shown in Fig. 4.17. The pressure variations in the shocked ambient gas due to waves are on the same level of several percent. Additionally, the region is bounded by a bow shock with a projected pressure jump of 20 to 30 %. This will eventually join the enclosed sound waves in the shocked ambient gas when the driving power ceases. However, for one activity cycle only one bow shock is expected, while sound waves in the shocked ambient gas provide numerous independent waves.

4.5 Discussion

In this chapter, we presented emission maps for three different processes – synchrotron, inverse-Compton of cosmic microwave background (IC/CMB) photons and bremsstrahlung radiation – and considered different inclination angles, source evolution as well as uncertainties originating from the chosen computational method. Although inverse-Compton emission and bremsstrahlung are both observable at X-ray frequencies, we do not combined them in an "total X-rays" image since their relative contributions depend on the density of the ambient gas, whether is is a dense cluster or only a group, and on the fraction of nonthermal elec-

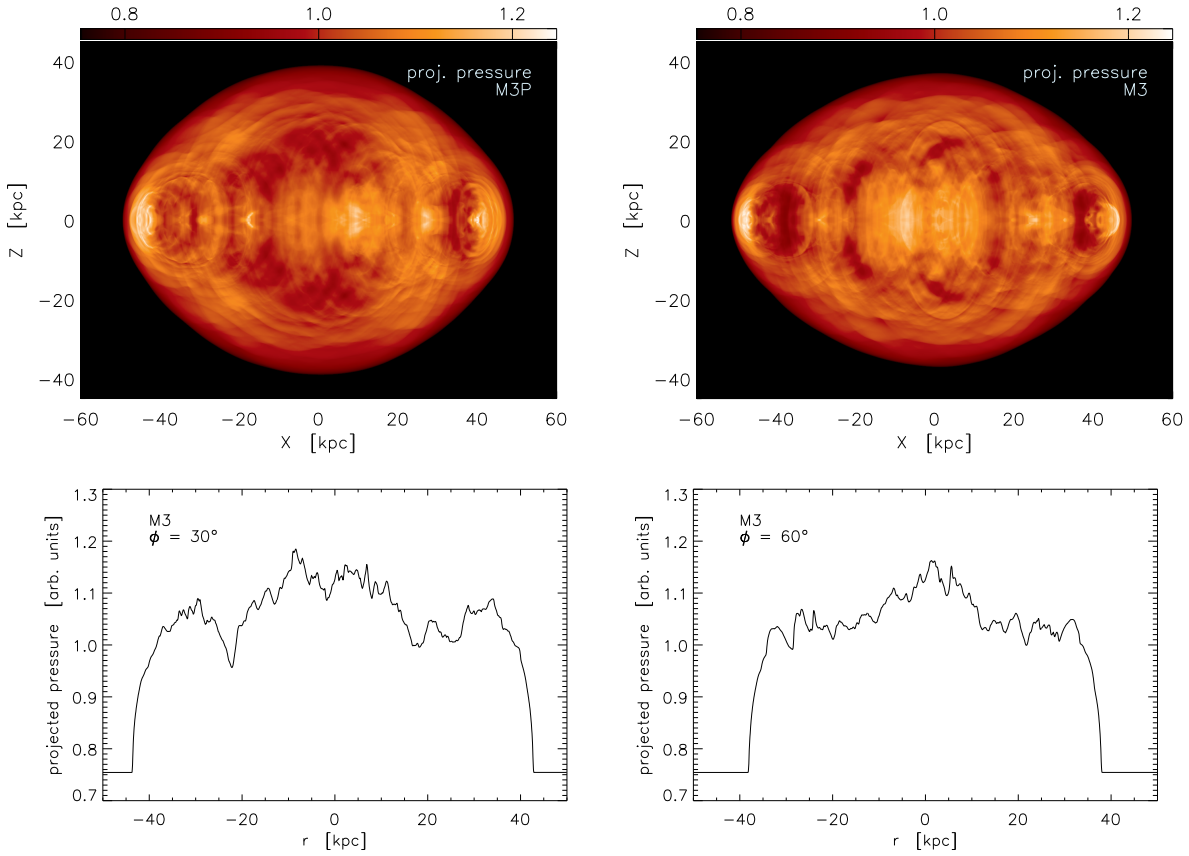

Figure 4.17: *Top:* Projected pressure maps of M3P and M3 at 15 Myr and $\theta = 70°$. *Bottom:* Slices through the projected pressure for M3 at two different angles ϕ to the horizontal x axis.

trons producing the inverse-Compton light relative to the bulk fluid. Furthermore, in observed sources one of these emission processes usually dominates.

We find that considerable differences arise from the different methods of deriving the emission-relevant variables: the magnetic field in magnitude and direction as well as the density of the emitting particles. Since the simulations only model the "bulk fluid", in contrast to the possibly different population of emitting relativistic electrons, the greatest uncertainties arise from the latter. The distribution of the emitting electrons will be largely changed by acceleration processes especially in the beams and the hotspots. It is known from observations that the radio spectral index, which is directly related to the electron power law index, varies within the source and shows a flatter spectrum in regions of suspected reacceleration. Additionally these electrons cool by their emission and the spectrum steepens as they migrate to lower energies. While naturally synchrotron emission and IC/CMB contribute to this cooling, it is conjectured that also inverse-Compton scattering of starlight photons (Kataoka & Stawarz, 2005) may cool down the electrons considerably. All these processes cannot be included within our single-fluid MHD model and the corresponding effects are hence absent in the emission maps. However, since the cooling is small compared to the bulk fluid internal energy, the dynamics of the sim-

ulation is not affected by this. Using the thermal pressure rather than the "tracer density" to describe the density of the nonthermal particles, some reacceleration can be mimicked, but we consider this approach less strict and rather phenomenological in the sense that we would get what we want to get. Only direct modelling of the nonthermal particles (as Tregillis et al., 2001, 2004) in combination with the large-scale evolution of very light jets is expected to result in significant improvement.

Turning towards the available quantities in our simulations, we find that the emission methods including the magnetic fields yield significantly different results. While emission maps derived from the hydrodynamical simulations give a first impression of the projected morphology and the sites of possible reacceleration, most of the features seen there are different from what is seen in MHD emission models and indicate that all these synchrotron maps have to be interpreted with great care. For example, the hydrodynamic emission models would predict that beams are, apart from emission by internal shocks, invisible within the cocoons.

Clearly there are also limitations in the fluid modelling, in addition to the emission processes. They become most evident for the question of hotspot visibility - both for synchrotron and inverse-Compton radiation. In axisymmetry, beams of very light (underdense) jets are more easily destabilized than in full 3D, since the cocoon vortices and relatively dense entrained ambient matter always pinch or disrupt the beam as they cannot be deflected or miss it. Hence, the larger the beam is, the more this artificial destabilization is effective and the less probable is an intact beam which can impact onto the ambient gas and produce a hotspot region. Furthermore, entrainment of cocoon matter in the beam and expansion of the beam due to additional thermalization weaken the beam gradually. However, while this sounds troublesome, it is not critical for the global evolution and the interaction with the ambient gas, where the beam details are mostly lost anyway ("dissipated") at the jet terminus and the simulation hence provides a reasonable description.

The "hotspots" in our emission maps are weak and highly variable in position and shape – from knotty appearance to an annular structure. Similar ring structures were seen in the simulations of Saxton et al. (2002b,a), although with purely hydrodynamical simulations. In our MHD case, the magnetic field configuration shows the annulus as two halves if the field direction is taken into account, since it is mostly toroidal there. For inclinations near 90°, these halves may appear as bar-like structures. Yet we caution that the strong hotspot variability is mostly due to artificially increased beam destabilization.

Due to wide lobes, the hotspots are generally recessed with respect to the outer lobe border and only inclination angles $\gtrsim 60°$ bring them further out. Mullin et al. (2008) examined whether median lobe lengths of narrow line (NLRG) compared to broad line radio galaxies (BLRG) as well as quasars are consistent with a unified model. While they find that the agreement is not significant, this may well be the case for a slightly improved "cocoon-aware" projection. For a radio source of true length l and width w they assume a projected relative length of $l'/l = \sin\theta$. However, if we account for the lobe width additionally, e.g. by modelling the cocoon as a cylinder with two hemispherical caps attached, we find

$$l'/l = \sin\theta + (w/l)\,(1 - \sin\theta)\,. \tag{4.40}$$

For a median ratio $w/l \approx 0.2$ and considering a wide distribution in inclination θ, the correction to the projected relative length will be ~ 0.1 larger than without considering the lobe

width. Hence, the median length ratios between quasars/BLRG and NLRG (their equation 6) will much better fit the observations (observed: 0.7, their prediction: 0.57, with lobe width correction: ≈ 0.67) and may become significant, confirming the unified model. While this is only a simple geometric example, it shows that it is important to consider also effects of the cocoon width for the interpretation of observations. Another example is the case of Pictor A, which is a BLRG and is expected therefore to be observed at a small inclination angle of $\theta \lesssim 45°$ by Hardcastle & Croston (2005). Here it is unclear in the light of typical lobe widths, why the hotspot is located far out at the lobe border, in contrast to the results of the emission maps. A narrowing cocoon might explain this, though the consequences of this would have to be examined more carefully, or Pictor A actually lies nearly in the plane of the sky, as argued by Saxton et al. (2002b).

The synchrotron morphology of the lobes is rather smooth and the emission fills the whole cocoon. While a cooling electron population will make only parts of the cocoon visible at higher frequencies, low-frequency radio observations (e.g. Cygnus A in Lazio et al., 2006, at 327 MHz) allow determination of the full cocoon shape at least for some sources. Future observations, e.g. with LOFAR or the SKA will allow observation of the central cocoon regions also for more distant and smaller sources, since the resolution at low frequencies is considerably improved.

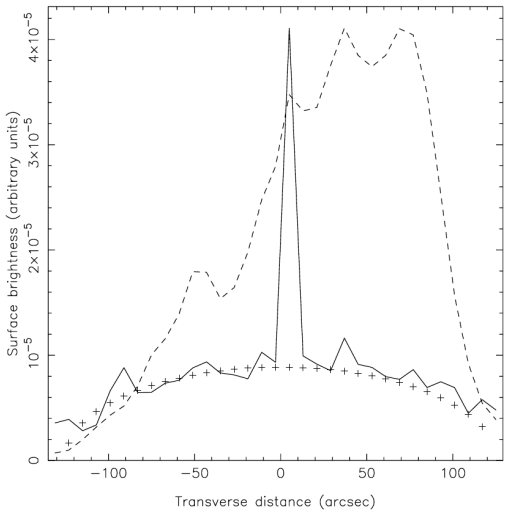

Figure 4.18: Surface brightness profile across the western lobe of Pictor A (solid line). It is extracted from a 45 arcsec wide region perpendicular to the beam at about half beam length and is binned in 8-arcsec bins. The central peak corresponds to the beam. Dashed line: radio emission at 1.5 GHz (7.5 arcsec resolution). The crosses show expected emission from a cylinder with uniform emissivity to guide the eye. Figure taken from Hardcastle & Croston (2005).

Supplementary to low-frequency radio observations, inverse-Compton emission in the X-rays already provides access to the low-energy particle population in the cocoon. Although effects of a varying magnetic field in the cocoon do not contribute here, we find similar results as in the low-frequency sychrotron maps. When the source has evolved for a long-enough time to forget about the perturbations due to the initial conditions, a smooth cocoon is visible, arising from a quite uniform distribution of the cocoon plasma. This is also seen in observations of

Pictor A by Hardcastle & Croston (2005), who find only little variation in X-ray brightness in a slice through the cocoon (Fig. 4.18), very similar to the corresponding slice in the simulated emission (Fig. 4.10).

The beam is visible brightly both in the observation as well as the emission map. We expect qualitative differences due to relativistic effects in the observations and the beam destabilization and expansion in the simulation. However, brightness variations at internal shocks in the beam are less pronounced since only compression of relativistic particles contributes but not additionally the compression of the magnetic field. Similarly to the synchrotron results, we find the lack of hotspots in the IC/CMB maps. However, for the heavy jets of the parameter study we find bright hotspots, since the higher jet densities make the beam less susceptible to the axisymmetry-caused destabilization.

Contrary to the previous emission processes, bremsstrahlung emissivity depends on the properties of the modelled thermal plasma with uncertainties arising only from the model setup and restrictions. Observations of cluster radio sources in the X-rays are now available for almost three dozen objects in clusters (McNamara & Nulsen, 2007). They exhibit cavities in the ambient gas as well as bow shocks surrounding them with low excentricities and low Mach numbers between 1 and 2 (cf. Fig. 1.7). While the presented simulations do not include a cluster density profile but a uniform ambient density and thus quantitative deviations are expected, we clearly find these cavities in our emission maps as well as thick layers of shocked ambient gas surrounded by a weak bow shock. More detailed studies have been conducted by Zanni et al. (2003) and Krause (2005), also including a realistic cluster environment. We conclude that very light jets naturally produce these kinds of cavities and that bow shock properties as aspect ratio, shock strength or size provide robust diagnostic tools for the radio source activity and the density contrast as discussed in Sect. 3.8.2. The stabilized jet heads we find in MHD simulations furthermore tend to show enhanced X-ray emission just in front of the head regions if the jet thrust is additionally supported by increased stability or the Lorentz force.

We newly find pressure waves within the shocked ambient gas which are excited by vortices and pressure waves in the cocoon. Quasispherical waves like those were found in Perseus A (Fabian et al., 2003, 2006) and have similar morphological properties and amplitude in projection. While they have been considered as being excited by varying source power, intermittent activity or natural oscillations of the perturbed radio cocoon (Shabala & Alexander, 2007), we attribute them to dynamical processes in the jet head like vortex shedding and conjecture that they provide a link to jet head dynamics and by their wavelength may be related with a typical vortex shedding frequency, which would be unobservable due to the long corresponding period. For this, however, jet head dynamics has to be simulated in more detail and without the axisymmetric restrictions.

5 Emission-Line Gas in High-Redshift Radio Galaxies

In this chapter, we describe results of ongoing research in collaboration with Martin Krause (MPE Garching) and Nicole Nesvadba (GEPI, Observatoire de Paris, Meudon) about the luminous ionized gas nebulae in radio galaxies at high redshift. We briefly introduce these sources and the "alignment effect", as well as new observations of four sources by integral-field spectroscopy and then two models about the origin and location of the emission-line gas, which are considered subsequently. The main part is to analyze our simulation data with respect to the kinematic properties of the observed gas, and discuss implications for the two models.

5.1 Ionized Gas Nebulae and Alignment Effect

Radio galaxies are observed up to high redshifts of $z \approx 5.2$ (van Breugel et al., 1999). The comoving space density of the high-power population rises by a factor of almost 1000 between redshift $z \sim 0$ and $z \sim 2$, but high-redshift radio galaxies still are rare objects. They are believed to be massive forming galaxies in the centers of proto-clusters and the progenitors of today's most massive elliptical galaxies. This is supported by their locations in overdensities, their large near-infrared luminosities, their ample star formation and their clumpy UV continuum morphologies (Miley & De Breuck, 2008). The galaxies not only have large stellar masses (up to $\sim 10^{12}\,M_\odot$), but also large amounts of hot gas (up to $10^{12}\,M_\odot$ with $\sim 10^{7.5}$ K) and molecular gas (up to $10^{11}\,M_\odot$). They often show luminous ($\sim 10^{44}$ erg s^{-1}) emission line regions with a huge extent (sometimes more than 100 kpc) and are aligned with the radio source for $z \gtrsim 0.6$ ("alignment effect"). The gas nebulae consist of an outer quiescent component (usually outside the radio structures) and an inner component with strongly distorted kinematics and clumpy and irregular structure (Villar-Martín, 2007). The alignment of the ionized gas with the radio source as well as the large velocities involved (FWHM often exceeding 1000 km s^{-1}) indicate vigorous interaction with the jet; however in some objects, illumination by the active galactic nucleus has considerable impact. In the local universe, similar interaction between the jet and the ambient gas is observed. Morganti et al. (2005) and Morganti (2008) report on large outflows of neutral hydrogen gas with velocities of ~ 1000 km s^{-1} in local radio galaxies seen by blue-shifted HI absorption lines.

Nesvadba et al. (2008) observed three high-redshift radio galaxies with the integral-field spectrograph SINFONI on the VLT, which allows to study the (rest-frame optical) spectra of the emission-line gas across their full two-dimensional surface. Fig. 5.1 shows the morphologies and kinematics of the ionized nebulae associated with the three radio galaxies MRC0316-257 ($z \approx 3.13$), MRC0406-244 ($z \approx 2.44$) and TXS0828+193 ($z \approx 2.57$). The spatial extent of the nebulae is 20 to 30 kpc in length and ≈ 10 kpc in width. The velocity fields are remarkably similar, showing two regions ("bubbles") with quite homogeneous projected velocities with an

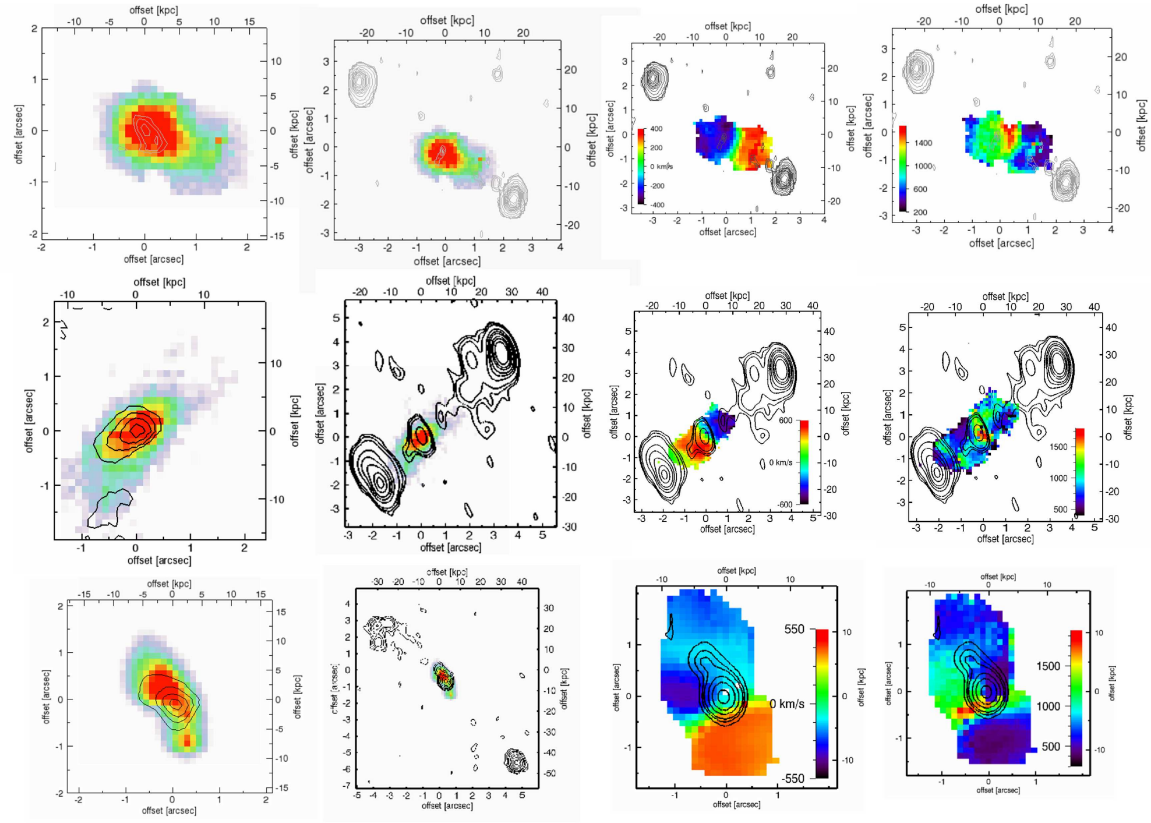

Figure 5.1: Morphologies and kinematic properties of MRC0316-257 (*top row*), MRC0406-244 (*middle row*), and TXS0828+193 (*bottom row*). *Left to right*: [OIII]λ5007 emission line morphologies with K-band continuum contours. [OIII]λ5007 emission line morphologies with 1.4 GHz radio contours. Velocity maps, colors show relative velocities in km s^{-1}, with 1.4 GHz radio contours. Maps of the line widths, colors show the FWHM in km s^{-1}, with 1.4 GHz radio contours. Figure adopted from Nesvadba et al. (2008).

abrupt transition near the radio core and relative velocities of $\sim$ 700 to 1000 km s^{-1} between the two regions. The line widths generally are in the range 500 to 1200 km s^{-1}, which exceeds the velocity gradients within the regions (apparent peaks in the central regions are probably artefacts and due to overlap of emission from the two regions). Hence this shows a large turbulent motion compared to the systematic velocities within the two bubbles. Whether the systematic velocities correspond to inflow or outflow is addressed by analysis of the radio data. In each of the sources, the northern lobe is more strongly polarized and has a somewhat flatter spectral index, which is interpreted as the northern lobes being the approaching lobes, respectively (Laing-Garrington effect and effects of Doppler boosting on the near side). Hence, the blue-shifted line-emission is associated with the near side, as would be expected for the case of a net outflow relative to the central galaxy.

Nesvadba et al. derive extinctions of $\sim$ 2 mag in the outer regions and $\sim$ 4 mag near the center for the Hβ wavelength and electron temperatures $\approx 10^4$ K from [OIII] line ratios.

Ionized gas masses $\sim 10^{10.6}\,M_\odot$ are found from measured electron densities ~ 500 cm^{-3} and luminosities $\sim 10^{45}$ erg s^{-1}. The authors speculate that the large ionized gas masses may have been heated from the cold molecular component, since ionized gas masses are larger and molecular gas masses smaller than expected for galaxies with stellar masses as large as has to be assumed for high-redshift radio galaxies. Furthermore they argue that both merging and disk rotation insufficiently explain the gas dynamics, while alignment, size, timescales and energy-injection rates support the radio source to be the driver if $\sim 10\,\%$ of the kinetic jet power is transferred to the kinetic energy of the gas.

5.2 Models of the Emission-Line Gas Location and Origin

To explain the morphology and kinematics of the emission-line gas, we consider two models. In the first model, hereafter referred to as "SAG model", the line emission originates from clouds embedded into the shocked ambient gas. This model is similar to the model proposed by Meisenheimer & Hippelein (1992), although those authors assume that the ambient gas clouds are compressed and heated by the bow shock passing over them and only radiate with some lag (corresponding to the cooling time scale). We assume a simpler model, where emitting clouds of indefinite origin (but possibly excited by the bow shock) are pushed outwards by drag forces from the outward-moving shocked ambient gas. Clearly the cloud velocities will depend on the efficiency of momentum transfer and cloud properties as mass and size, since they are embedded in the ambient gas with a filling factor significantly less than unity. For perfect coupling, the emitting clouds will be dragged along with the shocked ambient gas with identical velocity and hence can be determined directly from the shocked ambient gas kinematics. For weaker coupling the speeds completely depend on the cloud properties and the interaction time scale. Hence, for most kinds of clouds, those will either be dragged along with the shocked ambient gas, or remain approximately at their initial position with only small changes in velocity.

In the second model, the emitting clouds are located in the jet cocoon (hereafter referred to as "COC model"). This was recently proposed by Krause & Alexander (2007) based on 2D hydrodynamical simulations of multi-phase turbulence in the jet cocoon with optically thin cooling. The simulations started with a Kelvin-Helmholtz instability setup at the cocoon–ambient interface with a density contrast of 10^4 between the cocoon plasma and the ambient medium as well as dense clouds embedded in the ambient medium. The dense clouds were disrupted but the fragments remained cold and spread throughout the domain by the developing turbulence. This generated a multi-phase medium with a peak in the temperature distribution at $\sim 14\,000$ K, where shock heating and increased cooling counteract and produce the line-emitting phase responsible for the observed emission-line nebulae. Krause (2008) extended this to three dimensions and found a correlation between the emission luminosity and the kinetic energy of the cocoon plasma, with 10^{12} erg of kinetic energy in the cocoon corresponding to ~ 1 erg s^{-1} in line emission.

5.3 Results for the Shocked Ambient Gas Model

We use the simulation run M3 at a time $t = 15$ Myr to derive, which kinematic properties are expected for emission-line clouds located in the shocked ambient gas. We first reconsider the

drag forces on the emitting clouds embedded in the ambient gas. Assuming spherical clouds with mass M and density ρ_{cloud}, the acceleration by drag forces from the ambient gas of density ρ_{a} and velocity v_{a} can be approximated by

$$a = C\,\rho_{\mathrm{a}} v_{\mathrm{a}}^2\,M^{-1/3}\,\rho_{\mathrm{cloud}}^{-2/3} \tag{5.1}$$

where C is a constant depending on the shape of the cloud and of order 0.1. The corresponding "acceleration time scale" is

$$t_{\mathrm{acc}} \equiv \frac{v_{\mathrm{a}}}{a} \tag{5.2}$$

$$= 3 \times 10^6\,\frac{\left(\frac{M}{10^{-4}\,M_\odot}\right)^{1/3}\,\left(\frac{\rho_{\mathrm{cloud}}}{100\,m_{\mathrm{p}}\,\mathrm{cm}^{-3}}\right)^{2/3}}{\left(\frac{C}{0.1}\right)\,\left(\frac{\rho_{\mathrm{a}}}{0.01\,m_{\mathrm{p}}\,\mathrm{cm}^{-3}}\right)\,\left(\frac{v_{\mathrm{a}}}{1000\,\mathrm{km\,s}^{-1}}\right)}\,\mathrm{yr}\,. \tag{5.3}$$

Van Ojik et al. (1997) find a typical cloud mass of $10^{-4}\,M_\odot$ and cloud radius of 0.03 pc to be a reasonable description. Clouds with these properties are indeed expected to be dragged along with the shocked ambient gas within a time span corresponding to typical source ages. For clouds with significantly longer acceleration time scales, the velocities derived in the following would correspond to upper limits.

These considerations in mind, we analyze the projected radial velocities of the shocked ambient gas in the plane through the jet beam and the observer. Fig. 5.3 shows a density map of the data frame together with the borders of the 16 equidistant radial slices for an observer with inclination angle $\theta = 70°$. The slices are 6.25 kpc wide, roughly corresponding to the resolution of the observations. The cells within these slices are used to create histograms of the radial velocity (along the observer's line of sight). These histograms, in arbitrary units, are shown for some slices in Fig. 5.4. It shows an approaching and receding component for each slice, corresponding to the near and far side of the shocked ambient gas parts. These features typically have widths (FWHM) of 100 to 200 km s^{-1} and originate from varying velocities in the shocked ambient gas associated with the pressure waves there (for comparison: the sound

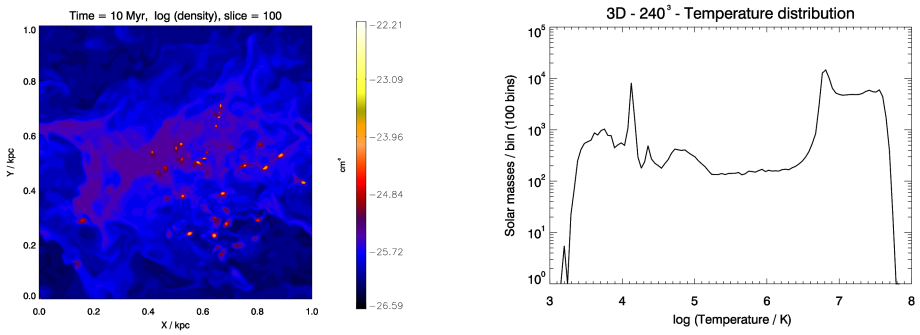

Figure 5.2: *Left:* Density slice through a simulation of multi-phase turbulence after 10 Myr. Embedded into the hot plasma are clouds of cooler gas, which become visible due to their line emission. *Right:* Corresponding temperature histogramm showing the different gas phases. Figure adopted from Krause (2008).

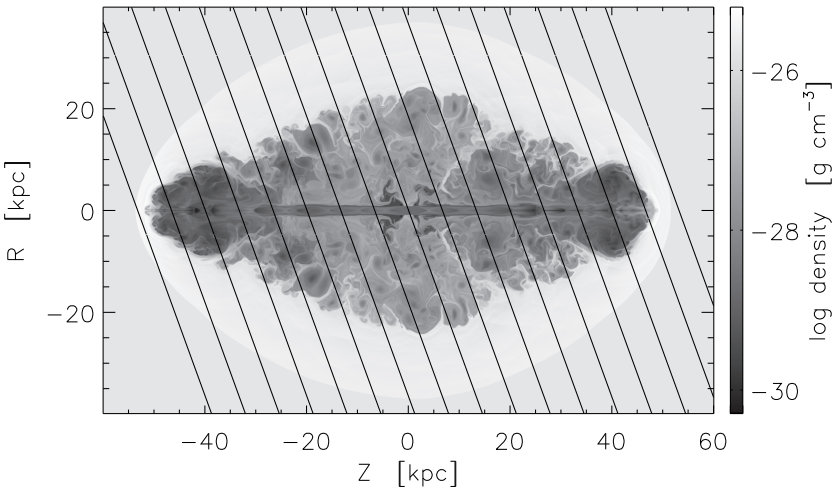

Figure 5.3: Slices used for the spatial resolution of the jet system. The projection uses an inclination of $\theta = 70°$ and 16 slices in the plane through the jet beam, viewed from an observer located in the lower half of the plot. The background image is a logarithmic density map of the exemplary simulation (M3, $t = 15$ Myr).

speed in the shocked ambient gas is ~ 1400 km s^{-1}). Since the shapes of the features depend on the pressure waves in the shocked ambient gas, it is clear that they vary significantly. However, their widths are small with respect to their offsets. If the line-emitting clouds were distributed uniformly within the shocked ambient medium, the histograms would correspond to the line profiles caused by Doppler shifting.

The position–velocity diagram in Fig. 5.5 shows the histograms for all slices with the counts corresponding to greyscale values in arbitrary (resolution-dependent) units. It shows two inclined and slightly curved bands with a systematic trend towards smaller (more negative) values on the side of the approaching jet, which is simply a projection effect as only the radial component of the gas motion is seen: the position of these "maximum velocity locations" is shifted towards the approaching (receding) jet head for the negative (positive) radial velocities, dependent on the inclination angle θ. For elliptically-shaped shocked ambient gas shells, an estimate for the core offset is, measured as fraction of the projection-independent semi-minor axis of the shocked ambient gas spheroid,

$$d = \pm \frac{\sin(\phi - \theta)}{\sqrt{1 - (1 - \mathcal{R}^{-2}) \cos^2 \phi}} \tag{5.4}$$

with $\phi = \arctan\left(\mathcal{R}^{-2} \tan\theta\right)$ and $\mathcal{R} = a/b$ (ratio of the proper semi-major and semi-minor axes of the spheroid). The function $d(\theta)$ is shown in Fig. 5.6. In our exemplary case with $\theta = 70°$, $\mathcal{R} = 1.4$ and $b \approx 30$ kpc, the positions of maximum velocity are expected at offsets of ± 10 kpc, in agreement with the location in Fig. 5.5.

The maximum value of the radial velocity corresponds to the (unprojected) outward velocity of the shocked ambient gas, which is related with the bow shock expansion speed (3.1) by the Rankine–Hugoniot shock jump conditions. Note that we measure the post-shock velocity,

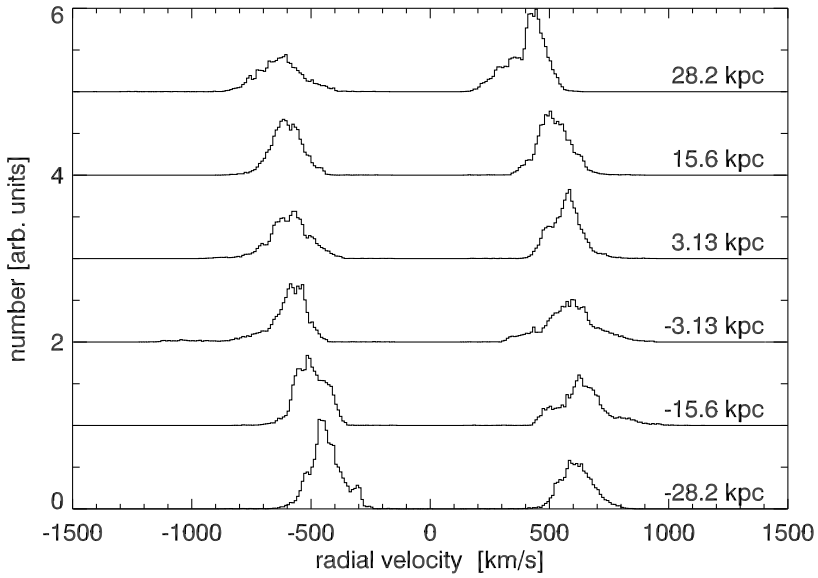

Figure 5.4: SAG model: Velocity distributions for the shocked ambient gas in some slices of M3 at 15 Myr. For clarity, they are shifted by 1, respectively. Inclination angle $\theta = 70°$, bin contributions ("counts") are in arbitrary units, 10 km s^{-1} bin size. The slices are labelled by their spatial offsets from core, increasing in the direction of the Z-axis. Due to projection of the shocked ambient gas velocity, the peaks shift with position.

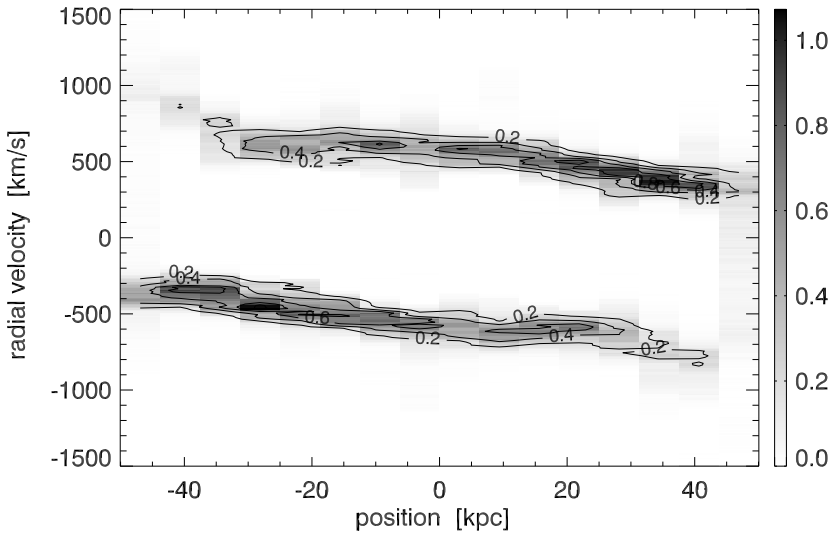

Figure 5.5: SAG model: Position–velocity diagram for M3 at 15 Myr. The greyscale corresponds to the histogram counts (in arbitrary units). For clarity, contours are overlaid. The inclination angle is $\theta = 70°$, velocity bin size 10 km s^{-1}. The position is measured as offset from core in plane of the sky.

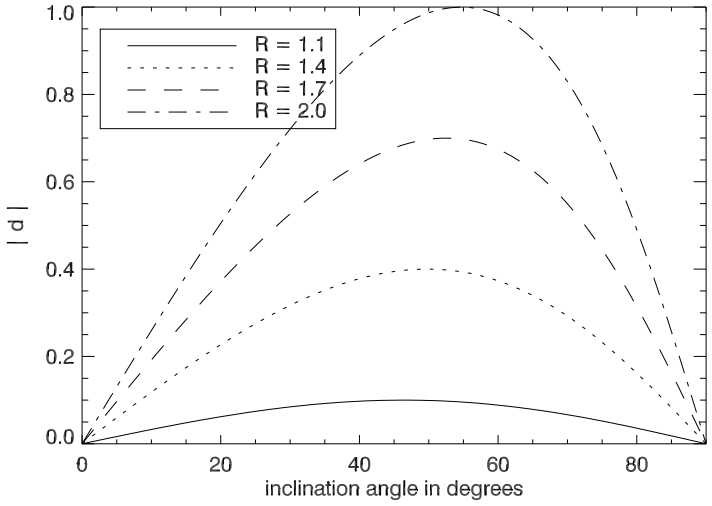

Figure 5.6: SAG model: $d(\theta)$ gives the "maximum velocity locations" in fractions of the SAG semi-minor axis as function of the inclination angle θ (Eqn. 5.4).

which for small Mach numbers can be smaller than the ambient sound speed. For the case of Fig. 5.5, where the bow shock is about Mach 1.5, the ambient gas outward velocity is ~ 0.6 times the ambient sound speed, corresponding to ~ 700 km s^{-1}, which is in good agreement with the maximum absolute value of the radial velocity.

At different evolutionary stages of the source, this radial velocity clearly will be different. Hence, in Fig. 5.7, we show velocity histograms of a slice through the core at 15 different times for an inclination $\theta = 90°$, however only for the cells on one side of the core (the far side, but the near side is identical with opposite sign). At early times, a very broad component starts at high velocities, caused by a rapidly propagating bow shock. Later, the feature becomes narrower and moves towards lower velocities (it also becomes stronger since the cell numbers along the line of sight increase). This is a consequence of a decelerating bow shock and slower shocked ambient gas motion. For heavier jets with high bow shock Mach numbers (M1 and M2), the radial velocities generally are higher, while they are lower for lighter jets (M4L).

We conclude that the observed distribution of velocities can be understood by considering the contributions of the source evolution (decelerating bow shock), the perturbations within the shocked gas (responsible for the feature width) and projection effects.

5.4 Results for Cocoon Model

While the kinematic properties of the emission-line gas could be directly derived from the simulation data for the SAG model by assuming coupled velocities, this differs for the COC model: the cooler ($\sim 10^4$ K) phase is only modelled by the multi-phase turbulence simulation, which has a much finer spatial grid. It is not possible to include this in the large-scale simulation, since the achievable resolutions are too coarse and time steps too large. Thus our approach is to combine both simulations for the analysis. The systematic velocities and available kinetic

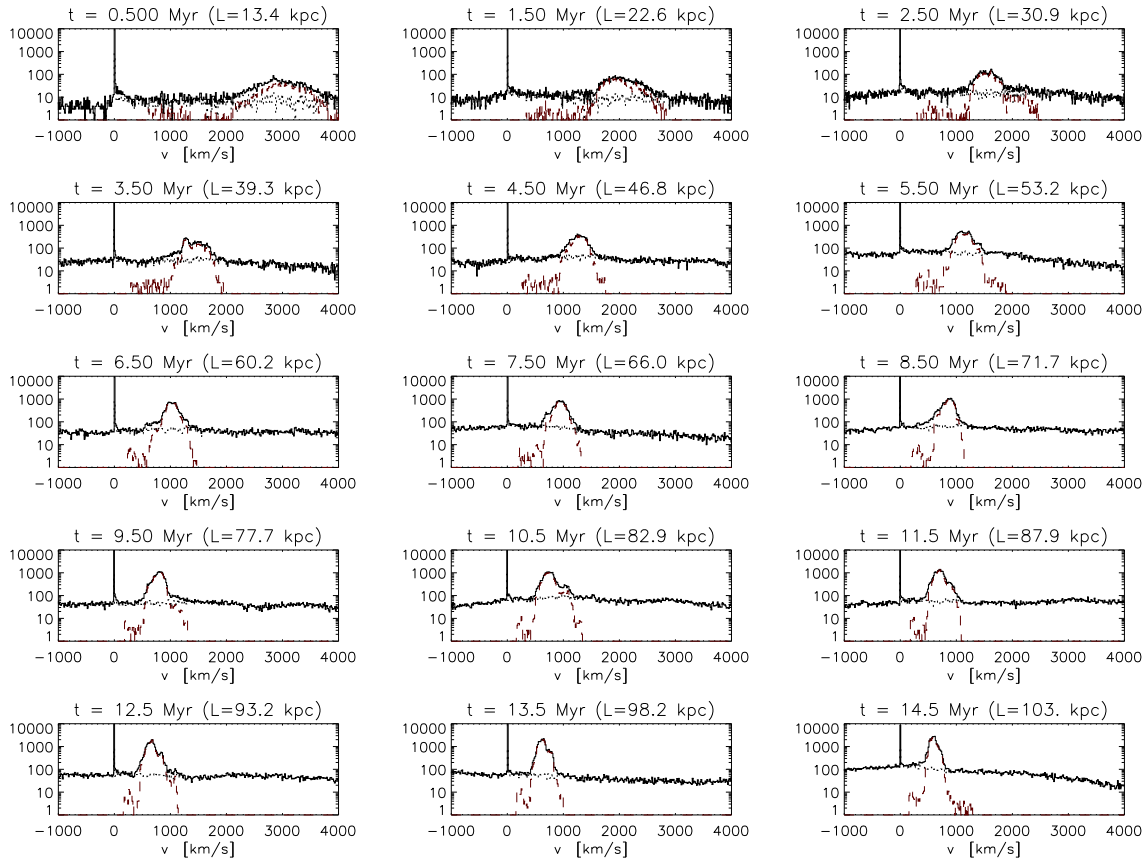

Figure 5.7: SAG model: Evolution of the velocity distribution for the M3 simulation in a slice through the core (averaged over 100 cells in Z direction for improved statistics). All cells located on one side of the core are considered for the histogram, the contributions from the shocked ambient (dashed) and the cocoon (dotted) are overplotted. The times and bow shock full lengths are given for every epoch, the inclination is $\theta = 90°$. The peak at $v = 0$ represents the undisturbed ambient gas.

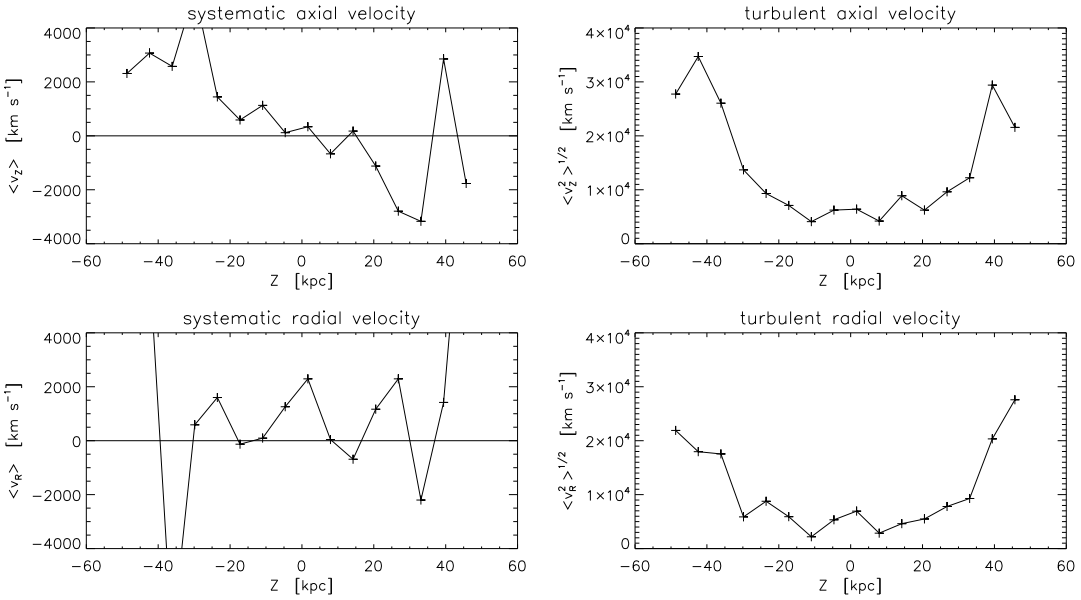

Figure 5.8: COC model: Systematic and turbulent velocities in the cocoon in the jet coordinate system, spatially resolved in axial direction. Only one half of the plane is considered here (upper half of Fig. 5.3), no projection.

energy in the cocoon are derived from the large-scale jet simulations ("macro physics"); the emission power, cool gas masses and turbulent velocities, in contrast, originate from the turbulence simulations ("micro physics"), with possibly additional contributions to the turbulent velocities by the large-scale models.

We will here focus on the results from the large-scale simulations, again using simulation run M3 at $t = 15$ Myr as reference. The turbulent velocities are only based on the large-scale turbulence, which cannot be easily translated into observable turbulent velocities. In Fig. 5.8, the cocoon motion is analyzed in the cylindrical coordinate system of the simulation (axial Z and radial R) for both contributions. This is done in 16 slices perpendicular to the full jet length. Near the jet heads ($Z \approx \pm 50$ kpc), very high velocities are found due to the backflow. More towards the midplane, the turbulent velocities level off to values of $\approx 5\,000$ km s^{-1} and the systematic velocities are around 1 000 km s^{-1}, with the axial component changing sign in the midplane. The systematic values are considerably distorted by large vortices (sizes of order of the slice width).

For comparison with observations, the radial velocities towards the observer are computed for 16 slices along the beam in the observer–jet beam plane for an inclination of $\theta = 70°$ (see Fig. 5.3). The slices are again 6.25 kpc wide, velocities are binned in 500 km s^{-1} bins and are positive for receding matter. The resulting histograms for six selected slices are shown in detail in Fig. 5.9, while Fig. 5.10 gives an overview by the position–velocity diagram. The large turbulent motion is responsible for the wide distributions, while systematic motion shifts them. There is a slight trend for positive (receding) velocities on the side where the jet approaches, and negative (approaching) velocities on the receding jet side. This can also be

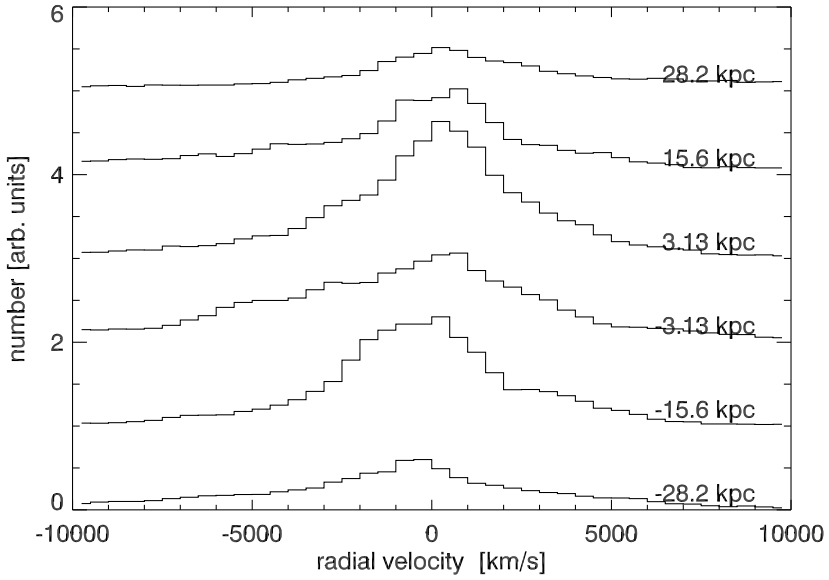

Figure 5.9: COC: Velocity distributions for some slices of M3 at 15 Myr. For clarity, they are shifted by 1, respectively. Inclination angle $\theta = 70°$, counts are in arbitrary units, 500 km s^{-1} bin size. The slices are labelled by their spatial offsets from the core in the plane of the sky, increasing in direction of the Z axis.

seen in Fig. 5.11, where the slice averages and standard deviations are shown. This effect comes from the orientation and is somewhat stronger for smaller inclination angles, but still, the systematic shift is smaller than the turbulent width. For an inclination of $\theta = 90°$, this systematic velocities are not present, as due to the axisymmetry the systematic R-velocity is exactly balanced by the mirrored contribution (on the other side of the axis) and only broadens the distribution insignificantly.

The kinetic jet power is the major energy input into the whole system. For the COC model, we measure the fraction of the input energy that is converted to kinetic energy of the cocoon gas. This can then be further related to kinetic energy in the cool emission line gas by the microscopic simulations. Fig. 5.12 shows the fraction of the total jet power that is found in the cocoon kinetic energy. As underdense jets convert most of their kinetic power into thermal energy (Section 3.5; O'Neill et al., 2005), with lighter jets showing higher thermalization, only a small percentage is found in the cocoon kinetic energy. For jets of different density contrast but with same lengths, we find values of 21 % for $\eta = 10^{-1}$, 11 % for $\eta = 10^{-2}$, 6 % for $\eta = 10^{-3}$ and 3 % for $\eta = 10^{-4}$ (M4L run). We note that the resolution study in Section 2.6 indicated that the cocoon kinetic energy fraction somewhat decreases for higher resolution. The kinetic energy in the shocked ambient gas is similar to or up to a factor of 2 higher than the kinetic energy in the cocoon, then generally levelling off with time towards cocoon values.

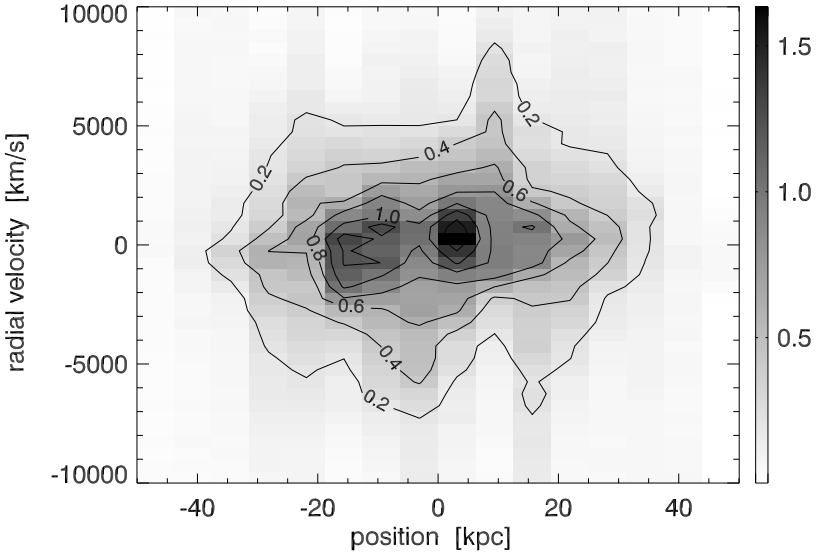

Figure 5.10: COC model: Position–velocity diagram of M3 at 15 Myr. Inclination $\theta = 70°$, bin contribution are in arbitrary units, 500 km s^{-1} bin size. Positions are offsets from the core in the plane of the sky.

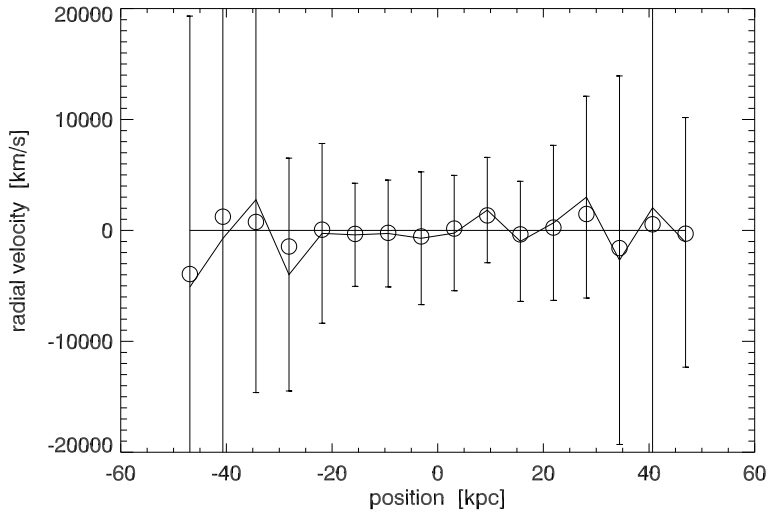

Figure 5.11: COC model: Velocity averages (solid line), median (circles) and standard deviation (vertical bars) for the slices through M3 at 15 Myr. Inclination angle $\theta = 70°$, positions are offsets from the core in the plane of the sky.

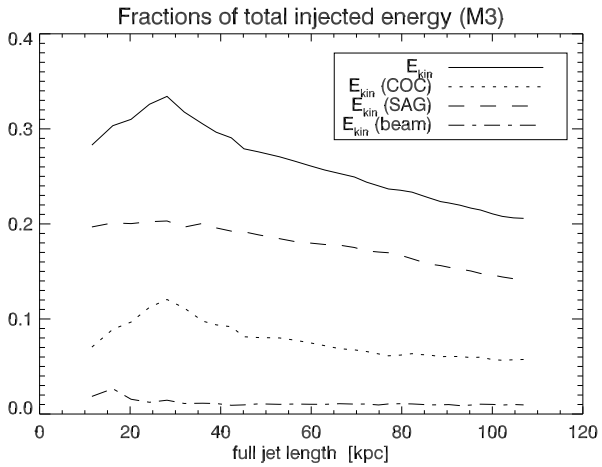

Figure 5.12: Fraction of the total jet power going into kinetic energy of the cocoon and the shocked ambient gas for the jet simulation M3. The beam contribution is *included* in cocoon, but it is also shown separately.

5.5 Discussion

We have analyzed our simulation data with respect to two models for the location of the emission-line gas found in high-redshift radio galaxies. In our SAG model, the emitting clouds are located in and dragged along with the shocked ambient gas, possibly emitting because they have been heated by the bow shock. The velocities of the shocked ambient gas indeed have values in the range of the observed ones for the approaching component, in particular if one considers the wider range due to the evolution of the source. Also, the gas on the approaching side shows higher approaching speeds than on the receding jet side, consistent with the observational data if only relative motion is considered. The contributions from the far side of the shocked ambient gas may be suppressed due to extincion. However, there is no sudden jump found in the systematic radial velocities near the core but only a gradual change between the two sides. Furthermore, the turbulent velocities are considerably smaller than the outward-directed systematic velocity. If the masses and densities of the emitting clouds have a wide range of masses and densities, resulting in different acceleration efficiencies, the width of the velocity distributions is expected to be larger since some clouds are dragged along with the ambient gas while others are only slightly accelerated. Yet, there is still no jump in the systematic velocity expected. One might also consider the morphology of the emission-line gas as a test. If the clouds are distributed all over the shocked ambient gas, the observed spatial distribution would be similar to the regions of enhanced emission in the bremsstrahlung emission maps (Sect. 4.4). Shells of line emission, however, are at odds with the observations (Fig. 5.1), where emission is concentrated towards the center.

The COC model assumes that the line-emitting gas clouds are generated in a turbulent multi-phase cocoon medium, stimulated by shearing and entrainment of ambient gas at the contact discontinuity. The magnitudes of the systematic velocities are of order 1000 km s^{-1}, however with notable variations due to large-scale vortices. The velocity distribution widths for the line-

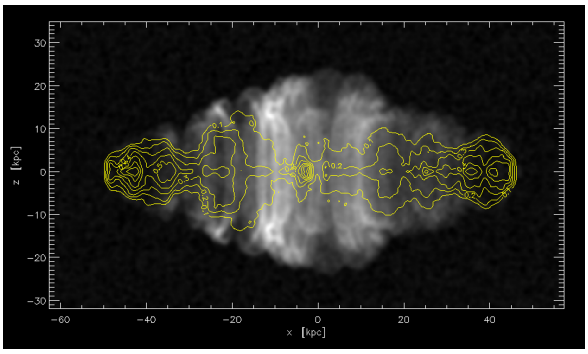

Figure 5.13: Simulated morphology for the COC model. The greyscale image shows the spatial distribution expected for emitting clouds within the cocoon. Contours show the extent of the radio emission (weighted with temperature to emphasize the lobes).

emitting gas have to be derived from the turbulence simulations of Krause & Alexander (2007), since the turbulent velocities seen in the large-scale simulations are only valid for the hot cocoon phase. The cooler and denser line-emitting gas shows lower turbulent velocities, which are in the range of few hundreds to 1000 km s^{-1}, depending on the density and temperature of the ambient gas (Krause & Alexander, 2007). These values are in reasonable agreement with the observed values. The systematic motion is found to be receding on the side of the approaching jet and approaching on the side of the receding jet side due to the large-scale backflow towards the midplane – in contrast to the directions inferred from observations. However, extinction effects may be important and weaken the emission from the far side of the cocoon. If this is considered, the near side contributes most to the emission and the systematic radial velocity (directed away from the jet axis, Fig. 5.8) could dominate on a brightness-weighted distribution. The observed jump in radial velocity at the core cannot be reproduced clearly. A transition between approaching and receding motion is, however, expected for sources not lying in the plane of the sky.

Fig. 5.13 shows the expected morphology of the emission-line gas if it is assumed to be distributed uniformly within the cocoon. The elongation along the radio source and the distribution around the center agree with the observed morphology. The correlation between emitted power and cocoon kinetic energy described by Krause (2008) allows a further check of this model. For 10^{60} erg of total injected power, 10^{58-59} erg are expected for the kinetic energy of the cocoon according to the large-scale simulations. For this energy, an emission-line luminosity of 10^{46-47} erg s^{-1} would be expected – much more than typically observed. We note, however, that this value is expected to decrease, if less ambient gas is available to the cocoon, e.g. due to suppressed entrainment.

We conclude that none of the models can explain all the kinematics and morphology of the emission-line gas at the current stage. Yet we pointed out possible explanations for the deviations. For the SAG model, the morphological differences seem to be most severe, while the COC model fails to reproduce the emission power. Both models cannot explain a distinct jump in radial velocities near the core. However, since this project is still in an early phase,

significant improvement can be expected and hence, further modelling is desirable to resolve the remaining problems.

6 Summary and Concluding Remarks

Jets are amongst the most spectacular features associated with active galactic nuclei (AGN) and understanding these objects properly is important not only for research on AGN themselves, but also for galaxy formation and evolution ("radio-mode" feedback) as well as the properties of galaxy clusters and cooling flows. Although the underlying physical model by Blandford & Rees (1974), interpreting double radio sources as being powered by two opposing jet beams, is more than 30 years old and there is a large number of observed sources, many questions are still unanswered. With increasing computing power within the last years, numerical simulations of jets including more physics have become possible and can help understanding the observed properties of radio sources. The central idea of the present work is to examine the effects of magnetic fields on the morphology, dynamics and evolution of powerful radio sources in clusters of galaxies. This may help understanding, why these sources often show stable and pronounced head regions and cocoons with mostly stable and smooth contact surfaces between the jet plasma and the ambient gas, while in hydrodynamic simulations they suffer from strong Kelvin-Helmholtz instabilities, giving them a ragged morphology. Also, observations of inverse-Compton emission from cocoons in the X-rays showed that magnetic fields in the cocoon are just a bit below equipartition, allowing them to have dynamical effects and at the same time raising the question, with regard to flux conservation, how these strong fields are created from a narrow equipartition jet beam that inflates the cocoon.

We performed magnetohydrodynamic simulations with the NIRVANA code (Ziegler & Yorke, 1997) in the realistic regime of very light (underdense) jets, which have so far only been studied with pure hydrodynamics. We attached great importance to a globally consistent setup by simulating both jets (back-to-back), keeping the bow shock inside the computational domain at all times and using a magnetic field topology with globally closed field lines. Yet, the simulations are restricted to axisymmetry and a uniform ambient density, which allows clearer identification of the underlying physical processes than possible in 3D and excludes effects of a varying density contrast during propagation.

The simulations show that already sub-equipartition fields with plasma $\beta \sim 10$ stabilize the jet head and suppress Kelvin-Helmholtz instabilities there, also reducing entrainment by more than a factor of 3. Additionally, we find a mechanism that is working in the jet head and amplifies the magnetic fields: In the presence of helical magnetic fields, the beam plasma generally starts to rotate and when it flows off the axis, forming the backflow, it is sheared and part of the huge kinetic power is transferred to magnetic energy. This effect is particularly strong in lighter jets. The resulting magnetic fields in the cocoon are strong enough to be able to damp Kelvin-Helmholtz instabilities there and stabilize the contact discontinuity between the jet plasma and the ambient cluster gas much more than anticipated without this effect. The shearing in the jet head furthermore provides an explanation for the strong (near equipartition) fields found in observations of jet cocoons.

The cocoons of very light jets exhibit strong turbulence, which is continuously driven by vortices from the jet head. The vortices excite pressure waves in the thick layers of shocked ambient gas. We suggest that these pressure waves, together with a bow shock that turns into an ordinary sound wave, correspond to the waves and ripples observed in sources as Perseus A and can be explained as a natural result of jet head dynamics instead of repeated activity of the galactic nucleus. The very light jets show bow shocks of low excentricity and low Mach number, and hence are able to reproduce bow shock properties found in X-ray observations of jet-related cavities, supporting our assumption of very underdense jets. The bow shocks and jet lengths evolve self-similarly, but the lateral cocoon expansion crucially depends on the cocoon pressure. For overpressured jets, the lateral expansion is also self-similar, but becomes slower when the cocoon approaches pressure balance with the ambient gas. The lighter jets also thermalize their kinetic energy efficiently, in agreement with results of other studies.

We calculated emission maps for both low-frequency radio emission as well as X-ray emission from inverse-Compton scattering of cosmic microwave background photons and thermal bremsstrahlung from the ambient cluster gas. The synchrotron maps, ignoring any Doppler beaming effects, show bright jets and pronounced jet heads. Inverse-Compton emission from the cocoon at X-ray energies appears relatively smooth and thermal bremsstrahlung emission from the ambient gas shows thick layers of enhanced brightness and cavities originating from the jet cocoon. Simulations also were also applied to the line-emitting ionized gas that is found in high-redshift radio galaxies, aligned with the radio source. Two models of the location and origin of this gas were examined, but so far it was not possible to reproduce all observed properties with the considered models.

The simulated sources qualitatively agree with observations of powerful radio sources. We believe that deviations are mostly due to the assumed axisymmetry and the uniform ambient density, based on results by Krause (2005), who relaxed these restrictions. However, it is clear that we will have to move to fully three-dimensional simulations, and first steps in this direction have been undertaken already. We are confident that the beams will then be significantly more stable and the cocoons will further approach the observed shapes for a realistic cluster profile. Relaxation of axisymmetry will be of great interest with regard to details of turbulence and the magnetic field topology in the cocoon, since conversion of toroidal to poloidal field will then occur and answer the question of magnetic field distribution in the cocoon. For high-redshift radio sources, a clumpy ambient medium is expected and it will be interesting to examine the resulting source morphology and how the total entrainment into the cocoon is modified by magnetic fields, possibly relevant for the understanding of the emission-line nebulae. A fascinating challenge will be to model the high-quality observations of Perseus A inside its cluster in 3D. Time-dependent jet injection will allow to study the long-term evolution of the source, where the cocoon plasma is expected to detach from the core and form two rising bubbles. Agreement of the pressure waves between simulation and observations encourages us that this can indeed be achieved by our jet model and we're on the right track.

Since the presented synchrotron maps but also the inverse-Compton maps computed from the simulation data show large, though expected, deviations from the observed appearance, modelling clearly has to be pushed forward by including the nonthermal component into the simulations. Only by including effects of reacceleration and cooling, a real comparison of simulation emission maps with observations will be possible. So far this has only been attempted by Tregillis et al. (2004), while the widely used numerical codes do not include this. It hence

may be desirable to persue this in the future. We note that another approach has already been chosen in the present simulations by implementing tracer particles, which are passively advected with the plasma and record their entire history of physical variables and shocks they are passing through. In a postprocessing step, the changes to an original electron distribution then may be tracked, yielding momentum spectra for the electrons at least at the locations of the (typically ≈ 1000) tracer particles. This part of the simulation data has not been used in this thesis, but the approach may be worthwhile to pursue.

Appendix A

Abbreviations and Variables

A.1 Abbreviations

2D	two-dimensional
2.5D	two-dimensional coordinates and three-dimensional vectors (sometimes also called 3D axisymmetric)
3D	three-dimensional
AGN	active galactic nucleus
BH	black hole
BLR	broad-line region
EH	synchrotron emission method deriving emissivity only from thermal pressure
EMSp	synchrotron emission method with magnetic field magnitude, relativistic particles are traced by thermal pressure
EMS	synchrotron emission method with magnetic field magnitude (scalar)
EMV	synchrotron emission method with magnetic field vectors
FWHM	full width at half maximum
HD	hydrodynamics
MHD	magnetohydrodynamics
NLR	narrow-line region

A.2 Units

c	speed of light	$= 2.9979 \times 10^{10}$ cm s^{-1}
pc	parsec	$= 3.086 \times 10^{18}$ cm
kpc	kiloparsec	$= 3.086 \times 10^{21}$ cm
$M_\odot$	solar mass	$= 1.99 \times 10^{33}$ g
yr	year	$= 3.16 \times 10^{7}$ s
eV	electron volt	$= 1.60 \times 10^{-12}$ erg
m_p	proton mass	$= 1.67 \times 10^{-24}$ g
k_B	Boltzmann constant	$= 1.38 \times 10^{-16}$ erg K^{-1}
nT	nano Tesla	$= 10\,\mu$G

A.3 Variables

(Z, R, ϕ)	cylindrical coordinates (simulation grid frame)
(x, y, z)	cartesian coordinates (observer's frame)
θ	inclination angle (between the observer's line of sight and the jet axis
ρ	density
n	particle number density
T	temperature
e	internal energy density
p	thermal gas pressure
$\mathbf{v}$	velocity
$\mathbf{B}$	magnetic field
$\mathbf{j}$	current density
$\mathbf{B}_\mathrm{p}$	poloidal magnetic field (in Z–R plane)
B_ϕ	toroidal magnetic field
β	plasma beta $= 8\pi p/B^2$
η	density contrast $= \rho_\mathrm{j}/\rho_\mathrm{a}$
r_j	jet radius
c_s	sound speed
c_A	Alfvén speed
c_ms	magnetosonic speed
γ	adiabatic index
$\bar{\mu}$	mean particle mass in units of m_p
ϵ	volumetric emissivity
Q_a	variable Q in ambient gas
Q_j	variable Q in jet
t	time
l	length
$\dot{M}$	accretion rate, mass flux
M_BH	black hole mass
r_S	Schwarzschild radius
L_Edd	Eddington luminosity
z	redshift (in cosmological context)

Bibliography

Abramowicz, M. A., Czerny, B., Lasota, J. P., & Szuszkiewicz, E. 1988, ApJ, 332, 646

Alexander, P. 2000, MNRAS, 319, 8

Alexander, P., Brown, M. T., & Scott, P. F. 1984, MNRAS, 209, 851

Alexander, P., & Leahy, J. P. 1987, MNRAS, 225, 1

Aloy, M. A., Ibáñez, J. M., Martí, J. M., Gómez, J.-L., & Müller, E. 1999, ApJ, 523,

Antonucci, R. 1993, ARA&A, 31, 473

Antonucci, R. R. J., & Miller, J. S. 1985, ApJ, 297, 621

Baade, W., & Minkowski, R. 1954, ApJ, 119, 206

Balbus, S. A., & Hawley, J. F. 1991, ApJ, 376, 214

Balsara, D. S., & Norman, M. L. 1992, ApJ, 393, 631

Barthel, P. D. 1989, ApJ, 336, 606

Begelman, M. C. 1996, in Cygnus A – Study of a Radio Galaxy, ed. C. L. Carilli & D. E. Harris (Cambridge University Press), 209

Begelman, M. C., & Cioffi, D. F. 1989, ApJ, 345, L21

Best, P. N., Kauffmann, G., Heckman, T. M., Brinchmann, J., Charlot, S., Ivezić, Ž., & White, S. D. M. 2005, MNRAS, 362, 25

Bicknell, G. V., Dopita, M. A., & O'Dea, C. P. O. 1997, ApJ, 485, 112

Bîrzan, L., Rafferty, D. A., McNamara, B. R., Wise, M. W., & Nulsen, P. E. J. 2004, ApJ, 607, 800

Blandford, R. 2008, in Astronomical Society of the Pacific Conference Series, ed. T. A. Rector & D. S. De Young, Vol. 386, 3

Blandford, R. D., & Payne, D. G. 1982, MNRAS, 199, 883

Blandford, R. D., & Rees, M. J. 1974, MNRAS, 169, 395

Blandford, R. D., & Znajek, R. L. 1977, MNRAS, 179, 433

Bodo, G., Massaglia, S., Ferrari, A., & Trussoni, E. 1994, A&A, 283, 655

Bodo, G., Rosner, R., Ferrari, A., & Knobloch, E. 1996, ApJ, 470, 797

Bodo, G., Rossi, P., Massaglia, S., Ferrari, A., Malagoli, A., & Rosner, R. 1998, A&A, 333, 1117

Bregman, J. N., Fabian, A. C., Miller, E. D., & Irwin, J. A. 2006, ApJ, 642, 746

Bridle, A. H. 1982, in Extragalactic Radio Sources, ed. D. S. Heeschen & C. M. Wade, Vol. 97, 121–128

Bridle, A. H., & Perley, R. A. 1984, ARA&A, 22, 319

Brunetti, G., Bondi, M., Comastri, A., & Setti, G. 2002, A&A, 381, 795

Brunetti, G., Setti, G., & Comastri, A. 1997, A&A, 325, 898

Cabral, B., & Leedom, L. C. 1993, in SIGGRAPH '93: Proceedings of the 20th annual conference on Computer graphics and interactive techniques (New York, NY, USA: ACM), 263–270

Camenzind, M. 1990, in Reviews in Modern Astronomy, ed. G. Klare, Vol. 3, 234–265

Camenzind, M. 2007, Compact Objects in Astrophysics: White Dwarfs, Neutron Stars, and Black Holes, Astronomy and astrophysics library (Berlin: Springer-Verlag, 2007)

Carilli, C. L., Perley, R. A., Dreher, J. W., & Leahy, J. P. 1991, ApJ, 383, 554

Carilli, C. L., & Taylor, G. B. 2002, ARA&A, 40, 319

Carvalho, J. C., & O'Dea, C. P. 2002a, ApJS, 141, 337

—. 2002b, ApJS, 141, 371

Celotti, A., & Blandford, R. D. 2001, in Black Holes in Binaries and Galactic Nuclei, ed. L. Kaper, E. P. J. van den Heuvel, & P. A. Woudt, 206

Celotti, A., Ghisellini, G., & Chiaberge, M. 2001, MNRAS, 321, L1

Cheung, C. C., Harris, D. E., & Stawarz, Ł. 2007, ApJ, 663,

Choi, E., Wiita, P. J., & Ryu, D. 2007, ApJ, 655, 769

Cioffi, D. F., & Blondin, J. M. 1992, ApJ, 392, 458

Clarke, D. A. 1993, in Jets in Extragalactic Radio Sources, ed. H. J. Röser & K. Meisenheimer, Vol. 421, 243

Clarke, D. A., Burns, J. O., & Norman, M. L. 1989, ApJ, 342, 700

Clarke, D. A., Harris, D. E., & Carilli, C. L. 1997, MNRAS, 284, 981

Clarke, D. A., Norman, M. L., & Burns, J. O. 1986, ApJ, 311, L63

Cox, C. I., Gull, S. F., & Scheuer, P. A. G. 1991, MNRAS, 252, 558

Croom, S. M., Smith, R. J., Boyle, B. J., Shanks, T., Miller, L., Outram, P. J., & Loaring, N. S. 2004, MNRAS, 349, 1397

Croston, J. H., Hardcastle, M. J., Harris, D. E., Belsole, E., Birkinshaw, M., & Worrall, D. M. 2005, ApJ, 626, 733

Croton, D. J., Springel, V., White, S. D. M., De Lucia, G., Frenk, C. S., Gao, L., Jenkins, A., Kauffmann, G., Navarro, J. F., & Yoshida, N. 2006, MNRAS, 365, 11

De Young, D. S. 2002, New Astronomy Review, 46, 393

Done, C., Gierliński, M., & Kubota, A. 2007, A&A Rev., 15, 1

Evans, C. R., & Hawley, J. F. 1988, ApJ, 332, 659

Evrard, A. E., Metzler, C. A., & Navarro, J. F. 1996, ApJ, 469, 494

Fabian, A. C. 1994, ARA&A, 32, 277

Fabian, A. C., Reynolds, C. S., Taylor, G. B., & Dunn, R. J. H. 2005, MNRAS, 363, 891

Fabian, A. C., Sanders, J. S., Allen, S. W., Crawford, C. S., Iwasawa, K., Johnstone, R. M., Schmidt, R. W., & Taylor, G. B. 2003, MNRAS, 344, L43

Fabian, A. C., Sanders, J. S., Taylor, G. B., Allen, S. W., Crawford, C. S., Johnstone, R. M., & Iwasawa, K. 2006, MNRAS, 366, 417

Falle, S. A. E. G. 1991, MNRAS, 250, 581

Fanaroff, B. L., & Riley, J. M. 1974, MNRAS, 167, 31

Feigelson, E. D., Laurent-Muehleisen, S. A., Kollgaard, R. I., & Fomalont, E. B. 1995, ApJ, 449,

Fender, R. P., Belloni, T. M., & Gallo, E. 2004, MNRAS, 355, 1105

Ferrari, A. 1998, ARA&A, 36, 539

Fixsen, D. J., Cheng, E. S., Gales, J. M., Mather, J. C., Shafer, R. A., & Wright, E. L. 1996, ApJ, 473, 576

Gabuzda, D. C., Vitrishchak, V. M., Mahmud, M., & O'Sullivan, S. P. 2008, MNRAS, 384, 1003

Gaibler, V., & Camenzind, M. 2008, in High Performance Computing in Science and Engineering '08 (accepted)

Gaibler, V., Camenzind, M., & Krause, M. 2007, Astronomische Nachrichten, 328, 668

Gaibler, V., Camenzind, M., & Krause, M. 2008, in Astronomical Society of the Pacific Conference Series, ed. T. A. Rector & D. S. De Young, Vol. 386, 32

Gaibler, V., Vigelius, M., Krause, M., & Camenzind, M. 2006, in High Performance Computing in Science and Engineering '06, ed. W. E. Nagel, W. Jäger, & M. Resch (Springer), 35

Garrington, S. T., Leahy, J. P., Conway, R. G., & Laing, R. A. 1988, Nature, 331, 147

Ghisellini, G. 2008, ArXiv e-prints, 801

Gizani, N. A. B., & Leahy, J. P. 2003, MNRAS, 342, 399

Goodger, J. L., Hardcastle, M. J., Croston, J. H., Kassim, N. E., & Perley, R. A. 2008, MNRAS, 386, 337

Graham, J., Fabian, A. C., & Sanders, J. S. 2008, MNRAS, 386, 278

Hardcastle, M. J., Alexander, P., Pooley, G. G., & Riley, J. M. 1999, MNRAS, 304, 135

Hardcastle, M. J., & Croston, J. H. 2005, MNRAS, 363, 649

Hardcastle, M. J., Worrall, D. M., Kraft, R. P., Forman, W. R., Jones, C., & Murray, S. S. 2003, ApJ, 593, 169

Hardee, P. E. 1984, ApJ, 277, 106

—. 2000, ApJ, 533, 176

—. 2007, ApJ, 664, 26

Hardee, P. E., & Clarke, D. A. 1992, ApJ, 400,

—. 1995a, ApJ, 449, 119

—. 1995b, ApJ, 451,

Hardee, P. E., Clarke, D. A., & Howell, D. A. 1995, ApJ, 441, 644

Harris, D. E., Carilli, C. L., & Perley, R. A. 1994, Nature, 367, 713

Harris, D. E., & Krawczynski, H. 2006, ARA&A, 44, 463

Heavens, A. F., & Meisenheimer, K. 1987, MNRAS, 225, 335

Heinz, S., Brüggen, M., Young, A., & Levesque, E. 2006, MNRAS, 373,

Jackson, J. D. 2002, Klassische Elektrodynamik, 3rd edn. (Berlin, New York: de Gruyter)

Jones, T. W. 2008, in Extragalactic Jets: Theory and Observations from Radio to Gamma Ray, Volume 386, ed. T. A. Rector & D. S. D. Young (Astronomical Society of the Pacific), 398–309

Jüttner, F. 1911, Annalen der Physik, 339, 856

Kaiser, C. R., & Alexander, P. 1997, MNRAS, 286, 215

Karzas, W. J., & Latter, R. 1961, ApJS, 6, 167

Kataoka, J., & Stawarz, . L. 2005, ApJ, 622, 797

Keppens, R., Meliani, Z., van der Holst, B., & Casse, F. 2008, A&A, 486, 663

Komissarov, S. S. 1999, MNRAS, 308, 1069

Komissarov, S. S., & Falle, S. A. E. G. 1998, MNRAS, 297, 1087

Kormendy, J. 2004, in Coevolution of Black Holes and Galaxies, ed. L. C. Ho, 1

Kössl, D., Müller, E., & Hillebrandt, W. 1990a, A&A, 229, 378

—. 1990b, A&A, 229, 397

—. 1990c, A&A, 229, 401

Kovalev, Y. Y., Lister, M. L., Homan, D. C., & Kellermann, K. I. 2007, ApJ, 668, L27

Krause, M. 2003, A&A, 398, 113

—. 2005, A&A, 431, 45

Krause, M., & Alexander, P. 2007, MNRAS, 376, 465

Krause, M., & Camenzind, M. 2001, A&A, 380, 789

Krause, M., Gaibler, V., & Camenzind, M. 2005, in High Performance Computing in Science and Engineering '05. Edited by Wolfgang E. Nagel, Willi Jäger, and Michael Resch. Springer 2005, 3

Krause, M. G. H. 2008, Memorie della Societa Astronomica Italiana, 79, to be published

Kundt, W., & Gopal-Krishna. 1980, Nature, 288, 149

Laidlaw, D. H., Davidson, J. S., Miller, T. S., Silva, M. d., Kirby, R. M., Warren, W. H., & Tarr, M. 2001, in VIS '01: Proceedings of the conference on Visualization '01 (Washington, DC, USA: IEEE Computer Society), 143–150

Laing, R. A. 1981, ApJ, 248, 87

—. 1988, Nature, 331, 149

Laing, R. A., Riley, J. M., & Longair, M. S. 1983, MNRAS, 204, 151

Lazio, T. J. W., Cohen, A. S., Kassim, N. E., Perley, R. A., Erickson, W. C., Carilli, C. L., & Crane, P. C. 2006, ApJ, 642,

Leahy, J. P. 2000, An Atlas of DRAGNs, http://www.jb.man.ac.uk/atlas/

Leahy, J. P., Muxlow, T. W. B., & Stephens, P. W. 1989, MNRAS, 239, 401

Leahy, J. P., & Williams, A. G. 1984, MNRAS, 210, 929

Leismann, T., Antón, L., Aloy, M. A., Müller, E., Martí, J. M., Miralles, J. A., & Ibáñez, J. M. 2005, A&A, 436, 503

Li, H., Lapenta, G., Finn, J. M., Li, S., & Colgate, S. A. 2006, ApJ, 643, 92

Lin, Y. T., Mohr, J. J., & Stanford, S. A. 2003, ApJ, 591, 749

Lind, K. R., Payne, D. G., Meier, D. L., & Blandford, R. D. 1989, ApJ, 344, 89

Liu, R., Pooley, G., & Riley, J. M. 1992, MNRAS, 257, 545

Longair, M. S. 1994, High energy astrophysics. Vol. 2: Stars, the Galaxy and the interstellar medium, 2nd edn. (Cambridge: Cambridge University Press,)

Macchetto, F., Marconi, A., Axon, D. J., Capetti, A., Sparks, W., & Crane, P. 1997, ApJ, 489, 579

Magliocchetti, M., & Brüggen, M. 2007, MNRAS, 379, 260

Magorrian, J., Tremaine, S., Richstone, D., Bender, R., Bower, G., Dressler, A., Faber, S. M., Gebhardt, K., Green, R., Grillmair, C., Kormendy, J., & Lauer, T. 1998, AJ, 115, 2285

Marti, J. M. A., Mueller, E., Font, J. A., Ibanez, J. M. A., & Marquina, A. 1997, ApJ, 479, 151

Massaglia, S., Bodo, G., & Ferrari, A. 1996, A&A, 307, 997

Matthews, A. P., & Scheuer, P. A. G. 1990a, MNRAS, 242, 616

—. 1990b, MNRAS, 242, 623

McNamara, B. R., & Nulsen, P. E. J. 2007, ARA&A, 45, 117

McNamara, B. R., Nulsen, P. E. J., Wise, M. W., Rafferty, D. A., Carilli, C., Sarazin, C. L., & Blanton, E. L. 2005, Nature, 433, 45

Meisenheimer, K., & Hippelein, H. 1992, A&A, 264, 455

Meisenheimer, K., Röser, H. J., Hiltner, P. R., Yates, M. G., Longair, M. S., Chini, R., & Perley, R. A. 1989, A&A, 219, 63

Meisenheimer, K., Yates, M. G., & Röser, H. J. 1997, A&A, 325, 57

Migliori, G., Grandi, P., Palumbo, G. G. C., Brunetti, G., & Stanghellini, C. 2007, ApJ, 668, 203

Miley, G., & De Breuck, C. 2008, A&A Rev., 15, 67

Mioduszewski, A. J., Hughes, P. A., & Duncan, G. C. 1997, ApJ, 476, 649

Miura, A., & Pritchett, P. L. 1982, J. Geophys. Res., 87, 7431

Mizuno, Y., Hardee, P., & Nishikawa, K. I. 2007, ApJ, 662, 835

Morganti, R. 2008, in Extragalactic Jets: Theory and Observation from Radio to Gamma Ray, ed. T. A. Rector & D. S. De Young, Vol. 386, 210

Morganti, R., Tadhunter, C. N., & Oosterloo, T. A. 2005, A&A, 444,

Mullin, L. M., Riley, J. M., & Hardcastle, M. J. 2008, ArXiv e-prints, 806

Narayan, R., & Yi, I. 1995, ApJ, 444, 231

Nesvadba, N. P. H., Lehnert, M. D., De Breuck, C., Gilbert, A. M., & van Breugel, W. 2008, submitted to A&A

Nishikawa, K. I., Koide, S., Sakai, J. I., Christodoulou, D. M., Sol, H., & Mutel, R. L. 1997, ApJ, 483,

Norman, M. L. 1993, in Astrophysical Jets, ed. D. Burgarella, M. Livio, & C. P. O'Dea (Cambridge University Press), 211–239

Norman, M. L., Winkler, K. H. A., & Smarr, L. 1983, in Astrophysical Jets, ed. A. Ferrari & A. G. Pacholczyk, Vol. 103, 227–250

Norman, M. L., Winkler, K. H. A., Smarr, L., & Smith, M. D. 1982, A&A, 113, 285

Nulsen, P. E. J., Hambrick, D. C., McNamara, B. R., Rafferty, D., Birzan, L., Wise, M. W., & David, L. P. 2005, ApJ, 625,

O'Neill, S. M., Tregillis, I. L., Jones, T. W., & Ryu, D. 2005, ApJ, 633, 717

Osterbrock, D. E., & Shaw, R. A. 1988, ApJ, 327, 89

Pacholczyk, A. G. 1970, Radio astrophysics. Nonthermal processes in galactic and extragalactic sources (Series of Books in Astronomy and Astrophysics, San Francisco: Freeman, 1970)

Pelletier, G. 2007, in Lecture Notes in Physics, Berlin Springer Verlag, ed. J. Ferreira, C. Dougados, & E. Whelan, Vol. 723, 77

Perley, R. A., Dreher, J. W., & Cowan, J. J. 1984, ApJ, 285,

Perley, R. A., Röser, H. J., & Meisenheimer, K. 1997, A&A, 328, 12

Perucho, M., Hanasz, M., Martí, J. M., & Miralles, J. A. 2007, Phys. Rev. E, 75, 056312

Perucho, M., & Martí, J. M. 2007, MNRAS, 382, 526

Peterson, J. R., Paerels, F. B. S., Kaastra, J. S., Arnaud, M., Reiprich, T. H., Fabian, A. C., Mushotzky, R. F., Jernigan, J. G., & Sakelliou, I. 2001, A&A, 365,

Rafferty, D. A., McNamara, B. R., Nulsen, P. E. J., & Wise, M. W. 2006, ApJ, 652, 216

Reynolds, C. S., Heinz, S., & Begelman, M. C. 2001, ApJ, 549, L179

—. 2002, MNRAS, 332, 271

Richards, G. T., Strauss, M. A., Fan, X., Hall, P. B., Jester, S., Schneider, D. P., Vanden Berk, D. E., Stoughton, C., Anderson, S. F., Brunner, R. J., Gray, J., Gunn, J. E., Ivezić, Ž., Kirkland, M. K., Knapp, G. R., Loveday, J., Meiksin, A., Pope, A., Szalay, A. S., Thakar, A. R., Yanny, B., York, D. G., Barentine, J. C., Brewington, H. J., Brinkmann, J., Fukugita, M., Harvanek, M., Kent, S. M., Kleinman, S. J., Krzesiński, J., Long, D. C., Lupton, R. H., Nash, T., Neilsen, Jr., E. H., Nitta, A., Schlegel, D. J., & Snedden, S. A. 2006, AJ, 131, 2766

Roca-Sogorb, M., Perucho, M., Gómez, J. L., Martí, J. M., Antón, L., Aloy, M. A., & Agudo, I. 2008, in Extragalactic Jets: Theory and Observation from Radio to Gamma Ray, ed. T. A. Rector & D. S. De Young, Vol. 386, 488

Romanova, M. M., & Lovelace, R. V. E. 1992, A&A, 262, 26

Rosen, A., Hardee, P. E., Clarke, D. A., & Johnson, A. 1999a, ApJ, 510, 136

Rosen, A., Hughes, P. A., Duncan, G. C., & Hardee, P. E. 1999b, ApJ, 516, 729

Rybicki, G. B., & Lightman, A. P. 1979, Radiative processes in astrophysics (New York, Wiley-Interscience, 1979. 393 p.)

Sanders, J. S., & Fabian, A. C. 2007, MNRAS, 381, 1381

Saxton, C. J., Bicknell, G. V., & Sutherland, R. S. 2002a, ApJ, 579, 176

Saxton, C. J., Bicknell, G. V., Sutherland, R. S., & Midgley, S. 2005, MNRAS, 359, 781

Saxton, C. J., Sutherland, R. S., Bicknell, G. V., Blanchet, G. F., & Wagner, S. J. 2002b, A&A, 393, 765

Scheck, L., Aloy, M. A., Martí, J. M., Gómez, J. L., & Müller, E. 2002, MNRAS, 331, 615

Scheuer, P. A. G. 1974, MNRAS, 166, 513

Scheuer, P. A. G. 1982, in Extragalactic Radio Sources, ed. D. S. Heeschen & C. M. Wade, Vol. 97, 163–165

—. 1995, MNRAS, 277, 331

Shabala, S., & Alexander, P. 2007, Ap&SS, 311, 311

Shakura, N. I., & Sunyaev, R. A. 1973, A&A, 24, 337

Shu, F. H. 1992, Physics of Astrophysics, Vol. II Gas Dynamics (University Science Books, ISBN 0-935702-65-2, 476 pp)

Smith, M. D., Norman, M. L., Winkler, K. H. A., & Smarr, L. 1985, MNRAS, 214, 67

Steenbrugge, K. C., & Blundell, K. M. 2008, MNRAS, 388, 1457

Stone, J. M., & Norman, M. L. 1992, ApJS, 80, 791

Sun, M., Jones, C., Murray, S. S., Allen, S. W., Fabian, A. C., & Edge, A. C. 2003, ApJ, 587, 619

Sutherland, R. S., & Bicknell, G. V. 2007, ApJS, 173, 37

Sutherland, R. S., & Dopita, M. A. 1993, ApJS, 88, 253

Tamura, T., Kaastra, J. S., Peterson, J. R., Paerels, F. B. S., Mittaz, J. P. D., Trudolyubov, S. P., Stewart, G., Fabian, A. C., Mushotzky, R. F., Lumb, D. H., & Ikebe, Y. 2001, A&A, 365,

Tregillis, I. L., Jones, T. W., & Ryu, D. 2001, ApJ, 557, 475

—. 2004, ApJ, 601, 778

Turk, G., & Banks, D. 1996, in SIGGRAPH '96: Proceedings of the 23rd annual conference on Computer graphics and interactive techniques (New York, NY, USA: ACM), 453–460

Urry, C. M., & Padovani, P. 1995, PASP, 107, 803

van Breugel, W., De Breuck, C., Stanford, S. A., Stern, D., Röttgering, H., & Miley, G. 1999, ApJ, 518,

van Ojik, R., Roettgering, H. J. A., Miley, G. K., & Hunstead, R. W. 1997, A&A, 317, 358

Vikhlinin, A., Kravtsov, A., Forman, W., Jones, C., Markevitch, M., Murray, S. S., & Van Speybroeck, L. 2006, ApJ, 640, 691

Villar-Martín, M. 2007, New Astronomy Review, 51, 194

Wardle, J. F. C., & Aaron, S. E. 1997, MNRAS, 286, 425

Willott, C. J., Rawlings, S., Blundell, K. M., Lacy, M., & Eales, S. A. 2001, MNRAS, 322, 536

Wilson, A. S., Smith, D. A., & Young, A. J. 2006, ApJ, 644,

Wise, M. W., McNamara, B. R., Nulsen, P. E. J., Houck, J. C., & David, L. P. 2007, ApJ, 659, 1153

Zanni, C., Bodo, G., Rossi, P., Massaglia, S., Durbala, A., & Ferrari, A. 2003, A&A, 402, 949

Zanni, C., Murante, G., Bodo, G., Massaglia, S., Rossi, P., & Ferrari, A. 2005, A&A, 429, 399

Zensus, J. A. 1997, ARA&A, 35, 607

Ziegler, U., & Yorke, H. W. 1997, Computer Physics Communications, 101, 54

Herzlichen Dank...

Diese Arbeit ist beileibe nicht im luftleeren Raum ($n \sim 0.01$ cm^{-3}) entstanden, sondern viele Leute haben dazu in der einen oder anderen Weise beigetragen. Besonders bedanken möchte ich mich bei...

... Max Camenzind für die Möglichkeit, diese Arbeit durchführen zu können, die zahlreichen anregenden Diskussionen und die stete Unterstützung,

... Klaus Meisenheimer für die prompte Übernahme des Zweitgutachtens,

... dem SFB 439 der Deutschen Forschungsgemeinschaft für die Finanzierung,

... dem HLRS in Stuttgart für die begehrte Rechenzeit,

... Martin Krause für die fortdauernde Zusammenarbeit und Unterstützung sowie die Einführung in die Jet-Physik,

... Marc Schartmann für den wertvollen gegenseitigen Austausch und das Korrekturlesen,

... meiner Verlobten Nicole ebenfalls für das Korrekturlesen und die unendliche Unterstützung,

... allen aktuellen und früheren Mitgliedern der Theoriegruppe, insbesondere meinem Gegenüber Steffen, Matteo, Jamie, Roman, Jürgen und den "Altvorderen" José und Matthias, für die überaus angenehme Atmosphäre,

... den Kaffee- und Teetrinkern sowie Kantinengängern der LSW für entspannende Pausen und Gespräche sowie geteiltes Leid,

... sowie allen Menschen, die mich in den letzten Jahren so sehr unterstützt haben.